

VOLUME 76

JULY 20, 1972

NUMBER 15

JPCHAX

THE JOURNAL OF
PHYSICAL
CHEMISTRY

PUBLISHED BIWEEKLY BY THE AMERICAN CHEMICAL SOCIETY

THE JOURNAL OF PHYSICAL CHEMISTRY

BRYCE CRAWFORD, Jr., *Editor*

STEPHEN PRAGER, *Associate Editor*

ROBERT W. CARR, Jr., FREDERIC A. VAN-CATLEDGE, *Assistant Editors*

EDITORIAL BOARD: A. O. ALLEN (1970-1974), J. R. BOLTON (1971-1975),
F. S. DAINTON (1972-1976), M. FIXMAN (1970-1974),
H. S. FRANK (1970-1974), R. R. HENTZ (1972-1976), J. R. HUIZENGA (1969-1973),
W. J. KAUZMANN (1969-1973), R. L. KAY (1972-1976), W. R. KRIGBAUM (1969-1973),
R. A. MARCUS (1968-1972), W. J. MOORE (1969-1973), J. A. POPLE (1971-1975),
B. S. RABINOVITCH (1971-1975), H. REISS (1970-1974), S. A. RICE (1969-1975),
F. S. ROWLAND (1968-1972), R. L. SCOTT (1968-1972),
R. SEIFERT (1968-1972), W. A. ZISMAN (1972-1976)

CHARLES R. BERTSCH, *Manager, Editorial Production*

AMERICAN CHEMICAL SOCIETY, 1155 Sixteenth St., N.W., Washington, D. C. 20036

Books and Journals Division

JOHN K CRUM, *Director*

JOSEPH H. KUNEY, *Head, Business Operations Department*

RUTH REYNARD, *Assistant to the Director*

©Copyright, 1972, by the American Chemical Society. Published biweekly by the American Chemical Society at 20th and Northampton Sts., Easton, Pa. 18042. Second-class postage paid at Washington, D. C., and at additional mailing offices.

All manuscripts should be sent to *The Journal of Physical Chemistry*, Department of Chemistry, University of Minnesota, Minneapolis, Minn. 55455.

Additions and Corrections are published once yearly in the final issue. See Volume 75, Number 26 for the proper form.

Extensive or unusual alterations in an article after it has been set in type are made at the author's expense, and it is understood that by requesting such alterations the author agrees to defray the cost thereof.

The American Chemical Society and the Editor of *The Journal of Physical Chemistry* assume no responsibility for the statements and opinions advanced by contributors.

Correspondence regarding accepted copy, proofs, and reprints should be directed to Editorial Production Office, American Chemical Society, 20th and Northampton Sts., Easton, Pa. 18042. Manager: CHARLES R. BERTSCH. Assistant Editor: EDWARD A. BORGER.

Advertising Office: Centcom, Ltd. (formerly Century Communications Corporation), 142 East Avenue, Norwalk, Conn. 06851.

Business and Subscription Information

Remittances and orders for subscriptions and for single copies,

and notices of changes of address and new professional connections, and claims for missing numbers should be sent to the Subscription Service Department, American Chemical Society, 1155 Sixteenth St., N.W., Washington, D. C. 20036. Allow 4 weeks for changes of address. Please include an old address label with the notification.

Claims for missing numbers will not be allowed (1) if received more than sixty days from date of issue, (2) if loss was due to failure of notice of change of address to be received before the date specified in the preceding paragraph, or (3) if the reason for the claim is "missing from files."

Subscription rates (1972): members of the American Chemical Society, \$20.00 for 1 year; to nonmembers, \$60.00 for 1 year. Those interested in becoming members should write to the Admissions Department, American Chemical Society, 1155 Sixteenth St., N.W., Washington, D. C. 20036. Postage to Canada and countries in the Pan-American Union, \$5.00; all other countries, \$6.00. Single copies for current year: \$3.00. Rates for back issues from Volume 56 to date are available from the Special Issues Sales Department, 1155 Sixteenth St., N.W., Washington, D. C. 20036.

This publication and the other ACS periodical publications are now available on microfilm. For information write to: MICROFILM, Special Issues Sales Department, 1155 Sixteenth St., N.W., Washington, D. C. 20036.

THE JOURNAL OF PHYSICAL CHEMISTRY

Volume 76, Number 15 July 20, 1972

JPCHAx 76(15) 2061-2186 (1972)

- Electron Spin Resonance Study of the Far-Ultraviolet Photolysis of Some Inorganic and Organic Compounds
..... **Keiji Kuwata,* Yashige Kotake, Koji Inada, and Mitsuo Ono** 2061
- A Comparison of the Radiolysis of Liquid Bromotrifluoromethane with the Radiolysis of
Liquid Trifluoroiodomethane **I. McAlpine and H. Sutcliffe*** 2070
- Electron and Hydrogen Atom Attachment to Aromatic Carbonyl Compounds in Aqueous Solution. Absorption
Spectra and Dissociation Constants of Ketyl Radicals **E. Hayon,* T. Ibata, N. N. Lichtin, and M. Simic** 2072
- Powder ENDOR Line Shapes: Nuclear Relaxation Induced by Motion of Nearby Electron Spins
..... **Daniel S. Leniart,* James S. Hyde, and Jacques C. Vedrine** 2079
- Proton ENDOR of γ -Irradiated Y-Type Zeolites
..... **Jacques C. Vedrine, James S. Hyde, and Daniel S. Leniart*** 2087
- A Spectroscopic Study of the Propionitrile-Iodine Molecular Complex
..... **John A. Maguire* and John J. Banewicz** 2098
- A Spectrophotometric and Thermodynamic Study of Donor-Acceptor Complexes of Carbazole
..... **E. L. Ong and Manjit Sambhi*** 2102
- Photoionization and Rydberg States of Tetraaminoethylenes in Organic Solutions
..... **Yoshihiro Nakato, Masaru Ozaki, and Hiroshi Tsubomura*** 2105
- Infrared Spectra and Dipole Moments of Hydrogen-Bonded Complexes. III. Adducts of
2,6-Dichloro-4-nitrophenol with Pyridine Bases **J. P. Hawranek,* J. Oszust, and L. Sobczyk** 2112
- A Thin-Sample Method for the Measurement of Permeability, Permittivity, and Conductivity in the
Frequency and Time Domain **Hugo Fellner-Feldegg** 2116
- Calculation of the Interaction Energy of One Molecule with Its Whole Surrounding. I. Method and
Application to Pure Nonpolar Compounds **Marie-José Huron* and Pierre Claverie** 2123
- Some Comments on the Rice-Allnatt Transport Theory **J. S. Ku and K. D. Luks*** 2133
- Scaled Particle Theory for Nonelectrolyte Solutions of Dilute Solid Solutes
..... **Abhijit Purkayastha and John Walkley*** 2138
- Ionic Solvation Numbers from Compressibilities and Ionic Vibration Potentials Measurements
..... **J. O'M. Bockris and P. P. S. Saluja*** 2140
- Ion-Pair Aggregation in Solutions of Complexes of Carbanion Salts and Macrocyclic Polyethers
..... **U. Takaki, T. E. Hogen Esch, and J. Smid*** 2152
- Initial Reaction of Nitrogen with Zirconium at 1440° **R. A. Sallach** 2156
- A Gas Chromatographic Reactor Study of the Kinetics of Dicyclopentadiene Dissociation
..... **Stanley H. Langer* and James E. Patton** 2159
- Solubility of Methanol in Compressed Nitrogen, Argon, Methane, Ethylene, Ethane, Carbon Dioxide, and
Nitrous Oxide. Evidence for Association of Carbon Dioxide with Methanol in the Gas Phase
..... **B. Hemmaplardh and A. D. King, Jr.*** 2170
- Thermodynamic Parameters for the Cyclooctatetraene Anion Radical Disproportionation as a Function of Ion
Pairing in Hexamethylphosphoramide **Gerald R. Stevenson* and Jesus Gilberto Concepción** 2176
- The Barrier to Internal Rotation in Amides. IV. *N,N*-Dimethylamides; Substituent and Solvent Effects
..... **Torbjörn Drakenberg,* Kjell-Ivar Dahlgvist, and Sture Forsén** 2178

COMMUNICATIONS TO THE EDITOR

- Identification of Reaction Intermediates by Microwave Spectroscopy. The Catalytic Reactions between Propylene and Deuterium over Zinc Oxide
 **Shuichi Naito,* Toshihiko Kondo, Masaru Ichikawa, and Kenzi Tamaru** 2184
- Kinetic Oscillations in the Oxidation of 2,4-Pentanedione by Bromate Ion, Catalyzed by Manganese(II)
 **Peter G. Bowers,* Karen E. Caldwell, and Deborah F. Prendergast** 2185

AUTHOR INDEX

- | | | | |
|---------------------------|-------------------------|--------------------------|------------------------|
| Banewicz, J. J., 2098 | Hawranek, J. P., 2112 | Kotake, Y., 2061 | Nakato, Y., 2105 |
| Bockris, J. O'M., 2140 | Hayon, E., 2072 | Ku, J. S., 2133 | Simic, M., 2072 |
| Bowers, P. G., 2185 | Hemmaplardh, B., 2170 | Kuwata, K., 2061 | Smid, J., 2152 |
| | Hogen Esch, T. E., 2152 | Langer, S. H., 2159 | Sobczyk, L., 2112 |
| Caldwell, K. E., 2185 | Huron, M.-J., 2123 | Leniart, D. S., 2079, | Stevenson, G. R., 2176 |
| Claverie, P., 2123 | Hyde, J. S., 2079, 2087 | 2087 | Sutcliffe, H., 2070 |
| Concepción, J. G., 2176 | | Lichtin, N. N., 2072 | Takaki, U., 2152 |
| | Ibata, T., 2072 | Luks, K. D., 2133 | Tamaru, K., 2184 |
| Dahlqvist, K.-I., 2178 | Ichikawa, M., 2184 | Maguire, J. A., 2098 | Tsubomura, H., 2105 |
| Drakenberg, T., 2178 | Inada, K., 2061 | McAlpine, I., 2070 | |
| | | Naito, S., 2184 | Vedrine, J. C., 2079, |
| Fellner-Feldegg, H., 2116 | King, A. D., Jr., 2170 | | 2087 |
| Forsén, S., 2178 | Kondo, T., 2184 | | Walkley, J., 2138 |
| | | Sallach, R. A., 2156 | |
| | | Saluja, P. P. S., 2140 | |
| | | Sambhi, M., 2102 | |
| | | Patton, J. E., 2159 | |
| | | Prendergast, D. F., 2185 | |
| | | Purkayastha, A., 2138 | |
| | | Ong, E. L., 2102 | |
| | | Ono, M., 2061 | |
| | | Oszust, J., 2112 | |
| | | Ozaki, M., 2105 | |

In papers with more than one author the name of the author to whom inquiries about the paper should be addressed is marked with an asterisk in the by-line.

THE JOURNAL OF PHYSICAL CHEMISTRY

Registered in U. S. Patent Office © Copyright, 1972, by the American Chemical Society

VOLUME 76, NUMBER 15 JULY 20, 1972

Electron Spin Resonance Study of the Far-Ultraviolet Photolysis of Some Inorganic and Organic Compounds[†]

by Keiji Kuwata,* Yashige Kotake, Koji Inada, and Mitsuo Ono

Department of Chemistry, Faculty of Science, Osaka University, Toyonaka, Osaka, Japan (Received December 24, 1970)

Publication costs borne completely by The Journal of Physical Chemistry

Intermediates in the solid-phase photolysis of alkanes, alcohols, ethers, water, and hydrogen peroxide were investigated at 20 and 77°K. Free-radical intermediates in the vapor-phase photolysis were also examined by a quenching technique at low temperature. In alkanes, alcohols, and ethers formation of ionic species is found when the energy of the far-uv light is higher than the ionization thresholds of these compounds. Also, photolytic conversion of the ionic species into secondary free radicals was examined. Photolytic conversion of the primary free radicals into secondary radicals by successive irradiations with uv light was also studied. In ice and solid hydrogen peroxide photolyzed at low temperature, a singlet spectrum with a line width of *ca.* 13 G was observed. In connection with this system, some other systems were also studied, leading to the assignment of this signal to the HO₂ radical.

Application of esr spectroscopy to photolyses in the visible and uv region has been widely studied by many investigators.

Photolysis in the far-uv region has several advantages compared to that in the ordinary uv region, *e.g.*, higher yield in the formation of free-radical intermediates, because of the greater extinction coefficients of molecules in the far-uv region and less possibility of photosensitization by contaminants. Pioneering work in this field has been done for inorganic compounds by Adrian, Cochran, and Bowers.¹

In the photochemistry of the far-uv region, special attention has been paid to photoionization because of its close connection to the primary process postulated in radiation chemistry.

Considering these points, an experimental study on the photolysis of some organic and inorganic compounds in the rigid phase and the vapor phase was carried out.

Because a very poor signal-to-noise ratio may be expected² in epr detection of vapor-phase heavy and unsymmetrical polyatomic free radicals, the products of

the photolysis in the vapor phase were examined after quenching in the rigid phase.

There are some difficulties in the analysis of esr spectra observed in the rigid phase which arise mainly from anisotropy in *g* factor and hf interaction. To reduce the difficulties in the analysis of spectra with large anisotropy, spectral simulation³ for the polycrystalline state, including anisotropy in the *g* factor or hf interaction, was useful.

In the first section of the present report the far-uv photolysis of organic compounds in the rigid phase is described, and the photolysis of water and hydrogen peroxide in the vapor and in the rigid phase is described in the second section.

[†] This work was presented as an invited paper at The Second Symposium on Electron Spin Resonance Spectroscopy, The University of Georgia, 1970.

(1) F. J. Adrian, E. L. Cochran, and V. A. Bowers, *Advan. Chem. Ser.*, **No. 36**, 50 (1962).

(2) *Cf.* A. Carrington and D. H. Levy, *J. Phys. Chem.*, **71**, 2 (1967).

(3) *Cf.* F. K. Knenbühl, *J. Chem. Phys.*, **33**, 1074 (1960); E. L. Cochran, F. J. Adrian, and V. A. Bowers, *ibid.*, **34**, 1161 (1961).

Experimental Section

Materials. All chemicals used were guaranteed grade and were thoroughly degassed and distilled under vacuum. With special caution against contamination with oxygen or carbon dioxide, some of the samples were repeatedly purified by vacuum distillation over freshly evaporated sodium film.

Photolysis and Measurement of ESR Spectra. A diagram of the apparatus for far-uv irradiation *in vacuo* is shown in Figure 1. Sample deposits on a cold finger of thin quartz tube which is cooled with liquid hydrogen or nitrogen contained inside. Far-uv light from a low-pressure discharge lamp is incident on the solid sample. This type of cold finger was quite effectively used at the boiling points of liquid hydrogen and nitrogen.

The sample was irradiated mainly with far-uv light of 121.6 nm from a low-pressure hydrogen discharge lamp,⁴ which was excited by microwave discharge in a TE₀₁₂ rectangular resonant cavity at 2500 MHz, with or without an oxygen filter.⁵ In other kinds of discharge lamps of bromine⁶ (154.6 nm), iodine⁶ (180–200 nm), nitrogen in Ar (120.0, 149.3, 174.3 nm), and mercury (184.9, 253.7 nm) were used for comparison of the effect of the light at different wavelengths.

After irradiation of the sample with far-uv light, the bottom of a dewar vessel was lowered into an esr cavity by contraction of a metal bellows outside of the dewar vessel.

The pressure of the whole system was kept at 10⁻⁵ Torr throughout irradiation and measurement of esr spectra.

In the case of vapor-phase photolysis using an extra glass adapter, the vapor of the reactant was irradiated as it passed across the beam of the far-uv light, and the products quickly deposited together with unreacted molecules or with Ar which was previously mixed for matrix isolation.

Another apparatus for the simplified operation is shown in Figure 2. In this method the sample condensed on the cold finger was once exposed to nitrogen atmosphere and quickly transferred to the quartz dewar vessel for esr measurement. Thus this method can be used when trace amounts of moisture, oxygen, and carbon dioxide from the air have no effect on the product. The principle of this method is essentially the same as that reported by Sevilla and Holroyd.⁷

In the analysis of spectra with fairly large *g*-factor anisotropy for the product water the spectrum simulation including *g*-factor anisotropy for the polycrystalline state was done by an NEAC 2200-500 computer.

Results and Discussion

Far-Uv Photolysis of Organic Compounds in the Rigid Phase. Hydrocarbons. *n*-Hexane after irradiation with far-uv light of 121.6 nm at 77°K showed the hfs of the alkyl radical, and the hfs became clear after irradiation with uv light for 10 sec.

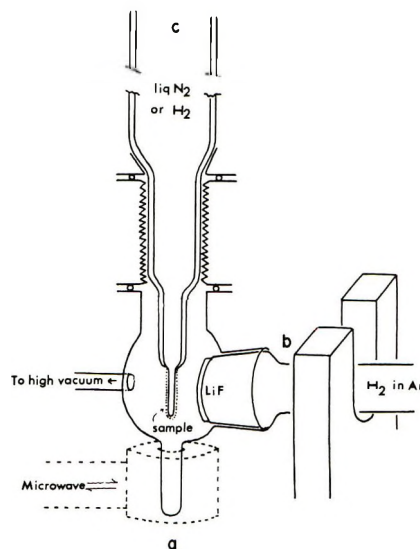


Figure 1. Schematic diagram of far-uv irradiation apparatus: (a) cavity for microwave discharge, (b) hydrogen discharge lamp, (c) quartz dewar vessel for liquid nitrogen or liquid hydrogen.

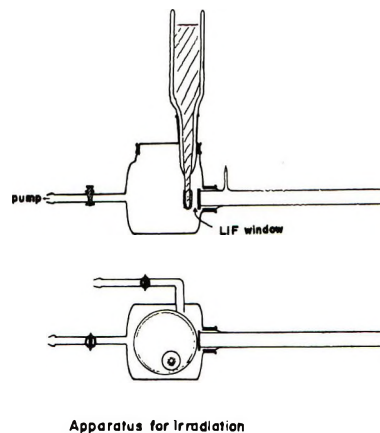


Figure 2. Schematic diagram of the apparatus for far-uv irradiation.

In the case of cycloheptane, a narrow-line spectrum was observed after irradiation with far-uv light for 20 min, and this spectrum changed quickly into a sextet spectrum by successive irradiations with uv light of 200–300 nm for a period of 10 sec or so, as shown in Figure 3. The irradiation was done by a low-pressure mercury lamp through a Toshiba UV D 25 glass filter.

(4) H. Okabe, *J. Opt. Soc. Amer.*, **54**, 478 (1964); J. R. McNesby and H. Okabe, *Advan. Photochem.*, **3**, 157 (1964).

(5) J. A. R. Samson, "Techniques of Vacuum Ultraviolet Spectroscopy," Wiley, New York, N. Y., p 204.

(6) K. Ono and Y. Tanaka, Preprints of the 19th Annual Meeting of the Chemical Society of Japan, Tokyo, 1966, 1Z128.

(7) M. D. Sevilla and T. A. Holroyd, *J. Phys. Chem.*, **74**, 2459 (1970).

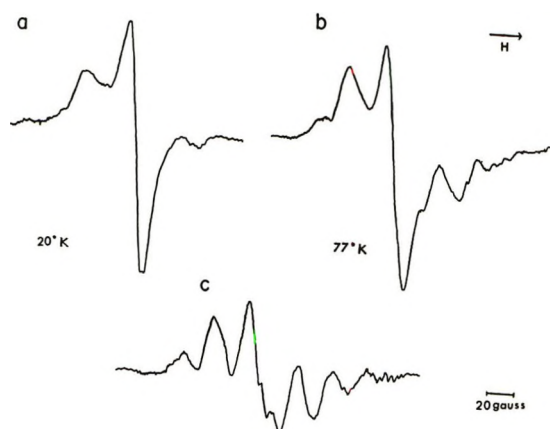


Figure 3. ESR spectra observed in cycloheptane irradiated with far-uv and uv light at 20 and 77°K: (a, b) spectra observed after irradiation with far-uv light of 121.6 nm at 20 and 77°K, respectively; (c) spectrum observed after successive irradiation of the sample of Figure 3a with uv light of 253.7–330 nm at 77°K.

The similar singlet spectrum was observed besides a doublet spectrum of the hydrogen atom in the case of *n*-octane.⁸ After bleaching of the sample with 200–300-nm light, a sextet spectrum appeared. The light of this region was exclusively effective for bleaching of the singlet spectrum.

In the case of isooctane, formation of the methyl radical was seen after bleaching for a period of longer than 20 min.

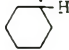

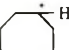
The characteristics of the singlet spectra for alkanes and the hfs for alkyl radicals which appeared after bleaching of the singlet spectra of the alkanes are summarized in Tables I and II. The assignments of the spectra for alkyl radicals were done by comparison of the observed spectra in the present system with those reported in the earlier investigations into the X-ray or γ -ray radiolysis of the *n*-alkanes⁹ and cycloalkanes¹⁰ at 77°K. These assignments could be tentatively confirmed by spectrum simulation with the hf coupling constants given before.

Table I: Characteristics of Singlet Lines Observed in Alkanes Irradiated at 77°K

Sample	g factor	Line width, ΔH_{msl} , G	Ionization threshold (gas phase), eV
<i>n</i> -Octane	2.0024 ± 0.0006	≥ 9	10.24, ^a 10.38 ^b
<i>n</i> -Heptane	2.0021 ± 0.0005	≥ 10	10.35, ^a 10.41 ^b
Cyclooctane	2.0021 ± 0.0005	11	10.67 ^b
Cycloheptane	2.0022 ± 0.0005	11	10.72 ^b
<i>n</i> -Hexane	2.0028 ± 0.0006	13	10.43, ^a 10.46 ^b

^a R. E. Honig, *J. Chem. Phys.*, **16**, 105 (1948). ^b Estimated values: A. Streitwieser, Jr., *J. Amer. Chem. Soc.*, **82**, 4123 (1960).

Table II: ESR Spectra of Alkanes Irradiated at 77°K

Sample	No. of lines in hfs	Hf coupling constant, G	Assignment ^a
<i>n</i> -Pentane	6	$A_\alpha = A_\beta \simeq 21$	$\text{RCH}_2\text{CHCH}_2\text{R}'$
<i>n</i> -Hexane	6	$A_\alpha = A_\beta \simeq 21$	$\text{RCH}_2\text{CHCH}_2\text{R}'$
<i>n</i> -Heptane	6	$A_\alpha = A_\beta \simeq 22$	$\text{RCH}_2\text{CHCH}_2\text{R}'$
<i>n</i> -Octane	6	$A_\alpha = A_\beta \simeq 20$	$\text{RCH}_2\text{CHCH}_2\text{R}'$
Cyclohexane	6	$A_\alpha = 22, A_\beta = 41$	
Cycloheptane	6	$A_\alpha = A_{\beta_1} \simeq 25,$ $A_{\beta_2} \simeq 21$	
Cyclooctane	5	$A_\alpha = 21$ $A_{\beta_1} = 42, A_{\beta_2} = 21$ $A_{\beta_3} < 7, A_{\beta_4} < 7$	

^a R, R' = CH₃ or C_{*n*}H_{2*n*+1} group.

An exceptionally weak singlet signal or none was observed in the cases of cyclohexane and *n*-heptane after irradiation by far-uv light, and alternatively the hyperfine structure of the alkyl radical had already appeared before bleaching, as shown in Figure 4a.

Because the ionization thresholds of these alkanes in the gas phase ranged from 10.2 to 10.4 eV, and considerable lowering of these values in the condensed phase seems to be possible, it is reasonable to expect

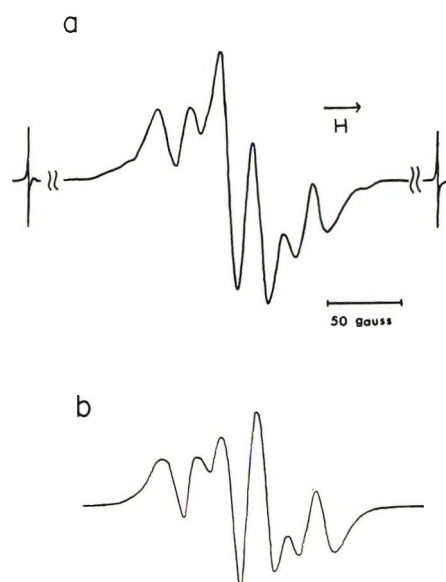


Figure 4. ESR spectra observed in cyclohexane irradiated with far-uv light at 77°K: (a) observed spectrum, (b) simulated spectrum with isotropic hyperfine interaction.

(8) K. Kuwata and K. Inada, *Tetrahedron Lett.*, 11 (1967).

(9) Cf. A. M. Bass and H. P. Broida, "Formation and Trapping of Free Radicals," Academic Press, New York, N. Y., 1960, pp 243–247.

(10) T. Ohmae, S. Onishi, K. Kuwata, H. Sakurai, and I. Nitta, *Bull. Chem. Soc. Jap.*, **40**, 226 (1967).

Table III: ESR Spectra of Alcohols Irradiated at 77°K

Sample	No. of lines in hfs	<i>g</i> factor	Hf coupling constant, G	Assignment
Methanol	3		$A_\alpha = 18.5$	Hydroxymethyl radical
	2		$A = 125$	Formyl radical
	4		$A = 22.5$	Methyl radical
Ethanol	(1)			
	5		$A_\alpha = A_\beta = 22.5$	Hydroxyethyl radical
	4		$A = 22$	Methyl radical
1-Propanol	1	2.0055 ± 0.001	$(\Delta H_{\text{msl}} \simeq 12)$	^a
	5		$A_\alpha = A_\beta = 21$	Hydroxy- <i>n</i> -propyl radical
	4		$A = 22$	Methyl radical
2-Propanol	1	2.0050 ± 0.001	$(\Delta H_{\text{msl}} \simeq 13)$	^a
	5		$A_\alpha = A_\beta = 21$	Hydroxyisopropyl radical
	4		$A = 22$	Methyl radical

^a These singlet lines were assigned to some ionic species later.

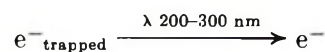
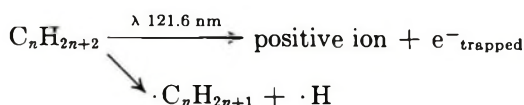
that these alkanes are photoionized through irradiation of far-uv light of 121.6 nm, the energy of photoquantum of which is 10.3 eV.

The single-line spectra observed in the alkanes were assigned to a kind of "trapped" electron in the rigid media because of the low values of their nearly isotropic *g* factors, the lack of hyperfine structure, the microwave saturation behavior, the sensitivity toward irradiation by uv light, and the luminescence after bleaching. However, there was a difference between the energy barrier of the electron trapping site of the solvated electron¹¹ in the polar solvents and the barrier of *ca.* 4.1 eV for the present case.

There is considerable evidence now that possible electron trapping sites are the impurities of greater electron affinity and "lattice imperfections" or "cavities" in the rigid state. An investigation to characterize the "trapped" electron in the rigid organic solvents has given evidence for the assignment of the narrow singlet spectrum to the carbon dioxide anion.¹² Such a narrow singlet spectrum was previously assigned to the "solvated" electron.

With caution against contamination by oxygen or carbon dioxide as an impurity for a possible electron trapping site, some of the samples for irradiation were purified in the vapor phase with freshly evaporated sodium film. For samples purified in such a way, however, no difference in spectra was observed.

There seems to be a limit in explanation of the nature of the electron trapping site in alkanes as far as our experimental knowledge is concerned, so we like to suggest here only the overall reaction schemes for the photochemical processes of alkanes with undefined nature of the ionic species.



Alcohols. Methanol irradiated at 20°K showed the spectra of the hydroxymethyl radical and the methyl radical but none for the formyl radical was found.

The absence of the formyl radical is a noticeable difference from those results obtained by the former^{11,13-20} investigators who irradiate methanol with uv light from a mercury arc.

After the temperature of the sample was raised to 77°K, motional narrowing of the lines in the spectrum of the hydroxymethyl radical was seen, and no thermal conversion of the hydroxymethyl radical into the formyl radical was seen.

In the irradiation at 77°K, a weak signal from the formyl radical was observed besides that from the hydroxymethyl radical. Upon irradiation of this sample with ordinary uv light of 253.7 nm, photolytic conversion of the hydroxymethyl radical into the formyl radical and the formation of small amount of the methyl radical were observed, and the intensity of hydroxy-

(11) Cf. C. Chachaty and E. Hayon, *J. Chim. Phys. Physicochim. Biol.*, **61**, 1115 (1964).

(12) P. M. Johnson and A. C. Albrecht, *J. Chem. Phys.*, **44**, 1845 (1966).

(13) C. F. Luck and W. Gordy, *J. Amer. Chem. Soc.*, **78**, 3240 (1956).

(14) B. Smaller and M. S. Matheson, *J. Chem. Phys.*, **28**, 1169 (1958).

(15) H. Zeldes and R. Livingston, *ibid.*, **30**, 40 (1959).

(16) L. H. Piette, "NMR and ESR Spectroscopy," Pergamon Press, New York, N. Y., 1960, p 221.

(17) P. J. Sullivan and W. S. Koski, *J. Amer. Chem. Soc.*, **84**, 1 (1962); **85**, 384 (1963).

(18) P. J. Sullivan and W. S. Koski, *ibid.*, **86**, 159 (1964).

(19) V. V. Voevodskii, The Fourth International Symposium on Free Radical Stabilization, Washington, D. C., 1959; B. W. Shelimor, N. V. Fok, and V. V. Voevodskii, *Kinet. Katal.*, **5**, 1008 (1964).

(20) H. S. Judeikis and S. Siegel, *J. Chem. Phys.*, **43**, 3625 (1965).

methyl radical decreased as that of the formyl radical increased.

Other alcohols were also photolyzed at low temperature, and the results of this esr spectroscopy are summarized in Table III. Identification of the radicals was done by comparison of the observed spectra in the present systems with those for the photolyzed or γ -irradiated alcohols.^{11,13-20}

Ethanol showed the spectrum of the hydroxyethyl radical^{18,20} and after uv irradiation, the sharp quartet spectrum of the methyl radical appeared. The spectra thus obtained are quite similar to those obtained by the former investigators.

In 1- and 2-propanol and 1-butanol, a new kind of singlet line spectrum was observed just after the far-uv irradiation with light of 121.6, 180-200, and 181.6 nm. These singlet line spectra were tentatively assigned to some ionic precursors formed by the photoionization of those alcohols for reasons discussed later.

In the cases of methanol and ethanol, the breaking down of the CO bond by far-uv irradiation was an initial step, whereas photoionization occurred in the cases of C₃ and C₄ alcohols.

In the vapor-phase photolysis of methanol and ethanol, only the hydroxymethyl and the hydroxyethyl radicals were trapped. The absence of the methyl and formyl radicals in the trapped products seems to show that these free radicals are not the primary products but the products of secondary photolysis. However, the possibility of missing these reactive intermediates during quenching could not be refuted.

It is added here that the formation of the methyl radical was found in the cases of C₁-C₃ alcohols and none was found in C₄ alcohols.

The increased difficulty of intramolecular energy transfer from the radical site at the α position to the terminal methyl group may be the reason for this difference between C₁-C₃ and C₄ alcohols.

Ethers. After irradiation of diethyl ether with far-uv light of 121.6 nm at 77°K, the spectrum for the ethoxy derivative of the ethyl radical was observed as shown in Figure 5a, and the spectrum changed into that of Figure 5b by successive irradiations by uv light of 253.7-330 nm. A quartet spectrum of the methyl radical appeared, and the resolution of the hfs for the derivative of the ethyl radical increased.

In the cases of di-*n*-propyl ether, however, a singlet line spectrum with a broad shoulder at lower field as shown in Figure 6 was observed after the irradiation with far-uv light of 121.6 nm at 77°K. By successive irradiations with uv light of 253.7-330 nm for 1 min, the hfs for the propoxy derivative of the *n*-propyl radical appeared.

As for di-*n*-butyl ether, the same result as that for di-*n*-propyl was obtained.

Table IV shows the characteristics of the spectra observed in the ethers irradiated.

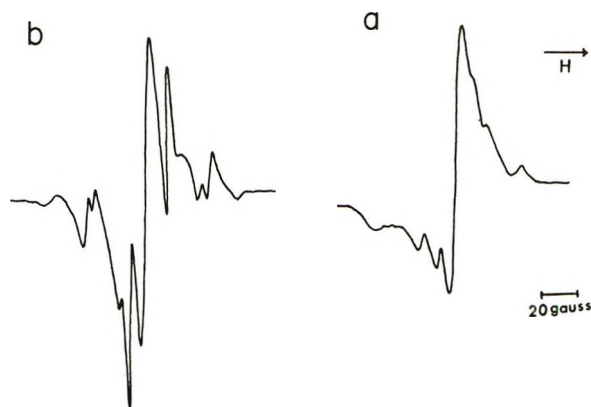


Figure 5. ESR spectra observed in diethyl ether: (a) spectrum observed after irradiation with far-uv light of 121.6 nm at 77°K, (b) spectrum observed after successive irradiation of the sample of Figure 5a with uv light of 253.7-330 nm at 77°K.

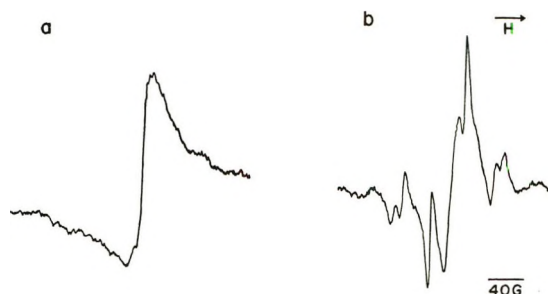


Figure 6. ESR spectra observed in di-*n*-propyl ether: (a) spectrum observed after irradiation with far-uv light of 121.6 nm at 77°K, (b) spectrum observed after successive irradiation of the sample of Figure 6a with uv light of 253.7-330 nm at 77°K.

In cyclic ethers the spectra of the trapped radicals were the same as those in γ irradiation of the corresponding ethers. In the case of 2-methyltetrahydrofuran, however, a quintet spectrum observed in the present system differs from the septet spectrum with slightly larger hf splitting, as has been described previously²¹ in the γ irradiation of the ether. In far-uv photolysis the spectra observed for the trapped radicals had slightly broader line widths compared to those from γ irradiation, so that the possibility of missing two extreme lines of the septet could not be excluded in the present study.

In the case of di-*n*-C₃ ethers, the methyl radical was formed after uv irradiation, whereas no methyl radical was observed in the case of di-*n*-C₄ ethers. This tendency is the same as that in alcohols as mentioned before.

The singlet line spectra observed after far-uv irradiation could be tentatively assigned to the ionic species as well as those observed in C₃ and C₄ alcohols for the same reason as in the cases of the alkanes. The other chemical attempts to examine the nature of these species for

(21) F. P. Sargent, *Can. J. Chem.*, **48**, 3453 (1970).

Table IV: ESR Spectra of Ethers Irradiated at 77°K


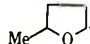
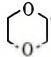
Sample	No. of lines in hfs	Hf coupling constant, G	Assignment
Diethyl ether	5	$A_\alpha \simeq A_\beta = 18$	$\text{CH}_3\dot{\text{C}}\text{HOCH}_2\text{CH}_3$
	4	$A = 22$	Methyl radical
Di- <i>n</i> -propyl ether	5	$A_\alpha \simeq A_\beta = 22$	$\cdot\text{CH}_2(\text{CH}_2\text{CH}_2)_2\text{O}(\text{CH}_2)_2\text{CH}_3$
	4	$A = 22$	Methyl radical
Di- <i>n</i> -butyl ether	5	$A_\alpha \simeq A_\beta = 21$	$\cdot\text{CH}_2(\text{CH}_2)_3\text{O}(\text{CH}_2)_3\text{CH}_3$
Tetrahydrofuran	5	$A_\alpha \simeq A_{\beta_1} = 18, A_{\beta_2} = 36$	
2-Methyltetrahydrofuran	5	$A_\alpha \simeq A_{\beta_1} = 18, A_{\beta_2} = 36$	 Methyl radical
	(4)	$A = 22$	
1,4-Dioxane	5	$A_\alpha = 16, A_{\beta_1} = 48, A_{\beta_2} < 10$	 Methyl radical
	(4)	$A = 22$	

Table V: Effect of Additives on the Formation of Ionic Species by Photoionization

System	Light source		
	H ₂ /Ar lamp $\lambda = 121.6 \text{ nm}$	N ₂ /Ar lamp $\lambda = 120.0, 149.3, 173.3 \text{ nm}$	I ₂ lamp $\lambda = 170.0 \sim 200.0 \text{ nm}$
1-Propanol	+	+	+
1-Propanol + CCl ₄	-	-	-
2-Methyltetrahydrofuran	(+), R·	+, (R·)	R·
2-Methyltetrahydrofuran + TMA ^a	(+), R·	-	-
2-Methyltetrahydrofuran + CCl ₄	R·	-	-
1,4-Dioxane	+	+	R·, (+)
1,4-Dioxane + CCl ₄	(+), R·	-	-

^a TMA = Trimethylamine.

the single lines were done by the addition of an electron-trapping reagent or a hole trapping reagent, and those results obtained are summarized in Table V.

The plus or minus symbols in the table mean appearance or disappearance of the singlet line spectrum, whereas the symbol R· shows the formation of the trapped radical in the system.

In the cases of 1-propanol and 1,4-dioxane, as the energy of photoquantum decreased, the effect of the addition of carbon tetrachloride as an electron trapping reagent on the formation of the ionic species became clear.

These results could be additional support for the formation of the ionic species formed by the photoionization of those organic compounds in the solid phase.

Far-Uv Photolysis of Water and Hydrogen Peroxide. Water and Deuterium Oxide. Radiolysis of ice with γ or β rays and photolysis of hydrogen peroxide with light of 253.7–330 nm have been extensively studied so far, and the main products in these systems were determined to be the OH radical²² and the HO₂^{22–26} radical. The photolysis of water with far-uv light in the rigid phase and in the vapor phase, and the photolysis of diluted hydrogen peroxide in the vapor phase, however, resulted in formation of different kinds of intermediates, as seen in Figures 7, 8, and 9.

Water and deuterium oxide irradiated in the solid state at 20 and 77°K as well as in the vapor phase showed the singlet line with a weak shoulder at lower field not far from the center of the spectrum.

By microwave discharge in the vapors of water and deuterium oxide, similar spectra with the stronger shoulder were observed.

This shoulder was at the position of the low-field peak of the HO₂ radical in the polycrystalline state, and after annealing the sample at 100°K it disappeared.

By annealing the sample up to 100°K the signal intensity decreased gradually, but no change in the shape of singlet spectrum was seen.

Deuterium substitution made the line width narrower in each case, and this fact shows that a part of the line width is caused by the hyperfine interaction with a proton in water.

(22) C. L. Aseltine and Y. W. Kim, *J. Phys. Chem. Solids*, **29**, 531 (1968).

(23) T. Ichikawa, M. Iwasaki, and K. Kuwata, *J. Chem. Phys.*, **44**, 2979 (1966).

(24) G. Czapski and B. H. Bielski, *J. Phys. Chem.*, **67**, 2180 (1963).

(25) F. J. Adrian, E. L. Cochran and V. A. Bowers, *J. Chem. Phys.*, **47**, 5441 (1967).

(26) S. J. Wyard, R. C. Smith, and F. J. Adrian, *ibid.*, **49**, 2780 (1968).

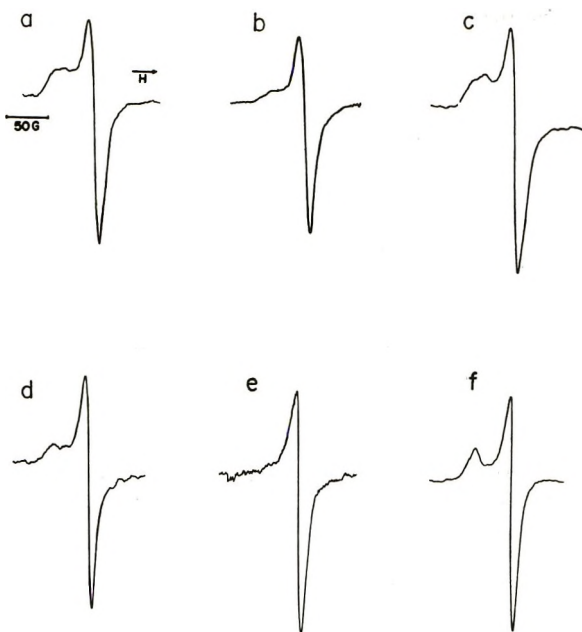


Figure 7. ESR spectra observed in water irradiated with far-uv light at 20 and 77°K: (a) water irradiated with far-uv light of 121.6 nm at 20 or 77°K, (b) water irradiated with far-uv light of 121.6 nm in the vapor phase, (c) transient intermediate formed by microwave discharge in water vapor, (d) deuterium oxide irradiated with far-uv light of 121.6 nm at 77°K, (e) deuterium oxide irradiated with far-uv light of 121.6 nm in the vapor phase, (f) transient intermediates formed by microwave discharge in deuterium oxide vapor.

There was no effect of temperature on the spectra in the range of 20–77°K, and this fact could exclude the possibility of motional effects on the spectra.

The effect of the energy of light was examined by replacing the light source with a low-pressure mercury lamp with LiF windows (for 181.6 nm), and only the reduction of the radical yield was seen.

Hydrogen Peroxide and Deuterium Peroxide. After irradiation with far-uv light of 121.6 nm, hydrogen peroxide and deuterium peroxide showed the same single line at the central part of the spectra for the HO₂ radical, and the same effect of deuteration was seen.

The HO₃ (or O₃⁻) Radical as the Origin of the Single Line Spectrum. This kind of single line was also observed after vapor-phase photolysis of hydrogen peroxide with uv light of 253.7 nm. In the case of dilute aqueous solutions of hydrogen peroxide, the single line was observed as shown in Figure 9a. This result was quite different from that for photolysis in the polycrystalline state of the same sample at 77°K with same uv light.

As far as the present authors know, no single line spectrum has been reported in those studies on water or hydrogen peroxide systems except the spectrum which was observed by Marx, *et al.*,²⁷ after annealing the condensate from the electron irradiation of water or deuterium oxide. This signal, however, was assigned by them to the HO₂ radical.

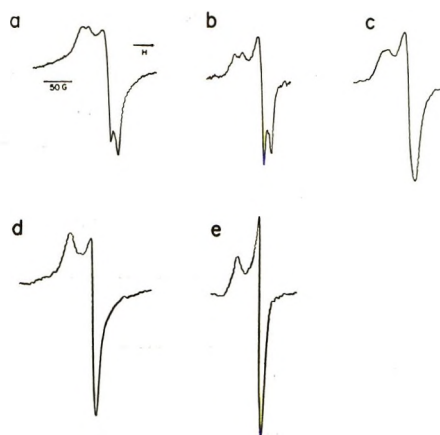


Figure 8. ESR spectra observed in hydrogen peroxide irradiated with far-uv light at 20 and 77°K: (a) hydrogen peroxide irradiated with far-uv light of 121.6 nm at 20 or 77°K, (b) hydrogen peroxide irradiated with far-uv light of 121.6 nm in the vapor phase, (c) transient intermediate formed by microwave discharge in hydrogen peroxide vapor, (d) deuterium peroxide irradiated with far-uv light of 121.6 nm at 77°K, (e) deuterium peroxide irradiated with far-uv light of 121.6 nm in the vapor phase.

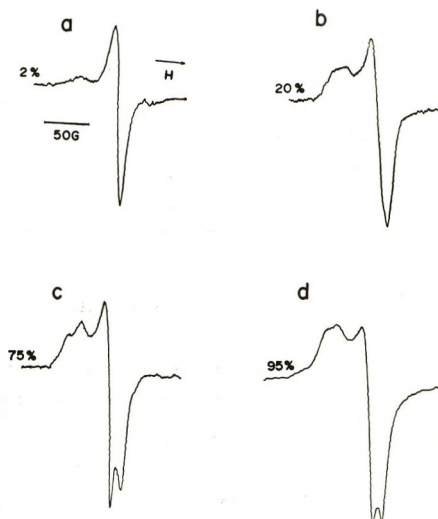


Figure 9. ESR spectra observed in hydrogen peroxide of various concentrations after vapor-phase photolysis with uv light: spectrum observed for (a) 2% aqueous solution of hydrogen peroxide, (b) 20% aqueous solution, (c) 75% aqueous solution, (d) 95% aqueous solution.

There was also experimental evidence which discarded the possibility of the trapped electron as the origin of this singlet spectrum. By the illumination of the sample with strong uv light or visible light there was no reduction of the signal intensity. The absence of power saturation may also be reason to discard the possibility of the trapped electron.

After photobleaching of γ -irradiated alkaline ice, Nazhat and Weiss²⁸ found a new center which shows a g

(27) R. Marx, S. Leach, and M. Horani, *J. Chim. Phys. Physicochim. Biol.*, **60**, 726 (1963).

(28) N. B. Nazhat and J. J. Weiss, *J. Chem. Phys.*, **74**, 4298 (1970).

Table VI: ESR Parameters of a Radical Formed in Water and Hydrogen Peroxide

System	g_x, g_y, g_z	g_{iso}	Line width, ΔH_{msl} , G	A, G
H ₂ O	2.008 ± 0.003	2.008	13.8 ± 0.2	
D ₂ O	2.008 ± 0.003	2.008	12.2 ± 0.2	
H ₂ O-O ₃		2.009	14	
75% H ₂ O ₂ (amorphous)	2.0036, 2.0346	2.0139		$A_{iso} = 12 \pm 1$
0.01% H ₂ O ₂ (polycryst)	2.0095, 2.0615	2.0268		$A_{iso} = 27$
H ₂ O ₂ -KOH		2.0085	14.6	

Table VII: g Factors of the Radicals Formed in Water and Hydrogen Peroxide or in Related Systems

System	g_x	g_y	g_z	g_{iso}	Line width, ΔH_{msl} , G		
HO Li ₂ SO ₄ -H ₂ O		2.005		2.064	$A_{iso} = 20.9$ G	a	
HO ₂ Li ₂ SO ₄ -H ₂ O		2.006		2.033	$A_{iso} = 12$ G	a	
O ₂ ⁻ Na ₂ O ₂		2.002		2.175	2.0597	b	
H ₂ O ₂ -urea	2.0009		2.0084	2.0886	2.0326	c	
Li ₂ SO ₄ -H ₂ O		2.002		2.088	2.0307	d	
H ₂ O (glass)		2.001		2.101	2.0343	e	
O ⁻ KOH-H ₂ O					2.0615	49.5	f
KOH-D ₂ O					2.0606	41.8	f
KCl		1.981		2.258	2.0733		g
O ₃ ⁻ KO ₃ , H ₂ O ₂ -KOH					2.012		b
NaO ₃		2.015		2.003	2.011		h
KClO ₄	2.0025		2.0174	2.0113	2.0104		h
NaBrO ₃	2.022		2.022	2.006	2.017		i
HO ₃ H ₂ O ₂ -H ₂ O		2.0045		2.0608	2.0233		j
RO ₃ CF ₃ OO CF ₃		$A_{VO} = 23.3, 14.0, \text{ and } 3.59$ G ^l		2.00373 ± 0.00001			k

^a From ref 22. ^b From ref 29. ^c From ref 23. ^d From ref 22. ^e From ref 30. ^f From ref 31. ^g From ref 32. ^h From ref 33. ⁱ From ref 34. ^j From ref 35. ^k From ref 36. ^l For three O atoms.

factor of 2.0048–2.0060 for the electron and the hf splitting due to alkali metal nuclei.

This center does not show power saturation. The characteristics of the epr measurement for this center are similar to those in the present case except the hf splitting; however, absence of the trapping site of alkali metal cation makes the formation of this kind of site difficult in the present case.

The esr parameters of this single line spectrum observed in water, hydrogen peroxide, in the aqueous solution of ozone after uv irradiation, and in the system of potassium hydroxide–hydrogen peroxide are listed in Table VI. The features of this single line are the nearly isotropic g factor of 2.008–2.009 and a line width of ca. 12 G.

Table VII shows the esr parameters for the possible transient intermediates^{29–35} formed in the related systems of water or hydrogen peroxide and for the RO₃ radical.

Fessenden³⁶ has suggested that radicals of the type RO₃ or HO₃ should have an isotropic g factor near 2.0035 and even in the solid should show a line width no greater than 10–15 G because of the relatively small g -factor anisotropy. On the basis of fairly good agreement of the nearly isotropic g factor found for RO₃ and O₃⁻ in

potassium hydroxide–hydrogen peroxide, sodium, or KClO₄ with that in the present systems, this single line could be assigned to the HO₃ radical or the O₃⁻ radical.

This assignment could be supported by the finding of the same single line spectra in the systems of ozone in water and ozone in diluted aqueous solutions of hydrogen peroxide, both irradiated with uv light from a high-pressure mercury arc. The broken line in Figure 10 shows the single line spectrum observed in the system of ozone in the dilute aqueous solutions of hydrogen peroxide. To leave this single line spectrum, the doublet spectrum of the OH radical formed in the dilute aqueous solutions of hydrogen peroxide was subtracted

(29) J. E. Benett, D. J. E. Ingram, and D. Schonland, *Proc. Phys. Soc. A*, **69**, 556 (1956).

(30) J. E. Benett, B. Mile, and A. Thomas, *Trans. Faraday Soc.*, **64**, 3200 (1968).

(31) P. N. Moorthy and J. J. Weiss, *Phil. Mag.*, **10**, 659 (1964).

(32) W. Sander, *Z. Phys.*, **169**, 353 (1962).

(33) A. D. McLachlan, M. C. R. Symons, and M. G. Townsend, *J. Chem. Soc.*, 952 (1959).

(34) T. Anderson, J. R. Byberg, and K. J. Olsen, *J. Phys. Chem.*, **71**, 4129 (1967).

(35) R. C. Smith and S. T. Wyard, *The 6th International Symposium on Free Radical Stabilization*, Cambridge, Mass., 1963.

(36) R. W. Fessenden, *J. Chem. Phys.*, **48**, 3725 (1968).

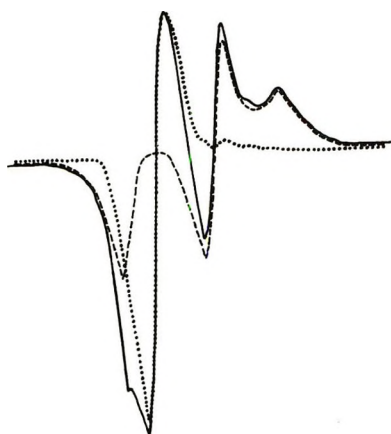
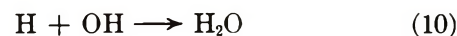
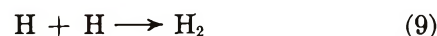
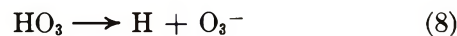
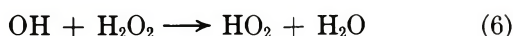
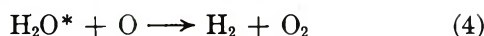
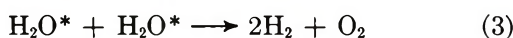
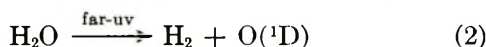
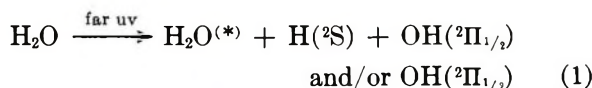


Figure 10. ESR spectra observed in the system of 0.01% aqueous hydrogen peroxide and ozone after irradiation by uv light. The broken line shows the spectrum for 0.01% aqueous hydrogen peroxide irradiated with uv light at 77°K. The solid line shows the spectrum observed in the system of 0.01% aqueous solution of hydrogen peroxide and ozone after uv irradiation at 77°K. The dotted line shows the difference between the broken line and the solid line.

from the mixture of both of them which was observed in the system of ozone in dilute hydrogen peroxide.

In the photolysis of water, formation of the HO_3 radical could be assumed to proceed through those steps included in eq 1-10.



Reaction 2 can generally occur in the far-uv photolysis with 121.6-nm light³⁷ in vapor phase. Thus, far-uv photolysis of water may include the primary transient intermediates such as H_2O^* , H, OH, and O.

Although the radiolysis of the polycrystalline or single crystalline ice frequently gave those spectra due to OH and H, it is surprising that no esr spectrum of OH was observed in the present study.

This may be interpreted as that the secondary complex reaction of OH will proceed in the amorphous condensate after trapping in the solid state at low temperature.

Because in the present system no characteristic doublet separation of 42 G for the OH radical in the polycrystalline state was observed at all, the OH radical may be consumed away to form the HO_2 or the HO_3 radicals *via* reactions 6 and 7. In fact, when the products of electric discharge in the water vapor were quickly condensed on a cold surface at low temperature, chemical analysis showed the formation of considerable amount of hydrogen peroxide.³⁸

In addition there may be considerable amounts of oxygen molecules formed by reactions 3 and 4, and the rather large possibility of reaction 7 as compared to reaction 6 could be supposed.

Acknowledgment. The authors express their sincere thanks to Professor Hiroshi Tsubomura of Osaka University for his helpful discussion on the designing of the far-uv light source.

(37) J. G. Calvert and J. N. Pitts, "Photochemistry," Wiley, New York, N. Y., 1966, p 200.

(38) A. M. Bass and H. P. Broida, "Formation and Trapping of Free Radicals," Academic Press, New York, N. Y., 1960, pp 289-292.

A Comparison of the Radiolysis of Liquid Bromotrifluoromethane with the Radiolysis of Liquid Trifluoroiodomethane

by I. McAlpine and H. Sutcliffe*

Chemistry Department, University of Salford, Salford M6 4WT, Lancashire, England (Received October 14, 1971)

Publication costs borne completely by The Journal of Physical Chemistry

The radiolysis of bromotrifluoromethane in the liquid phase at room temperature has been examined. The products and 100 eV yields are: tetrafluoromethane, 0.62; hexafluoroethane, 0.25; dibromodifluoromethane, 0.98; and bromine, 0.22. In the presence of iodine the products and some 100-eV yields are: tetrafluoromethane, 0.05; hexafluoroethane, 0.11; trifluoroiodomethane, 3.54; dibromodifluoromethane, and probably bromodifluoroiodomethane. These results are compared with those obtained previously for liquid trifluoroiodomethane.

The radiolysis of liquid trifluoroiodomethane has been studied and shown to give the following products and 100-eV yields: tetrafluoromethane, 0.37, hexafluoroethane, 1.03, and iodine, 1.36.¹ This work was interpreted in terms of C-I bond breakage followed by reactions of the subsequently formed excited and thermal $\text{CF}_3\cdot$ radicals. It was of interest, therefore, to compare this system with bromotrifluoromethane, where the C-X bond (X = Br or I) is much stronger.

Experimental Section

Bromotrifluoromethane was obtained from Du Pont (its purity was checked by gas chromatographic analysis) and used without further purification. Sample preparation and irradiation, dosimetry, and gas chromatographic analysis were carried out as previously described.¹

Irradiation of Liquid Bromotrifluoromethane. Bromotrifluoromethane (13.16 mmol) was irradiated for 68 hr; the dose received was 4.317×10^{21} eV. The products were fractionated *in vacuo* through traps cooled to -96 , -131 , and -196° , the fraction condensed at -196° being recycled. The fraction condensed at -96° was bromine, which was determined by reaction with potassium iodide solution followed by titration of the liberated iodine with sodium thiosulfate solution. The fraction condensed at -131° contained dibromodifluoromethane (0.076 mmol) together with silicon tetrafluoride and traces of bromotrifluoromethane and possibly bromopentafluoroethane. The fraction condensed at -196° contained bromotrifluoromethane (12.63 mmol), tetrafluoromethane (0.044 mmol), and hexafluoroethane (0.018 mmol); per cent composition was determined by gas chromatography.

Irradiation of Liquid Bromotrifluoromethane and Iodine. A mixture of bromotrifluoromethane (12.82 mmol) and iodine (6.72 mmol) was irradiated for 65 hr; the dose absorbed by the mixture was 8.078×10^{21} eV.

The products were fractionated *in vacuo* through traps cooled to -63 , -96 , -131 , and -196° . The fraction condensed at -63° contained iodine and bromine. The fraction condensed at -96° (0.066 mmol) contained dibromodifluoromethane together with another product (A) which had infrared absorption at $12.7 \mu\text{m}$. The intensity of the bands at $8.8 \mu\text{m}$ and $9.3 \mu\text{m}$ was also too high for dibromodifluoromethane alone. The fraction condensed at -131° contained trifluoroiodomethane (0.475 mmol) together with small amounts of dibromodifluoromethane and the unknown compound A. The fraction condensed at -196° contained bromotrifluoromethane (12.00 mmol), tetrafluoromethane (0.034 mmol), hexafluoroethane (0.014 mmol), and traces of silicon tetrafluoride and trifluoroiodomethane.

Irradiation of Liquid Trifluoroiodomethane with Iodine. A mixture of trifluoroiodomethane (25.37 mmol) and iodine (1.00 mmol) was irradiated for 41 hr; the dose absorbed by the mixture was 7.885×10^{21} eV. The products were separated and analyzed as described previously to yield tetrafluoromethane (0.008 mmol), hexafluoroethane (0.05 mmol), iodine, and unreacted trifluoroiodomethane.

Results and Discussion

The results, in terms of products and 100-eV yields, are given in Table I, together with those for liquid trifluoroiodomethane.

The high yield of tetrafluoromethane obtained from bromotrifluoromethane relative to that obtained from trifluoroiodomethane is attributed to the reduced radical-scavenging ability of bromine relative to that of iodine. This is further demonstrated by the markedly reduced yield of tetrafluoromethane from both substrates in the presence of iodine. This difference in yield of tetrafluoromethane from the two substrates is

(1) I. McAlpine and H. Sutcliffe, *J. Phys. Chem.*, **74**, 1422 (1970).

Table I

	Br ₂ I ₂	CF ₄	C ₂ F ₆	CF ₃ I	CBr ₂ F ₂ / CF ₂ I ₂
Liquid CF ₃ Br	0.22	0.62	0.25		0.98
Liquid CF ₃ Br + I ₂		0.05 ^a	0.11 ^a	3.54 ^a	
Liquid CF ₃ I ^b	1.36	0.37	1.03		c
Liquid CF ₃ I + I ₂		0.06 ^a	0.39 ^a		

^a Calculated using total dose received by the mixture. ^b See ref 1. ^c A small amount of CF₂I₂ is formed at high dose.

also additional evidence in favor of an excited radical reaction rather than fluorine abstraction by a CF₃⁺ ion. Reaction of CF₃⁺ with bromine or iodine would not be expected to proceed at significantly different rates, and the yields of tetrafluoromethane from trifluoroiodomethane or bromotrifluoromethane would be approximately the same or slightly less in the case of the bromo compound, reflecting the difference in C-X bond dissociation energies.

The significant difference in the yield of hexafluoroethane from the two systems makes it necessary to reconsider the previously postulated recombination of thermalized CF₃· radicals as the mechanism of formation of hexafluoroethane. Since thermalization of excited radicals is expected to be very similar in the two media, a more likely alternative is an excited radical-molecule, or ion-molecule reaction



or



If this were the case, the molecule having the weakest C-X bond, namely CF₃I, would be expected to give the greatest yield of hexafluoroethane, as is observed.

The remaining point of difference between the two reactions is the high yield of dibromodifluoromethane. This observation is attributed to the greater stability of the ·CF₂Br radical relative to the ·CF₂I radical. This high yield of dibromodifluoromethane is also re-

flected by the considerably reduced yield of free halogen relative to the trifluoroiodomethane radiolysis.

The Unknown Compound A. The radiolysis of bromotrifluoromethane in the presence of iodine results in the formation of an unknown compound in admixture with dibromodifluoromethane. This mixture shows infrared absorption bands at 1135, 1080 and 788 cm⁻¹. The 788-cm⁻¹ band is probably due to bromodifluoroiodomethane, since this band lies approximately halfway between the ν_{Br}(asym) band of CBr₂F₂ (816 cm⁻¹) and the ν_I(asym) band of CF₂I₂ (740 cm⁻¹).² This type of spectroscopic behavior has been observed before for the compounds CBr₂F₂, CF₂BrCl, and CF₂Cl₂, as shown in Table II.³ Note also that the C-F stretching frequencies vary very little from molecule to molecule, a phenomenon which will be expected in the series CBr₂F₂, CF₂BrI, and CF₂I₂; hence the enhancement of the intensities of the 1135- and 1080-cm⁻¹ bands in the mixture CF₂Br₂ and CF₂BrI.

Table II

CF ₂ Br ₂	CF ₂ BrCl	CF ₂ Cl ₂
ν _{F(s)} 1088	ν _{F(s)} 1102	ν _{F(s)} 1101
ν _{F(a)} 1150	ν _{F(a)} 1150	ν _{F(a)} 1159
ν _{Br(a)} 829	ν _{Cl} 872	ν _{Cl(a)} 906
ν _{Br(s)} 621	ν _{Br} 648	ν _{Cl(s)} 667

Bromodifluoroiodomethane is a predictable product, by the reaction of the bromodifluoromethyl radical with iodine.

Acknowledgments. I. McAlpine wishes to thank the Science Research Council for a maintenance award, during the tenure of which this work was carried out.

(2) E. K. Plyler and N. Acquista, *J. Res. Nat. Bur. Stand.*, **48**, 92 (1952).

(3) I. McAlpine and H. Sutcliffe, *Spectrochim. Acta, Part A*, **25**, 1723 (1969).

Electron and Hydrogen Atom Attachment to Aromatic Carbonyl Compounds in Aqueous Solution. Absorption Spectra and Dissociation Constants of Ketyl Radicals

by E. Hayon,^{*1} T. Ibata,² N. N. Lichtin,² and M. Simic³

*Pioneering Research Laboratory, U. S. Army Natick Laboratories, Natick, Massachusetts 01760, and
Chemistry Department, Boston University, Boston, Massachusetts 02215 (Received February 2, 1972)*

Publication costs assisted by the U. S. Army Natick Laboratories

The technique of pulse radiolysis-absorption spectroscopy has been used to study the addition of hydrated electrons and H atoms to a number of compounds incorporating both carbonyl and aromatic groups. The absorption spectra of the electron adducts and their oxygen-protonated conjugate acids have been determined for acetophenone, 9,10-anthraquinone-2-sulfonate, benzamide, benzil, benzoin, benzophenone, and fluorenone. The pK_a values for all of these radicals except those derived from benzoin have been evaluated as have the bimolecular decay rates of the anion radicals. Bimolecular decay rates of the protonated electron adducts of acetophenone, 9,10-anthraquinone-2-sulfonate, and benzamide were also measured. Specific rates of addition of the hydrated electron to all the substrates for which resultant spectra were determined as well as anthrone, dibenzylketone, 1,4-naphthoquinone-2-sulfonate, 1,2-naphthoquinone-4-sulfonate, and phenylacetone have been found to fall in the range $(1.1-3.6) \times 10^{10} M^{-1} \text{sec}^{-1}$. Spectra of the H-atom adducts and bimolecular specific rates of decay of these adducts have been determined for acetophenone, 9,10-anthraquinone-2-sulfonate, benzamide, benzil, benzophenone, fluorenone, and 1,4-naphthoquinone-2-sulfonate. Systematic aspects of the dependence on structure of the reactivity toward addition of e_{aq}^- and H atoms, of the pK_a 's of protonated electron adducts, and of the various spectra are discussed.

There is considerable interest in determining the specific role of quinones, ketones, and related compounds in biological reactions, and their importance in electron transport and oxidative phosphorylation mechanisms has been established for some of them.⁴

No detailed study has been carried out previously to investigate the reactions of solvated electrons and hydrogen atoms with aromatic carbonyl compounds and to differentiate the sites of attachment and the rates of reactions of these two reducing species.

The absorption spectra of a number of ketyl radicals have been observed on flash photolysis of aromatic ketones in the presence of an H-atom donor (*e.g.*, see ref 5-8). In only a few cases, however, have the full spectra, extinction coefficients, and acid-base dissociation constants been determined.

In the present work solvated electrons and hydrogen atoms have been produced by pulse radiolysis of aqueous solutions and allowed to react with aromatic carbonyl compounds. The absorption spectra of the H atom and of the electron adducts, and of their protonated forms, derived from a number of aromatic carbonyl compounds have been determined. The reaction rate constants for addition of e_{aq}^- and H atoms and the pK_a values of the protonated electron adducts have also been measured.

Experimental Section

The general method and experimental technique of pulse radiolysis used has already been described.^{9,10} A double monochromator and a pulsed xenon lamp was used throughout this work.

All solutions were thoroughly degassed by bubbling with argon gas. The OH radicals produced from the radiolysis of water were scavenged in presence of excess *tert*-butyl alcohol. The radical from *tert*-butyl alcohol

(1) U. S. Army Natick Laboratories.

(2) Chemistry Department, Boston University. Support under Grants No. R 01 RH 00394 and R 01 EC 0092 of the Environmental Control Administration of the U. S. Public Health Service is gratefully acknowledged.

(3) National Academy of Science-National Research Council Research Associate at the Natick Laboratories.

(4) R. A. Morton, Ed., "Biochemistry of Quinones," Academic Press, New York, N. Y., 1965.

(5) G. Porter and F. Wilkinson, *Trans. Faraday Soc.*, **57**, 1686 (1961).

(6) A. Beckett and G. Porter, *ibid.*, **59**, 2038 (1963).

(7) J. A. Bell and H. Linschitz, *J. Amer. Chem. Soc.*, **85**, 528 (1963).

(8) A. Beckett, A. D. Osborne, and G. Porter, *Trans. Faraday Soc.*, **60**, 873 (1964).

(9) M. Simic, P. Neta, and E. Hayon, *J. Phys. Chem.*, **73**, 3794 (1969).

(10) J. P. Keene, E. D. Black, and E. Hayon, *Rev. Sci. Instrum.*, **40**, 1199 (1969); E. Hayon, *J. Chem. Phys.*, **51**, 4881 (1969).

absorbs⁹ below ~ 280 nm and has a low extinction coefficient. The presence of the alcohol increased the solubility of the aromatic ketones in water. In all cases, the concentrations of ketone were adjusted to scavenge all the e_{aq}^- or H atoms produced under the experimental conditions employed. To determine the second absorption bands of the ketyl radicals or radical anions in the far-uv region, these solutions were diluted and normalized to the spectra obtained at higher solute concentrations.

Dosimetry was carried out⁹ using ~ 0.1 M KCNS solution and an $\epsilon_{500} = 7.6 \times 10^3$ M⁻¹ cm⁻¹. The extinction coefficients were derived based on $G(e_{aq}^-) = G(OH) = 2.8$, and $G(H) = 0.55$.

Considerable care was taken to minimize the photolysis of these aqueous solutions. Appropriate liquid and/or glass filters were used to filter the monitoring light from the xenon lamp. In addition, a synchronized shutter was used which opened for a total time duration of ~ 5 msec.

The aromatic ketones were obtained from Eastman Chemicals and from Matheson Coleman and Bell. In all cases, the ketones were purified and recrystallized from alcohol.

Results

Specific Rates of Addition of e_{aq}^- and H atoms. The specific rates of reaction of the hydrated electron with a variety of aromatic carbonyl compounds—ketones, quinones, diketone, acyloin, and amide—were determined by following the decay of e_{aq}^- at 700 nm. Hydroxyl radicals were scavenged by 0.1 M *tert*-BuOH and the pH was maintained at ~ 9.2 by ~ 2 mM sodium tetraborate. The rate constants obtained are presented in Table I. Although they are all close to the diffusion-controlled limit some significant variations of reactivity with structure are apparent. Both phenyl acetone and dibenzyl ketone (α, α' -diphenylacetone) react twice as fast as does acetone.¹¹ Further acceleration is apparent when carbonyl is directly bonded to phenyl and there is no difference between the reactivity of acetophenone and benzophenone, both of which are five times as reactive as acetone. A small further increase in reactivity results when O and O' positions of benzophenone are joined in anthrone and fluorenone. The reactivity of the benzoyl group is reduced by the vicinal CHOHC₆H₅ group in benzoin, while benzil is as reactive as fluorenone. The formally similar naphthaquinone is half as reactive as benzil. Particularly interesting is the high reactivity of benzamide which reacts about 10^3 times as fast as acetamide.¹²

Specific rates of reaction of some of the substrates with H atoms were determined from the rates of formation of the corresponding H-atom adducts observed at appropriate wavelengths. Hydroxyl radicals were scavenged by 1.0 M *tert*-butyl alcohol and the hydrated

Table I: Rates of Reaction of e_{aq}^- and H Atoms with Aromatic Carbonyl Compounds in Aqueous Solution

Aromatic carbonyl compounds	$k(e_{aq}^- + S)$, M ⁻¹ sec ⁻¹ ^a	$k(H + S)$, M ⁻¹ sec ⁻¹ ^b
Acetophenone	2.8×10^{10}	$3.4 \pm 0.6 \times 10^9$
9,10-Anthraquinone-2-sulfonate	2.2×10^{10}	$4.1 \pm 0.3 \times 10^9$
Anthrone	3.3×10^{10}	...
Benzamide	1.9×10^{10} (1.7×10^{10}) ^c	...
Benzil	3.6×10^{10}	$1.0 \pm 0.2 \times 10^{10}$
Benzoin	1.7×10^{10}	...
Benzophenone	2.8×10^{10}	$5.6 \pm 0.3 \times 10^9$
Dibenzyl ketone	1.1×10^{10}	...
Fluorenone	3.3×10^{10}	$5.4 \pm 0.6 \times 10^9$
1,4-Naphthaquinone-2-sulfonate	2.6×10^{10}	$6.8 \pm 0.4 \times 10^9$
1,2-Naphthaquinone-4-sulfonate	1.7×10^{10}	...
Phenylacetone	1.2×10^{10}	...

^a Rate constant values $\pm 10\%$. ^b Determined from the rate of formation of the H-atom adduct, values $\pm 30\%$. ^c From ref 11.

electrons were converted into H atoms by maintaining a pH of 1.0. The resulting second-order rate constants



$$k_1 = 2.3 \times 10^{10} \text{ M}^{-1} \text{ sec}^{-1} \text{ (ref 11)} \quad (1)$$

are listed in Table I. These specific rates are about half an order of magnitude lower than the specific rates of addition of the hydrated electrons. Their values, like those of e_{aq}^- , vary over a factor of ~ 3 , but the differences do not parallel those observed with e_{aq}^- and are apparently due to different factors.

Spectra and pK_a Values of Ketyl Radicals

Benzophenone. The transient optical absorption spectrum of the benzophenone ketyl radical is shown in Figure 1. Absorption maxima at 545 and 332 nm were found in good agreement with results obtained by flash photolysis⁶ (545 and 330 nm). Only the band in the visible region has been reported^{13,14} in previous pulse radiolysis work. The weak band with $\lambda_{max} \sim 390$ nm observed at pH 4.9 in Figure 1 is due to the H-atom adducts to benzophenone (see Figure 2). These H atoms are produced in the radiolysis of water with a $G(H) = 0.55$.

In alkaline solutions, a considerable shift in the absorption spectrum of the ketyl radical anion can be seen

(11) M. Anbar and P. Neta, *Int. J. Appl. Radiat. Isotopes*, **18**, 493 (1967).

(12) E. Hayon, T. Ibata, N. N. Lichtin, and M. Simic, *J. Amer. Chem. Soc.*, **93**, 5388 (1971).

(13) G. E. Adams, J. H. Baxendale, and J. W. Boag, *Proc. Roy. Soc. Ser. A*, **277**, 549 (1964).

(14) E. J. Land, *ibid.*, **305**, 457 (1968).

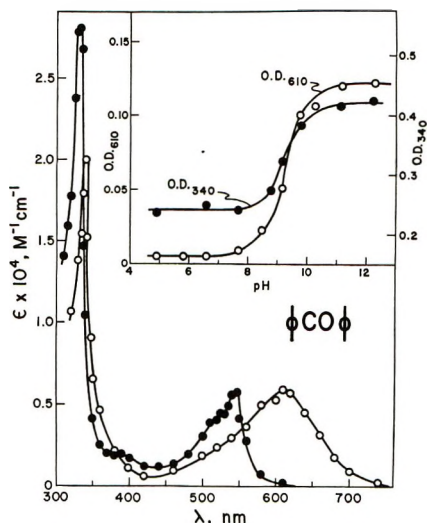


Figure 1. Optical absorption bands of the benzophenone ketyl radical (●, pH 4.9) and radical anion (○, pH 12.3). Insert: absorbance at 340 and 610 nm as a function of pH.

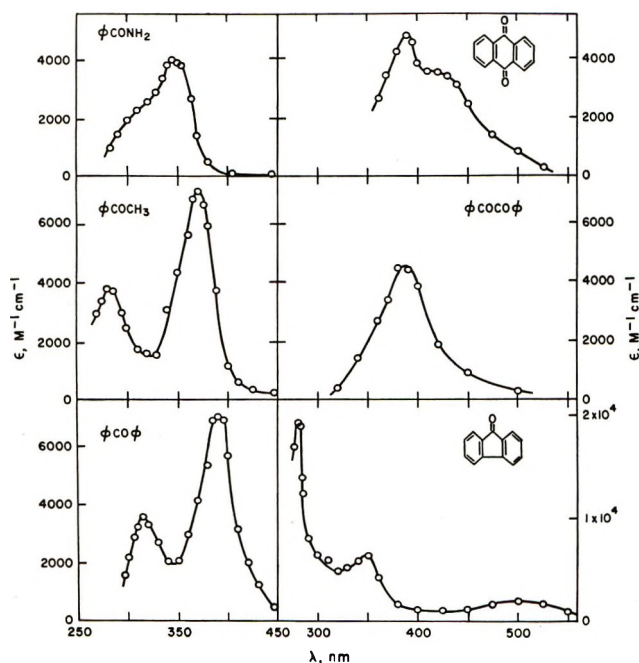


Figure 2. Optical absorption spectra of the H-atom adducts to some aromatic ketones. Spectra obtained in aqueous 1-2 M *tert*-butyl alcohol solutions, at pH 1.0.

(Figure 1), with λ_{\max} at 615 and 339 nm, as compared to 630 and 339 nm obtained by flash photolysis.⁶

The narrow intense absorption bands in the uv region have not been previously presented. To show that these bands are due to the ketyl radical and radical anions of benzophenone, corresponding to the well-known absorption bands in the visible region, the acid-base equilibrium of the ketyl radical was investigated at 610 and at 340 nm (see inset Figure 1). From these "titration" curves, a $pK_a = 9.25 \pm 0.1$ was obtained at both 610 and 340 nm, in agreement with the reported⁶ value of $pK_a = 9.2$.

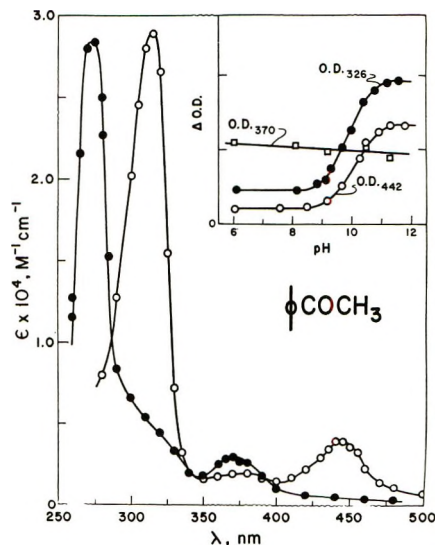
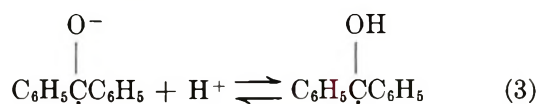
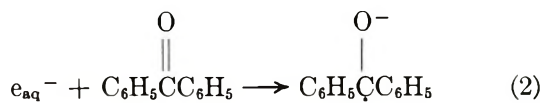


Figure 3. Optical absorption bands of the acetophenone ketyl radical (●, pH 5.6) and radical anion (○, pH 12.2). Insert: absorbance at 326, 370, and 442 nm as a function of pH.

The following reactions are considered



and under certain experimental conditions, the fast ($k_3 \geq 10^{10} M^{-1} sec^{-1}$) rate of protonation of the ketyl radical anion could be observed. Various values for the extinction coefficient of $(C_6H_5)_2\dot{C}OH$ have been determined and are summarized by Land.¹⁴ The value obtained in this work $\epsilon_{545} = 5.5 \times 10^3 M^{-1} cm^{-1}$ should be compared with the recent¹⁴ value of $\epsilon_{538} = 3.2 \times 10^3 M^{-1} cm^{-1}$. The extinction coefficients of the other bands and species, as well as the decay kinetics of these radicals, are given in Table II.

Acetophenone. The absorption spectra of the ketyl radical and radical anion of acetophenone are shown in Figure 3. In addition to the bands^{8,15} in the visible region, very intense bands are observed in the near-uv region of the spectrum. The band with $\lambda_{\max} \sim 370$ nm obtained at pH 5.6 (Figure 3) is that of the H-atom adduct to acetophenone (see Figure 2); the second band of the H-atom adduct can also be seen to contribute to the observed spectrum of the acetophenone ketyl radical. In addition to the intense band with $\lambda_{\max} 273$ nm, a relatively weak band with $\lambda_{\max} \geq 410$ nm can be seen (Figure 3). The acetophenone ketyl radical anion has bands at 445 and 314 nm. These bands are in fair agreement with those reported by Beckett, *et al.*,⁸ from flash photolysis studies.

(15) H. Lutz and L. Lindquist, *Proc. Chem. Soc.*, 493 (1971).

Table II: Absorption Maxima, Extinction Coefficients, Decay Kinetics, and pK_a Values of Ketyl Radicals and Radical Anions of Some Aromatic Carbonyl Compounds

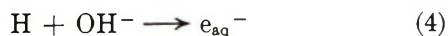
Aromatic carbonyl compound	Ketyl radical			pK_a	Ketyl radical anion		
	λ_{max} , nm	ϵ , $M^{-1} cm^{-1}$	$2k$, $M^{-1} sec^{-1}$		λ_{max} , nm	ϵ , $M^{-1} cm^{-1}$	$2k$, $M^{-1} sec^{-1}$
Acetophenone	273	2.9×10^4	...	9.9 ± 0.2	314	2.9×10^4	...
Benzophenone	332	2.9×10^4	1.8×10^9	10.1 ± 0.2	445	4.1×10^3	9.7×10^8
	545	5.5×10^3	2.0×10^9	9.25 ± 0.1	339	2.0×10^4	...
Benzamide	295	2.3×10^4	4.4×10^9	7.7 ± 0.2	615	6.1×10^3	<i>a</i>
	430	4.5×10^3	5.2×10^9	...	320	2.9×10^4	8.1×10^8
Fluorenone	347	1.6×10^4	3.8×10^9	...	440	5.6×10^3	7.3×10^8
	362	1.3×10^4	4.4×10^9	6.3 ± 0.2	360	1.1×10^4	...
	520	1.1×10^3	450	6.2×10^3	...
Benzil	372	8.8×10^3	1.1×10^9	...	362	6.4×10^3	<i>a</i>
	495	2.0×10^3	...	5.5 ± 0.2	545	3.6×10^3	<i>a</i>
Benzoin	310	9.0×10^3	312	2.5×10^4	...
					460	2.9×10^3	...
9,10-Anthraquinone-2-sulfonate	387	1.4×10^4	1.6×10^9	...	398	9.8×10^3	1.6×10^9
				...	465	8.0×10^3	...
				3.9 ± 0.2	496	9.5×10^3	1.3×10^9
				

* Complex decay kinetics.

No extinction coefficients appear to have been obtained in earlier investigations. These values for the acetophenone ketyl radicals and radical anions are given in Table II.

The acid-base properties of the acetophenone ketyl radical were followed at 442 and at 326 nm to show that both bands are due to the ketyl radical. A $pK_a = 10.1 \pm 0.2$ at 442 nm and a $pK_a = 9.9 \pm 0.2$ at 326 nm were obtained. These values are considerably lower than the $pK_a = 10.9$ found by Beckett, *et al.*⁸ No explanation is apparent to account for this significant difference.

The change in absorbance at 370 nm was followed as a function of pH (see insert Figure 3) to show that this band is not due to the ketyl radical but to the H-atom adduct to acetophenone. The small decrease in OD_{370} with increase in pH is probably due to the shift with pH of the overlap of the spectra of the ketyl radicals, as well as to the partial conversion in alkaline solution of H atom into e_{aq}^- .



Benzamide. The electron adducts of benzamide and its conjugated acid have apparently not been observed previously. The ketyl radical has an absorption spectrum with maxima at 430 and 295 nm; see Figure 4. In alkaline solutions when the anion radical is present, the absorption bands are shifted to 440 and 320 nm, respectively. The acid dissociation constant of the ketyl radical of benzamide has a $pK_a = 7.7 \pm 0.2$. It is interesting to note that this pK_a value is significantly lower than the pK_a of the ketyl radical of $C_6H_5COCH_3$.

The H-atom adduct to benzamide has a maximum at ~ 350 nm (Figure 2), and its contribution to the ob-

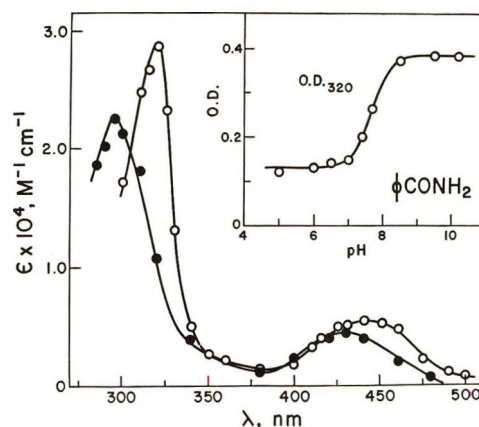


Figure 4. Optical absorption bands of the benzamide ketyl radical (\bullet , pH 5.5) and radical anion (\circ , pH 9.5). Insert: absorbance at 320 nm as a function of pH.

served spectra of the ketyl radicals in that wavelength region can be seen in Figure 4.

The extinction coefficients and decay kinetics of the benzamide ketyl radicals are given in Table II.

Benzil and Benzoin. Figure 5 shows the absorption spectra of the ketyl radical and radical anion of benzil in aqueous solution. The ketyl radical has absorption maxima at 495 and 372 nm (compared to 490 and 365 nm obtained⁸ by flash photolysis). The ketyl radical anion has maxima at 545 and 362 nm (compared⁸ to 550 and 330–380 nm). Another absorption band below ~ 310 nm could be seen for both the neutral and the alkaline forms, but could not be accurately measured due to the strong absorption of benzil itself in that wavelength region.

The pK_a of the benzil ketyl radical was determined at 540 nm (insert, Figure 5) and a $pK_a = 5.5 \pm 0.2$

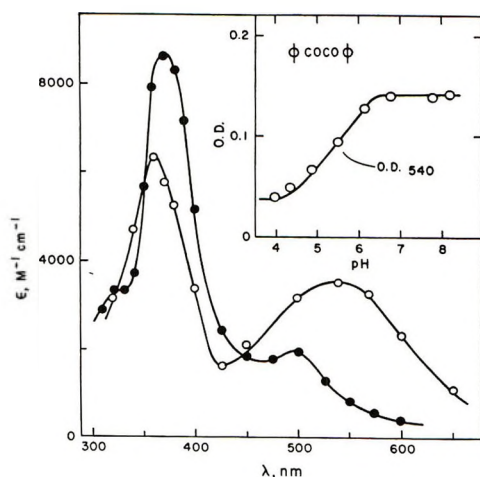


Figure 5. Optical absorption bands of the benzil ketyl radical (\bullet , pH 4.2) and radical anion (\circ , pH 8.2). Insert: absorbance at 540 nm as a function of pH.

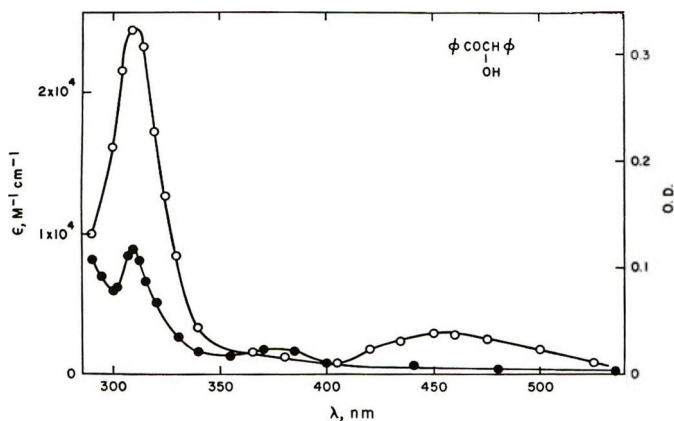


Figure 6. Optical absorption bands of the benzoin ketyl radical (\bullet , pH 4.9) and radical anion (\circ , pH 12.6).

was derived. This compared with a $pK_a = 5.9$ reported by Beckett, *et al.*⁸

The absorption spectra of the ketyl radicals of benzoin are shown in Figure 6. Owing to the instability of the species produced, it was not possible to derive the dissociation constant of this ketyl radical. The spectrum determined at pH 12.6 is presumed to be that of the ketyl radical anion.

Anthraquinone. The absorption spectra of the semiquinone radical and radical anion of 9,10-anthraquinone-2-sulfonate (A) are shown in Figure 7. The spectrum of the radical anion A^- has maxima at 496, 465, and 398 nm, and these are close to 500 and 390 nm reported in both pulse radiolysis¹⁶ and flash photolysis¹⁷ studies. The radical AH has one main band with λ_{max} at 387 nm.

The H-atom adduct to A has maxima at 390 and ~ 425 nm (Figure 2) and can be seen to contribute to the absorption spectra of the semiquinone radicals shown in Figure 7.

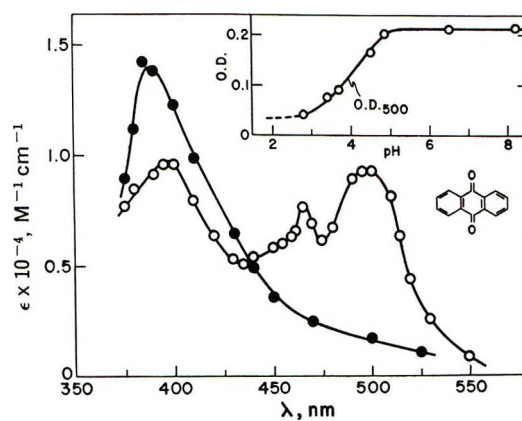


Figure 7. Optical absorption bands of the 9,10-anthraquinone-2-sulfonate ketyl radical (\bullet , pH 3.5) and radical anion (\circ , pH 8.3). Insert: absorbance at 500 nm as a function of pH.

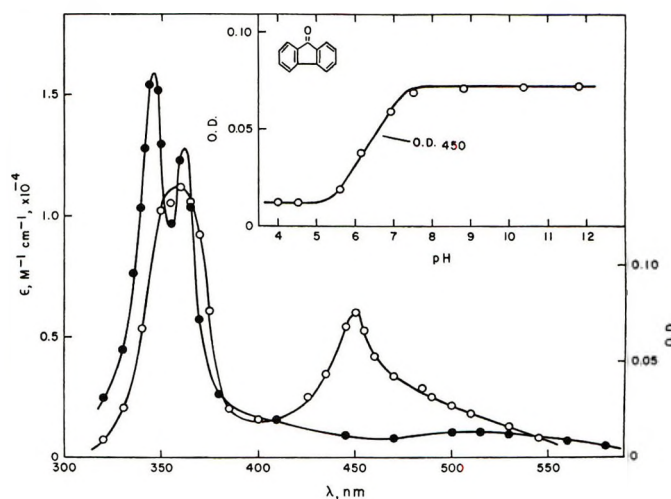


Figure 8. Optical absorption bands of the fluorenone ketyl radical (\bullet , pH 4.3) and radical anion (\circ , pH 12.2). Insert: absorbance at 450 nm as a function of pH.

The dissociation constant of the semiquinone AH was determined by following the change of absorbance at 500 nm with pH. A value of $pK_a = 3.9 \pm 0.2$ was obtained, which is higher than the value of 3.25 reported by Hulme, *et al.*¹⁶ A value of $pK_a = 4.0$ has been obtained¹⁸ for the semiquinone radical of benzoquinone.

The extinction coefficients given in Table II for the semiquinone radicals of A are in good agreement with those reported¹⁶ recently.

Fluorenone. The full absorption spectra and dissociation constant of the ketyl radicals of fluorenone

(16) B. E. Hulme, E. J. Land, and G. O. Phillips, *Chem. Commun.*, 518 (1969).

(17) N. K. Bridge and G. Porter, *Proc. Roy. Soc., Ser. A*, **244**, 277 (1958); G. O. Phillips, N. W. Worthington, J. F. McKellar, and R. R. Sharpe, *Chem. Commun.*, 835 (1967).

(18) G. E. Adams and B. D. Michael, *Trans. Faraday Soc.*, **63**, 1175 (1967).

apparently have not been determined.¹⁹ The ketyl radical of fluorenone has absorption maxima at 520, 362, and 347 nm (see Figure 8), with extinction coefficients ranging from $1.1 \times 10^3 M^{-1} \text{ cm}^{-1}$ at 520 nm to $1.6 \times 10^4 M^{-1} \text{ cm}^{-1}$ at 347 nm. The ketyl radical anion has a relatively sharp band at 450 nm, another broader band at 360 nm, and a third band hidden under the 450-nm band at higher wavelengths. Since the H-atom adduct of fluorenone has bands at 500, 348, and 270 nm which are relatively strong (Figure 2), the contribution due to this radical has been corrected in Figure 8. Hence the spectra of the ketyl radicals shown in Figure 8 do not include a contribution from the H-atom adduct.

The acid-base property of this ketyl radical was monitored at 450 nm, and a $pK_a = 6.3 \pm 0.2$ was obtained.

H-Atom Adducts to Aromatic Ketones. Figure 2 combines the optical absorption spectra of the H-atom adducts of benzamide, acetophenone, benzophenone, anthraquinone, benzil, and fluorenone. Significant differences are observed in the number of bands, absorption spectra, and extinction coefficients of these radicals (see Table III). Second bands at lower wave-

Table III: Absorption Maxima, Extinction Coefficients, and Decay Kinetics of H-Atom Adducts of Some Aromatic Carbonyl Compounds

Aromatic carbonyl compound	H-Atom adduct ^a		
	λ_{max} , nm	ϵ_{max} , $M^{-1} \text{ cm}^{-1}$ ^b	$2k$, $M^{-1} \text{ sec}^{-1}$ ^b
Acetophenone	285	3.8×10^3	...
	370	7.3×10^3	4.1×10^9
Benzophenone	315	3.6×10^3	...
	390	7.2×10^3	3.2×10^9
Benzamide	350	4.0×10^3	2.0×10^9
Fluorenone	270	2.0×10^4	...
	348	6.5×10^3	2.6×10^9
	500	2.0×10^3	...
Benzil	385	4.6×10^3	1.3×10^9
9,10-Anthraquinone-2-sulfonate	390	4.8×10^3	1.9×10^9
1,4-Naphthoquinone-2-sulfonate	380	9.4×10^3	1.2×10^9

^a Determined in aqueous solution at pH 1.0. ^b Values to $\pm 15\%$.

lengths and with lower extinction coefficients can be seen for benzamide, acetophenone, and benzophenone. Presumably in this case, as with the other aromatic ketones, the addition of H atoms takes place at more than one site. It is interesting to note that this addition reaction is not specific, whereas the attachment of electrons to aromatic ketones occurs almost exclusively with the carbonyl group. A similar selectivity has recently been observed for 2-, 3-, and 4-benzoylpyridines.²⁰

Discussion

Relative Reactivity of the Reactions of e_{aq}^- and H. In spite of the fact that the specific rate of reaction of the electron with the various aromatic carbonyl compounds is in every case greater than $10^{10} M^{-1} \text{ sec}^{-1}$, systematic variation of reactivity with structure is apparent. It was previously^{12,21} pointed out that a correlation between structure and reactivity in the very fast reactions of OH radicals with amides occurs but the reactions are about one-tenth as great as the present ones. Dependence of the reactivity of the various carbonyl compounds on their molecular structure appears to correlate the intramolecular properties not, for instance, with differences in solvation. Specific rates of reaction with H atoms also vary with structure but the reactivity sequence does not parallel that followed in reactions of e_{aq}^- . Clearly different factors determine the sequences for the two radicals.

A large effect of structure on reactivity is observed in the reaction of benzamide with e_{aq}^- for which $k(e_{\text{aq}}^- + \text{amide})$ is between 10^2 and 10^3 times as large as it is for a number of aliphatic amides.¹² This difference contrasts with the *ca.* fivefold difference in reactivity between acetone and acetophenone, although in both cases reactivity is increased by conjugation of carbonyl with the aromatic ring.

The specific rate of reaction of benzene with e_{aq}^- is similar¹¹ to those of the aliphatic amides.¹² Theoretical inspection of these differences would require quantum mechanical calculations. Such calculations have been reported for benzoic acid²² and have been carried out for benzamide.²³ Both EHMO and CNDO calculations show that the lowest unoccupied molecular orbital of benzamide is characterized by high p character at all carbon atoms, oxygen, and nitrogen, indicating extensive delocalization. Both calculations indicate a large net positive charge at the carbonyl carbon. According to the CNDO calculations addition of an electron to the lowest unfilled orbital has little effect on its composition in terms of atomic orbitals. Similar features pertain to benzoic acid and benzoate. Just how they relate to the high specific rates of reaction with e_{aq}^- is not clear as yet.

The initial site of interaction of e_{aq}^- appears to be with the carbonyl groups of these aromatic compounds. Conjugation of the odd electron with the rest of the molecule follows, as has been observed by esr studies (see ref 19, and other references therein). Similarly, e_{aq}^- initially attaches itself to the $>C=O$

(19) N. Hirota and S. I. Weissman, *J. Amer. Chem. Soc.*, **86**, 2538 (1964); H. V. Carter, B. J. McClelland, and E. Warhurst, *Trans. Faraday Soc.*, **56**, 455 (1960).

(20) D. A. Nelson and E. Hayon, unpublished data.

(21) N. N. Lichtin, *Israel J. Chem.*, **9**, 397 (1971).

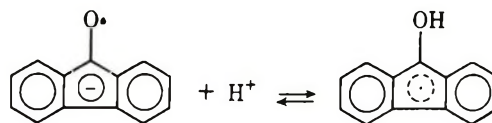
(22) M. Simic and M. Z. Hoffman, *J. Phys. Chem.*, **76**, 1398 (1972).

(23) Private communication from Dr. Richard H. Mann.

groups in substituted pyrimidines²⁴ (e.g., uracil, thymine, cytosine, orotic acid, etc.). It is suggested that the resulting odd electron also interacts strongly with the 5,6 double bond in pyrimidines. Keto-enol tautomerism further enhances such a conjugation.

Dependence of pK_a Structure on Protonated Electron Adducts. In all cases the negatively charged electron adducts are much more basic than the corresponding neutral molecules. The similarity of the equilibrium constants of the radicals derived from acetophenone and benzophenone suggests that the dominant influence is similar with changes in delocalization energy consequent upon protonation of the electron adduct. The difference between them is similar in magnitude to the difference in acidity of acetic and benzoic acids. The neutral radical derived from fluorenone, which differs from benzophenone by linkage of ortho positions of the two phenyl groups, has a dissociation constant $\sim 10^3$ times as great as that of benzophenone. This large difference can be associated with the cyclopentadiene nature of the central ring of

fluorenone. In the anion radical this ring has an electron distribution analogous to that of the cyclopentadienyl anion, a species which is unusually stable because the aromatic sextet is filled. Protonation on oxygen removes an electron from the central ring with concomitant loss of stabilization. The even greater



acidities of the neutral radicals derived from benzil and 9,10-anthraquinone-2-sulfonate can be related to the greater loss of resonance stabilization resulting when the symmetrical anion radicals are converted into unsymmetrical species by protonation. Qualitative consideration of the "inductive effect" of the amino group suggests that the neutral radical derived from acetamide should be more acidic than the radicals derived from acetophenone or benzophenone.

(24) E. Hayon, *J. Chem. Phys.*, **51**, 4881 (1969).

Powder ENDOR Line Shapes: Nuclear Relaxation Induced by Motion of Nearby Electron Spins

by Daniel S. Leniart,* James S. Hyde, and Jacques C. Vedrine¹

Varian Associates, Analytical Instrument Division, Palo Alto, California 94303 (Received May 20, 1971)

Publication costs assisted by Varian Associates

The line shape and intensity of electron-nuclear double resonance (ENDOR) spectra in powders is determined, in part, by the specific form of the mechanism(s) that produce nuclear spin-lattice relaxation. In all cases investigated, nuclear relaxation is assumed to stem from modulation of the electron-nuclear dipolar (END) interaction. The initial model considered assumes that the unpaired electron is trapped in a cage and undergoes a series of jumps between at least two equally probable sites. The dimensions of the cage are such that any fluctuations in angle are severely restricted, and this jumping motion results only in a modulation of the interparticle distance between the trapped H atom and surrounding nuclei outside the cage. It is shown that the dominant relaxation component of the surrounding nuclei is proportional to $\sin^4 \theta$ and leads to a doubly peaked ENDOR spectrum. The second model assumes that the trapped electron resides in a cage whose walls are at infinite potential, and the system is treated quantum mechanically as a particle in a three-dimensional box. The thermal lattice motions of the cage modulate the dipolar interaction in some random manner to produce a spectral density which differs from that of the jump model by the appearance of a Boltzmann factor describing the particle populations and a frequency term corresponding to the quantized transitions induced between the energy levels of the box. It is shown that for particle transition frequencies, $\omega_{\nu\nu'}$, which are less than or equal to spin transition frequencies, $\omega_e \pm \omega_n$, the quantum mechanical spectral densities reduce to those of the semiclassical jump model. As the temperature is reduced below 20°K the ENDOR line shape expected from the "box" model is shown to resemble that of a matrix ENDOR signal. At very low temperatures a change in both the ENDOR line shapes and intensities is predicted.

I. Introduction

We have been concerned for some time in this laboratory with the development of methods for performing and analyzing electron-nuclear double resonance experiments on unordered solids, so-called powder ENDOR.²⁻⁷ The motivation is improved epr resolution from systems where sufficiently large single crystals cannot be prepared. It is nevertheless assumed that the local order is high such that the sample can be visualized as a large number of crystallites isotropically distributed in orientation.

The companion paper to this one describes an ENDOR experiment on Y-type zeolites γ -irradiated at 77°K.⁸ Hydrogen atoms are trapped and the ENDOR experiment is performed on protons in the vicinity of the trapped atoms. The present theoretical analysis was developed during the course of this experiment. It is this type of sample which is envisioned throughout, although we have attempted to generalize the analysis.

If a double resonance experiment is to be performed on a system having a nuclear longitudinal relaxation time, T_{1n} , that can be made comparable to the electronic longitudinal relaxation time, T_{1e} , then the intensity and line shape of the stationary ENDOR signal are dependent on the magnitude and mechanism of this nuclear relaxation. In general, the overall line shape of a powder ENDOR signal may be written as

$$f(\nu) = k \int_0^r \int_0^\pi \int_0^{2\pi} T_{1n}^{-1}(r, \theta, \phi) \times g(\nu - \nu_0(r, \theta, \phi)) r^2 \sin \theta \, d\phi d\theta dr \quad (1)$$

where $g(\nu - \nu_0(r, \theta, \phi))$ is the spin-packet distribution function—which is commonly assumed to be either Gaussian or Lorentzian—centered at a resonant frequency $\nu_0(r, \theta, \phi)$ that may be orientation dependent, T_{1n}^{-1} is proportional to the number of nuclear spins relaxing per unit time, and k is a constant which affects the amplitude, but not the shape, of the entire spectrum. Equation 1 implies that T_{1e} is orientation independent.

Hyde,^{2a} *et al.*, initially investigated this problem from the standpoint of ENDOR and evaluated eq 1 using a

- (1) Varian Associates Postdoctoral Fellow, 1970.
- (2) (a) J. S. Hyde, G. H. Rist, and L. E. G. Eriksson, *J. Phys. Chem.*, **72**, 4269 (1969); (b) A. L. Kwiram, *Bull. Amer. Phys. Soc.*, **88**, 4763 (1968).
- (3) G. H. Rist and J. S. Hyde, *J. Chem. Phys.*, **50**, 4532 (1969).
- (4) L. E. G. Eriksson, J. S. Hyde, and A. Ehrenberg, *Biochim. Biophys. Acta*, **192**, 211 (1969).
- (5) G. H. Rist, J. S. Hyde, and T. Vanngard, *Proc. Nat. Acad. Sci. U. S.*, **67**, 79 (1970).
- (6) G. H. Rist and J. S. Hyde, *J. Chem. Phys.*, **52**, 4633 (1970).
- (7) J. S. Hyde, T. Astlund, L. E. G. Eriksson, and A. Ehrenberg, *Rev. Sci. Instrum.*, **41**, 1598 (1970).
- (8) J. C. Vedrine, J. S. Hyde, and D. S. Leniart, *J. Phys. Chem.*, **76**, 2087 (1972).

special set of conditions. They assumed that the unpaired electron spin, evenly distributed over a sphere of radius $r_0 < 3.5 \text{ \AA}$, interacted with surrounding nuclei assumed to be in a uniform continuous distribution throughout the matrix. The nuclear resonance frequency was determined solely by the electron-nuclear dipolar interaction and a spin-packet line shape of Lorentzian character was employed. They postulated a specific form of the nuclear relaxation and proceeded to solve eq 1 using a variety of limits when performing the integration over dr ; *i.e.*, they calculated the line shape for various values of the dipolar interaction. Their results show that an unpaired electron which interacts with a continuous distribution of protons will give rise to an ENDOR signal whose position is unshifted from the free proton resonance frequency and whose intensity and line shape are dependent on the magnitude of the dipolar term. Their calculations are in agreement with the experimental results which consistently show a single resonance peak at the free proton frequency. This particular type of spectrum has been coined as the matrix ENDOR signal.

In the present work we investigate the class of powder ENDOR line shapes produced by the interaction of an unpaired electron spin with a single nucleus. The spin Hamiltonian includes contributions from the nuclear Zeeman, isotropic hyperfine, and electron-nuclear dipolar interactions which may produce a variety of ENDOR line shapes depending on their magnitudes relative to each other. A second equally important factor contributing to the line shape is the form of the dominant mechanism that produces nuclear relaxation. A few of the more probable relaxation mechanisms are discussed, and their effects on the ENDOR lines are given explicitly in the form of computer simulations.

The new ideas presented here are largely concerned with nuclear relaxation induced by the END interaction when (a) a trapped H atom undergoes random motion within the cage and (b) the trapped H atom is quantized within the cage in much the same manner as is the model of a particle in a box. These models are then related to the ENDOR line shapes that can be expected from powder samples.

II. Effect of Nuclear Relaxation on ENDOR Line Shape

Case I. T_{1n}^{-1} Independent of θ and ϕ . Initially we make the simplifying supposition that the nuclear relaxation probability is a constant which may be removed from the integrand of eq 1 and included in k . All rotationally invariant interactions which induce relaxation, such as a fluctuation in the hyperfine splitting whose form is written as a scalar product, $\mathcal{H}_1 = a(t)I \cdot S$, may be grouped in this category. For an electron interacting with protons at specific distances (*i.e.*, shells of protons), the spectral line shape is then written as

$$f(\nu, r) = \sum k r_i^2 \int_0^{2\pi} \int_0^\pi e^{-(\omega(r_i, \theta, \phi) - 2\pi\nu)^2 / (T_2^{-1})^2} \sin \theta d\theta d\phi \quad (2)$$

where the resonant frequency $\omega(r_i, \theta, \phi)$ is determined from the Hamiltonian $\mathcal{H}(r_i, \theta, \phi)$ describing the spin system of interest. When dealing with zeolites the appropriate Hamiltonian is simply

$$\mathcal{H} = \mathcal{H}_Z + \mathcal{H}_{FC} + \mathcal{H}_D(r_i, \theta, \phi) \quad (3)$$

where

$$\mathcal{H}_Z = g_e \beta_e \mathcal{H}_0 S_z + g_n \beta_n H_0 I_{z_i} \quad (4a)$$

$$\mathcal{H}_{FC} = \hbar \gamma_e a_i I_i \cdot S = \hbar \gamma_e a_i I_{z_i} S_z \quad (4b)$$

$$\begin{aligned} \mathcal{H}_D(r_i, \theta, \phi) &= \\ & \sum_i g_e \beta_e g_n \beta_{n_i} \left\{ \frac{\vec{I}_i \cdot \vec{S}}{r_i^3} - \frac{3(\vec{I}_i \cdot \vec{r}_i)(\vec{S} \cdot \vec{r}_i)}{r_i^5} \right\} \quad (4c) \\ &= \sum_i g_e \beta_e g_n \beta_{n_i} (3 \cos^2 \theta - 1) S_z I_{z_i} \\ &= \sum_i \pm \alpha_i (3 \cos^2 \theta - 1) I_{z_i} \end{aligned}$$

and $\alpha_i = g_e \beta_e g_n \beta_{n_i} / 2r_i^3$. When investigating samples other than zeolites, one may wish to include additional interactions such as quadrupole, zero field, etc., but here we will restrict ourselves to the three interactions mentioned above and examine their effects on powder ENDOR of protons.

If the hyperfine interaction is negligible ($a_i = 0$), the ENDOR position will be determined by the Zeeman interaction only, and the ENDOR line shape by the END interaction. When monitoring a particular epr hyperfine line (*e.g.*, $m_I = -1/2$) with the microwave field and sweeping the radiofrequency through nuclear resonance, each nucleus will resonate at two possible frequencies depending upon the sign of m_s (*cf.* eq 4c). If the sample is a powder, the intensity distribution obtained by integrating eq 2 over $0 \leq \theta_i \leq \pi/2$ is similar to that given by Pake and others.^{9,10} If each spin-packet line shape is represented by a Gaussian distribution with a half-width of half-height, T_2^{-1} , equal to some fraction of the magnitude of the dipolar interaction (*e.g.*, $0.1\alpha_i$), then the simulated line shape is given in Figure 1.

Under certain conditions it is possible to obtain an ENDOR line shape from a hydrogen atom and only one proton that is (1) a single line centered at the free proton frequency, ν_i , produced by a dipolar interaction which is small compared to the spin-packet line width, $\alpha_i < T_2^{-1}$; (2) a doublet with peaks $\nu \pm \alpha_i$ when the single line above is split by a larger dipolar interaction, $\alpha_i > T_2^{-1}$; and (3) a doublet with two distinct peaks at

(9) G. E. Pake, *Phys. Rev.*, **16**, 327 (1948).

(10) (a) P. Kottis and R. Lefebvre, *J. Chem. Phys.*, **39**, 393 (1963); (b) P. Kottis and R. Lefebvre, *ibid.*, **41**, 379 (1964); (c) J. A. Ibers and J. D. Swalen, *Phys. Rev.*, **127**, 1914 (1962); (d) J. D. Swalen and H. M. Gladney, *IBM J. Res. Develop.*, **11**, 515 (1964).

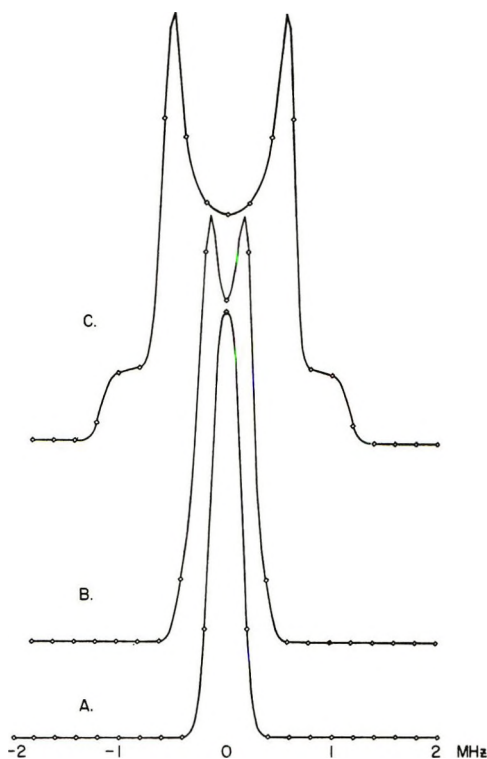


Figure 1. ENDOR spectra computed for a Gaussian line shape of width $T_2^{-1} = 90$ kHz: A, $\alpha_i = 105$ kHz; B, $\alpha_i = 210$ kHz; C, $\alpha_i = 580$ kHz; $a_i = 0.0$ kHz for all spectra.

$\nu \pm \alpha_i$ and two distinct shoulders at $\nu \pm 2\alpha_i$ when the dipolar interaction is very large, $\alpha_i \gg T_2^{-1}$. If these outside shoulders are present in an ENDOR display, they will never develop into distinct peaks.

The situation changes rather dramatically if a_i is now finite and, as is commonly observed, greater than the magnitude of the dipolar interaction. The effect of the hyperfine interaction is to shift the nuclear resonance frequency centrosymmetrically about that of the free proton to establish two new resonant frequencies centered at $\gamma \pm \nu_e a_i / 2$. Now the ENDOR positions as well as the ENDOR line shapes depend on m_s ; however, the latter depend on the sign of a_i as well. If a_i is positive (negative), the powder ENDOR signal corresponding to $m_s = 1/2$ will be shifted to lower (higher) frequency (see Figure 2).

If the ratio $(\alpha_i / T_2^{-1}) \gg 1$, the ENDOR line shape will have a peak and a shoulder both above and below the free proton frequency centered at $\nu \pm \gamma_e a_i / 2$. However, the frequency separation of the ENDOR peaks for a positive splitting constant will be $(\gamma_e a_i + 2\alpha_i)$ MHz compared to a shoulder separation of $(\gamma_e a_i - 4\alpha_i)$ MHz. On the other hand, if a_i is negative, the peak-to-peak separation of $(\gamma_e a_i - 2\alpha_i)$ now becomes less than the shoulder to shoulder separation of $(\gamma_e a_i + 4\alpha_i)$ MHz. ENDOR of powders under these conditions thus provides an easy, convenient method for determining the sign of the hyperfine splitting constant.³ If the ratio (α_i / T_2^{-1}) is roughly equal to unity,

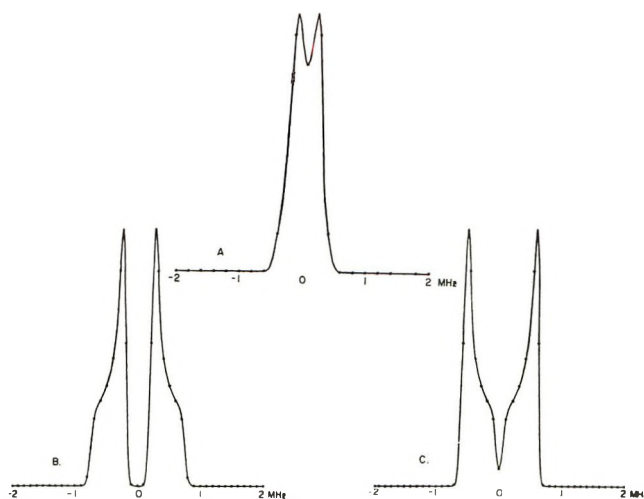


Figure 2. A, The ENDOR line shape computed for a Gaussian line shape of width $T_2^{-1} = 90$ kHz, $a_i = 0.0$, $\alpha_i = 210$ kHz; B, $T_2^{-1} = 60$ kHz, $a_i = 400$ kHz, $\alpha_i = 175$ kHz; C, $T_2^{-1} = 60$ kHz, $a_i = -400$ kHz, $\alpha_i = 175$ kHz.

the shoulders will disappear; however, the sign of a_i can still be determined from the absolute value of the theoretical peak-to-peak splitting by plotting the theoretical spectrum employing both positive and negative values of a_i and comparing each of these results with the experimental value of the peak-to-peak separation. It would be impossible to extract the sign of a_i when $(\alpha_i / T_2^{-1}) \ll 1$ since the value of $\alpha_i \ll \gamma_e a_i$, ν .

This general description of ENDOR line shapes is valid when the nuclear relaxation time is constant. However, the line shape is substantially altered when specific nuclear relaxation mechanisms are postulated whose radical and/or angular dependencies are functions of time.

Case II. T_{1n} , a Function of r, θ, ϕ . There have been a number of mechanisms proposed that cause the nuclear spin to relax. When an unpaired electron spin is present in the sample, the dominant nuclear relaxation arises from the electron-nuclear dipolar interaction. In powders or crystals where the electron and nuclei occupy fixed positions in space, nuclear relaxation may occur by either of two mechanisms: (1) the fluctuating magnetic field at the nucleus that arises from the relaxing electron,¹¹ or (2) changes in the magnitude of the dipolar interaction caused by unusual motion.

(1) *Nuclear Relaxation via Electronic Relaxation.* Since the reorientation correlation time, τ_c , of a crystallite approaches infinity, almost no relaxation will result from Brownian motion of the nuclear and electron spins. Modulation of the dipolar interaction may then be achieved by the relaxing electron spin of characteristic time T_{1e} . Only the pseudosecular term of the dipolar interaction ($\propto S_z I_{\pm}$) provides a nuclear relaxation path whose magnitude is proportional to $(T_{1e} / (1 +$

(11) C. T. Trammell, H. Zeldes, and R. Livingston, *Phys. Rev.*, **110**, 630 (1958).

$\omega_n^2 T_{1e}^2)) \sim (\omega_n^2 T_{1e})^{-1}$. All other paths involve terms $(T_{1e}/(1 + (\omega_e \pm \omega_n)^2 T_{1e}^2)) \sim (\omega_e^2 T_{1e})^{-1}$ and may be neglected since $(\omega_n/\omega_e)^2 \sim 10^{-6}$. Abragam¹² has calculated the nuclear relaxation time in a dilute paramagnet as a function of θ and r_{n_i}

$$T_{1n_i}^{-1} = (9/16) \gamma_e^2 \gamma_{n_i}^2 \hbar^2 \sin^2 \theta \cos^2 \theta r_{n_i}^{-6} (\omega_{n_i}^2 T_{1e})^{-1} \quad (5)$$

The ENDOR spectrum for a nucleus n_i , at a distance r_i , from the electron spin can be determined by performing the integration

$$f(\nu, r_i) = k \int_0^\pi T_{n_i}^{-1}(\theta, r_i) \times e^{-[(\omega_z + \omega_{FC} + \omega_D(r_i, \theta, \phi) - 2\pi\nu)/(T_2^{-1})^2] r_i^2 \sin \theta d\theta} \quad (6)$$

Figure 3 shows the effect on the ENDOR line shape of nuclear relaxation *via* the pseudosecular term of the dipolar interaction in the presence of a relaxing electron. The physical basis for the change from a doublet to a single matrixlike ENDOR line is that $\cos^2 \theta \sin^2 \theta$ has a maximum of 45° which is rather close to the dipolar magic angle of 54.7° , resulting in a buildup of intensity very near the free proton frequency independent of the strength of the dipolar interaction.

We have solved the integral for various values of the line width T_{2n}^{-1} , the radical separation r_{n_i} , and the contact interaction a_{n_i} . The effect of the first two parameters is to narrow or broaden the line without changing its resonance position, while the hyperfine coupling produces two lines of similar shape at resonance frequencies $\nu_{n_i} \pm \gamma_e a_{n_i}/2$.¹³ The general effect of the angular dependence of this particular type of relaxation is to transform the Pake doublet type of powder spectrum having peaks at $\nu_{n_i} \pm \alpha_i$ (as expected from a purely dipolar interaction) into a single matrix ENDOR-like spectrum centered at ν_{n_i} (see Figure 3).

(2) *Nuclear Relaxation via Motional Processes.* In the event that the physical or chemical properties of the system under investigation permit the unpaired electron or nuclear spin to undergo random motion in a time, τ_c , which is much less than T_{1e} , then the dipolar interaction will be modulated by the faster motion and the nuclear relaxation mechanisms may become liquidlike in nature. If the characteristic time of this motion is such that $\omega_e \tau_c \sim 1$, then nuclear relaxation may occur *via* all five components of the irreducible spherical tensor representation of the dipolar interaction¹⁴ (see Table I). The magnitudes of the nonsecular terms, $A^{(0)}$ and $A^{(\pm 2)}$, now become comparable to the pseudosecular term, $A^{(\pm 1)}$, and cross relaxation, as well as pure nuclear spin flips, becomes a veritable mechanism for relaxing the spin I.

(a) *Physical Model.* We choose for our model a powder sample whose molecular skeleton is constructed in a manner so as to create a myriad of naturally occurring cavities. As, for example, in zeolite systems the three types of cages that are found may be described by

Table I: Spherical Tensor Components^a of the END Interaction

$$\mathcal{H}_D = \bar{I} \cdot \bar{T}_D \cdot \bar{S} = \sum_q F_D^{(q)}(t) A_D^{(-q)}$$

	$F^q(t)$	$A^{(q)}$
$q = 0$	$(\hbar \gamma_e \gamma_n) \left(\frac{1 - 3 \cos^2 \theta}{r^3} \right)$	$I_z S_z - 1/4(I_+ S_- + S_+ I_-)$
$q = \pm 1$	$(\hbar \gamma_e \gamma_n) \left(\frac{\sin \theta \cos \theta e^{\pm i \phi}}{r^3} \right)$	$3/2(I_z S_\pm + S_z I_\pm)$
$q = \pm 2$	$(\hbar \gamma_e \gamma_n) \left(\frac{\sin^2 \theta e^{\pm i 2 \phi}}{r^3} \right)$	$3/4(I_\pm S_\pm)$

^a The $F^{(q)}$ are classical lattice parameters whose time dependence may be contained in θ and/or r . The $A^{(q)}$ are operators of the spin system which is coupled to the lattice. $f^q(\theta) = F^q(\theta)r^3$.

various dimensions and shapes. The unpaired electrons or H atoms which are produced upon γ irradiation of the sample may then become encapsulated in one or more of these sites. Experimental evidence substantiates this model¹⁵ and Adrian¹⁶ has proposed a theoretical interpretation of the experimental data by describing the effects of the nature of the trapping site on powder epr spectra.

Assume that a proton is located somewhere outside the cage at a given distance, \bar{r}_{n_i} , from the trapped electron such that the magnitude of the dipolar interaction between them is not negligible. The hydrogen atom will undergo random motion within the cage at a frequency that may be estimated from the natural line width of the available spectroscopic data. This motion modulates the dipolar interaction by changing both the magnitude and direction of the vector \bar{r}_{n_i} as shown in Figure 4. However, since the H atom is trapped, the magnitude of the fluctuations in orientation, θ_{n_i} , is severely limited when compared, for example, to that of a liquid.¹⁷ It seems quite reasonable to assert that although some angularly independent liquidlike nuclear relaxation will occur from changes in the orienta-

(12) A. Abragam, "The Principles of Nuclear Magnetism," Oxford University Press, London, 1961, p 380.

(13) In cases where the spin packet is extremely narrow and $\ll \alpha$, it is theoretically possible to split the ENDOR line since the two maxima differ by 7° (see Figure 5 of ref 2a). However, it is highly unlikely that one would arrive at a set of conditions where the splitting can be observed experimentally.

(14) (a) J. H. Freed and G. K. Fraenkel, *J. Chem. Phys.*, **39**, 326 (1963); (b) J. H. Freed, Doctoral Thesis, Columbia University, New York, N. Y., 1962.

(15) (a) S. W. Foner, E. L. Cochran, V. A. Bowers, and C. K. Jen, *J. Chem. Phys.*, **32**, 963 (1960); (b) R. A. Weeks and M. Abraham, *ibid.*, **42**, 68 (1965).

(16) F. J. Adrian, *ibid.*, **32**, 972 (1960).

(17) If the trapping site dimensions are rather large, the magnitude of the angular excursions will increase proportionally and the contribution to nuclear relaxation *via* fluctuations in the orientation will increase.

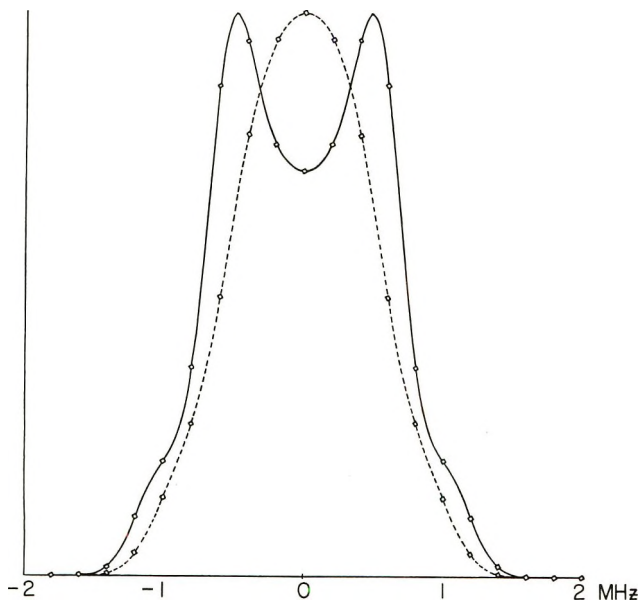


Figure 3. A comparison of the ENDOR line shapes resulting from two different types of nuclear relaxation. The solid line gives the ENDOR line shape when T_{1n} is assumed to be independent of angle. The computed spectrum employs a Gaussian line shape of width $T_2^{-1} = 200$ kHz and $\alpha_i = 600$ kHz. The dashed line assumes $T_{1n} \propto \sin \theta \cos^2 \theta$ and uses a Gaussian line shape whose width and dipolar interaction are 200 and 600 kHz, respectively.

tion, the *dominant nuclear relaxation* will stem from modulation of the interparticle distance, $\bar{r}_{n,i}$, and will possess a definite angular dependence.

(b) *Dynamical Model for Relaxation.* To describe the motion of the trapped H atom we employ the standard model which involves jumps between discrete states and for which we shall assume the transition probabilities are given by first-order rate constants.^{14,18} For simplicity, consider the case where there are only two discrete states which exist with any significant probability inside the cage. These states, A and B, have associated with them lifetimes τ_A and τ_B and internuclear distances r_A and r_B , respectively



We assume that this motion is a stationary, random stochastic process whose complete description is given by the conditional probability $P(A, t_1, B, t_2)$. This is the probability that a system which is in state A at time t_1 will be in state B at some later time t_2 . Since the process is stationary, it depends only on $t_2 - t_1 = \tau$, so that $P(A, t_1, B, t_2) = P_A(B, \tau)$.

By writing the first-order rate equations for states A and B at equilibrium and using the set of initial conditions that the H atom resides first in state A and then in state B, the two corresponding pairs of conditional probabilities may be obtained

$$P_A(A, t) = P_A + P_B e^{-t/\tau} \quad (8a)$$

$$P_A(B, t) = 1 - P_A(A, t) \quad (8b)$$

and

$$P_B(A, t) = 1 - P_B(B, t) \quad (8c)$$

$$P_B(B, t) = P_B + P_A e^{-t/\tau}$$

where

$$P_A = \tau_A / (\tau_A + \tau_B) \quad (9a)$$

$$P_B = \tau_B / (\tau_A + \tau_B) \quad (9b)$$

The calculation of the correlation function for a jump model is given by

$$g(\tau) = \overline{F_i(t)F_i(t + \tau)} = \sum_{\gamma=A,B} P_\gamma F_i(\gamma) \sum_{\delta=A,B} P_\delta F_i(\delta) \quad (10)$$

The time dependence of the classical lattice functions, $F_i(t)$ of Table I, is found only in $r_i(t)$. Since each component $F^{(0)}$, $F^{(\pm 1)}$, and $F^{(\pm 2)}$ is proportional to $(r_i(t))^{-3}$, the correlation function of eq 10 becomes

$$g^m(\tau) = [f^m(\theta)]^2 [(\bar{r}^{-3})^2 + P_A P_B (\Delta r^{-3})^2 e^{-t/\tau}] \quad (11)$$

where the $f^m(\theta)$ are given in Table I and

$$(\bar{r}^{-3})^2 = (P_A r_A^{-3} + P_B r_B^{-3})^2 \quad (11a)$$

$$(\Delta r^{-3})^2 = (P_A r_A^{-3} - P_B r_B^{-3})^2 \quad (11b)$$

The first term of eq 11 is the average value of the dipolar interaction, which determines line positions and frequency shifts but does not contribute to relaxation.¹⁹ The second term gives rise to a spectral density, $j(\omega)$, which leads to line broadening and relaxation. The spectral density is given by

$$j^m(\omega) = \int_0^\infty g^m(\tau) e^{-i\omega\tau} d\tau \quad (12)$$

and integration of eq 12 leads to the relaxation probabilities of Table II.

It is reasonable to assume that under most experimental conditions the period of the random motion of the trapped H atom is $\ll \omega_e^{-1}$ and $\ll \omega_n^{-1}$ (*vide infra*). Thus, the relaxation of each component, $W^{(m)}$, is directly proportional to the correlation time. If the unpaired electron ($S = 1/2$) interacts with a proton ($I = 1/2$) outside the cage, evaluation of the matrix elements shows that, when the angular dependence is excluded, the magnitude of the relaxation *via* $W^{(\pm 1)}$ and $W^{(\pm 2)}$ is greater than that from $W^{(0)}$ by about an order of magnitude. Upon including the angular dependence, the ENDOR line shape (for a specific value of ν_z , $\gamma_e a_n / 2$,

(18) G. K. Fraenkel, *J. Phys. Chem.*, **71**, 139 (1967).

(19) It is interesting to note that if another motion, *e.g.*, molecular tumbling or vibration having a characteristic time τ_v , were present and statistically independent of the jumping, the first term of eq 15 would give rise to relaxation *via* fluctuations in orientation. The second term would still contribute to the relaxation of the system but would now be described by a characteristic time $\tau_e^{-1} = \tau^{-1} + \tau_v^{-1}$ instead of τ^{-1} .

Table II^a

$$W^{(\pm 1)}_{m_S, m_I \rightarrow m_S \pm 1, m_I \pm 1} = \frac{9}{4} (\gamma_e \gamma_n \hbar^2)^2 \frac{\sin^2 \theta \cos^2 \theta}{\Delta r^6} \left(\frac{\tau}{1 + \omega_n^2 \tau^2} \right) |\langle m_S, m_I | S_z I_{\pm} | m_S, m_I \pm 1 \rangle|^2$$

$$W^{(0)}_{m_S, m_I \rightarrow m_S \pm 1, m_I (\mp 1)} = \frac{1}{16} (\gamma_e \gamma_n \hbar^2)^2 \frac{(1 - 3 \cos^2 \theta)^2}{\Delta r^6} \left(\frac{\tau}{1 + \omega_n^2 \tau^2} \right) |\langle m_S, m_I | S_{\pm} I_{\pm} | m_S \pm 1, m_I \mp 1 \rangle|^2$$

$$W^{(\pm 2)}_{m_S, m_I \rightarrow m_S \pm 1, m_I \pm 1} = \frac{9}{16} (\gamma_e \gamma_n \hbar^2)^2 \frac{\sin^4 \theta}{\Delta r^6} \left(\frac{\tau}{1 + \omega_n^2 \tau^2} \right) |\langle m_S, m_I | S_{\pm} I_{\pm} | m_S \pm 1, m_I \pm 1 \rangle|^2$$

For a spin system $S = 1/2$; $I = 1/2$

$$|\langle m_S; m_I | S_z I_{\pm} | m_S; m_I \pm 1 \rangle|^2 = 1/4$$

$$|\langle m_S; m_I | S_{\pm} I_{\mp} | m_S \pm 1; m_I \mp 1 \rangle|^2 = 1$$

$$|\langle m_S; m_I | S_{\pm} I_{\pm} | m_S \pm 1; m_I \pm 1 \rangle|^2 = 1$$

^a The lattice-induced transition probabilities arising from the electron-nuclear dipolar interaction are proportional to Δr^{-6} . The matrix elements for a one electron, one proton system are given.

and α) produced by each component of the relaxation becomes

$$f(\nu, \tau) = k \int_0^{\pi/2} W^{(m)}(r, \theta) e^{-[\omega(r, \theta, \phi) - 2\pi\nu] / (T_2^{-1})^2} r^2 \sin \theta d\theta \quad (13)$$

and the observed ENDOR line shape, which is a superposition of all components, each properly weighted, is given in Figure 5. This type of analysis reveals three most interesting properties. (1) The pseudosecular term produces an ENDOR line shape with maximum intensity at frequencies²⁰ $\nu_z \pm \gamma_e a_n / 2$ and a width which is proportional to the magnitude of α , just as in the case of nuclear relaxation *via* the relaxing electron of eq 5, but, whereas in the latter case it dominated the ENDOR line shape, now the contribution it makes to the overall line shape is almost negligible. (2) The nonsecular term, $W^{(0)}$, has associated with it a line shape that has maximum intensity at both $\theta = \pi/2$ and $\theta = 0^\circ$ and zero intensity at 54.7° . Generally these peaks have rather narrow line widths associated with them and would make a substantial contribution to the overall line shape if it were not for the fact that the numerical factor that multiplies the angular dependence is about one tenth that of the $W^{(\pm 1)}$ and $W^{(\pm 2)}$ terms. Under reasonably good resolution this term may contribute shoulders or perhaps even separate peaks to the total line shape, but their intensities will be greatly diminished compared to those produced by the dominant component of the relaxation. (3) The $\sin^4 \theta$ dependence of the $W^{(\pm 2)}$ component has maximum intensity at $\pi/2$ and zero intensity at 0° . The intensity maximum has a correspondingly narrow line width associated with it and is the *dominant relaxation mechanism of the dipolar interaction*. Hence, one would expect the overall ENDOR line shape to have maximum intensities at frequencies $\nu_z \pm \gamma_e a_n / 2 \pm \alpha$. If the ratio of $(\alpha / T_2^{-1}) \gg 1$, then one might expect addi-

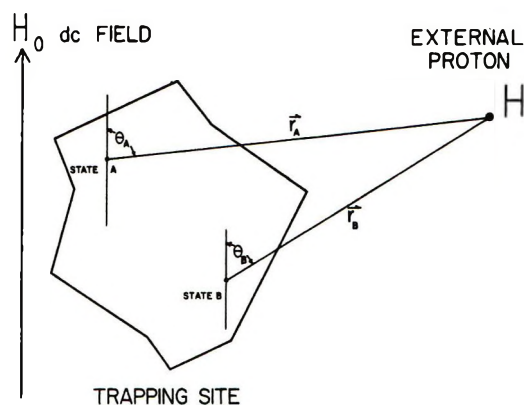


Figure 4. A physical model of the H-atom trapping site. The unpaired electron is assumed to jump between at least two sites, A and B. This motion changes both θ and τ_i , but the amplitude of the angular fluctuations is small compared to fluctuations in the magnitude of τ_i .

tional peaks or shoulders to be found at $\nu_z \pm \gamma_e a_n / 2 \pm 2\alpha$.²¹

(c) *Quantum Mechanical Model*. At this point it is appropriate to consider other models that may describe the mechanisms of spin-lattice relaxation and compare the resulting ENDOR line shape with that derived from the jump model. If the walls of the β cage are assumed to be at infinite potential, the trapped H atom is analogous to a particle in a three-dimensional box. The size of a sodalite cage determines the allowed energy levels and the boundary conditions at the walls define the nature of the eigenfunctions. The particle populations are obtained by taking a thermal Boltzmann distribution over the different allowed states. To produce spin relaxation the particle-in-a-box must be coupled to

(20) Recall ν_z occurs at $\theta = 54.7^\circ$ whereas the pseudosecular term peaks at 45° . However, this small difference is averaged out when both $m_S = +1/2$ and $m_S = -1/2$ are considered.

(21) In both cases the sign of the hyperfine splitting has been assumed to be positive. If it is negative then replace the \pm preceding both terms by \mp .

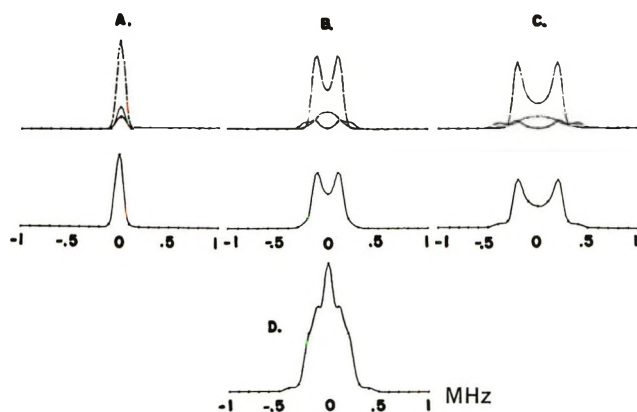


Figure 5. ENDOR line shapes produced by all five components of the nuclear relaxation probability. The upper portion of A, B, and C shows a dashed line depicting the double resonance line shape related to $W(\pm 2) \propto \sin^4 \theta$, a dotted line depicting the contribution from the $W(\pm 1) \propto \sin^2 \theta \cos^2 \theta$ terms, and a solid line showing the $W(0) \propto (1 - 3 \cos^2 \theta)^2$ component. The lower portions of A, B, and C are superpositions of the three line shapes shown above. D is a superposition of the lower three spectra of A, B, and C.

The data used to compute these line shapes is as follows: A, $T_2^{-1} = 50$ kHz, $a_n = 0.0$, $\alpha_i = 20$ kHz; B, $T_2^{-1} = 50$ kHz, $a_n = 0.0$, $\alpha_i = 132$ kHz; C, $T_2^{-1} = 50$ kHz, $a_n = 0.0$, $\alpha_i = 225$ kHz.

the thermal lattice modes of motion and this coupling arises from the END interaction of the spin system (unpaired electron plus hydroxyl proton). The hydroxyl protons which form a part of the sodalite cage may be considered as fixed in the lattice and the dipolar interaction is modulated by those thermal modes of motion that affect the internuclear distance, r_{ni} . In this case the relaxing spin system gives up a quantum of energy which may induce a corresponding transition from some particle energy level. The state of the spin system plus particle is properly described by the density matrix $\rho_{\alpha\nu, \beta\nu'}$, where α, β refer to spin states and ν, ν' refer to particle states.²²⁻²⁴ Hence, for this model the dipolar interaction must be treated quantum mechanically as opposed to the semiclassical treatment used to describe the jump model.

Following the work of Freed, one may solve for the time evolution of the density matrix in the interaction representation

$$\rho^*(t) = -i[\mathcal{H}_D^*(t), \rho^*(t)] \quad (14)$$

where $\mathcal{H}_D(t)$ is the dipolar term operating on both the spin and vibrational states of the system. Assuming that (1) $\rho(t) = \lambda(t)\sigma(t)$ where $\lambda(t)$ and $\sigma(t)$ are the reduced density matrices depending on only vibrational and spin degrees of freedom, respectively, and that (2) the thermal motions of the lattice are random with a mean time interval τ which is short enough so (3) $\sigma(t)$ is not appreciably changed and only (4) $\lambda(t)$ is affected (*i.e.*, the thermal perturbations have no matrix elements between spin states), the resulting spectral density analogous to eq 12 (and Table II) may be written as

$$j_{qq'}(\omega_{\alpha\beta} + \omega_{\nu\nu'}) = \sum_{\nu\nu'} Z(\nu) e^{-E_\nu/kT} F_{\nu\nu'} F_{\nu'\nu} [\tau/1 + (\omega_{\alpha\beta} + \omega_{\nu\nu'})^2 \tau^2] - \langle F^{(q)} \rangle \langle F^{(q')} \rangle [\tau/1 + \omega_{\alpha\beta}^2 \tau^2] \quad (15)$$

The final assumption made to formally solve eq 14 is that the vibrational states are given by a Boltzmann distribution and the postvibrational distribution is independent of the distribution just before a vibration occurs. The basic nature of the quantum mechanical model is that the thermal motions represent a very strong particle perturbation which rapidly restores the vibrational states to equilibrium, while the dipolar interaction, $\mathcal{H}_D(t)$, is a much weaker perturbation that slowly tends to bring the spins to equilibrium.

The spectral density of eq 15 reduces to the form of the semiclassical formulation similar to the relaxation probabilities given in Table II when the relaxing spin state induces no change in the vibrational configuration of the system. This process may be visualized in the following manner. The thermal vibrations cause a broadening of the H-atom eigenenergies. In general, the natural infrared line widths obtained for the O-H atoms comprising the β cage are of the order of 10 cm^{-1} at room temperature corresponding to the $\tau \sim 0.5 \times 10^{-12} \text{ sec}$.²⁵ If we assume that the thermal molecular vibrations are also of this order, then each quantized particle level is broadened by nearly $\Delta\omega = 2 \times 10^{12} \text{ sec}^{-1}$. The quantum of energy, $\omega_{\alpha\beta}$, emitted by the relaxing spin system ($\sim 10^{11} \text{ sec}^{-1}$) is now well within the frequency spread ($2 \times 10^{12} \text{ sec}^{-1}$) of a particular H-atom eigenenergy [$\omega = 3n^2\pi^2/8ma^2 \sim 10^{12} \text{ sec}^{-1}$ ($n = 1$)] found in a cubical box of length 6.6 \AA .²⁶ Thus the spin system may relax without changing the energy level of the particle and $\omega_{\nu\nu} = 0$. The diagonal matrix elements become

$$F_{\nu\nu} = \frac{8}{l^3} \int_0^l [(x - x_0)^2 + (y - y_0)^2 + (z - z_0)^2]^{-3/2} \prod_{q=x,y,z} \sin^2(\nu_q \pi q/l) d\tau \quad (16)$$

and the nuclear transition probability for the H atom located outside the box at (x_0, y_0, z_0) is given by

$$2W_n = \left[\sum_{\nu} Z(\nu) e^{-E_\nu/kT} F_{\nu\nu}^2 - \left(\sum_{\nu} B(\nu) F_{\nu\nu} \right)^2 \right] \frac{\tau}{1 + \omega_{\alpha\beta}^2 \tau^2} \quad (17)$$

(22) J. H. Freed, *J. Chem. Phys.*, **41**, 7 (1964).

(23) J. H. Freed, *ibid.*, **45**, 1251 (1966).

(24) J. H. Freed, lecture presented at NATO Summer School on Electron-Spin Relaxation in Liquids, Spätind, Norway, Aug 1971.

(25) (a) J. W. Ward, *J. Catal.*, **9**, 396 (1967); (b) J. B. Uytterhoeven, R. Schoonheydt, B. V. Liengme, and W. K. Hall, *ibid.*, **13**, 425 (1969); (c) J. W. Ward and R. C. Hansford, *ibid.*, **13**, 364 (1969); (d) J. W. Ward, Proceedings of the 2nd International Conference on Molecular Sieve Zeolites, Worcester, Mass., Sept 1970.

(26) See note 17 of ref 22.

Here $B(v)$ is the Boltzmann distribution in vibrational states.

An alternative situation is present if the energy levels of the box are separated by a frequency $\omega_{vv'} \sim \omega_e \pm \omega_n$; then the relaxing spin system may be accompanied by a corresponding particle transition. However, if $(\omega_{\alpha\beta} + \omega_{vv'})\tau$ is still less than unity (case i), the quantum mechanical formulation of the relaxation probability will remain quite similar to that predicted from semiclassical theory

$$2W_n = \left[\sum_{vv'} Z(v) e^{-E_v/kT} F_{vv'} F_{v'v} - \sum_v B(v) F_{vv} \sum_{v'} B(v') F_{v'v'} \right] \tau \quad (18)$$

where the off-diagonal elements of F are given by

$$F_{vv'} = \left\langle \prod_q \sin(v_q' \pi q/l) | r^{-3} \right| \prod_q \sin(v_q \pi q/l) \rangle \quad (19)$$

and r^{-3} is defined in eq 16. Although no experimental ir data at 20°K could be found, the ENDOR experiments on zeolites⁸ indicate that $W_n \propto \tau$ and the system may still be treated semiclassically, exhibiting ENDOR line shapes previously discussed in this section.

Upon reducing the temperature (case ii) either the particle populations change or the eigenenergy broadening decreases, or both, such that $(\omega_{\alpha\beta} + \omega_{vv'})\tau > 1$. Now W_n is given by eq 15

$$2W_n = j_{q\alpha}(\omega_{\alpha\beta} + \omega_{vv'}) \quad (20)$$

and two situations may arise which affect the ENDOR line shape. First, if pure nuclear relaxation from the pseudosecular terms of the dipolar interaction is dominant, *i.e.* $(\omega_{\alpha\alpha'} + \omega_{vv'})^2 \tau^2 \ll (\omega_{\alpha\beta} + \omega_{vv'})^2 \tau^2$, a pile up of ENDOR intensity at frequencies $|\nu_n \pm \gamma_e a_n/2|$ would be expected as described in section III. Second, when the magnitude of the particle energy separation is such that $(\omega_{\alpha\beta} + \omega_{vv'})$, $(\omega_{\alpha\alpha'} + \omega_{vv'}) \sim \omega_{vv'}$, then the $W^{(\pm 2)}$ terms would once again dominate the double resonance line shape. However, the magnitude of each component of the relaxation, $W^{(n)}$, obtained quantum mechanically, would be reduced by the ratio $[\tau_{\text{jump}}/(\omega_{vv'}^2 \tau)^{-1}]$ when compared to that of the jump model.

III. Discussion

(a) *Solid State vs. Jump Model.* We have not implied that the conventional solid state model for relaxation of nuclei by means of electronic relaxation modulating the dipolar interaction is inoperative. It is appropriate to estimate the magnitude of this mechanism compared with relaxation induced by motion. In a two-jump model at 20°K the relaxation dominant ($W^{(\pm 2)}$) term is proportional to $\tau/(1 + \omega_e^2 \tau^2) \cong \tau \cong 10^{-12}$ sec.²⁶ In the conventional solid state model at 15 MHz the pseudosecular ($W^{(\pm 1)}$) term is proportional to $T_{1e}/(1 + \omega_n^2 T_{1e}^2) \sim (\omega_n^2 T_{1e})^{-1}$ and is equal to 10^{-12}

sec only when $T_{1e} \sim 10^{-4}$ sec. Thus both mechanisms can, in principle, be of the same order of magnitude. However, the line shape that arises from the $\sin^4 \theta$ dependence of the jump model is vastly different from the line shape attributed to the $\sin^2 \theta \cos^2 \theta$ dependence of the solid state model so that they should be readily distinguishable.

(b) *Particle-in-a-Box vs. Jump Model.* We have reached the conclusion that at 20°K the quantum mechanical model reduces to the form of the jump model and the semiclassical treatment is a reasonable approximation. If the broadening of the H-atom energy levels is decreased substantially, as one may expect at lower temperatures, such that $\Delta\omega < 10^{11}$ sec⁻¹, then for spin relaxation to occur, $\omega_{vv'}$ must be finite. For a box which is roughly the size of the β cage, the two lowest-lying eigenstates are separated by a frequency of $\sim 2 \times 10^{11}$ sec⁻¹ and at $T < 10^\circ\text{K}$ the lower level is significantly populated. Under these conditions the spectral density describing the nonsecular and pseudosecular relaxation probabilities would be expected to contain the Boltzmann factor and frequency, $\omega_{vv'}$, of the corresponding particle population and transition, respectively. Now, depending on the magnitude of $(\omega_{\alpha\beta} + \omega_{vv'})^2 \tau^2$, the ENDOR line shape may be quite different from that predicted by the jump model. An interesting area of speculation is the temperature dependencies of the particle-in-a-box and jump models. ENDOR experiments over a range of temperature might yield interesting information on the local motion of a paramagnetic impurity and its coupling to the lattice. In this connection we remark that the size of the box or cage, or the total excursions of the H atoms, affect τ . In many practical circumstances τ is not too far from ω_e^{-1} and ENDOR experiments at other microwave frequencies might be appropriate.

(c) *Spin Diffusion.* Many interesting possibilities exist from the point of view of persons interested in relaxation processes. For example, it is conventional to assume rapid nuclear spin diffusion in wide line nmr of dilute paramagnets and to assume a critical radius inside of which spin diffusion cannot occur. This critical radius model would have to be modified in the presence of motion as discussed here. Also since ENDOR is sensitive to nuclei *inside* the critical radius it would be appropriate to make the connection between relaxation of distant nuclei (using nmr) and relaxation of nearby nuclei (using ENDOR).

(d) *Summary.* From the point of view of using these results for interpretation of powder ENDOR spectra, the conclusion is that for temperatures $\geq 20^\circ\text{K}$, the term $W^{(\pm 2)} \propto \sin^4 \theta$ dominates the relaxation, resulting in two sharp well-defined peaks, one on each side of the free proton frequency. In the practically common case of negligible contact interactions, the peaks arise from a buildup of intensity at $\theta = \pi/2$. They may be simply related to the radial distance by

$(40/\bar{r}^3) = |\nu_z - \nu_{\text{peak}}|$ in megahertz. In the companion paper it is shown that the experimentally obtained ENDOR spectra cannot be simulated by the conventional solid-state model. It was, in fact, just this observation that led to the present development of an alternative relaxation model.

Acknowledgment. One of us (J. C. V.) thankfully acknowledges a grant from NATO which made it possible for him to perform this work at Varian Associates in Palo Alto, Calif. We also wish to thank Professor Jack H. Freed for many helpful discussions and suggestions.

Proton ENDOR of γ -Irradiated Y-Type Zeolites

by Jacques C. Vedrine,¹ James S. Hyde, and Daniel S. Leniart*

Varian Associates, Analytical Instrument Division, Palo Alto, California 94303 (Received May 20, 1971)

Publication costs assisted by Varian Associates

This study is the initial application of electron-nuclear double resonance (ENDOR) to zeolites, and is, therefore, concerned to a large degree with methodology. Hydrogen atoms are trapped during γ irradiation and the interactions between the atoms and surrounding protons are measured by ENDOR. Motion of the hydrogen atom modulates the dipolar interaction, causing nuclear relaxation of the protons which determines the nature of the ENDOR response. Well-resolved lines have been observed in H-Y-type zeolites. In this system it has been determined that the hydrogen atom is trapped in the center of the sodalite cage, and interactions with four different kinds of protons have been found. Sample treatment cycles found to be reversible using other methods have been found to be irreversible using ENDOR spectroscopy.

Introduction

Many electron paramagnetic resonance (epr) experiments have been carried out by various workers on heterogeneous catalysts that have been subjected to the following treatment: careful degassing at some elevated "calcination" temperature, exposure at some other temperature to a gas or vapor, partial degassing at still another "activation" temperature, and subsequent γ irradiation at 77°K.¹⁻⁵ Hydrogen atoms are generally observed and occasionally other damage products. The hydrogen hyperfine couplings and g values may be shifted somewhat from the free atom value,^{6,7} the hydrogen atom yields and epr line widths vary rather considerably, and "spin flip" satellite lines of varying intensities are seen on either side of the hyperfine lines. From this intrinsic information content in the epr spectra, various inferences are made concerning the correlation with the Brønsted (H⁺) activity,^{2a,8} the environment around the trapped hydrogen atoms, and the interaction of the gases with the catalysts. The present work represents an effort to apply, within this same general framework, the technique of electron-nuclear double resonance (ENDOR), with its intrinsically higher effective spectral resolution, to the investigation of hydrogen atom trapping sites of Y-type zeolites.

In the ENDOR experiments performed here we have adjusted the applied magnetic field to one of the hydrogen atom hyperfine lines and then slowly swept the incident nuclear radiofrequency through the region a few megahertz on either side of the free proton frequency, thus measuring the weak super-hyperfine interactions between the hydrogen atom and the surrounding protons. These are the interactions that give rise to the observed widths of the hydrogen atom epr hyperfine lines. To a very good approximation, the hydrogen atom spectra are isotropic. Thus all orientations contribute with equal intensity to the proton

(1) Varian Associates Postdoctoral Fellow, 1970.

(2) (a) P. H. Emmett, R. Livingston, H. Zeldes, and R. J. Kokes, *J. Phys. Chem.*, **66**, 921 (1962); (b) V. B. Kazansky, G. B. Pariisky, and V. V. Voevodsky, *Discuss. Faraday Soc.*, **No. 31**, 203 (1961).

(3) (a) J. C. Vedrine, G. Dalmay, and B. Imelik, *J. Chim. Phys.*, **65**, 1780 (1968); (b) J. C. Vedrine, G. Dalmay, and B. Imelik, "Proceedings of the Colloque Ampere," Vol. XV, North-Holland Publishing Co., Amsterdam, 1969, p 304.

(4) J. E. Wertz, J. W. Orton, and P. W. Auzins, *Discuss. Faraday Soc.*, **No. 31**, 140 (1961).

(5) J. H. Lunsford and J. P. Jayne, *J. Chem. Phys.*, **44**, 1487 (1966).

(6) S. N. Foner, E. L. Cochran, V. A. Bowers, and C. K. Jen, *ibid.*, **32**, 963 (1960).

(7) F. J. Adrian, *ibid.*, **32**, 972 (1960).

(8) A. Abou Kais, J. C. Vedrine, J. Massardier, G. Dalmay, and B. Imelik, *C. R. Acad. Sci., Paris, Ser. C*, **272**, 883 (1971).

ENDOR spectra. We refer to experiments of this type as powder ENDOR.

In the companion to this paper,⁹ we have developed a theory of powder ENDOR relevant to the present work. Using this theory, it has been possible to obtain computer simulations of the ENDOR spectra. The adjustable parameters in such a fit are (a) the number of spectroscopically inequivalent proton sites, (b) the radial distances between the proton sites and the hydrogen atom, (c) the relative populations of these sites, and (d) the amount of Fermi contact interactions with the protons. Thus, quite a lot of structural information can be obtained in those cases where well-resolved ENDOR spectra are observed with a good signal-to-noise ratio. In other circumstances, the interpretation is more qualitative, but often it is possible to reach meaningful conclusions particularly by comparison of the spectra from a series of samples treated in various ways. Additional ENDOR experiments on unordered solids are given in ref 10–12, and a general review of the ENDOR method in ref 13.

The basic zeolite building block is the elementary tetrahedron of AlO_4 or SiO_4 . There are four crystallographically inequivalent oxygen atoms, labeled O1, O2, O3, and O4, bonded to each Si,Al atom. In Y-type zeolites considered here there are 2.4 Si for each Al. Only one Al can be bonded to each oxygen. That is, the structure Al–O–Al does not exist. In the vicinity of each Al there is a cation or molecule that can neutralize the Al minus charge. These tetrahedra are arranged to form cuboctahedra, also called sodalite cages or β cages. Each sodalite has eight hexagonal faces and six square faces. Roughly each sodalite contains a spherical cavity 6.6 Å in free diameter with 2.2 Å free diameter access through the hexagonal faces. Each sodalite is joined at four of the hexagonal faces to four other sodalites in tetrahedral symmetry. These junctions between two sodalite cages are formed by parallel hexagonal faces creating small cages known as hexagonal prisms. In Figure 1, which is modeled after a figure by Smith,¹⁴ one can see a sodalite cage and three of the four hexagonal prisms associated with it. Each intersection in this figure is a tetrahedral site occupied either by Al or Si. Midway between each intersection an oxygen is located. The Si–O–Si bonds form an angle of about 143°. The resulting O locations on one tetrahedral site are indicated in the figure. We have imagined that a hydroxyl proton could be on any one of the four oxygens and have indicated the positions of these protons in the figure. There can, of course, be only one such hydroxyl proton on a particular Al. The assembly of sodalites forms large supercages (also called α cages). A supercage is formed by four hexagonal faces from four sodalites, six square faces from six other sodalites, 12 square faces from hexagonal prisms, and four large apertures which lead to other supercages. The supercages are roughly spherical with a diameter

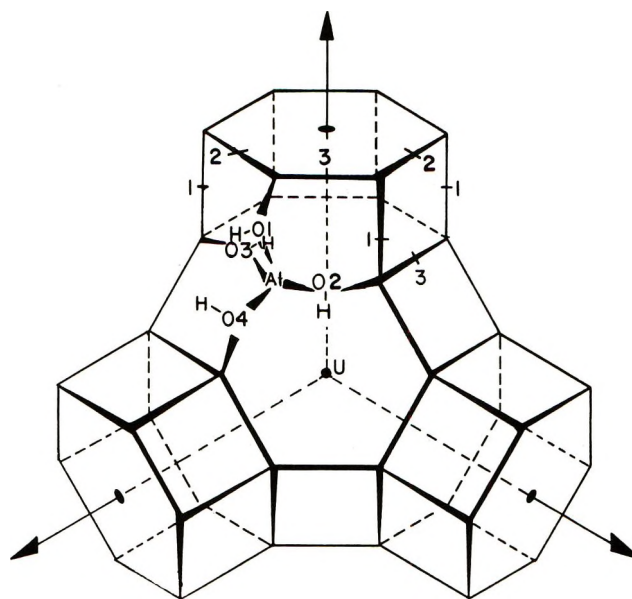


Figure 1. The sodalite cage with three of the four attached hexagonal prisms shown. One Al tetrahedral site is illustrated in detail and hydroxyl protons are imagined to be on each of the four adjacent oxygens.

of 13 Å, and the connecting apertures are nearly round with a free diameter of 8 Å. On a per-unit-cell basis there are eight supercages, eight sodalite cages, and 16 hexagonal prisms. The unit cell is 24.7 Å on a side. Helpful drawings have been given by Breck¹⁵ and Meier and Olson.¹⁶

All sample preparations in the present work began with ammonium zeolite (NH_4 -Y type) that had been exposed to air and contained water and various other adsorbed gases. Upon heating this material under vacuum at 150°, substantially all of the extraneous gases, much of the water, and a small amount of ammonia are evolved. A maximum yield of hydrogen atoms is observed after γ irradiation from samples heated at this temperature.⁸ It seems likely that the residual physically adsorbed water inhibits the formation of hydrogen atoms, and that these atoms come from the NH_4^+ base exchange cations. In the following it often will be convenient to refer to this particular

(9) D. S. Leniart, J. S. Hyde, and J. C. Vadrine, *J. Phys. Chem.*, **76**, 2079 (1972).

(10) J. S. Hyde, G. H. Rist, and L. E. G. Eriksson, *ibid.*, **72**, 4269 (1968).

(11) G. H. Rist and J. S. Hyde, *J. Chem. Phys.*, **52**, 4633 (1970).

(12) L. E. G. Eriksson, J. S. Hyde, and A. Ehrenberg, *Biochim. Biophys. Acta*, **192**, 211 (1969).

(13) J. S. Hyde in "Magnetic Resonance in Biological Systems," A. Ehrenberg, B. G. Malmstrom, and T. Vaangard, Ed., Pergamon Press, Oxford, 1967, p 81.

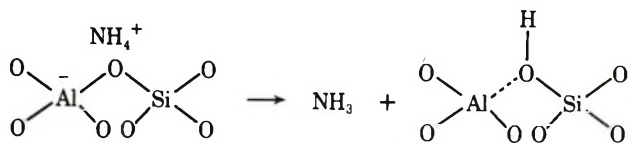
(14) J. V. Smith, Proceedings of the 2nd International Conference on Molecular Sieve Zeolites, Worcester, Mass., Sept 8–11, 1970, p 401.

(15) D. W. Breck, *J. Chem. Educ.*, **41**, 678 (1964).

(16) W. M. Meier and D. H. Olson, *Advan. Chem. Ser.*, **No. 102**, 386 (1970).

sample preparation as type I, and to use the same type I label for the resulting epr and ENDOR spectra and for the hydrogen atom sites giving rise to these spectra.

When Y-type zeolites containing NH_4^+ are heated to 400° under vacuum, NH_3 is evolved; substantially no NH_4^+ remains. The protons that are formed on release of NH_3 cannot screen the negative charge on the alumina tetrahedra in the same way as do the much larger NH_4^+ or Na^+ cations. Uytterhoeven, *et al.*,¹⁷ suggested that the protons react with the lattice oxygen to form OH groups that were not present in the parent material. They give rise to two strong infrared bands at 3550 and 3650 cm^{-1} . The intensity of these acid



OH bands is modified by introductions of basic compounds such as NH_3 , pyridine, piperidine, propylene, etc. Olson and Dempsey¹⁸ review the infrared literature on H-Y-type zeolites, emphasizing the uncertainties and disagreement in the literature in the assignment of these OH bonds to particular oxygens. They argue on the basis of rather indirect X-ray evidence that the 3550- cm^{-1} band arises from OH groups in the hexagonal prisms on O3 oxygens. These OH groups are relatively inaccessible. The 3650- cm^{-1} band has been associated with more accessible OH groups at the O1 oxygens. These are the bridging oxygens between the faces of the hexagonal prisms and they extend into the supercages (see Figure 1). Ward¹⁹ has systematically reviewed the literature on structural hydroxyl groups.

A second maximum in hydrogen atom yield upon γ irradiation is observed as a function of activation temperature at 400° .⁸ The hydrogen atoms almost certainly arise from a rupture of acidic OH bonds. We use the notation "type II" to refer to this sample preparation and to the resulting sites and spectra. One of the objects in the present work was to obtain structural information on the hydroxyl groups and to compare it with X-ray and infrared studies. The hydrogen atom is viewed as a "spin-label" and useful structural information would depend on the existence of a small number of hydrogen atom trapping sites, preferably one, in known locations, and not associated with structural defects or impurities. It will be argued later in this paper that the hydrogen atoms are trapped in unique sites in the geometrical centers of the sodalite cages and that the geometry of OH groups can indeed be studied with the ENDOR method.

Upon calcination at 550° the OH groups are removed, there being almost no hydrogen left in the material, and an irreversible change in crystal structure occurs.

Experimental Procedures

Sample Preparation. Ammonium zeolite was pre-

pared from Linde sodium Y-type zeolite by base exchange at room temperature with an aqueous solution of ammonium chloride. Numerous exchanges resulted in a degree of exchange of 90% as determined by chemical analysis. Some experiments also were carried out with a 98% exchanged NH_4 -Y zeolite kindly provided by Professor M. Boudart. Sample material from the two sources resulted in identical ENDOR spectra.

These samples were evacuated on a conventional vacuum system for 2 or 3 hr at room temperature before slowly increasing the temperature at the approximate rate of $60^\circ/\text{hr}$. All of the samples were maintained at the desired temperature overnight under a vacuum of less than 10^{-4} Torr. For better degassing, the 8-mm sample tubes were set horizontally such that the powder layer thickness was less than 2 mm.²⁰

This sample preparation was sufficient for our prototype investigation of type I and type II systems. Subsequently, other samples were prepared by introducing various vapors at room temperature into the vacuum system—either saturating vapor pressure for liquids or about 100 Torr for gases. We used propylene, methane, and ammonia (all Matheson, CP), pyridine (Aldrich Chemical Co.), D_2O (Diaprep, Inc., 99.8%), and distilled water. The liquids were initially degassed by the freeze-pump-thaw technique. An additional step was employed for pyridine of drying over activated molecular sieves before distilling to a second flask for degassing. The duration of the vapor contact was 3–4 hr. In some cases samples were subsequently evacuated at a second activation temperature for at least 6 hr. We use a notation 400- NH_3 -155, for example, to describe a sample, where the first number gives the first activation temperature, the center entry is the vapor, and the final number is the second activation temperature.

Irradiation was carried out with the sample in liquid nitrogen using a γ -ray source of 0.8 Mrad/hr for 15 hr (dose about 12 Mrads) at Raychem Co. in Menlo Park, Calif. After irradiation, the defects in the quartz sample tube were removed by tilting the sample tube so that the powder went to the other end of the tube, maintaining that end in liquid nitrogen and annealing the defects with a torch.

Equipment and Technique. The spectra have been recorded using an E-9 Varian epr spectrometer equipped with an E-700 ENDOR system. This commercial apparatus is described in principle in ref 21. Experiments at 90°K were performed with a nitrogen flow

(17) J. B. Uytterhoeven, L. G. Christner, and W. K. Hall, *J. Phys. Chem.*, **69**, 2117 (1965).

(18) D. H. Olson and E. Dempsey, *J. Catal.*, **13**, 221 (1969).

(19) J. W. Ward, Proceedings of the 2nd International Conference on Molecular Sieve Zeolites, Worcester, Mass., Sept 8–11, 1970, p 682.

(20) G. T. Kerr, *J. Catal.*, **15**, 200 (1969).

(21) J. S. Hyde, *J. Chem. Phys.*, **43**, 1806 (1965).

system, and experiments between 10 and 30°K with a liquid helium boil-off system described in ref 22.

Careful measurements of microwave frequencies and magnetic fields were made to determine hyperfine splittings and g values with high precision. The techniques were similar in principle to those described by Segal, Kaplan, and Fraenkel.²³ Accuracies were ± 0.1 G and were limited by the epr line width and signal-to-noise ratio.

Epr Results and Discussion

Hyperfine Splittings and g Values. When ammonium zeolite is treated according to procedure I, *i.e.*, simply activating at 150° and irradiating at 77°K, a hydrogen atom doublet is obtained with a hyperfine splitting of 499.5 ± 0.2 G. The line width is 3.15 G and the g value is 2.0023 ± 0.0001 , where a second-order correction has been introduced. When the material is treated according to procedure II, *i.e.*, activating at 400° and irradiating, a hydrogen atom doublet is obtained with a splitting of 501.7 ± 0.2 G, line width of 1.25 G, and a g value of 2.0023 ± 0.0001 . These hyperfine splittings can be compared with the value of 506.7 G for free protons.

No line shape asymmetry could be detected, as would be expected if the hydrogen atom hyperfine interaction or g tensor were anisotropic. Line widths and shapes remained unchanged when the samples were investigated using a microwave frequency of 35 GHz.⁸

In these systems the trapped H atom is almost free; the magnitude of the g value and hyperfine splittings are attributed to the isolated radical while small changes in these parameters are due to the interaction between the trapped radical and its environment. Adrian²⁴ has calculated the shifts found for hydrogen atoms trapped in rare gas matrices. We can attempt to use his results by assuming that the fully coordinated Si-O units may be simulated by argon atoms.

Assuming a nonpolar matrix, Adrian considered the effects of both van der Waals forces and Pauli exclusion forces on trapped hydrogen atoms. The effect of the former is dominant at large distances and tends to expand the H atom wave function resulting in a reduction of the hyperfine splitting. The latter interaction dominates at close distances and contracts the wave function resulting in an increase of the hyperfine splitting. A plot of hyperfine shift *vs.* radial distance thus goes from a positive value to a negative value and then asymptotically to zero. The Pauli or exchange interaction also leads to a negative shift in the g value.

Much of the succeeding analysis will focus on H-Y zeolites—that is, on material prepared according to procedure II where the trapped hydrogen atom interacts with structural hydroxyl groups. Our epr data show a change of $-0.98 \pm 0.04\%$ in the hyperfine splitting for this sample. The most probable hydrogen atom trapping site consistent with Adrian's theory is the

geometrical center of the sodalite cage. The walls of this cage consist of 24 Si(Al) atoms at a distance of 5.0 Å, 12 O atoms (O3) at a distance of 4.3 Å, and 12 O atoms (O2) at a distance of 4.5 Å. Assuming that this wall can be equated to 30 argon atoms at an average distance of about 4.6 Å results in good agreement between theory and experiment for the hyperfine interaction. Moreover, the predicted g shift is negligible, also in nearly perfect agreement with experiment. We have considered the center of the hexagonal prism as a possible trapping site. However, fairly large positive hyperfine shifts and large negative g shifts are predicted, in disagreement with experiment.

Hydrogen Atom Yields. Returning to a description of other aspects of the epr behavior, the yield of H atoms is about the same for both type I and type II samples and is estimated to be about 10^{18} atoms/g. For type II samples, there are about 10^{21} OH groups and 0.1% are converted into hydrogen atoms. The yields increase linearly with dose up to about 5.2 Mrads and saturate at higher doses.

Microwave Power Saturation. Progressive saturation experiments have been carried out on both type I and type II samples at 80 and 10°K. (H atoms disappear above 90°K.) The saturation appears homogeneous, consistent with Bloch equations. We consider this result surprising; we expected to observe saturation behavior characteristic of inhomogeneously broadened hyperfine lines.^{25,26} Saturation occurs at an incident power of 0.8 mW for type II samples and 1.6 mW for type I. These are the incident powers where the saturation parameter is $1/2$. Most remarkably, there was no observed temperature dependence of the powers at which saturation occurs. These saturation results are adequate for the present purposes: *viz.* optimizing the ENDOR signal-to-noise ratios; they are, however, sufficiently unusual that a more serious study probably using pulse methods would seem to be appropriate.

Satellite Lines. On either side of each hyperfine line spaced an amount approximately equal to the nuclear Zeeman interaction, intense satellite lines have been observed. The satellites arise from induced transitions involving a change of both electron and nuclear magnetic quantum numbers.²⁷ These "forbidden" transitions are observed because of a mixing of nuclear states, with mixing coefficients given by the ratio of the electron-nuclear dipolar interaction to the nuclear Zeeman interaction. These two interactions determine both the position and the intensity of the contribution from each

(22) U. Ranon and J. S. Hyde, *Phys. Rev.*, **141**, 259 (1966).

(23) B. G. Segal, M. Kaplan, and G. K. Fraenkel, *J. Chem. Phys.*, **43**, 4191 (1965).

(24) F. J. Adrian, *ibid.*, **32**, 972 (1960).

(25) A. M. Portis, *Phys. Rev.*, **91**, 1071 (1953).

(26) J. S. Hyde, *ibid.*, **119**, 1492 (1960).

(27) G. T. Trammell, H. Zeldes, and R. Livingston, *ibid.*, **110**, 630 (1958).

nearby proton of each crystallite, and the actual satellite lines would be constructed of a summation over all crystallite orientations and over all protons.

There is a definite relationship between these satellite lines and the powder ENDOR spectra under consideration here. The characteristics of each are determined by the same interactions: nuclear Zeeman and electron-nuclear dipolar. If satellite lines are seen in the epr spectrum, one can expect successful ENDOR; if they are absent, ENDOR between the electron and matrix protons has generally been impossible to detect. In ENDOR the two interactions determine the position of the contribution from each proton of each crystallite, and the dipolar interaction determines the intensity of the contribution inasmuch as it determines the nuclear relaxation probability. Indeed, it appears generally true that the intensities of ENDOR signals and of the epr satellites are proportional to each other.

In a rigid system, the ratio of the intensities of satellite line to central line has been given by Trammell, *et al.* (ref 27, eq 25)

$$\frac{I_s}{2I_n} = \frac{3(H_e)^2}{20(H_0)^2} = \frac{3(\gamma_e \hbar)^2}{20(H_0)^2} \cdot \frac{1}{\gamma^6} \quad (1)$$

This expression is for a single electron interacting with a single proton and angular dependences have been dropped. Here H_e is the magnetic field at the proton from the electron. At 1 Å, this field is 19 kG. These are induced transition probabilities; there is no consideration of relaxation phenomena. Stationary ENDOR signals are proportional to the nuclear longitudinal relaxation probability. If the fluctuating dipolar field from the relaxing electron relaxes the proton (ref 28, p 380), it can be shown that

$$\frac{T_{1e}}{T_{1N}} = \frac{3(H_e)^2}{10(H_0)^2} \quad (2)$$

which has the same form as eq 1. This is a specific situation where satellite and ENDOR signals are proportional to each other.

In the present work (see also the companion paper, ref 9), it has been determined that motion of the hydrogen atom plays an important role in determining the nature of the relaxation of nearby protons, and attention has been focused particularly on radial motion. It is clear that such motion also will affect that satellite epr lines; eq 1 will no longer be valid since the motion will give rise to a time dependence of the mixing coefficients. This would appear to be a useful further calculation, perhaps modeled after Shimizu's work on the effects of torsional motion on satellite lines.²⁹

The intensity and shape of satellite lines has been used by Vedrine as a probe of the environment of the H atom in irradiated zeolites and aluminum hydroxides.³⁰ Differences were observed between samples treated in various ways, but the resolution or informa-

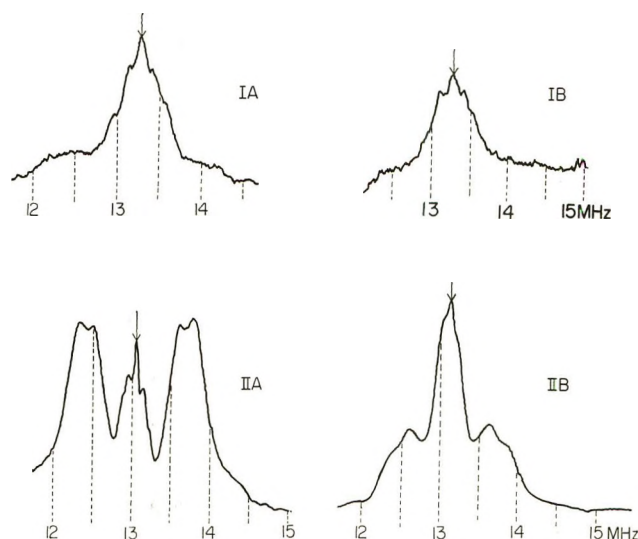


Figure 2. ENDOR spectra of $\text{NH}_4\text{-Y}$ zeolite: I, activated at 150° ; II, activated at 400° ; A, observed at 15°K ; B, observed at 80°K . The arrows indicate the free proton frequency.

tion content was substantially lower than has been achieved in the present work using ENDOR and interpretation was difficult.

ENDOR Results on Type I and Type II Samples

The ENDOR spectra for these samples at 15 and 80°K are shown in Figure 2. In Table I we have tabulated the positions of the peaks and have also attempted to give internally consistent relative H-atom yields and internally consistent ENDOR intensities for all samples studied here.

Type I spectra show peaks at ± 0.14 MHz and shoulders at ± 0.30 MHz. Type II spectra show these same features, and in addition, well-defined peaks are seen at ± 0.56 and ± 0.72 MHz. These latter peaks show a marked temperature dependence. The dependence is reversible; there is no partial bleaching at the higher temperature. The ENDOR intensity of these strongly coupled lines relative to the center line is also dependent on the level of saturating microwave power. Looking back at Figure 2, IA, one can imagine that these well-defined peaks correspond approximately to the weak pedestal observed there and that the apparent decrease of the pedestal in Figure 2, IB is consistent with the decrease observed in Figure 2, IIB. We conclude tentatively that the trapping sites in type I and type II samples are similar and that hydrogens, one from each NH_4^+ , in type I samples are approximately in the same locations as the hydroxyl protons of type II samples. The other NH_4^+ protons may be in less well-defined locations, causing some loss of resolution.

(28) A. Abragam, "The Principles of Nuclear Magnetism," Oxford University Press, Oxford, 1961.

(29) H. Shimizu, *J. Chem. Phys.*, **42**, 3603 (1965).

(30) J. C. Vedrine, to be published.

Table I: Summary of Epr and ENDOR Results

Sequence	Epr line width, G	H-atom yield, arb. units	Couplings from ENDOR, MHz	Matrix ENDOR intensity, arb. units
150	3.15	1.0	0.60, 0.28	1.0
375	1.25	0.75	1.45, 1.12, 0.30, 0.15	1.0
175-D ₂ O-150	2.75 (H)	0.4	No resolved lines	1.7
	2.3 (D)	0.3	No resolved lines	1.9
400-D ₂ O-150	1.25 (H)	0.06	No ENDOR	
	1.0 (D)	0.2	No ENDOR	
450-H ₂ O-150	1.6	0.4	No resolved lines	0.8
400-H ₂ O-380	1.25	0.1	No ENDOR	
380-NH ₃ -(no degassing)	1.25	0.75	1.00, 0.30	5.0
335-NH ₃ -145	1.25	1.3	1.10, 0.35	0.8
	3.1			
400-NH ₃ -155	1.3	2.6	1.00, 0.25	1.2
	3.0			
450-NH ₃ -420	1.25	0.35	1.04, 0.35, 0.15	2.1
400-pyr-150	2.6	0.01	No ENDOR	
400-pyr-200	1.25	0.01	No ENDOR	
375-pyr-375	1.6	0.4	1.15	2.0
380-C ₃ H ₆ -(no degassing)	1.25	1.5	1.04	10.0
420-C ₃ H ₆ -310	1.25	0.4	0.95, 0.20	17.0
650-C ₃ H ₆ -(no degassing)	1.7	0.07	No ENDOR	
450-CH ₄ -(no degassing)	1.25	0.5	1.00, 0.22	20.0

The information content in type I spectra is not high enough to justify a more detailed analysis, but the good spectra from type II samples do justify more elaborate interpretation. In the next section we apply the theory of powder ENDOR developed in the companion paper⁹ to the present situation and demonstrate that it is capable of explaining these type II spectra.

Computer Simulation of ENDOR Spectra

Introduction. The powder ENDOR line shape attributed to a single proton is determined by the Hamiltonian and by the specific type of nuclear relaxation that the proton undergoes. The spectrum is described by the shape function

$$f(\nu, r_i) = k \int_0^{\pi/2} W_n(\theta, r_i) e^{-h(\mathcal{H}_z + \mathcal{H}_D(\theta, r_i) + \mathcal{H}_{FC})^2 / (T_2m^{-1})^2} r_i^2 \times \sin \theta d\theta \quad (3)$$

where $W_n(\theta, r_i)$ is the nuclear relaxation probability, r_i is the radial vector between the hydrogen atom and the proton, θ is the angle between r_i and the applied magnetic field, and the remaining notation is given in the companion paper.⁹

Several models have been tested, evaluating eq 3 and comparing computer simulated spectra with actual ENDOR spectra. Each nuclear spin packet was assumed to have an intrinsic line width T_{2n}^{-1} of 50 kHz in all calculations.

The first model tested was to drop the explicit angular dependence of W_n , varying the relative magnitudes of \mathcal{H}_D and \mathcal{H}_{FC} in an effort to achieve a best fit. In nmr of dilute paramagnetic solids,³¹ it is customary

to drop the angular dependence of nuclear relaxation caused by the electron, at least outside of a certain critical radius, because of nuclear spin diffusion. If $\mathcal{H}_D \gg \mathcal{H}_{FC}$, the calculation amounts to fitting the experimental ENDOR spectrum by a sum of several Pake doublets.³² The outer peaks could be described fairly well by the pole arising from crystallites oriented such that $\theta = 90^\circ$ (*i.e.*, $(3 \cos^2 \theta - 1) = -1$), but the shoulders at $\theta = 0$ (*i.e.*, $(3 \cos^2 \theta - 1) = 2$) were not present experimentally. In addition, the valleys at $\nu_z \pm 0.325$ MHz (see Figure 1, IIA) were not well reproduced. It was possible to overcome some of these problems if it was assumed that $\mathcal{H}_{FC} \gg \mathcal{H}_D$. This circumstance seemed physically improbable, since it implies that the protons are quite far from the hydrogen atom ($\sim 7-8 \text{ \AA}$) but that the hydrogen atom interacts sufficiently strongly with the lattice to transfer considerable spin density to the proton through several chemical bonds. Moreover, we have been unable in a detailed way to justify the dropping of the angular dependence because of nuclear spin diffusion.

A second model that has commonly been used to describe nuclear relaxation in solids containing paramagnetic impurities is modulation of the dipolar interaction *via* the relaxing electron.²⁸ This mechanism was used to describe the matrix ENDOR line that has been observed in various powder spectra;¹⁰ however, in the zeolite system it appears to be quite inappropriate. The main reason for disregarding it is that the $\sin^2 \theta \cdot \cos^2 \theta$ dependence of W_n leads to a buildup of ENDOR

(31) W. E. Blumberg, *Phys. Rev.*, **119**, 79 (1960).

(32) G. E. Pake, *J. Chem. Phys.*, **16**, 327 (1948).

intensity at the free proton frequency. $\sin^2 \theta \cos^2 \theta$ is a maximum at 45° , which is close to the magic angle of 54.7° where the dipolar interaction is zero. Again, if one assumes that $\mathcal{H}_{FC} \gg \mathcal{H}_D$, the ENDOR spectra can be simulated. A small \mathcal{H}_D is required to get sufficiently narrow ENDOR lines and a_i must be about 0.700 MHz. This set of circumstances is subject to the same criticism as the first trial model.

The failure of these models has led to a consideration of the possible effects on proton relaxation of hydrogen atom motion modulating the electron–nuclear dipolar interaction. This model is discussed in detail in the companion paper⁹ and is outlined here.

Effects of Motion of the Trapped Atom. The epr data and, as we shall see, the ENDOR spectra indicate that the hydrogen atom is trapped in the sodalite cage. The nuclei of the atoms forming this cage lie on a spherical shell approximately 9.4 Å in diameter, and the free diameter of the cage is 6.6 Å. The entrances to the cage have a free diameter of about 2.2 Å, about the same as a hydrogen atom; below about 80°K the atom is trapped and above that temperature it escapes. There is no doubt that the atom will move in this cage, but a detailed description of the motion is of course difficult to make. If we allow the walls of the sodalite cage to be of infinite potential, it is possible to obtain an approximate estimate of the vibration frequency. One assumes Maxwell–Boltzmann statistics, attributing $kT/2$ of energy to each degree of freedom. At 20°K this frequency is in the high microwave range of 10^{12} Hz.

If one constrains the atom to the 6.6 Å diameter cage and considers the effect of motion on the dipolar interaction with hydroxyl protons, it is apparent that the magnitude of any angular fluctuations resulting from this motion is extremely limited and has very little effect on the nuclear relaxation. On the other hand, the magnitude of the fluctuations of r_i can be quite large and have a profound effect on the dipolar interaction with the hydroxyl protons.

In ref 9, the effect of this radial motion on W_n was analyzed. The Hamiltonian itself (the exponential part of eq 3) is affected by this rapid motion only inasmuch as r_i is replaced by \bar{r}_i . A jump model between two states was assumed. The dipolar interaction was written in a tensorial representation, and the five components were treated individually. A composite ENDOR spectrum was then simulated by adding them together—that is, by adding five integrals of the form of eq 3 for each proton.

The $\sin^2 \theta \cos^2 \theta$ pseudosecular $W^{\pm 1}$ terms cause a rather broad weak line at the free proton frequency. The total ENDOR line shape is quite insensitive to these terms. The $(3 \cos^2 \theta - 1)^2$ nonsecular W^0 term is doubly peaked and the associated line widths are rather narrow. However, the $\sin^4 \theta$ nonsecular $W^{\pm 1}$ terms are also sharply peaked and about an order

of magnitude greater than the W^0 term. In our simulations all terms have been included, but the $W^{\pm 2}$ terms make the dominant contribution to the experimentally observed line shape with two peaks at $\nu_z \pm (\gamma_e a_i/2 + \alpha_i)$ (or $-\alpha_i$ if the spin density is of opposite sign). This type of analysis is applicable when the motion of the trapped H atom is described by a jump model having a characteristic time $\tau_c < \omega_e^{-1} \ll \omega_n^{-1}$.

Comparison with Experiment. The experimental spectrum of Figure 2 (IIA) shows a narrow matrix ENDOR line at 13.15 MHz and four other pairs of lines: $\nu_z \pm 100$, $\nu_z \pm 175$, $\nu_z \pm 557$, and $\nu_z \pm 715$ kHz. There are four distinctively different types of surrounding hydrogen nuclei.

It was convenient in the computer program to simulate the matrix ENDOR line, which actually arises from very weak interaction with a large number of distant protons, by a weak interaction with a single proton. In Figure 3 then, for each of the five protons we show the W^0 , $W^{\pm 1}$, and $W^{\pm 2}$ contributions, and the resultant. In Figure 4, the five resultants are added to simulate the entire ENDOR spectrum. This figure should be compared with Figure 2, IIA. Adjustable parameters have been \bar{r}_i ; and also the intensity of the contribution from each proton site, since there is no *a priori* reason to expect the different possible hydroxyl proton sites to be populated in some specific manner.

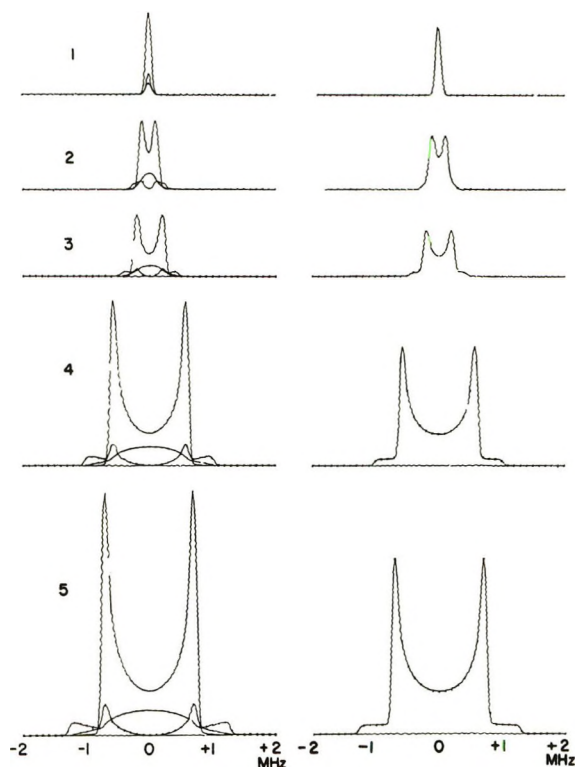


Figure 3. The left-hand side shows for each of the five \bar{r}_i 's used to simulate the ENDOR spectrum of Figure 2, IIA, W^0 , $W^{\pm 1}$, and $W^{\pm 2}$. The right-hand side is the summation of these terms for each \bar{r}_i . The relative weights of the contributions are the same as used in the final simulation of Figure 4.

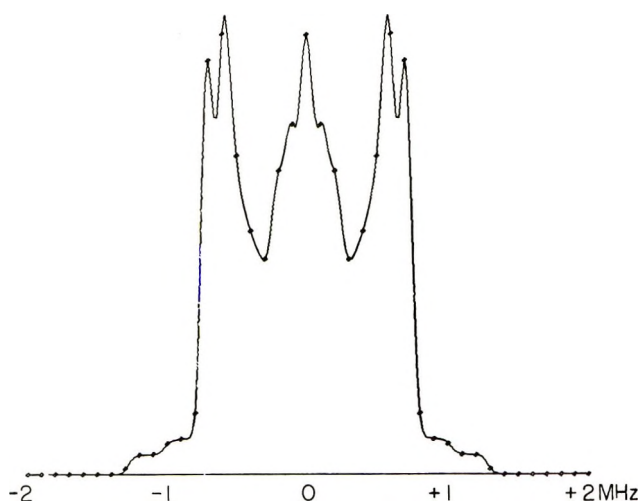


Figure 4. Computer simulation obtained by adding the five right-hand lines of Figure 3. The resultant spectrum should be compared with the experimental spectrum Figure 2, IIA.

A 60-kHz Fermi contact term has been included in the Hamiltonian for the two more strongly coupled protons, but the results are not very sensitive to this small interaction. In Table II, we list the values of \bar{r}_i , α_i , a_i , and the relative numbers of protons required for the simulation of Figure 4.

Table II: Parameters for the Computer Simulation of Figure 4

Proton	Fermi contact a_i , kHz	Dipolar coupling α_i , kHz	Relative number of protons
1	0.0	20	60
2	0.0	132	3.4
3	0.0	225	1.3
4	60.0	540	0.9
5	60.0	670	1.0

Interpretation of the ENDOR Experiment: Location of Structural Hydroxyl Groups. From the X-ray data of Olson and Dempsey,¹⁸ one can calculate the distances from the center of the sodalite cage to each of the nearby oxygens. These distances are given in Table III. It is interesting to estimate the distances from the sodalite center (site U) to hydroxyl protons imagined to be located on each of the oxygens. We assume that the hydroxyl proton lies in the plane formed by the Si–O–Si bonds, with the O–H bond bisecting the angle and pointing away from the Si–O–Si angle. These distances are given in Table III. We have also ordered the values of \bar{r}_i obtained by ENDOR in this table.

We are of the opinion that the correspondence between \bar{r}_i 's listed in Table III and the estimated distances is a remarkable one. We have concluded that

it is most probable that hydroxyl protons can occur on any of the four oxygen sites with substantially equal probability (see Table II), and we assign the ENDOR peaks in the manner indicated in Table III. The dipolar interaction is very sensitive to distance. Many models have been tested in the course of the present work, and this one seems untortured, based on sound assumptions, and in very much better agreement than anything else considered. This agreement is, in fact, the principal experimental verification of the soundness of the relaxation analysis and of the assignment of the hydrogen atom to the sodalite cage.

Table III: Comparison of Distances Obtained by X-Ray Crystallography and ENDOR (in ångströms)

Site U to nearby oxygens by X-ray ^a	Site U to estimated locations of nearby hydroxy protons	Site U to nearby protons by ENDOR (\bar{r}_i)		
U-O3	4.318	U-O3H	3.81	3.91
U-O2	4.509	U-O2H	4.29	4.20
U-O4	5.166	U-O4H	6.16	5.62
U-O1	6.521	U-O1H	7.14	6.72
U-O3 (2nd shell)	7.372	U-O3H (2nd shell)	7.18	

^a Reference 18.

This conclusion is at variance with the commonly accepted interpretation of X-ray experiments. It is of course possible that all four oxygen sites are occupied at low temperatures used for the ENDOR experiment but not at higher temperatures. We are of the opinion after studying the infrared literature, however, that no experiments have been performed that indicate that *only* two oxygens can accept hydroxyl protons; rather, they indicate that there are *only* two inequivalent hydroxyl protons.

We have tried to interpret the ENDOR data in accordance with the accepted assignment of hydroxyl protons to O3 and O1 only. The problem, of course, is "Why are there so many lines?" One possibility is that the two \bar{r}_i values 3.91 and 4.20 arise from first shell O3 H protons, but that there are two kinds of these protons depending on whether there are two or three aluminum atoms in the hexagonal face between the hexagonal prism and the sodalite cage. A perturbation of geometry of 0.3 Å seems too large, however, and it remains difficult to account for the line at $\bar{r}_i = 5.62$ Å.

Parenthetically, it is an interesting question as to what determines whether a proton will bond to the O1, O2, O3, or O4 oxygens on a particular Al. We suggest that it may in fact be the particular local arrangements of Si and Al that shift the potential minimum from one oxygen to another.

ENDOR and Epr Following Exchange with Various Gases

H₂O and D₂O. The following samples were prepared: 450-H₂O-150, 400-H₂O-380, 400-D₂O-150, and 175-D₂O-150. The results of epr and ENDOR experiments are summarized in Table I.

a. *175-D₂O-150.* This sample yielded H- and D-atom hyperfine lines of approximately equal intensity. This partial exchange indicates that there exist NH₄⁺ protons that are inaccessible to D₂O or are not exchangeable. Intense hydrogen satellite lines were seen on both D and H hyperfine lines. We hoped to determine by ENDOR whether or not the proton distributions around the H and D atoms were the same. The difference in epr widths between H- and D-atom hyperfine lines indicates that there must be some difference in local environments. ENDOR spectra resembling type I (Figure 2, IA) were obtained and differences observed, but the quality of the spectra was not high enough to permit definitive statements.

b. *400-D₂O-150.* The weak H-atom epr and absence of proton ENDOR for the D line indicates substantially complete exchange of hydroxyl protons. We can formulate, but not answer, the question: Why are hydroxyl protons exchangeable with D₂O while NH₄⁺ protons are only partially exchangeable?

c. *450-H₂O-150.* The ENDOR spectra were of type I, whereas if all H₂O had been removed by heating at 150° and the sample had been restored to its condition after activation at 450°, type II spectra would have been obtained. Elimination of ammonia at 450° either creates binding sites for water sufficiently tight to inhibit water release by subsequent heating at 150° or produces a loss in crystallinity.

d. *400-H₂O-380.* The low atom yield and complete absence of ENDOR indicates that even after a second activation treatment at 380° the sample has not been restored to its pristine type II conditions. Thus water is either strongly chemically absorbed on sites liberated by the elimination of ammonia or the sample loses its crystallinity nearly completely.

Adsorption of Ammonia. Samples of type II (activation temperature of about 400°) are deammoniated with acid hydroxyl groups at the cation sites. Infrared experiments indicate that ammonia can be introduced reversibly onto such samples with the elimination of both OH bands and the appearance of NH₄⁺ bands.¹⁷ It seemed desirable to perform similar experiments with our ENDOR technique.

a. *380-NH₃-(No Degassing).* Good epr and ENDOR spectra were obtained, Figure 5, A. Some ENDOR lines present in type II samples (Figure 2, IIA) disappear after introduction of ammonia (Figure 5, A). Thus, there may be some correspondence between the ir and ENDOR experiments. However, the absence of well-resolved ENDOR lines does not mean very

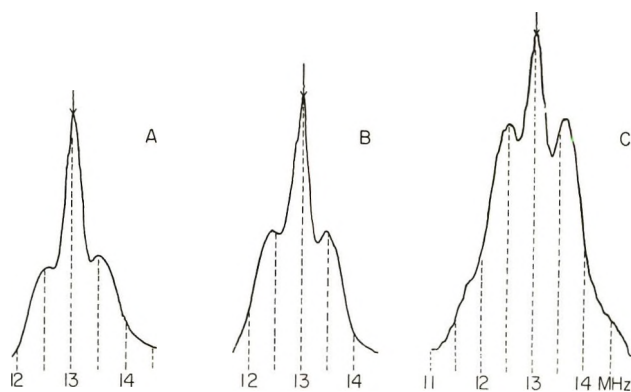


Figure 5. ENDOR spectra: A, 380-NH₃-(no degassing); B, 400-NH₃-155; C, 450-NH₃-420 at 15°K.

much. With NH₃ introduced, there will be more protons around and all of them will contribute to the ENDOR spectrum. The presence of the 1-MHz coupling, assuming that it has the same origin in both ENDOR spectra, however, permits a very interesting conclusion to be drawn: In deammoniated Y-type zeolites there exists a proton that cannot be correlated with either of the two acid hydroxyl bands seen by ir spectroscopy.

b. *400-NH₃-155.* This sample showed two epr H-atom hyperfine lines, a sharp 1.3-G line superimposed on a broad 3.0-G line. This did not seem to be the result of incomplete exchange, but rather an indication that two different hydrogen atom trapping sites exist. The epr widths correspond to type I and to type II epr spectra. If the epr resonant condition is adjusted primarily to the 3.0-G line, a type I ENDOR spectrum is observed, while a type II spectrum is observed if the magnetic field is set on the peak of the derivative of the 1.3-G line. These results were confirmed in an additional sample prepared according to the cycle 335-NH₃-145 (see Table I).

We have a fairly high level of confidence in our result that type II preparation leads to trapping of hydrogen atoms in the sodalite cage. The fact that two sites are clearly present in the 400-NH₃-155 sample plus the observation that the type I epr hyperfine coupling is quite close to that of the free atom suggest that the trapping site for type I sample preparation may be somewhere else, presumably in a larger cage, such as the supercage.

If the deammoniation-ammoniation cycle were fully reversible, we would expect the cycle 400-NH₃-155 to result in the same ENDOR spectrum as type I, except perhaps for minor differences from gases other than NH₃ that are still trapped in type I samples (activation at 150°) but are removed at 400°. The ENDOR spectrum (Figure 5, B) and the epr spectrum are not the same as for type I samples, and we conclude that the deammoniation-ammoniation cycle is not fully reversible.

c. 450-NH₃-420. The ENDOR spectrum of this sample showed the main features of the prototype type II sample, but in general the resolution was poorer (Figure 5, C). It may be that more ammonia can be held in the zeolite after the water has been removed than was there in the original sample after Na exchange and that some of the trapped NH₃ is not lost at 400°. The epr spectrum at $g = 2.00$ is different from that of the initial prototype type II sample and the change is probably due to ionization of an adsorbed ammonium ion. The additional protons from the ammonia result in more possibilities for dipolar interaction, a broader matrix ENDOR line, and a less well-defined ENDOR spectrum.

Adsorption of Pyridine. Pyridine is a base (less ionic than NH₃) that can be adsorbed on acid OH groups, resulting in the disappearance of the ir bands at 3650 and 3550 cm⁻¹.^{33,34} Moreover, upon degassing at 200° after pyridine adsorption at room temperature, only the 3550-cm⁻¹ band reappears. To compare these results with ENDOR, three type II samples were made: 400-pyr-150, 400-pyr-200, and 375-pyr-375. This experiment was unsuccessful since in the first two cases the yield of H atoms was very small; no satellite lines and no ENDOR spectra were observed. At the same time, intense epr signals and ENDOR signals from pyridinium ions at $g = 2.00$ were seen.

ENDOR spectra were obtained from the third sample (375-pyr-375) which were quite similar to those of the 400-NH₃-150 sample. This shows that desorption of pyridine at 375° is not complete, a result confirmed by the observation of pyridinium ion epr and ENDOR spectra in this sample.³⁵ We conclude that some pyridine molecules stay adsorbed on the catalyst after evacuation at 375° under vacuum and that this adsorption is stronger than that of NH₃.

Adsorption of Propylene. Infrared experiments show that propylene is a weak base chemically adsorbed on type II zeolite acidic sites that give rise to the 3650-cm⁻¹ band, and that it can be reversibly evacuated at

250°.³³ Two type II samples have been prepared: 380-C₃H₆-(no degassing) and 420-C₃H₆-310. Intense hydrogen atom epr spectra with satellites together with excellent ENDOR spectra were obtained. Weak propylene ion epr spectra also were observed in both samples. Introduction of ammonia into type II samples eliminates both ir bands, while introduction of propylene eliminates just one. It was felt that this difference might also be evidenced in the ENDOR spectra, but this is not the case. The spectra in Figure 6, A,B appear qualitatively similar to those of Figure 5, A,B,C. The relative heights of the inner and outer lines have changed by a factor of 2, suggesting that C₃H₆ contributes more intensity to the inner matrix ENDOR line than does NH₃. The ENDOR spectrum of the second sample, 420-C₃H₆-310, is quite similar to that of the 400-NH₃-155 sample, indicating that ammonia is desorbed more readily than propylene.

In a further experiment, propylene was introduced at room temperature after activation of the zeolite at 650°, without additional treatment. The yield of H atoms dropped by two orders of magnitude with respect to type II preparation. This experiment shows that calcination destroys the hydrogen atom trapping sites, since large numbers of hydrogen atoms are expected to be released by irradiation of this sample.

Adsorption of Methane. Methane is known to be physically but not chemically adsorbed by zeolites.³⁶ The sequence of sample preparation was 450-CH₄-(no degassing). Again, somewhat poorly resolved type II spectra were observed. The ratio of central/outer line ENDOR intensities was 2.0 compared with 0.9 for the pure prototype II sample. Presumably the relative increase of the central line by about a factor of 2 arises from weak dipolar couplings between the hydrogen atoms and the methane protons. It can be concluded that methane does not neutralize acidic sites and does not modify the H atom yield, either by affecting the number of sites or the number of atoms available.

Conclusions

Comparison of ENDOR and Infrared Spectroscopy in the Study of Zeolites. We have attempted to establish in a qualitative manner the relationship between ir and ENDOR spectroscopy. The latter experiment is performed at low temperatures. The process of γ irradiation gives rise to thermal spikes or local heating that is quickly quenched. Hydrogen atoms are trapped and the distribution of hydroxyl groups or other proton-containing groups may also be affected by this process. Infrared experiments are usually done at higher tem-

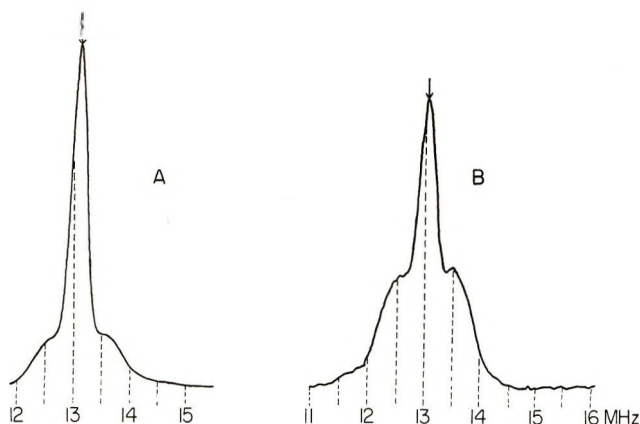


Figure 6. ENDOR spectra: A, 380-C₃H₆-(no degassing); B, 420-C₃H₆-310 at 15°K.

(33) B. V. Liengme and W. K. Hall, *Trans. Faraday Soc.*, **62**, 3229 (1966).

(34) J. W. Ward, *J. Phys. Chem.*, **71**, 3106 (1967).

(35) J. C. Vadrine, D. S. Leniart, and J. S. Hyde, to be published.

(36) J. L. White, A. N. Jelli, J. M. Andre, and J. J. Fripiat, *Trans. Faraday Soc.*, **63**, 461 (1967).

peratures where proton mobility can be substantial. Thus, the samples employed in the two methods are not in identical states.

ENDOR sees all protons within the immediate environment of the trapped atom, but it is not easy to say to what kind of chemical group the proton belongs; it may permit the detection of certain chemical groups, but overlap and difficulties in interpretation make it quite easy to fail to detect structures actually present. ENDOR gives a sharp structural picture near the trapped atom with resolution fading rapidly with increase in radial distance from the atom; it to a fair approximation weighs a contribution from a particular group equally regardless of where it is located in the zeolite lattice.

ENDOR then is an interesting analytical tool for the study of catalysts, with strengths and weaknesses. The information gained partially overlaps that from other methods but is to a considerable degree different. This is the primary motivation for further studies of this type. This paper has been concerned with methodology, and we believe we have established the usefulness of this new technique.

Nuclear Relaxation and the Theory of Powder ENDOR. Theoretically in the companion paper⁹ and experimentally in the present paper we have considered the effect of motion of the trapped hydrogen atom on relaxation of nearby nuclei. The nuclear relaxation probability is dominated by a term with $\sin^4 \theta$ dependence, where θ is the angle between the radial vector and the applied field. This gives rise to two well-defined peaks in a powder sample where all orientations are equally probable, one on either side of the free proton frequency. This is a very encouraging result from the point of view of obtaining well-resolved powder ENDOR spectra.

The relaxation model can be refined by further analysis and experiment and may permit more detailed information about hydrogen atom motion to be obtained. One experimental observation not yet explained is that introduction of fairly inactive gases such as propylene or methane seems to sensitize the ENDOR response (see Table I).

Location of Trapped Atoms. Detailed interpretation of ENDOR spectra hinges on knowing the location of trapped hydrogen atoms. In type II sample preparation (activation at 400°, where water and ammonia have been driven off) it has been concluded from the present work that the atom is trapped in the sodalite cage with its average position at the center or so-called U site.

The various experiments indicate, with less assurance, that type I preparation (activation at 150°, only water driven off) leads to a trapping site (or sites) in a quite different location. One puzzling problem is why the epr hyperfine line width is greater for type I than for type II samples, while the superhyperfine interactions that have been detected are larger for type II than type I samples. A possible explanation is that the epr line width for type I samples arises from a distribution of hydrogen atom hyperfine couplings.

H-Y Type Zeolites. The main conclusion concerning structural hydroxyl groups is that there appear to be four inequivalent protons around the trapped hydrogen atom in positions not very different from what we would expect if a hydroxyl group could be located on any one of the four oxygens. At least one of these detected protons remains substantially unchanged by subsequent introduction of NH_3 , suggesting that it cannot be assigned to an acidic OH group.

Hydrogen Atom Yields. Roughly the hydrogen atom yield saturates with increasing dose at a level that is independent of sample history with two exceptions: (1) when a scavenger such as pyridine is introduced, and (2) when the activation temperature is above 500°. The saturation yield is about 10^{18} atoms/g, which is of the order of 0.1% of the protons present.

Reversibility. No strictly reversible sample preparations have been found in the present work. The introduction of any gas in the cycle 400-gas-400 results in some loss of ENDOR resolution. In addition, we have been unable to convert samples yielding type II spectra into samples yielding type I spectra by any process we have investigated. On the basis of infrared spectroscopy it has been argued that ammonium zeolite can be converted into H-Y zeolite by heating, and converted back into ammonium zeolite by the introduction of NH_3 . We have been unable to reproduce completely this result using ENDOR spectroscopy. We conclude that the concepts of chemical reversibility and reversibility as determined by various physical techniques must be used with caution.

Acknowledgment. One of us (J. C. V.) thankfully acknowledges a grant from NATO which made it possible for him to perform this work at Varian Associates in Palo Alto, Calif. We are indebted to Professor M. Boudart of the Chemistry Department of Stanford University for the use of his laboratory while preparing some of the samples and to Dr. Colin Munday, Raychem Corporation, Menlo Park, Calif., for providing sample irradiation facilities.

A Spectroscopic Study of the Propionitrile–Iodine Molecular Complex

by John A. Maguire* and John J. Banewicz

Department of Chemistry, Southern Methodist University, Dallas, Texas 75222 (Received July 19, 1971)

Publication costs assisted by The Robert A. Welch Foundation

The formation equilibrium constant, K , for the molecular complex formed between propionitrile and iodine in heptane and carbon tetrachloride was determined from spectral data in the visible region at 25°. Analysis of the data using a Scott type of equation yielded values of K that were wavelength dependent. This variation in the determined value of K was attributed to a variation in the optical properties of both the complexed and uncomplexed iodine molecules with increasing propionitrile concentration. An equation that corrects for these variations was developed and the analysis gave values of K that were constant to within $\pm 5\%$. The average value of K at 25° for the propionitrile–iodine complex in heptane was found to be $0.96 M^{-1}$.

Introduction

We have been investigating the stabilities and thermodynamics of formation of the molecular complexes formed between iodine and a series of aliphatic nitriles, using spectrophotometric methods. In the course of this investigation we have noted discrepancies between the values of the formation equilibrium constant, K , for the propionitrile– I_2 complex in carbon tetrachloride obtained in this laboratory and those reported by Klaboe.¹ An examination of the results indicated that these discrepancies could not be blamed entirely on experimental indetermination but were due in part to the fact that the equilibrium constants were determined at different wavelengths. A detailed study of the propionitrile– I_2 system was undertaken to examine the apparent wavelength dependence of K .

Experimental Section

Materials. Reagent grade iodine was purified by sublimation from potassium iodide before use.

Eastman propionitrile, free of isonitrile, EK 528, was purified by stirring with calcium hydride, followed by treatment with P_2O_5 , then fractionation. The distilled nitrile was stored over a molecular sieve (Linde 3A) until used. The propionitrile was checked by glpc and found to contain less than 0.2 ppt water. No other impurities were detectable by glpc. Baker GC-Spectrophotometric grade carbon tetrachloride and B & A Instrument grade heptane were used without further purification except that dry nitrogen was bubbled through the solvents before use.

Preparation of Solutions and Procedure. All solutions were prepared by weight as described previously.² Mixing and handling of the solutions were carried out in a drybox to insure against moisture contamination.

The spectra were determined using either a Beckman Model DK2A recording spectrophotometer or a Beckman Model DU spectrophotometer. The temperature of the solutions in the spectrophotometers was con-

trolled to within $\pm 0.1^\circ$ using thermostated cell compartments.

The general procedure used in obtaining the spectra has already been described.² In this procedure the difference between the absorbance (A) of the iodine–nitrile solution and the absorbance (A_0) of a reference solution containing the same total iodine concentration was read directly. Because of the strong absorption of the nitrile in the ultraviolet, the charge-transfer band could not be used. Continuous plots of $A - A_0$ were made in the visible region using the DK2A spectrophotometer. These plots showed that the magnitude of $A - A_0$ reached maxima at about 535 and 460 nm. For the DU runs, selected wavelengths were used in the range between 440 and 560 nm. All readings were taken at 25°.

Results and Discussion

From the value of $A - A_0$ at a particular nitrile concentration (C_D) and a total iodine concentration (C_A), the quantity $[C_D C_A / (A - A_0)](X)$ was calculated at each wavelength. If only a 1:1 complex exists and Beer's law is obeyed by all species, then a plot of X vs. $C_D + C_A$ should yield a straight line according to the equation²⁻⁴

$$C_D + C_A = (\epsilon_C - \epsilon_A)X - K^{-1} \quad (1)$$

in which K is the formation equilibrium constant of the complex, ϵ_C is its molar absorptivity, and ϵ_A is the molar absorptivity of free I_2 . This equation, which is a modification of that first proposed by Scott,⁴ is the one usually used in analyzing spectroscopic data to obtain values of formation equilibrium constants. In deriving this equation, the absorptivity of the free nitrile is

(1) P. Klaboe, *J. Amer. Chem. Soc.*, **85**, 871 (1963).

(2) J. A. Maguire, A. Bramley, and J. J. Banewicz, *Inorg. Chem.*, **6**, 1752 (1967).

(3) N. J. Rose and R. S. Drago, *J. Amer. Chem. Soc.*, **81**, 6138 (1959).

(4) R. L. Scott, *Recl. Trav. Chim. Pays Bas*, **75**, 778 (1956).

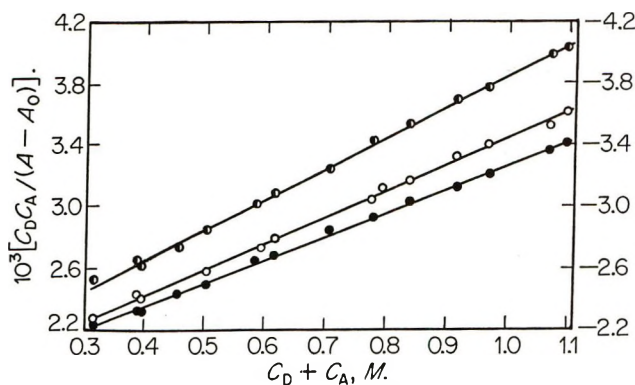


Figure 1. A plot of $C_D C_A / (A - A_0)$ vs. $C_D + C_A$ at 25° for 460 (●), 475 (●), and 540 (○) nm. The left-hand ordinate is for 460 and 475 nm; the right-hand ordinate is for 540 nm.

assumed to be zero and the concentration of complex small compared to the nitrile concentration. In cases where the complex concentration becomes important an additional term of the form, $-(A - A_0)/(\epsilon_C - \epsilon_A)$, is added to the right-hand side of eq 1. A value of K can be calculated from the intercept and $\epsilon_C - \epsilon_A$ from the slope. Typical plots are shown in Figure 1. In the concentration range of C_D from 0.2 to 1.1 M , such plots appear to be linear. The best values of K and $\epsilon_C - \epsilon_A$ were calculated from eq 1 by the method of least squares and are listed in Table I.

Table I: Values of K and $\epsilon_C - \epsilon_A$ for the Propionitrile-Iodine System Obtained from Low-Concentration Data at 25° Using Eq 1

Wave-length, nm	Solvent CCl_4		Solvent C_7H_{16}	
	$K^{a,b}$	$\epsilon_C - \epsilon_A^b$	$K^{a,b}$	$\epsilon_C - \epsilon_A^b$
440	0.39 ± 0.02	664 ± 25	0.71 ± 0.02	579 ± 10
445	0.42 ± 0.02	689 ± 21	0.77 ± 0.02	610 ± 9
450	0.45 ± 0.02	696 ± 22	0.81 ± 0.01	642 ± 6
455	0.48 ± 0.02	688 ± 19	0.84 ± 0.01	660 ± 6
460	0.51 ± 0.02	657 ± 17	0.86 ± 0.01	663 ± 6
465	0.52 ± 0.02	615 ± 17	0.99 ± 0.02	615 ± 7
470	0.56 ± 0.02	534 ± 12	1.02 ± 0.02	566 ± 7
475	0.60 ± 0.01	450 ± 6	1.09 ± 0.02	500 ± 5
520	0.47 ± 0.03	-557 ± 24	0.86 ± 0.03	-480 ± 9
530	0.51 ± 0.01	-606 ± 9	0.97 ± 0.02	-565 ± 7
535	0.51 ± 0.01	-612 ± 8		
540	0.51 ± 0.01	-599 ± 8	0.98 ± 0.02	-588 ± 8
550	0.53 ± 0.01	-515 ± 9	1.01 ± 0.02	-535 ± 6
560	0.53 ± 0.02	-415 ± 13	1.04 ± 0.03	-442 ± 8

^a K in M^{-1} . ^b Uncertainties are standard deviations.

For the propionitrile- I_2 complex in carbon tetrachloride, Klaboe¹ reports values of K at 20° of 0.41, 0.44, and 0.44 at 430, 435, and 440 nm, respectively. Because of the difference in temperature, a direct comparison of Klaboe's results and those in Table I cannot be made. However, if one uses the value of

ΔH° of -2.7 kcal/mol found for the system,⁵ K can be corrected to 20°. This corrected value at 440 nm is 0.43, in excellent agreement with Klaboe's value at this wavelength. The small but systematic variation of K with wavelength seen in Table I indicates that even though the plots shown in Figure 1 seem to be linear, the assumptions on which eq 1 is based are not completely valid.

Deranleau⁶ has examined in detail the theory of measurement of equilibrium constants for weak complexes and has emphasized the importance of the concentration range in analyzing data for such complexes. According to Deranleau, data should be obtained over a wide range of the saturation fraction, s (in this case the fraction of I_2 complexed). In the optimum range of s , between 0.2 and 0.8, relative errors in K and $\Delta\epsilon$ are minimized. A large portion of the saturation fraction region should be covered before any model can be considered proven and for low saturation fractions apparent linearities of plots similar to Figure 1 are of little use in establishing a model.

The results shown in Table I are in the s range from 0.2 to 0.5 in the case of heptane and from 0.1 to 0.33 for carbon tetrachloride, assuming that the calculated values of K are approximately correct. Table II lists the determined values of K and $\epsilon_C - \epsilon_A$ for the propionitrile-iodine system in heptane when the s range is extended to about 0.7. For these high-concentration studies heptane was used as a solvent. In this solvent the values of K are higher than in carbon tetrachloride. In addition, complications due to solvent competition, such as those described by Carter,⁷ should be minimized. The effect of the range of s on the determined values of K and $\epsilon_C - \epsilon_A$ obtained using eq 1 can be seen by a comparison of Tables I and II. The determined values of K are both concentration and wavelength dependent. This is especially evident in the 400-nm region.

Figure 2 shows some typical plots of X vs. $C_D + C_A$ for these higher concentration studies.

Using the values of K and $\epsilon_C - \epsilon_A$ listed in Table II, values of $A - A_0$ were calculated for different donor concentrations and the differences between the calculated and observed values of $A - A_0$ determined. Figure 3 shows these differences in $A - A_0$ as a function of donor concentration at wavelengths of 445 and 475 nm. Similar behavior was noted at the other wavelengths and indicates that, although Figure 2 appears to be linear, a definite curvature does exist. In addition, the isosbestic point was found to blue shift by about 2 nm per unit molar increase in C_D . This shift in the isosbestic point is an indication that, in addition

(5) J. A. Maguire and J. J. Banewicz, to be published.

(6) D. A. Deranleau, *J. Amer. Chem. Soc.*, **91**, 4044, 4050 (1969).

(7) S. Carter, J. N. Murrell, and E. J. Rosch, *J. Chem. Soc.*, 2048 (1965).

Table II: Analysis of Propionitrile-I₂ in Heptane at 25°. High-Concentration Data

λ, nm	Eq 1		Eq 2			Eq 2 (using K _{Av} = 0.962)	
	K ^{a,b}	ε _C - ε _A ^b	K ^a	B	a	B	a
445	0.69 ± 0.01	658 ± 7	0.90	527	34	502	40
460	0.88 ± 0.01	653 ± 4	0.99	593	17	607	13
465	0.95 ± 0.01	614 ± 2	0.92	631	-5	611	1
475	1.13 ± 0.01	483 ± 3	0.96	545	-18	543	-18
520	0.76 ± 0.01	-516 ± 4	0.92	-441	-20	-427	-24
540	0.95 ± 0.01	-588 ± 2	0.99	-573	-4	-583	-1
560	1.02 ± 0.01	-442 ± 1	1.05	-431	-3	-460	4

$$K_{Av} = 0.96 \pm 0.04^c$$

^a K in M⁻¹. ^b Uncertainties are standard deviations. ^c Uncertainty is average deviation.

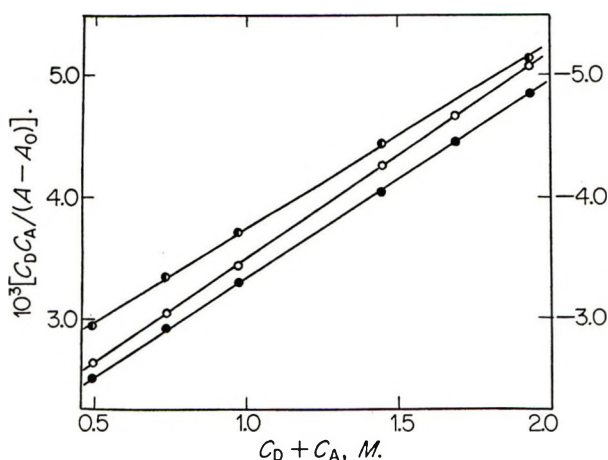


Figure 2. A plot of $C_D C_A / (A - A_0)$ vs. $C_D + C_A$ at 25° for 445 (●), 465 (●), and 540 (○) nm. The left-hand ordinate is for 445 and 465 nm; the right-hand ordinate is for 540 nm.

to the 1:1 complex, some new absorbing species is being formed by the interaction of the nitrile and iodine or that the free and complexed iodine are not obeying Beer's law.

Although the influence of higher complexes on Scott plots has been extensively examined,⁸ very little work has been done on the consequences of deviations from Beer's law.⁹ The sensitivity of the visible I₂ band to its environment has been noted by Voigt,¹⁰ who measured the spectra of I₂ in a number of different solvents. In most solvents the visible I₂ band was found to blue shift from its gas-phase position. Voigt has proposed that in addition to charge-transfer and contact charge-transfer interactions, exchange repulsion of the excited state of I₂ with nonbonding electron pairs may be a further cause of the blue shifts. This was proposed to account for the small blue shifts noted for I₂ in the alkyl chlorides and perfluorocarbons in which no contact-charge-transfer bands have been observed. The exact mechanism of this effect is not completely understood, but it seems to involve a weak, nonbonding, yet specific interaction between electron pairs on the solvent and the iodine molecule.

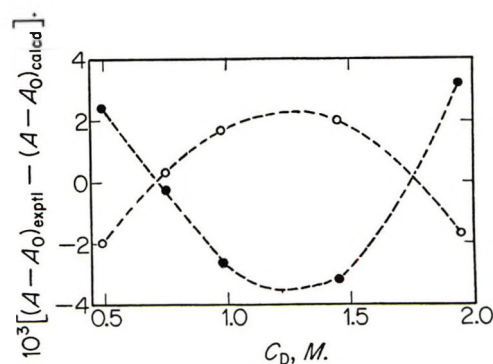


Figure 3. Differences in experimental and calculated values of $A - A_0$ obtained from eq 1: 445 (●) and 475 (○) nm.

In order to cover a meaningful portion of the saturation fraction range, the mole fraction of nitrile must be increased to about 0.26. These high propionitrile concentrations will materially change the nature of the solvent. It would be unusual if the spectral properties of the free and complexed iodine were not altered. The effect that these changes will have on plots of X vs. $C_D + C_A$ will be determined by the functional dependence of ϵ_C and ϵ_A on nitrile concentration. A reasonable assumption is that the molar absorptivities of the free and complexed iodine vary in a linear fashion with C_D . This would be expected if the interactions between excess nitrile and iodine were specific ones, similar to those proposed by Voigt. Thus if $\epsilon_C = \epsilon_C^0 + aC_D$ and $\epsilon_A = \epsilon_A^0 + bC_D$, the equation relating X to $C_D + C_A$ becomes

$$C_D + C_A = BX + aXC_D - K^{-1} \quad (2)$$

where $B = \epsilon_C^0 - \epsilon_A^0 + bK^{-1}$.

In obtaining this equation the concentration of complex is assumed to be small compared to the donor concentration.

(8) G. D. Johnson and R. E. Bowen, *J. Amer. Chem. Soc.*, **87**, 1655 (1965).

(9) R. Foster, "Organic Charge-Transfer Complexes," Academic Press, New York, N. Y., 1969.

(10) E. M. Voigt, *J. Phys. Chem.*, **72**, 3300 (1968).

The high-concentration data were analyzed using eq 2, and the results are listed in Table II. If eq 2 is valid, then identical values of K should be obtained at the different wavelengths. Although experimental scatter does exist, the systematic variation in K with wavelength seems largely to have been eliminated and the values of K are the same to within about $\pm 5\%$. In view of the small deviations from linearity for which eq 2 attempts to correct, the agreement among the values of K is considered to be satisfactory.

An analysis of the data was also carried out using the method proposed by Scatchard.¹¹ It has been shown⁶ that under certain conditions this method is more sensitive to complications than is the Scott treatment; in addition, the two methods weight experimental points differently. Equations 1 and 2 can be converted to the Scatchard form by multiplying both sides by K/X . The quantitative results obtained from the Scatchard treatment were essentially the same as those listed in Tables I and II. This indicates that in this case the difference in the weighting of the experimental points does not significantly affect the results.

The values of $A - A_0$ calculated by eq 2, using the parameters listed in Table II, were in excellent agreement with the experimental values. For 24 of the 39 experimental points there was no difference between the experimental and calculated values of $A - A_0$, in most of the other cases the difference was 0.001 absorbance unit, and in no circumstance was the difference greater than 0.003. Furthermore, the discrepancies that were found showed no trend with donor concentration.

Although the agreement between the calculated and experimental values is excellent, it should be pointed out that the additional term in eq 2 automatically ensures a better fit than could be obtained from eq 1. The sensitivity of $A - A_0$ to the value of K can be assessed using the sharpness of fit criterion of Conrow, Johnson, and Bowen.¹² The sharpnesses were calculated at the individual wavelengths and found to range from a minimum of 10 at 450 nm up to a value of 410 at 475 nm. The average value of K was calculated to be 0.962. The best values of K and a calculated at each wavelength using this average value of K are also listed in Table II.

The magnitude and sign of a determine the curvature in plots of X vs. $C_D + C_A$, which in turn gives rise to the variations in K found in Tables I and II. The opposing shapes of the curves shown in Figure 3 illustrate the different curvatures produced by positive and negative values of a . It is of interest to note that the variation in a with wavelength is consistent with a blue shift of the visible complex peak with increasing donor concentration. Only in spectral regions where a is quite small can eq 1 be used.

Johnson and Bowen,⁸ in summarizing the criteria for the establishment of a 1:1 molecular complex, state that if a variation of K with wavelength is found it is a strong indication that termolecular complexes are also present. The general equations relating the absorbance of the solution to concentrations of donor and acceptor for the case of 1:1 and 1:2 complexes have been reported by these investigators. Under the conditions where the concentration of donor is large compared to both of the complexes, the equation relating $C_D + C_A$ to X differs in functional form from eq 2 only in the addition of a C_D^2 term. The inclusion of this term permits an even more precise fit of the experimental data. However, this improvement was found to be beyond that permitted by the inherent experimental uncertainty. That is, the value of $A - A_0$ cannot be read to any better than ± 0.001 OD unit, and any fit better than this is superfluous. We feel therefore that eq 2 can adequately account for our results, and the assumption of the existence of higher order complexes is not necessary.

Interpretation of optical data can be complicated not only by the formation of termolecular complexes but also by deviations from Beer's law when only 1:1 complexes are formed. In systems involving the formation of weak complexes where high donor concentrations are needed to cover a sufficient range of s values, a great deal of caution must be exercised in interpreting optical data. In particular, if equations similar to eq 1 are to be used, data must be obtained over a wide range of wavelengths and evidence of any curvature noted. Even when apparently linear plots are found, slight curvatures can produce rather drastic variations in the determined values of K with wavelength. When such evidence is found, more complex equations are required which correct for complications caused by higher order complexes or changes in the optical properties of the absorbing species. When the curvature is slight, it may not be possible to distinguish unambiguously between these two cases.

For the propionitrile-I₂ system, the assumption that the optical properties of the absorbing species are altered as nitrile is added accounts for the experimental results.

Acknowledgment. The authors wish to thank the Robert A. Welch Foundation of Houston, Texas, for support of this project through Grants No. N-142 and N-056.

(11) G. Scatchard, *Ann. N. Y. Acad. Sci.*, **51**, 660 (1949).

(12) K. Conrow, G. Johnson, and R. Bowen, *J. Amer. Chem. Soc.*, **81**, 6138 (1959).

A Spectrophotometric and Thermodynamic Study of Donor-Acceptor Complexes of Carbazole

by E. L. Ong and Manjit S. Sambhi*¹

Department of Chemistry, University of Malaya, Pantai Valley, Kuala Lumpur, Malaysia (Received October 12, 1971)

Publication costs borne completely by The Journal of Physical Chemistry

The spectrophotometric and thermodynamic properties of donor-acceptor complexes of carbazole with 2,3-dichloro-5,6-dicyanobenzoquinone (DDQ), tetracyanoethylene (TCNE), 9-dicyanomethylene-2,4,7-trinitrofluorenone (DTF), and 2,4,7-trinitrofluorenone (TNF) have been evaluated. The reliability of formation constants (K_c) as obtained by the Benesi-Hildebrand and Rose-Drago methods is discussed. The trends in K_c values, the standard enthalpies of formation (ΔH_f°), and the oscillator strengths (f) of the charge-transfer (CT) bands suggest that the stabilities of these complexes cannot be interpreted solely in terms of CT forces.

Introduction

The nature of intermolecular bonding in donor-acceptor complexes has been the subject of extensive investigation from both the theoretical and the experimental points of view. Briegleb^{2,3} had postulated an electrostatic model to account for the stabilities of certain π - π complexes. Mulliken⁴ in 1952 proposed a charge-transfer theory which has been extensively used to explain and interpret the properties associated with donor-acceptor complexes.

Donor-acceptor complexes have been commonly described as CT complexes and it has been widely accepted that CT forces play a dominant role in determining the ground-state properties of these complexes even though Mulliken⁴ had clearly pointed out that classical intermolecular forces may play a significant role in determining the stabilities of such complexes. It has been shown recently^{5,6} that normal van der Waals forces are responsible for the ground-state properties of certain π complexes and in certain aromatic-halogen and aromatic-TCNE complexes,⁷ electrostatic, CT, and exchange repulsion interactions make important contributions to the stabilities of these complexes.

In complexes held together mainly by CT forces, one would expect that K_c , ΔH_f° , and f would increase steadily in a series of complexes between a common donor and a number of acceptors of increasing electron affinity.^{8,9} We have measured the spectral and thermodynamic characteristics of carbazole complexes of DDQ, TCNE, DTF, and TNF in order to determine whether CT forces are mainly responsible for the stabilities of these complexes in the ground state. The reliability of K_c as obtained by the Benesi-Hildebrand¹⁰ and Rose-Drago¹¹ methods is discussed.

Experimental Section

Materials. DDQ was recrystallized twice from dry methylene chloride; mp 212–213°.

TCNE was recrystallized twice from dry methylene chloride and sublimed under high vacuum. The white solid obtained melted at 198–200°.

DTF was recrystallized twice from dry methyl cyanide; mp 267°. *Anal.* Calcd for $C_{16}H_5N_5O_6$: C, 52.89; H, 1.38; N, 18.25. Found: C, 52.49; H, 1.37; N, 19.20.

TNF was recrystallized from a 3:1 nitric acid-water mixture and dried under vacuum over phosphorus pentoxide and silica gel; mp 175–176°.

1,2-Dichloroethane was partially dried over calcium chloride, refluxed over calcium hydride, and fractionally distilled through a 35-cm Vigreux column.

Spectrophotometric Measurements. The spectra were recorded by a Perkin-Elmer 137 UV spectrophotometer. Spectrophotometric data required to evaluate complex stoichiometry and thermodynamic parameters were obtained by measuring the absorbances of donor-acceptor solutions prepared by weighing appropriate quantities of donor and acceptor in standard volumetric flasks and filling the flasks to the mark with 1,2-dichloroethane. The absorbance of each solution was measured

- (1) Author to whom correspondence should be addressed.
- (2) G. Briegleb, *Z. Phys. Chem., Abt. B*, **31**, 58 (1935).
- (3) G. Briegleb, "Zwischenmolekulare Kräfte und Molekülstruktur," Enke Verlag, Stuttgart, 1937.
- (4) R. S. Mulliken, *J. Amer. Chem. Soc.*, **74**, 811 (1952).
- (5) M. J. S. Dewar and C. C. Thompson, Jr., *Tetrahedron, Suppl.*, **7**, 97 (1966).
- (6) R. J. W. Le Fevre, D. V. Radford, and P. J. Stiles, *J. Chem. Soc. B*, 1297 (1968).
- (7) J. L. Lippert, M. W. Hanna, and P. J. Trotter, *J. Amer. Chem. Soc.*, **91**, 4035 (1969).
- (8) R. S. Mulliken and W. B. Person, *Ann. Rev. Phys. Chem.*, **13**, 107 (1962).
- (9) R. Foster, "Organic Charge-Transfer Complexes," Academic Press, London, 1969.
- (10) H. A. Benesi and J. H. Hildebrand, *J. Amer. Chem. Soc.*, **71**, 2703 (1949).
- (11) M. J. Rose and R. S. Drago, *ibid.*, **81**, 6138 (1959).

without delay with a Hilger H700 spectrophotometer fitted with a water-thermostated cell compartment. The temperature was maintained constant to within $\pm 0.1^\circ$. The CT absorption shows no change during the time required for the absorbance measurements. Matched silica rectangular cells with ground-glass stoppers were employed for all spectroscopic measurements.

Complex stoichiometry was determined by Job's method¹² of continuous variation. The Rose-Drago method¹¹ was used to evaluate K_c and the maximum molar absorptivity (ϵ_{\max}) for the complexes at 30, 40, 50, and 60°. The Benesi-Hildebrand method¹⁰ was used to determine K_c and ϵ_{\max} at the above temperatures for the TCNE and TNF complexes while the data for the DDQ and DTF complexes were obtained at 30° only. (The least-squares method was used to calculate the slope and intercept of the Benesi-Hildebrand plot.) The standard enthalpies for complex formation were obtained from the slopes of the van't Hoff plots of $\log K_c$ vs. $1/T$. Again, the least-squares method was employed. The standard entropies (ΔS°) and free energies (ΔG°) were evaluated in the normal manner. The oscillation strengths of the CT bands at 30° were evaluated experimentally by the equation⁸

$$f = 4.3 \times 10^{-9} \epsilon_{\max} \Delta \nu_{1/2}$$

where ϵ_{\max} is the maximum molar absorptivity and $\Delta \nu_{1/2}$ is the half-width of the band. f for the TNF CT band was not calculated as the band was not completely resolved.

Results

Solutions of carbazole in 1,2-dichloroethane were colorless and the addition of π -electron acceptors DDQ, TCNE, DTF, and TNF resulted in the immediate formation of intense colors. The spectra of these solutions were characterized by broad featureless bands which had λ_{\max} at 625, 605, 540, and 425 $m\mu$, respectively. The band due to the addition of TNF was not completely resolved and λ_{\max} was obtained by differential spectroscopic techniques.

These broad bands can be assigned to the formation of intermolecular CT transition between the π -electron acceptors and the carbazole molecule. This assignment is supported by the observation that the electron affinities (EA) of DDQ, TCNE, DTF, and TNF are 1.95, 1.80, 1.45, and 1.0 eV¹⁰ while the CT absorption maxima frequencies (ν_{\max}) are 1.986, 2.048, 2.296, and 2.915 eV, respectively. This relationship between EA and ν_{\max} is to be expected from theoretical considerations.⁴ The CT bands for the complexes are shown in Figure 1.

Plots of absorbances vs. mole fraction of donor had maxima occurring at 0.5 mole fraction, and according to Job's method of continuous variation¹² this means that the complexes have 1:1 stoichiometry in solution.

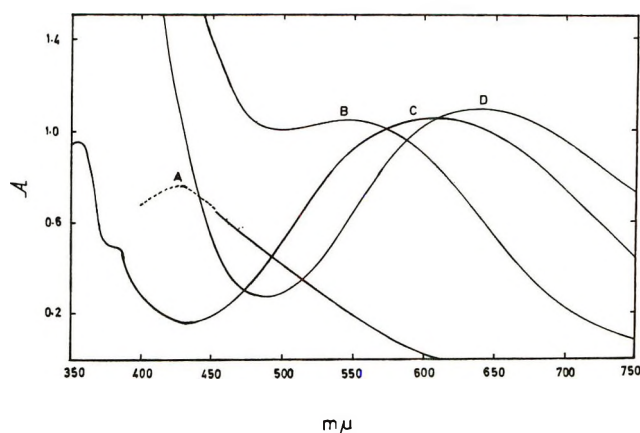


Figure 1. The charge-transfer bands for carbazole complexes: (A) TNF, (B) DTF, (C) TCNE, (D) DDQ.

The successful use of Benesi-Hildebrand and Rose-Drago equations for 1:1 complexes readily confirmed this result. The donor and acceptor concentrations were varied generally from 10^{-3} to 10^{-1} M . The spectral and thermodynamic results are shown in Tables I and II, respectively.

Discussion

The spectrophotometric evaluation of K_c and ϵ_{\max} has been discussed critically by a number of authors.¹³⁻¹⁶ Person¹⁵ has shown that for weak com-

Table I: The Spectral Characteristics of the Carbazole Complexes of TNF, DTF, TCNE, and DDQ in 1,2-Dichloroethane

Acceptor	λ_{\max} , $m\mu$	Temp., $^\circ C$	ϵ_{\max}		$\Delta \nu_{1/2}$, cm^{-1}	f
			a	b		
TNF	425	30	1420	1390 ± 15^c		
		40	1440	1390 ± 30		
		50	1420	1395 ± 15		
		60	1400	1385 ± 15		
DTF	540	30	1510	1540 ± 20	5880	0.039
		40		1490 ± 15		
		50		1450 ± 20		
		60		1440 ± 15		
TCNE	605	30	1480	1480 ± 40	6940	0.044
		40		1520 ± 10		
		50	1500	1480 ± 30		
		60	1500	1550 ± 20		
DDQ	625	30	1690	1680 ± 10	5120	0.038
		40		1700 ± 50		
		50		1690 ± 10		
		60		1700 ± 20		

^a Benesi-Hildebrand procedure. ^b Rose-Drago procedure.

^c Uncertainties are expressed as standard deviations.

(12) P. Job, *Ann. Chim. (Paris)*, 10, 113 (1928).

(13) S. Carter, J. N. Murrell, and E. J. Rosch, *J. Chem. Soc.*, 2048 (1965).

(14) P. R. Hammond, *ibid.*, 479 (1964).

(15) W. B. Person, *J. Amer. Chem. Soc.*, 87, 167 (1965).

(16) D. A. Deranleau, *ibid.*, 91, 4044 (1969).

Table II: The Thermodynamic Characteristics of the Complexes

Acceptor	Temp, °C	K_c , l. mol ⁻¹		$-\Delta G^\circ$, kcal mol ⁻¹	$-\Delta H_f^\circ$, kcal mol ⁻¹	$-\Delta S^\circ$, eu
		a	b			
TNF	30	5.9	5.88 ± 0.05 ^c	1.06	2.9	5.9
	40	5.1	5.04 ± 0.05			
	50	4.5	4.52 ± 0.05			
	60	4.1	4.1 ± 0.10			
DTF	30	13.7	13.6 ± 0.25	1.6	3.1	4.9
	40		11.6 ± 0.21			
	50		10.2 ± 0.25			
	60		8.5 ± 0.10			
TCNE	30	2.9	2.89 ± 0.09	0.64	2.9	7.4
	40	2.5	2.45 ± 0.04			
	50	2.1	2.16 ± 0.05			
	60	1.9	1.87 ± 0.05			
DDQ	30	28.1	28.2 ± 0.2	2.0	5.1	10.2
	40		21.4 ± 0.2			
	50		16.5 ± 0.1			
	60		13.1 ± 0.1			

^a Benesi-Hildebrand procedure. ^b Rose-Drago procedure.
^c Uncertainties are expressed as standard deviations.

plexes the Benesi-Hildebrand treatment gives reliable results if the initial concentration of the donor $[D]_0$ is between 0.1 and 9.0 times the value of $1/K_c$. This allows K_c and ϵ_{\max} to be separately evaluated. This condition was met in all our Benesi-Hildebrand determinations. The differences in the K_c values of the complexes are significant as ΔK is greater than 3 times the standard deviation in all cases.¹⁵

Deranleau¹⁶ has shown that for weak molecular complexes an accurate evaluation of K_c and ϵ_{\max} can best be obtained when the saturation fraction s is between 0.2 and 0.8 and measurement over 75% of the curve, *e.g.*, the Scatchard¹⁷ plot, is required before the proposed 1:1 complex model can be considered to be verified by the use of any single equilibrium equation. The saturation factor s is defined by Deranleau¹⁶ as the ratio of the concentration of the complex to the initial concentration of the most dilute component. On this s scale Person's criterion of donor concentration between $0.1/K_c$ and $9/K_c$ corresponds to saturation fractions of 0.09 and 0.9, respectively. In our experiments s values were in the region of 0.1 and 0.25 and since our

standard deviations in K_c and ϵ_{\max} are small, it is reasonable to say that 1:1 complexes do exist at least in the region of s covered in our experiments.

The Rose-Drago plots were characterized by a large degree of sharpness¹⁸ as the intersection of the lines occurred at one point. This large degree of sharpness indicative of a reliable K_c value was achieved by reducing the experimental errors to a minimum and choosing experimental conditions such that the concentration of the acceptor was held fairly constant while the donor concentrations were varied over a wide range. This gives lines with significantly different slopes.

The K_c values of carbazole complexes of TNF, DTF, TCNE, and DDQ at 30° are 5.88, 13.6, 2.89, and 28.2 l. mol⁻¹, and the respective ΔH_f° values are 2.9, 3.1, 2.9, and 5.1 kcal mol⁻¹. Clearly, order of acceptor strength based on K_c values would be different from the order based on ΔH_f° values and no linear relationship exists between ΔH_f° and ΔS° (see Table II). However, ΔH_f° indicates that the TNF, DTF, and TCNE complexes are of comparable stability in spite of their divergent electron affinities of 1.0, 1.45, and 1.80 eV, respectively. The ΔH_f° for the DDQ complex at 30° is significantly greater than ΔH_f° of the TCNE complex while their electron affinities are similar being 1.95 eV for DDQ and 1.80 eV for TCNE. These observations suggest the CT forces are not solely responsible for the stabilities of these complexes.

Perhaps an estimate of CT in the ground state of these complexes may be reflected in the f values of the absorption bands. The f values for the DTF and DDQ complexes are similar while the K_c and ΔH_f° values are distinctly different, suggesting that other forces besides CT forces have to be considered when describing the stabilities of these complexes.

Conclusion

The spectral and thermodynamic properties of these complexes do not subscribe to the view that these complexes in the ground state are held together mainly by CT forces.

(17) G. Scatchard, *Ann. N. Y. Acad. Sci.*, **51**, 660 (1949).

(18) K. Conrow, G. D. Johnson, and R. E. Bowen, *J. Amer. Chem. Soc.*, **86**, 1025 (1964).

Photoionization and Rydberg States of Tetraaminoethylenes in Organic Solutions

by Yoshihiro Nakato, Masaru Ozaki, and Hiroshi Tsubomura*

Department of Chemistry, Faculty of Engineering Science, Osaka University, Toyonaka, Osaka, Japan
(Received January 17, 1972)

Publication costs borne completely by The Journal of Physical Chemistry

Absorption and emission spectra and photoionization curves of tetrakis(dimethylamino)ethylene (TMAE) in some organic solvents have been measured. It has been found that the ionization thresholds for TMAE in *n*-pentane and benzene at 25° lie at about 4.20 ± 0.15 and 3.65 ± 0.15 eV, respectively, from which the energies of the excess electrons in these solvents are estimated to be slightly less than that of the free electron under vacuum. For TMAE in ether, an additional weak photocurrent has been observed in the lower energy region, probably attributable to spontaneous formation of solvated electrons from the Rydberg states of TMAE in ether. The Rydberg nature of the fluorescent state of TMAE, a conclusion which is consistent with the behavior of the first absorption band, has been deduced from the characteristic dependence of the fluorescence spectra on the solvent rigidity and polarity. The fluorescence spectrum of TMAE in benzene has been tentatively assigned to a transition from a charge-transfer state, where benzene molecules around TMAE act as electron acceptors.

Introduction

The photoelectron ejection from tetramethyl-*p*-phenylenediamine (TMPD) in rigid or fluid hydrocarbons occurs sometimes by the two-step, biphotonic processes with the lowest triplet state as the intermediate.¹⁻⁴ Cadogan and Albrecht determined the ionization threshold for TMPD in 3-methylpentane at 77°K, by monitoring the cation production spectroscopically, to be 5.9 eV,⁵ only a little lower than the gas phase, adiabatic ionization potential (≈ 6.20 eV).^{6,7} They also reported a weak, isotropic absorption from the triplet state extending from 380 to 470 nm and interpreted it as due to the transitions from the triplet state to the pseudo-Rydberg states.⁸ Very recently, the ionization thresholds of TMPD in fluid *n*-hexane and tetramethylsilane were reported to be about 4.5 eV or higher from photocurrent measurements by using monochromatic light.³

The photoionization phenomena of organic molecules in polar solvents are more complicated. Rather conflicting reports have been made by many investigators.⁹⁻¹⁵ Recently, Ottolenghi summarized these data and proposed a mechanism in which two-step, biphotonic processes take place with the "semi-ionized" state as the intermediate.¹⁵

Recent observation of transient photocurrents induced by laser illumination in several fluid silanes and hydrocarbons showed the appearance of photoejected electrons with relatively high mobilities, $0.02-93 \text{ cm}^2 \text{ V}^{-1} \text{ sec}^{-1}$.³ Similar results have been obtained by other techniques.¹⁶ The formation of mobile (or "dry") electrons as precursors of trapped or solvated electrons both in polar rigid matrices at 77°K and in

water at room temperature has also been proposed as a result of the radiolysis of these fluids or matrices.¹⁷

- (1) K. D. Cadogan and A. C. Albrecht, *J. Chem. Phys.*, **51**, 2710 (1969), and many papers cited there.
- (2) N. Yamamoto, Y. Nakato, and H. Tsubomura, *Bull. Chem. Soc. Jap.*, **39**, 2603 (1966); **40**, 451 (1967).
- (3) S. S. Takeda, N. E. Houser, and R. C. Jarnagin, *J. Chem. Phys.*, **54**, 3195 (1971), and papers cited there.
- (4) M. Tamir and M. Ottolenghi, *Chem. Phys. Lett.*, **6**, 369 (1970).
- (5) K. D. Cadogan and A. C. Albrecht, *J. Phys. Chem.*, **72**, 929 (1968).
- (6) M. Batley and L. E. Lyons, *Mol. Cryst.*, **3**, 357 (1968).
- (7) Y. Nakato, M. Ozaki, A. Egawa, and H. Tsubomura, *Chem. Phys. Lett.*, **9**, 615 (1971).
- (8) K. D. Cadogan and A. C. Albrecht, *J. Phys. Chem.*, **73**, 1868 (1969).
- (9) H. I. Joscheck and L. I. Grossweiner, *J. Amer. Chem. Soc.*, **88**, 3261 (1966).
- (10) C. Hélène, R. Santus, and P. Douzou, *Photochem. Photobiol.*, **5**, 127 (1966); R. Santus, A. Hélène, C. Hélène, and M. Potak, *J. Phys. Chem.*, **74**, 550 (1970).
- (11) For TMPD: (a) Y. Nakato, N. Yamamoto, and H. Tsubomura, *Bull. Chem. Soc. Jap.*, **40**, 2480 (1967); (b) T. Imura, N. Yamamoto, and H. Tsubomura, *ibid.*, **43**, 1670 (1970); (c) R. Potashnik, M. Ottolenghi, and R. Bensasson, *J. Phys. Chem.*, **73**, 1912 (1969); (d) J. T. Richards and J. K. Thomas, *Trans. Faraday Soc.*, **66**, 621 (1970).
- (12) For pyrene and perylene: (a) K. Kawai, N. Yamamoto, and H. Tsubomura, *Bull. Chem. Soc. Jap.*, **43**, 2266 (1970); (b) J. T. Richards, G. West, and J. K. Thomas, *J. Phys. Chem.*, **74**, 4137 (1970); (c) K. H. Grellmann, A. R. Watkins, and A. Weller, *J. Luminescence*, **1**, 2, 678 (1970); (d) R. Potashnik, Ph.D. Thesis, The Hebrew University of Jerusalem (1971); (e) K. H. Grellmann and A. R. Watkins, *Chem. Phys. Lett.*, **9**, 439 (1971).
- (13) For naphtholate anion: (a) M. Ottolenghi, *J. Amer. Chem. Soc.*, **85**, 3557 (1963); (b) C. R. Goldschmidt and G. Stein, *Chem. Phys. Lett.*, **6**, 299 (1970).
- (14) J. Jousset-Dubien and R. Lesclaux, *Israel J. Chem.*, **8**, 181 (1970).
- (15) M. Ottolenghi, *Chem. Phys. Lett.*, **12**, 339 (1971).
- (16) R. M. Minday, L. D. Schmidt, and H. T. Davis, *J. Chem. Phys.*, **54**, 3112 (1971), and papers cited there; Y. Maruyama, a private communication to the authors.

The study of the Rydberg states in relation with the ionization continua in amorphous media seems to be of growing importance, but still undeveloped at present.¹⁸ Recently, it was reported that the lowest Rydberg states of ethylene, acetylene, and benzene were observed in rare gas matrices at 20 or 40°K.^{19,20} The absorption bands corresponding to the transitions to these states showed appreciable blue shifts relative to those in the gas phase, and the results were interpreted in a similar way as those for the atomic impurities in rare gas solids.²¹ A new band appearing at 1612 Å in a benzene-krypton system at 40°K was also tentatively assigned to the transition to an $n = 3$ Wannier state of the benzene impurity, from which the ionization threshold was estimated to lie at about 7.75 eV,¹⁹ about 2.0 eV lower than the gas phase ionization potential. Similar blue shifts (or apparent disappearances) were observed for the absorption bands of alkyl-substituted ethylenes²² and other small organic compounds²³ in the form of thin films or organic glasses, and for some bands of organic molecules in inert gases at high pressures,^{22,24} and were attributed to the Rydberg nature of these bands. It was also reported that the large red shifts in the fluorescence spectra of alkylamines in polar solvents could be explained by the solvation of the Rydberg fluorescent states.²⁵

Recently, we found that tetrakis(dimethylamino)ethylene (TMAE) has remarkably low gas phase ionization potential of about 5.4 eV together with very low-lying Rydberg states.^{7,26} In this paper we are going to report and discuss the results of measurements of absorption and emission spectra and photoionization curves of TMAE in organic solutions.

Experimental Section

The preparation and handling of TMAE, which is highly reactive with atmospheric oxygen, were described previously.²⁶ *n*-Pentane, isopentane, and methylcyclohexane were purified in the same way as described previously.²⁶ Ether was purified by shaking with a 10% sodium bisulfite solution for 2 hr, then washed successively with 0.5% sodium hydroxide, dilute sulfuric acid, and saturated sodium chloride solutions, dried with calcium chloride, refluxed with sodium wire, and distilled through a Widmer column. Tetrahydrofuran was left overnight in contact with sodium wire, refluxed for several hours with new wire, and distilled through a Widmer column. Commercially available benzene was purified by shaking successively with concentrated sulfuric acid until free from coloring; it was then washed with water, dilute sodium hydroxide, and water, followed by drying with calcium chloride. The benzene was crystallized three times in ice-water bath; one-fourth was discarded each time as unfrozen liquid. It was then dried with sodium wire and distilled through a Widmer column. These solvents were further dried with sodium mirrors in ampoules

connected to a vacuum line just before use. The air contained in solvents was removed before TMAE was dissolved.

Absorption spectra were measured with a Cary Model 15 spectrophotometer. Emission spectra were measured with an Aminco-Bowman spectrofluorimeter. Steady-state photocurrents were measured as functions of photon energy. A 500-W xenon dc lamp and a Shimadzu grating monochromator (F 3.5) were used for the photoionization. The half-width of the monochromatized light was normally 10 or 5 nm. Toshiba glass filters were used in front of sample cells when required to remove higher order or scattered light. The spectral distribution of the light intensity at the cell position was determined by use of a photomultiplier coated with sodium salicylate thin film. A quartz sample cell with two platinum-plate electrodes (10 × 40 mm) held parallel to each other by tungsten wire-glass seals was used for the measurements of both photocurrents and absorption spectra, from which relative concentrations of TMAE were determined. The measurements of steady-state currents were made with a commercial picoammeter.

Results

Absorption and fluorescence spectra of TMAE in various solvents and in the gas phase are shown in Figure 1. It should be noted that the absorption spectra in MP, ether, and tetrahydrofuran (THF) are almost identical with each other though the spectrum in THF is not included in Figure 1 to avoid complication. Here, MP is a mixed solvent consisting of methylcyclohexane and isopentane in a volume ratio of 1:1. The shoulder of the gas absorption spectrum at about

(17) (a) From studies on electron and hole scavenging reactions: W. H. Hamill and his collaborators, *J. Phys. Chem.*, **73**, 1341, 2750 (1969); **74**, 2885, 3914 (1970); *Trans. Faraday Soc.*, **66**, 2533 (1970); B. L. Bales and L. Kevan, *J. Phys. Chem.*, **74**, 1098 (1970); S. Arai, A. Kira, and M. Imamura, *ibid.*, **74**, 2102 (1970); (b) from picosecond pulse radiolysis studies: M. J. Bronskill, R. K. Wolff, and J. W. Hunt, *J. Chem. Phys.*, **53**, 4201, 4211 (1970); (c) from studies on a recombination luminescence: H. B. Steen, *J. Phys. Chem.*, **74**, 4059 (1970).

(18) Theoretical consideration on the Wannier exciton states in dense media: S. A. Rice and J. Jortner, *J. Chem. Phys.*, **44**, 4470 (1966).

(19) B. Katz, M. Brith, A. Ron, B. Sharf, and J. Jortner, *Chem. Phys. Lett.*, **2**, 189 (1968).

(20) B. Katz and J. Jortner, *ibid.*, **2**, 439 (1968).

(21) G. Baldini, *Phys. Rev.*, **137**, A508 (1965). See also J.-Y. Roncin, N. Damany, and J. Romand, *J. Mol. Spectrosc.*, **22**, 154 (1967).

(22) A. J. Merer and R. S. Mulliken, *Chem. Rev.*, **69**, 639 (1969) and papers cited there; F. H. Watson, Jr., and S. P. McGlynn, *Theoret. Chim. Acta (Berl.)*, **21**, 309 (1971).

(23) M. B. Robin, H. Basch, N. A. Kuebler, *J. Chem. Phys.*, **51**, 45 (1969); H. Basch, M. B. Robin, and N. A. Kuebler, *ibid.*, **51**, 52 (1969); **49**, 5007 (1968).

(24) M. B. Robin and N. A. Kuebler, *J. Mol. Spectrosc.*, **33**, 274 (1970), and papers cited there.

(25) Y. Muto, Y. Nakato, and H. Tsubomura, *Chem. Phys. Lett.*, **9**, 597 (1971).

(26) Y. Nakato, M. Ozaki, and H. Tsubomura, *Bull. Chem. Soc. Jap.*, **45**, 1299 (1972).

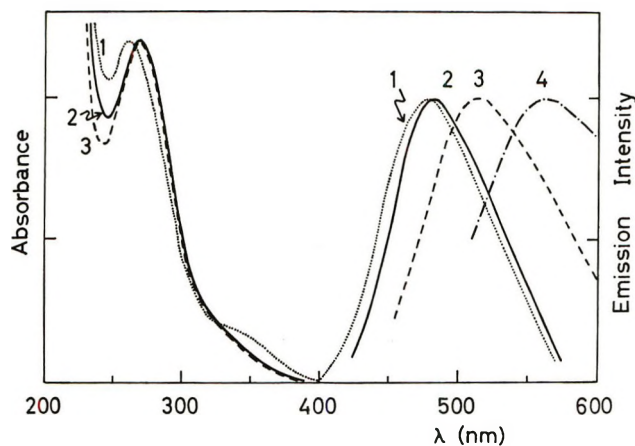


Figure 1. Absorption and fluorescence spectra of TMAE; curve 1 for the vapor, curve 2 for the MP solution, curve 3 for the ether solution, and curve 4 for the THF solution. Fluorescence intensities are normalized at the fluorescence peaks (see text) and are corrected for the spectral sensitivity curve of the photomultiplier used. Excitation wavelengths range from 390 to 250 nm, on which the positions and shapes of fluorescence spectra do not depend.

350 nm seems to be blue-shifted in the solution spectrum. The absorption spectra in the gas phase and in the MP solution have been already reported and discussed in a previous paper.²⁶

The fluorescence spectrum in the gas phase shows a maximum at 477 nm and is rather strong. The fluorescence spectrum in the MP solution is also fairly intense and shows slight red shift relative to that in the gas phase. In polar solvents, however, the fluorescence spectra show large red shift (λ_{\max} 486 nm (MP), 514 (ether), and 564 (THF)) and remarkable decrease in emission intensity (the relative fluorescence intensities in MP, ether, and THF are roughly 1.00:0.2–0.1:0.05–0.01, respectively). These tendencies become stronger with growing solvent polarity. The fluorescence spectra of TMAE reported in papers on the chemiluminescent reaction of TMAE with oxygen^{27,28} show relatively good agreement with the present data.

Temperature effects on the absorption and fluorescence spectra of TMAE in the MP solution are shown in Figure 2. The first absorption band shown as a shoulder at room temperature is blue-shifted and very much weakened in the MP rigid glass at 77°K. The fluorescence spectrum at 77°K shows large blue shift (λ_{\max} at 77°K is 441 nm) relative to that at room temperature, the intensity being nearly the same.

Absorption and fluorescence spectra of TMAE in benzene at room temperature are shown in Figure 3, together with those in MP. The absorption spectrum in benzene has a definite swelling in the region of 290 to 350 nm, compared with that in MP. The fluorescence spectrum in benzene (λ_{\max} 424 nm) shows remarkable blue shift relative to that in MP or in the gas phase. The fluorescence intensity in benzene is somewhat weaker than that in MP.

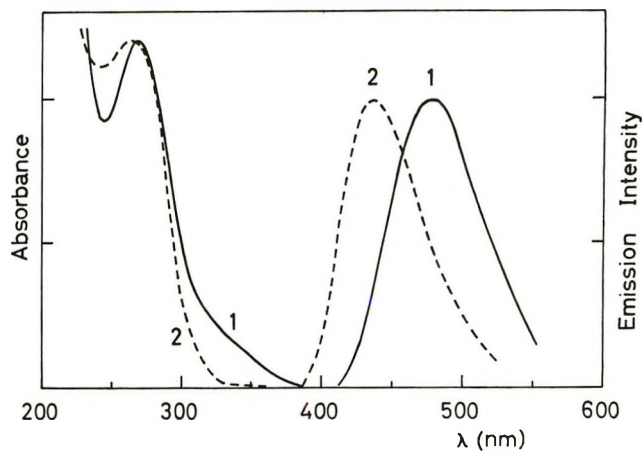


Figure 2. Temperature effects on the absorption and fluorescence spectra of TMAE; curve 1 for the MP solution at room temperature and curve 2 for the same at 77°K. Spectra are illustrated in the same way as in Figure 1.

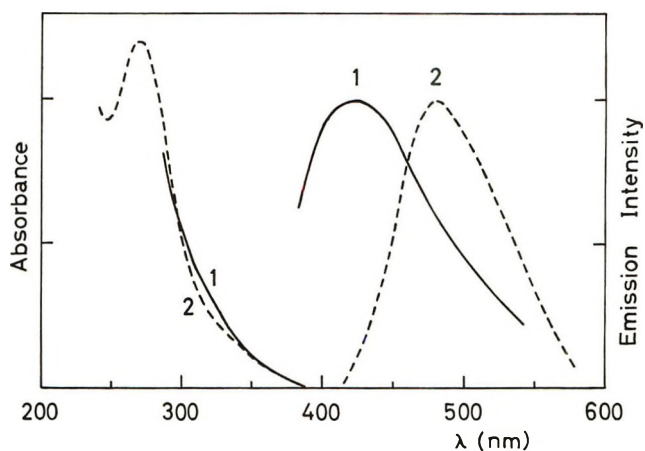


Figure 3. Absorption and fluorescence spectra of TMAE; curve 1 for the benzene solution at room temperature and curve 2 for the MP solution at room temperature. Spectra are illustrated in the same way as in Figure 1.

Photocurrents for TMAE measured with steady illumination both in *n*-pentane and in ether are shown as functions of photon energy in Figure 4,²⁹ where the ordinate shows photocurrents divided by the intensity of illumination. As the photocurrent for TMAE in *n*-pentane increases with the photon energy rather gradually, it is difficult to determine the photocurrent threshold accurately. The photocurrent threshold for TMAE as determined from the present result is 4.20 ± 0.15 eV in *n*-pentane at 25°.³⁰

(27) A. N. Flechter and C. A. Heller, *J. Phys. Chem.*, **71**, 1507 (1967); N. Wiberg, *Angew. Chem.*, **80**, 809 (1968).

(28) M. Hori, K. Kimura, and H. Tsubomura, *Spectrochim. Acta, Part A*, **24**, 1397 (1968).

(29) In the wavelength region shorter than that shown in Figure 4, the intensity of the xenon lamp used as the light source is so weak that the effect of scattered light of the monochromator becomes serious. An uncorrected photoionization curve was obtained, showing a peak at about 45 kK, which is, however, a little dubious.

(30) Strictly speaking, this should be regarded as an upper limit for the ionization threshold; also see ref 32.

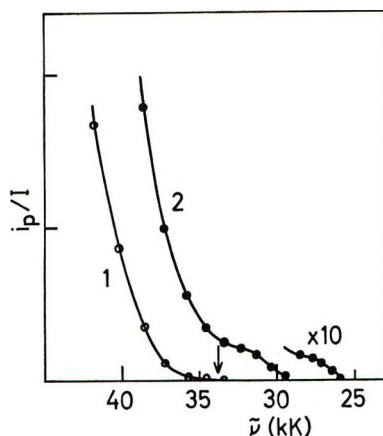


Figure 4. Photoionization curves of TMAE in solutions; curve 1 for the *n*-pentane solution and curve 2 for the ether solution. I and i_p are the light intensity for excitation and the photocurrent, respectively. The photocurrent observed at the threshold, indicated by an arrow for the *n*-pentane solution, is about 2×10^{-13} A. Experimental points are denoted by circles. The half-width of light for the excitation is 10 nm. The electric field applied is *ca.* 400 V/cm.

The photoionization curve for TMAE in ether at 25° shows considerable red-shift compared with that in *n*-pentane. It is to be noted that much larger photocurrents are observed in ether than in *n*-pentane; *e.g.*, the ratio of the photocurrent observed in ether to that in *n*-pentane at 270 nm is about 1000 in the same experimental condition.

It should be mentioned that the photocurrent values shown in Figure 4 involve the effect of the recombination processes of charge carriers.

The photocurrent for TMAE in benzene has also been measured. The ionization threshold at 25° is determined to be 3.65 ± 0.15 eV from the present work. The photocurrent observed at this threshold is about 2×10^{-13} A.

Discussion

Ionization Thresholds in Nonpolar Solvents. The potential energy for an electron ejected from a solute molecule into a nonpolar solvent can be set as

$$V(r) = -e^2/\epsilon r + V_s \quad (1)$$

where r is the distance between the electron and the center of the parent cation, ϵ is the high-frequency dielectric constant of the solvent, and V_s is the potential energy of the electron due to the randomly oriented solvent. In the region where r is very large

$$V(r) = V_s \quad (2)$$

The ionization threshold for a solute molecule, M, in a solution, $I_s(M)$, might be defined as the excitation energy from the ground state of M to the bottom of the "ionization continuum."³¹ Let us designate the energy of the electron lying at the bottom of the ionization continuum³¹ with respect to that of a free electron

at rest under vacuum as $E_s^\circ(e)$. $I_s(M)$ can be related with the gas phase ionization potential of M, $I_g(M)$, as (Figure 5)

$$I_s(M) = I_g(M) + S(M) - S(M^+) + E_s^\circ(e) \quad (3)$$

where $S(M)$ is a solvation energy for M due to electronic polarization of the solvent and $S(M^+)$ that for the cation, M^+ . There are "Rydberg" states or "Wannier-type exciton" states below the ionization continuum in the solution, which are the states of the cation-electron pair bound loosely by the Coulomb potential, $-e^2/\epsilon r$. Only the lowest Rydberg state is indicated in Figure 5.

The photocurrent in nonpolar solutions should rise up where the photon energy exceeds the energy difference from the ground state to the ionization continuum. The ionization threshold, $I_s(M)$, can, therefore, be determined experimentally from the threshold of the photocurrent.³²

Free charge carriers might be formed in some cases by autoionization from discrete states lying above the ionization threshold to which the solute is first excited. For TMAE in *n*-pentane, the photocurrent can be observed from *ca.* 295 nm, and the photoionization curve has no correlation with the absorption band observed at 270 nm in the same solution, as seen from Figure 1 and 4. If the autoionization were to occur from the excited state corresponding to the 270-nm band, some swelling should be found in the photoionization curve at around 270 nm. Therefore, the photocurrent for TMAE in *n*-pentane in this region seems to be due to the direct transition from the ground state of TMAE to the ionization continuum.³³

The rather gradual increase of the photoionization yield curve for TMAE in *n*-pentane can be attributed to two factors. One is the change of the molecular shape upon ionization, as frequently observed for the ionization of amines and olefins as well as TMAE in the gas phase.²⁶ There is another factor especially in solutions. When a photoejected electron is thermalized at a distance, say, r_0 from the parent cation, the probability that the electron becomes free from the Coulomb potential of the parent cation is given by $\exp(-r_c/r_0)$, where r_c is the critical distance defined by

(31) The electrons in the bottoms of the ionization continua in nonpolar solvents such as *n*-pentane at room temperature seem to correspond to the relatively high mobility electron reported,^{3,16} probably being in thermal equilibria with the solvents.

(32) While the photoejected electron migrates away from the parent cation, it is frequently scattered by solvent molecules and loses part of its kinetic energy. This process decreases the yield of the current carriers. Therefore, precise determination of the true (or adiabatic) ionization threshold is rather difficult. L. Onsager, *Phys. Rev.*, **54**, 554 (1938); A. Mozumder and J. L. Magee, *J. Chem. Phys.*, **47**, 939 (1967); A. Mozumder, *ibid.*, **48**, 1659 (1968).

(33) This interpretation is supported by the fact that the photoionization curve for 1,1',3,3'-tetramethyl- $\Delta^{2,2'}$ -bi(imidazolidine) (TMBI) in *n*-pentane is almost the same as that for TMAE in *n*-pentane (an unpublished result), although the absorption spectrum of TMBI is very much different from that of TMAE. The ionization potential of TMBI is nearly equal to that of TMAE (see ref 26).

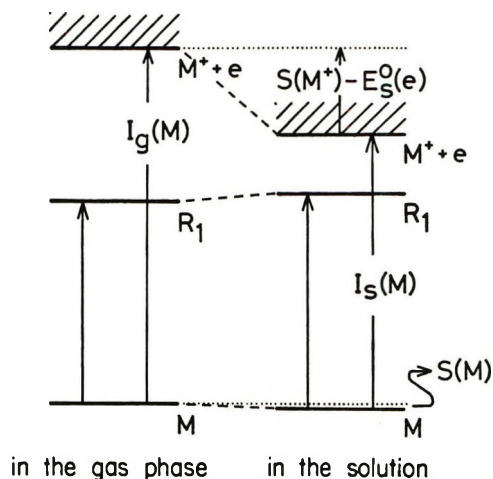


Figure 5. The energy level diagram showing the ionization continua and the lowest Rydberg states of TMAE in the gas phase (left) and in the nonpolar solution (right). Here, M, R₁, and M⁺ are the ground state, the first Rydberg state, and the cation of TMAE, respectively.

$e^2/\epsilon r_c = (3/2)kT$.³² The higher the photon energy, the larger becomes the mean value of r_0 and so the photocurrent yield. Therefore, the photoionization curve increases gradually with the photon energy after crossing the ionization threshold.

It is of great interest to note that $E_s^o(e)$, the ground state energy of the excess electron in *n*-pentane, can be estimated from our experimental values by using eq 3. Taking 5.4 eV for I_g ^{7,26} and 4.2 eV for I_s , from the present result, and also estimating $S(\text{TMAE})$ to be 0.1 eV from heats of solutions of amino compounds and $S(\text{TMAE}^+)$ to be 1.1 eV by applying the Born equation, where TMAE^+ is assumed to be a sphere of radius 3 Å, then we obtain $E_s^o(e) \approx -0.2$ eV. Similarly, the value of $E_s^o(e)$ in benzene can be estimated to be about -0.5 eV by using 3.65 eV as I_s for TMAE in benzene. As discussed later, $E_s^o(e)$ in ether prior to dipole relaxation also seems to be nearly equal to that in *n*-pentane.

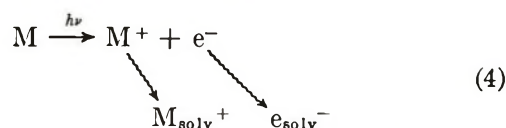
Although there are some reports on the electron mobility in organic media,^{3,16} there have been no studies on another important quantity, the ground state energy of the excess electron in such media, $E_s^o(e)$. The present result is, to our knowledge, the first of the direct experimental derivation of such a quantity.³⁴ The values of $E_s^o(e)$ obtained might be qualitatively interpreted as follows. It is thought that the excess electron in *n*-pentane spends most part of its time in narrow vacant spaces between *n*-pentane molecules, based on the large, negative electron affinity of *n*-pentane. The electron will, therefore, have large kinetic energy in *n*-pentane, as an electron in a small box has, which is compensated by long-range polarization energy for the electron. Thus, $E_s^o(e)$ takes a small, negative value. Similar interpretation might be possible even for ether.

Benzene, unlike *n*-pentane, has lower vacant orbitals or, in other words, a small, negative electron affinity. It is also reported that benzene acts as an electron-trap in alkanes.³⁵ The physical nature of the excess electron in benzene may, therefore, be appropriately represented as a benzene anion whose site is moving from a benzene molecule to another. If this is true, $E_s^o(e)$ is approximated as $-EA(\text{B}) - S(\text{B}^-)$, where $EA(\text{B})$ is the vertical electron affinity of benzene and $S(\text{B}^-)$ the solvation energy for the benzene anion due to the electronic polarization of benzene. Assuming $EA(\text{B})$ to be from -1.0 to -1.5 eV,³⁶ and estimating $S(\text{B}^-)$ to be 1.6 eV by use of the Born equation, we get $E_s^o(e) \approx -0.1$ to -0.6 eV, which agrees roughly with the observed value.

Ionization Thresholds in Polar Solvents. When charged species are generated in polar solvents, orientational polarization follows immediately. The potential energy for the charged species, therefore, becomes a function of time, whose time constant is of the order of rotational motions of solvent molecules.³⁷ As the electronic excitation processes are much faster than such rotational motions, the excitation energies to the ionization threshold and the Rydberg states in polar solutions are regarded to be essentially the same as those in nonpolar solutions.

The photoionization curve of TMAE in ether can be divided into two parts from the inspection of Figure 4: (a) a steeply rising part in the region higher than 34 kK, and (b) a shoulder in the lower energy region (34–25 kK). These two parts can be tentatively interpreted as follows: part a, due to the direct transition to the ionization continuum and part b due to the spontaneous formation of solvated electrons from the Rydberg states of TMAE.

According to this interpretation, the photoejection process in part a can be described as



Here, e^- means a mobile, not solvated electron in the ionization continuum in ether and e_{solv}^- the solvated electron free from the parent cation. The photocur-

(34) For rare gas liquids, the experimental and theoretical studies were reported: B. E. Springett, J. Jortner, and M. H. Cohen, *J. Chem. Phys.*, **48**, 2720 (1968), and papers cited there.

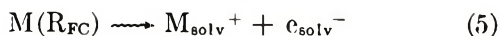
(35) K. Yoshinaga, N. Yamamoto, and H. Tsubomura, *J. Luminescence*, **4**, 417 (1971); also see, for example, S. Khorana and W. H. Hamill, *J. Phys. Chem.*, **74**, 2885 (1970).

(36) The electron affinity of benzene was reported to be about -1.50 eV by theoretical calculations and by an electron scattering method. From the kinetics of electrode processes, -0.54 and -0.36 eV were also reported: J. B. Birks, "Photophysics of Aromatic Molecules," Wiley-Interscience, London, 1970, p 462.

(37) The formation time of a hydrated electron in aqueous solutions at room temperature was reported to be $\lesssim 10^{-11}$ sec from the picosecond pulse radiolysis studies.^{17b}

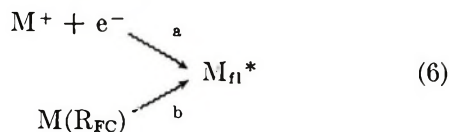
rent threshold in part a should correspond to the bottom of the ionization continuum of TMAE in ether in the Franck–Condon state, lying at around 34 kK, nearly equal to that in *n*-pentane.³⁸ It can, therefore, be deduced that $E_s^0(e)$ in ether is also nearly equal to that in *n*-pentane, because $S(M^+)$ in ether and in *n*-pentane should be nearly equal to each other before relaxation.

The process of spontaneous formation of solvated electrons (free from the parent cations) from the Rydberg states can be described as



where $M(R_{FC})$ indicates molecule M in the Franck–Condon, Rydberg state. Process 5 includes trapping and solvation of the Rydberg electron whose orbital extends over solvent molecules, accompanied by their orientational motions. The energy required for the separation of the cation and electron is compensated by the solvation energies for them. Such a process is expected only in polar solutions and is interesting from the viewpoint of additional lowering of the ionization energies in polar solvents, though the yield is not so large compared with that due to the direct transition to the ionization continuum.

It is to be noted here that the fluorescence excitation spectrum was found to extend up to higher energy regions, even beyond the ionization threshold for TMAE in ether (also in *n*-pentane and THF).³⁹ This suggests the presence of two other processes



where M_{fl}^* indicates molecule M in the fluorescent state, or the solvated lowest Rydberg state retaining fairly large valence shell character, as will be discussed later. Process 6a means that the electron excited to the ionization continuum is scattered by solvent molecules and thermally relaxes to the lowest Rydberg state. The Franck–Condon, Rydberg states, $M(R_{FC})$, especially the higher ones, can be regarded as cation–electron pairs, largely separated and only loosely bound by the Coulomb potential. Thus, processes 6a and b can both be regarded as the recombination processes.

The rate of solvation process of the ejected electron was reported to be so high ($\gtrsim 10^{11} \text{ sec}^{-1}$),³⁷ that processes 4 and 5 are regarded to have rate constants high enough to compete with the alternative relaxation processes 6a and b. Thus, we conclude that the molecules excited to the ionization continuum or to the Rydberg states partly form free charge carriers (the solvated cations and electrons) and partly form the fluorescent state.

One might propose the alternative path *via* the fluorescent state as the ionization process in polar solvents



This process seems to be possible from the energetic viewpoint, since the energies of the solvated ionized state ($M_{solv}^+ + e_{solv}^-$) and the fluorescent state are roughly estimated to be nearly equal to each other in ether. But, if this process would be the main process, the photoionization curve in ether (Figure 4) should be parallel to the absorption spectrum (Figure 1), at least in the region from 25 to 33 kK, as is the case for the fluorescence excitation spectrum, in contradiction with the experimental results. It can, therefore, be concluded that process 7 is not the main process, especially for the ionization from the higher Rydberg states.

Solvent Effects on the Lowest Rydberg State. The first absorption band of TMAE shown as a shoulder at 350 nm has been assigned previously²⁶ to the transition to the lowest Rydberg state, mainly from the blue shift of the absorption bands in solutions relative to that in the gas phase. The fluorescence spectrum of TMAE described in this paper can be concluded to originate from this lowest Rydberg state, based on the wavelength correlation between the first absorption band and fluorescence spectrum in the gas phase. It must be mentioned that such a lowest Rydberg state should be regarded as a state of “mixed valence shell–Rydberg character,” strongly affected by the core structure, as seen from the large quantum defect δ of 0.7 and from the relatively small size of the Rydberg orbital ($r_{max} = 2.9 \text{ \AA}$) reported previously.²⁶

The blue shift of the first absorption bands in solutions relative to that in the gas phase shows that the energies of the Franck–Condon, Rydberg states in solutions are higher than that in the gas phase, as shown in Figure 5. This blue shift might be caused by repulsive interactions between the electron in the Rydberg orbital and the solvent molecules,⁴⁰ as mentioned qualitatively before. The more drastic change of the first absorption band in the MP rigid glass at 77°K compared with that in MP at room temperature is attributed to the increase of the density of the solvent MP at 77°K relative to that at room temperature.

(38) The apparent red shift of the steep part of the photoionization curve in ether compared with that in *n*-pentane is mostly due to the very high photoionization yield in ether, as mentioned in the previous section.

(39) According to preliminary experimental results, no correspondence between the fluorescence excitation spectrum and the absorption band at 270 nm was observed both in the gas phase and in these solutions, showing absence of relaxation processes from the excited state at 270 nm to the fluorescent state.

(40) The detailed nature seems to be very complicated. Deformation of the Rydberg orbital and also configurational mixings between the Rydberg configuration and the charge-transfer-to-solvent configurations as well as the configurations in which the solvent molecule is excited must be taken into account. Here arises a question why the lowest Rydberg band is blue-shifted, just opposite to the red shift of the ionization continuum, as shown in Figure 5. This seems to be explainable roughly by taking account of the decrease of the long-range polarization energy for the Rydberg states compared with the infinitely separated electron–cation pair (the ionized state).

The behavior of fluorescence spectra in solution can be explained as follows. In the nonpolar solution at room temperature, it seems that the relaxation process of the solvent from the Franck-Condon state to the equilibrium fluorescent state leads to the expansion of the cavity within which the molecule in the Rydberg state is situated, so as to lower the repulsion between the solvent molecules and the electron in the Rydberg orbital. Thus, the fluorescence spectrum in the nonpolar solution at room temperature appears in almost the same region of wavelength as that in the gas phase. As such a relaxation process of the solvent is restricted in the rigid glass at 77°K, the fluorescence spectrum at 77°K is predicted to be at shorter wavelengths than the gas phase spectrum, in agreement with the observation.⁴¹

Another interesting feature is the large red shift of fluorescence spectrum as the solvent becomes more polar. This is explained in terms of large stabilization due to the solvation of TMAE in the lowest Rydberg state, accompanied by the orientation of the solvents around the emitting molecule. A similar large red shift has already been reported for the fluorescence of aliphatic amines in polar solvents and explained in the same way.²⁵ It is to be noted that this "solvated Rydberg state" may be close to the "semi-ionized state" proposed as a photoactive intermediate in polar solvents by Ottolenghi.^{11c,15}

Benzene Solutions of TMAE. The result that the fluorescence spectrum of TMAE in benzene is apparently blue-shifted from that in the gas phase does not seem to be consistent with the reasonings made above. The absorption spectrum of this system shows a definite swelling around 320 nm that is not found in the spectra for other solvents. We tentatively interpret these abnormalities for benzene as being caused by a CT interaction between TMAE as a donor and benzene as an acceptor. The contact CT absorption bands between TMAE and aromatic hydrocarbons such as pyrene, anthracene, and perylene were observed at around 2.5 eV.⁴² Since the difference of electron affinities between benzene and these aromatic hydrocarbons is estimated to be about 1.0–2.0 eV,^{36,43} the contact CT absorption band between TMAE and benzene can be predicted to be at around 3.5 to 4.5 eV (or 350 to 280 nm), in good agreement with the position of the swell appearing in the absorption spectrum. The fluorescence spectrum seems to correspond well with this swelling.

Based on the CT interaction mentioned above, schematic potential energy curves for TMAE in contact with a benzene molecule are shown in Figure 6. The potential energy for the $M \cdots B$ pair arises from the normal van der Waals force and the exchange repulsion force. For the $R_1 \cdots B$ pair with the effective size of R_1 much larger than that of M , the repulsive exchange energy⁴⁰ sets in at distances larger than that

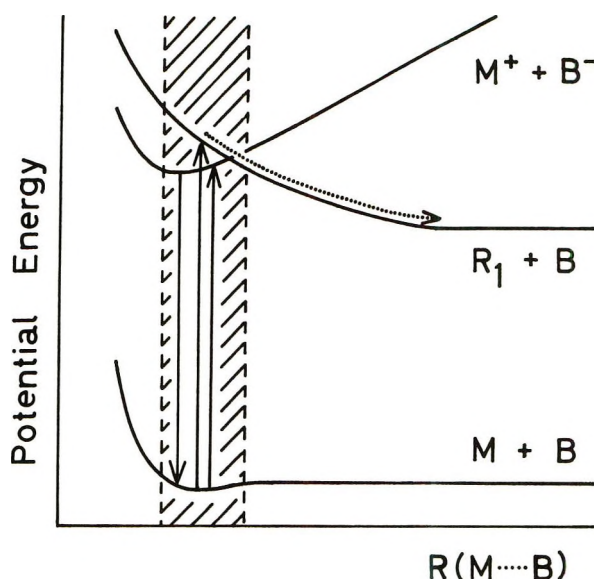


Figure 6. Schematic potential energy curves for TMAE in benzene as a simple two-body problem. Here, M , R_1 , and M^+ are the ground state, the first Rydberg state, and the cation of TMAE, respectively. B is the ground state of benzene and B^- the benzene anion. $R(M \cdots B)$ means the distance between the TMAE and the nearest benzene molecule. The range of $R(M \cdots B)$ expected in the benzene solution of TMAE is indicated by hatching.

for the $M \cdots B$ pair, as shown in Figure 6. In the MP solution, the potential energy curve for TMAE in the Rydberg state in contact with the solvent molecule is thought to be similar to the $R_1 \cdots B$ curve, and it explains the blue shift of the first absorption band compared with the gas phase spectrum. On excitation, the relaxation process of the solvent schematically shown by an arrow with a dotted line in Figure 6 takes place and, as the result, the fluorescence spectrum in MP does not shift appreciably from that in the gas phase. In the benzene solution, however, the CT configuration ($M^+ \cdots B^-$) will play an important role at small distances, whose potential curve probably crosses that for ($R_1 \cdots B$). Thus, a potential minimum is expected to exist in the excited state. In the region of proper ($M \cdots B$) distances, indicated by hatching in Figure 6, excited TMAE will fall into the potential

(41) The first absorption band observed as a shoulder at 350 nm in the gas phase is drastically changed in the MP matrix at 77°K, in which only a tail down to ca. 370 nm is observed, probably assigned to the transition to the first Rydberg state. On the basis of the fairly good correlation between this tail and the fluorescence spectrum in the same matrix, it can be concluded that this fluorescence also originates from the lowest Rydberg state.

(42) P. R. Hammond and R. H. Knipe, *J. Amer. Chem. Soc.*, **89**, 6063 (1967).

(43) The adiabatic electron affinities of anthracene and pyrene were reported to be 0.42 or 0.552 and 0.39 or 0.579 eV, respectively, by an equilibrium electron capture method. R. S. Becker and E. Chen, *J. Chem. Phys.*, **45**, 2403 (1966); also see ref 36. Strictly speaking, the vertical electron affinities should be used for CT absorption bands. Unfortunately, such data are unavailable at present.

minimum, from which the fluorescence is emitted. If the potential minimum is higher than the energy of separated states ($R_1 + B$), the apparent blue shift of the fluorescence is to be observed. Although the establishment of the above interpretation needs further work, this TMAE-benzene system seems to offer an interesting example for the study on the relation between the

Rydberg state in the solution and the contact CT (or CT to solvent) state.⁴⁴

(44) NOTE ADDED IN PROOF. After the manuscript was sent to the journal, we were informed that Holroyd and Allen studied the photoelectron ejection from metal surfaces into nonpolar liquids and determined the energies of the excess electrons. The value in *n*-pentane, for instance, -0.01 eV, is rather close to our present one. R. A. Holroyd and M. Allen, *J. Chem. Phys.*, **54**, 5014 (1971).

Infrared Spectra and Dipole Moments of Hydrogen-Bonded Complexes. III.

Adducts of 2,6-Dichloro-4-nitrophenol with Pyridine Bases

by J. P. Hawranek,* J. Oszust, and L. Sobczyk

Institute of Chemistry, University of Wrocław, Wrocław, Poland (Received December 6, 1971)

Publication costs borne completely by The Journal of Physical Chemistry

Stability constants, ir spectra, and dipole moments of hydrogen-bonded complexes of 2,6-dichloro-4-nitrophenol with various pyridine bases in CCl_4 were determined at 25°. The contribution of proton transfer to the enhancement of dipole moment along the hydrogen bonding and the intensity of the OH stretching vibration band is discussed.

In previous parts of this series^{1,2} the stability constants, integrated intensities, and other spectral features of the stretching vibration of the proton-donor group, as well as dipole moments of weak hydrogen-bonded complexes formed by diphenylamine and 2,4,6-trimethylphenol with various bases mainly pyridine derivatives, were studied. From the dipole moment measurements the polarity of the hydrogen bonding in these complexes could be evaluated

$$\Delta\vec{\mu} = \vec{\mu}_{AD} - \vec{\mu}_A - \vec{\mu}_D \quad (1)$$

where A, D, and AD denote the acceptor (B), donor (AH), and hydrogen-bonded complex (AH...B), respectively; $\Delta\vec{\mu}$ is the excess dipole moment along the AH...B axis resulting from the hydrogen-bond formation. The analysis of the results obtained led to the conclusion that the enhancement of the dipole moment along the AH...B bond in "weak" hydrogen bonds, 0.2–0.5 D, originates mainly from the electrostatic inductive effect, resulting in the $A^-—H^+...B$ structure.^{1,2} Also literature data on ir intensities¹ and polarities² of weak hydrogen bonds were summarized.

In stronger hydrogen bonds, besides the electrostatic inductive contribution, additional effects are of importance: the charge-transfer (delocalization) effect corresponding to the $A^-—H...B^+$ structure, and the

proton-transfer process leading to the tautomeric equilibrium $AH...B \rightleftharpoons A^-...H—B^+$.

The aim of this work was to determine the polarity of the hydrogen bonding in complexes formed by 2,6-dichloro-4-nitrophenol with a series of pyridine derivatives of varying basicity. As these complexes are stronger than those of diphenylamine and mesitol, it was expected to obtain some information about the role of the mentioned effects in hydrogen-bonded systems. Symmetric pyridine derivatives were chosen to avoid arbitrariness during the calculation of $\Delta\vec{\mu}$. As the equilibrium constants and dipole moments are solvent dependent, a systematic study under identical experimental conditions was undertaken.

Experimental Section

The experimental conditions during the estimation of stability constants and dipole moments of the hydrogen-bonded adducts were the same as previously described.^{1,2} The equilibrium constants were determined by measuring the maximum intensity of the absorption band of the stretching vibration of the "free" OH group of the donor, in solutions containing the

(1) J. P. Hawranek and L. Sobczyk, *Acta Phys. Polon., Sect. A*, **39**, 639 (1971).

(2) J. P. Hawranek and L. Sobczyk, *ibid.*, *Sect. A*, **39**, 651 (1971).

Table I: Stability Constants and Ir Spectral Data of 2,6-Dichloro-4-nitrophenol Complexes

Proton acceptor	$pK_a(B)$	K , l. mol ⁻¹	$\nu_s(\text{OH})$, cm ⁻¹	$\Delta\nu$, cm ⁻¹	$2b$, cm ⁻¹	$B \times 10^{-4}$, l. mol ⁻¹ cm ⁻²	B/B^0	ϵ , l. mol ⁻¹ cm ⁻¹
2,4,6-Collidine	7.52	546 ± 8	2400	1200				60
4-Picoline	6.00	315 ± 7	2550	1050	900	34.1	16.3	105
Pyridine	5.19	163 ± 2	2650	950	800	31.9	15.3	110
3-Chloropyridine	2.84	33.3 ± 0.3	2920	680	740	31.2	14.9	116
3,5-Dichloro- pyridine	0.49	8.1 ± 0.4	3000	600	640	27.5	13.2	119
2,6-Dichloro-4- nitrophenol			3500	0	26.0	2.09	1	226

donor and acceptor in CCl₄. The measurements were carried out on a Unicam SP-700 spectrophotometer in the Central Laboratory of the Chemical Faculty, Technical University of Wrocław. The temperature was maintained constant at 25 ± 0.2°. The spectral slit width of the instrument was exactly known (2–3 cm⁻¹). The peak height was corrected for the slit distortion using Ramsay's tables.³ The absolute intensity of this band was calculated using Ramsay's method of direct integration.³ The intensity and other ir data of the corresponding absorption band of the "bound" OH group were determined on a Perkin-Elmer Model 621 ir spectrophotometer. As these bands are extremely broad, the correction for the slit distortion is negligible in this case. Assuming a Lorentz profile of each side of the band, with different widths b_l and b_r of the "left" and "right" part of the band, respectively, the absolute intensity is given by

$$A = \frac{\pi}{2}(b_l + b_r) \ln \left(\frac{I_0}{I} \right)_{\max} \quad (2)$$

where $(b_l + b_r)$ is the total width of the band at half-intensity. As the true band shapes are not of the "pure" Cauchy (Lorentz) form,¹ this assumption will lead to a systematic error (overestimation), which, however, will be less than the experimental uncertainty in our case.

No mathematical separation of the absorption bands of the "free" and "bonded" OH group was necessary, as the hydrogen bonding in 2,6-dichloro-4-nitrophenol complexes is relatively strong and the spectral shift is considerable.

The dipole moments of the compounds and complexes were determined by measuring the density and electric permittivity of CCl₄ solutions at 25 ± 0.05°. The solvent (CCl₄) and acceptors were purified by standard methods, dried, and stored over molecular sieves. 2,6-Dichloro-4-nitrophenol (Fluka, pure) was crystallized twice from ethanol and stored in a vacuum desiccator over anhydrous MgSO₄.

Results

The $\nu_s(\text{OH})$ absorption band of the proton donor obeys the Lambert-Beer law; the measurements were

carried out in the concentration range 7×10^{-4} to 3×10^{-3} M. The molar extinction coefficient equals 226 ± 5 l. mol⁻¹ cm⁻². No self-association of the donor was detected.

During the estimation of equilibrium constants of the formation of the complexes, initial concentrations of 1×10^{-3} to 6×10^{-3} M of the donor were used. The acceptors were taken in a 2- to 20-fold excess; as a reference, a solution of the acceptor at the same concentration was used. The stability constants (with mean-square errors of six to seven measurements) of the 2,6-dichloro-4-nitrophenol complexes are given in Table I. The positions, widths, and intensities of the absorption bands of the bonded OH group could be measured only approximately. The bands are very broad, hence the location of the maximum is arbitrary. The $\nu_s(\text{OH})$, $2b$, and $\Delta\nu$ values of these bands are given with an error of ±30 cm⁻¹. The bands are asymmetric, the half-width of the low-frequency side of the band being greater than that of the high-frequency side. This asymmetry increases with the strength of the hydrogen bonding, so that in case of the 2,4,6-collidine complex on the low-frequency side of the peak a continuous absorption begins, and even a rough evaluation of the intensity is impossible.

The dipole moment of 2,6-dichloro-4-nitrophenol was determined from a series of seven measurements in the concentration range 0.001–0.003 (mole fraction); no self-association phenomena were observed. A value of 3.18 ± 0.01 D was obtained, with Hedstrand's constants^{2,4} $\alpha\epsilon_1 = 13.66$ and $\beta = 0.1661$. The molar polarization at infinite dilution, $P_{2\infty}$, is equal to 256.2 cm³. The sum of electronic and atomic polarizations was replaced by the refraction for the sodium D line, calculated from bond refraction data⁴ (47.04 cm³).

The dipole moments of each of the 1:1 complexes were determined by measuring the electric permittivity and density of solutions of known initial concentrations of the donor and acceptor. Using the spectroscopically determined stability constant (Table I), the equilibrium concentrations of the complex (as well as of the donor

(3) D. A. Ramsay, *J. Amer. Chem. Soc.*, **74**, 72 (1952).

(4) J. W. Smith, "Electric Dipole Moments," Butterworths, London, 1955.

Table II: Dipole Moments of Polarity of the Hydrogen Bonding in 2,6-Dichloro-4-nitrophenol Complexes

Proton acceptor	α_{AD}	β_{AD}	$P_{AD\infty}$	$\mu_{AD}[D]$	$\Delta\bar{\mu}[D]$	$X_{PT}, \%$
2,4,6-Collidine	46.95	0.610	1748	8.96 ± 0.08	3.98	34.2
4-Picoline	33.41	0.578	1243	7.51 ± 0.07	2.02	13.1
Pyridine	28.82	-0.383	1103	7.06 ± 0.03	1.97	12.6
3-Chloropyridine	22.51	0.296	873	6.20 ± 0.02	1.56	8.2
3,5-Dichloropyridine	14.00	-0.603	586	4.94 ± 0.02	1.05	2.7

and acceptor) in the solutions could be calculated. Next, the molar polarization of the complex (and its dipole moment) was evaluated, using the extrapolation procedure described in ref 2 as method 3. The results are collected in Table II; extrapolation parameters α_{AD} and β_{AD} , molar polarizations of the complexes $P_{AD\infty}$, and finally dipole moments of the complexes are quoted.

The equilibrium concentrations of the formed complexes were usually about 0.1 mol % . The error given in Table II is the mean-square error of six to eight measurements.

Discussion

As can be seen from Table I, the stability constants of the complexes, the spectral shifts ($\Delta\nu$), half-widths (2b), and integrated intensities of the $\nu_s(\text{OH})$ absorption band ($B = (1/cl) \int_{-\infty}^{+\infty} \ln(I^0/I) d\nu$, where c is the concentration in moles per liter, l is the path length in centimeters, ν is the wavenumber in reciprocal centimeters) of the bonded OH group of the donor, increase with the basicity of the proton acceptor. The variation of these band parameters due to hydrogen-bond formation is greater than in the case of 2,4,6-trimethylphenol and diphenylamine complexes,¹ according to the more pronounced acidic character of the donor molecule ($pK_a = 3.68$).

The position of the $\nu_s(\text{OH})$ absorption band of the donor ($\sim 3500 \text{ cm}^{-1}$), ascribed to the free OH group, indicated that it is in fact intramolecularly hydrogen bonded to chlorine atoms in ortho positions of the molecule. Hence, the $\Delta\nu$ values, given in Table I, were elevated at about 100 cm^{-1} , as the absorption band of the stretching vibration of the OH group of phenols occurs usually about 3600 cm^{-1} ; e.g., Stone and Thompson⁵ have found a value of 3593 cm^{-1} for *p*-nitrophenol. Also, the intensity of the $\nu_s(\text{OH})$ band of 2,6-dichloro-4-nitrophenol ($2.09 \times 10^4 \text{ l. mol}^{-1} \text{ cm}^{-2}$) is similar to that of the corresponding band of *p*-nitrophenol ($1.71 \times 10^4 \text{ l. mol}^{-1} \text{ cm}^{-2}$ after Stone and Thompson⁵ and $2.17 \times 10^4 \text{ l. mol}^{-1} \text{ cm}^{-2}$ according to Flett,⁶ after conversion from absolute intensity units). Although the intensity values for the $\nu_s(\text{OH})$ band of the 2,6-dichloro-4-nitrophenol complexes are higher than in case of 2,4,6-trimethylphenol and diphenylamine,¹ the B/B^0 ratios are relatively low, and the plot of B/B^0 vs. $\Delta\nu$ does not give a common straight line. It may be caused by the fact that the B^0 value

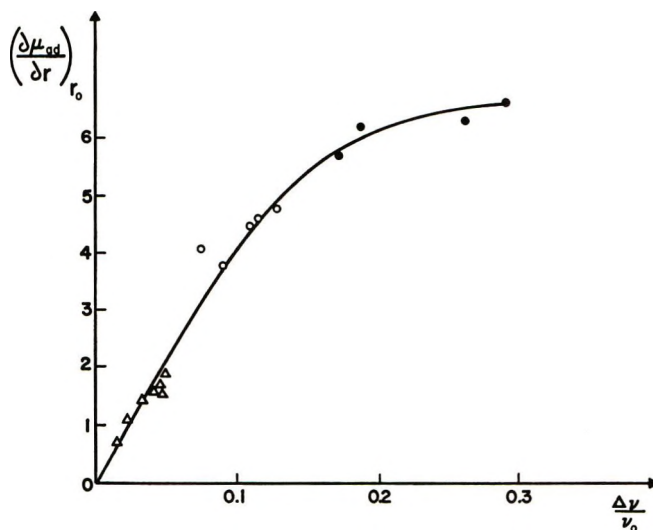


Figure 1. The plot $(\partial\mu_{add}/\partial r)_{r_0}$ vs. $\Delta\nu/\nu_0$: (Δ) diphenylamine complexes, (\circ) mesitol complexes,^{1,2} (\bullet) data obtained in this work for 2,6-dichloro-4-nitrophenol adducts.

is more than twice as high as in case of 2,4,6-trimethylphenol; on the other hand, the intensity values for 2,6-dichloro-4-nitrophenol complexes are probably underestimated because of the large wing at the low-frequency side of the band center. The change in the behavior of hydrogen-bonded systems of varying strength is well reflected in the plot of the increment of the dipole moment derivative $(\partial\mu_{add}/\partial r)_{r_0}$ (calculated from intensity data according to formula 12, ref 1) vs. $\Delta\nu/\nu_0$, shown in Figure 1 (see also data in Table III).

Table III

Acceptor	$\Delta\nu/\nu_0$	$(\partial\mu_{OH}/\partial r_{OH})_{r_0} D, \text{ \AA}$	$(\partial\mu_{add}/\partial r_{OH})_{r_0} D, \text{ \AA}$
2,4,6-Collidine	0.333		
4-Picoline	0.292	8.75	6.58
Pyridine	0.264	8.46	6.29
3-Chloropyridine	0.189	8.37	6.20
3,5-Dichloropyridine	0.167	7.86	5.69
2,6-Dichloro-4-nitrophenol	0	2.17	0

(5) P. J. Stone and H. W. Thompson, *Spectrochim. Acta*, **10**, 17 (1957).

(6) M. S. C. Flett, *ibid.*, **10**, 21 (1957).

In the series of 2,6-dichloro-4-nitrophenol complexes an abrupt fall of the molar extinction coefficient for 2,4,6-collidine complex, and simultaneously an almost continuous absorption of the low-frequency side of the band, is observed. This behavior reflects also in dielectric data and will be discussed later.

Using the dipole moments of the donor and complexes, determined in this work, and the dipole moments of the acceptors, measured previously² in the same experimental conditions, it was possible to calculate the polarity of the hydrogen bonding in these complexes, $\Delta\vec{\mu}$. During the calculation of $\Delta\vec{\mu}$ the following assumptions have been made: (1) the intramolecular hydrogen bonding to the chlorine atoms in the ortho positions of the donor molecule is broken and the change of the charge distribution resulting from this process can be neglected;⁷ (2) during the formation of the intermolecular H bond the charge redistribution occurs only in the O—H···N fragment of the complex; and (3) the H bond is linear.

In the symmetric pyridine derivatives the dipole moment vector has the direction of the 1-4 axis of the molecule (which is also the direction of the lone electron pair at the N atom). The dipole moment vector of 2,6-dichloro-4-nitrophenol forms an angle of 142° with the OH bond. Thus, in case of complexes with symmetric bases, $\Delta\vec{\mu}$ can be calculated from a simple vector scheme: the observed dipole moment of the complex is a vector sum of the ($\vec{\mu}_{\text{base}} + \Delta\vec{\mu}$) vector acting along the N···H—O direction and the $\vec{\mu}_{\text{donor}}$ vector, which forms an angle of 142° with this direction. The possible rotation of the components around the O—H···N axis will not influence the results. In 3-chloropyridine the dipole moment of the molecule forms an angle of 35° with the 1-4 axis; a free rotation of components of the complex has been assumed during the calculation of $\Delta\vec{\mu}$ in this case. The $\Delta\vec{\mu}$ values are given in Table II.

From our previous data on weak hydrogen-bonded complexes, an electrostatic inductive effect of 0.4–0.5 D can be expected in this case.² Thus, the observed polarities of the hydrogen bonding of the 2,6-dichloro-4-nitrophenol complexes have their origin in some additional effects.

The role of the proton-transfer phenomenon in the phenols-triethylamine systems was discussed previously by Ratajczak and Sobczyk.⁸ The dependence of the equilibrium constant of the proton-transfer reaction, K_{PT} , on the $\Delta\text{p}K_{\text{a}}$ value, where $\Delta\text{p}K_{\text{a}}$ is the difference between $\text{p}K_{\text{a}}$ of the acid and base, can be expressed by

$$\log K_{\text{PT}} = \xi(\delta - \Delta\text{p}K_{\text{a}}) \quad (3)$$

δ and ξ are constants, δ being connected with the free energy of solvation. As a consequence of this model a linear relationship between $\Delta\vec{\mu}$ and the molar fraction of the proton-transfer species, X_{PT} , is obtained

$$\Delta\vec{\mu} = \Delta\vec{\mu}_0 + \Delta\vec{\mu}_1 X_{\text{PT}} \quad (4)$$

where $\Delta\vec{\mu}_0$ is the polarity of the H bond in non-proton-transfer complexes; $\Delta\vec{\mu}_1$ is the polarity in ion pairs. Using this expression, X_{PT} can be found from experimental $\Delta\vec{\mu}$ data, providing that $\Delta\vec{\mu}_0$ and $\Delta\vec{\mu}_1$ are known. The values found for the 2,6-dichloro-4-nitrophenol complexes with pyridine bases are slightly shifted in comparison to those for phenol-triethylamine presented in Figure 2 by the solid line. This may be explained by the change of the δ parameter. It has been assumed in the X_{PT} calculations that for the 2,6-dichloro-4-nitrophenol systems $\Delta\vec{\mu}_0$, *i.e.*, the increase of dipole moment without proton transfer, is constant and equal 0.8 D. This assumption could be questionable, as the CT (delocalization) effect has been neglected. It has been previously emphasized that the CT contribution could be the main reason that ξ is less than 1. Also the assumption that the $\Delta\vec{\mu}_1$ value for the proton-transfer ion pairs is the same as in phenols-triethylamine complexes (9.3 D) is arbitrary. In Figure 2 an additional point was added for the picric acid-pyridine system ($\Delta\vec{\mu} = 6.45$ D, $X_{\text{PT}} = 60.7\%$).⁹

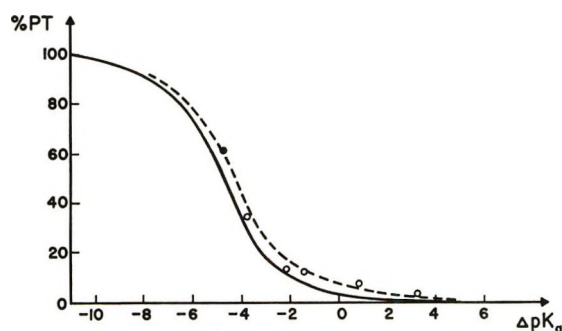


Figure 2. The plot % PT vs. $\Delta\text{p}K_{\text{a}}$: solid line corresponds to the data obtained for phenols-triethylamine,⁷ (●) value for picric acid-pyridine complex,⁸ (○) present data for 2,6-dichloro-4-nitrophenol adducts.

With the increase of $\Delta\vec{\mu}$ there appear some anomalies in the infrared absorption spectrum of the investigated systems, especially in the intensity of the OH stretching vibration band (the occurrence of continuous absorption). This broad absorption, covering all the infrared region, is typical for systems where $\Delta\vec{\mu}$ values indicate a considerable molar fraction of proton-transfer species (but not for complexes of pure ion pair type!). The anomalies of infrared spectrum can be discussed in terms of double-minimum potential functions of the H bond. A convincing theoretical treatment of the broad absorption, based on the tunneling effect, has

(7) A. Koll, H. Ratajczak, and L. Sobczyk, *Roc. Chem.*, **44**, 825 (1970).

(8) H. Ratajczak and L. Sobczyk, *Bull. Acad. Pol. Sci., Ser. Sci. Chem.*, **18**, 93 (1970); *J. Chem. Phys.*, **50**, 556 (1969).

(9) L. Sobczyk and J. K. Syrkin, *Roc. Chem.*, **30**, 881 (1956).

been proposed by Zundel.¹⁰ It is based on the idea of fluctuations of protonic energy levels, resulting from the splitting of vibrational states. These fluctuations are caused by the environmental field, inducing a continuous level distribution. This effect may be especially pronounced in cases when the two potential energy minima are nearly equivalent, *i.e.*, in H bonds with large $\Delta\bar{\mu}$ values (intermediate between $\Delta\bar{\mu}_0$ and $\Delta\bar{\mu}_1$), which is observed in our case.

Thus, the $\Delta\bar{\mu}$ values can be described by means of a formal proton-transfer model, and the ir data seem to

support the conclusion that this effect is of great importance in the investigated systems. It should be remembered, however, that $\Delta\bar{\mu}$ and X_{PT} were calculated based on assumptions which may be to some extent questionable. Also, the contribution of the electron delocalization cannot be neglected. Further studies are needed to clarify the role of these two effects in H bonds of intermediate strength.

(10) G. Zundel, *Allg. Prakt. Chem.*, **21**, 329 (1970); see also E. G. Weidemann and G. Zundel, *Z. Phys.*, **198**, 288 (1967).

A Thin-Sample Method for the Measurement of Permeability, Permittivity, and Conductivity in the Frequency and Time Domain¹

by Hugo Fellner-Feldegg

Hewlett-Packard Laboratories, Palo Alto, California 94304 (Received January 4, 1972)

Publication costs assisted by the Hewlett-Packard Company

A method for measuring the permeability, permittivity, and conductivity of materials using thin samples in coaxial lines is presented. In the time domain, one obtains directly the impulse response of the permeability and permittivity and the step response of the conductivity in a single measurement over a frequency range which is limited only by the rise time of the oscilloscope-pulse generator system and the duration of the applied pulse. There is a linear superposition of these material parameters which facilitates the transformation between time and frequency domain. The only condition is the maximum thickness of the sample, which depends on the material parameters and the frequency range used. The required sample volume is approximately 1 μ l.

Introduction

Some time ago time domain reflectometry was introduced for the measurement of dielectric relaxation properties in the range of 30 psec to about 100 nsec.² It allowed the determination of high- and low-frequency permittivity and the relaxation time from a single time domain measurement over a range which required a fairly substantial instrument investment in the past. The method used only the first reflection from the interface air-dielectric, which made it easy to interpret. It required, on the other hand, rather long coaxial sample cells for the measurement of long relaxation times and also required the Fourier transformation into the frequency domain for nonideal dielectrics.³ This single-reflection time domain reflectometry has been shown to produce surprisingly precise data.⁴

Recently Nicolson and Ross⁵ have reported a method which uses a combination of both the reflected and transmitted wave from samples of arbitrary thickness

to measure the complex permittivity and permeability, using Fourier transformation. We have used a similar approach of applying transmission line theory for the measurement of material properties and found that reducing the sample thickness below a certain value and terminating the line with a matched load simplify the result considerably and give directly the impulse response of the permeability and permittivity, and the step response of the conductivity. Thus, it is possible to derive the transient behavior of the material from the time domain or from the frequency domain without the

(1) This method was first reported at the meeting of the Dielectrics Discussion Group, Bedford College, University of London, April 5-7, 1971.

(2) H. Fellner-Feldegg, *J. Phys. Chem.*, **73**, 616 (1969).

(3) (a) T. A. Whittingham, *ibid.*, **74**, 1824 (1970); (b) H. Fellner-Feldegg and E. F. Barnett, *ibid.*, **74**, 1962 (1970).

(4) A. Suggett, P. A. Mackness, and M. J. Tait, *Nature (London)*, **228**, 456 (1970).

(5) A. M. Nicolson and G. F. Ross, *IEEE Trans. Instrum. Meas.*, **19**, 377 (1970).

requirement of long sample cells for the measurement of long relaxation times. Furthermore, the sample volume is in the microliter range, which is of advantage in many applications.

The equipment required is the same as described in ref 2. There, a sampling oscilloscope and a tunnel diode pulse generator were used for measurements in the microwave region. Since the thin-sample method, reported here, is not limited in the lower frequency range by the sample length, real time oscilloscopes and suitable pulse generators may be used for measurements below a few hundred megahertz.

Mathematical Treatment

We will first derive the equations for the frequency domain using a well-known transmission line equation, and then transform the result into the time domain.

The input impedance Z of a transmission line of an impedance Z_1 and length l , terminated with Z_0 (see Figure 1) is given by

$$Z = Z_1 \frac{1 - \rho \exp(-2\gamma l)}{1 + \rho \exp(-2\gamma l)} \quad (1)$$

where γ is the propagation constant and ρ is the reflection coefficient of a line of the impedance Z_0 , terminated with Z_1 .

The line with the impedance Z_1 is obtained by filling a coaxial line of the characteristic impedance Z_0 with the sample of a length l . The sample shall have a relative permittivity $\kappa^* = \kappa' - j\kappa''$, a conductivity σ , and a relative permeability $\mu^* = \mu' - j\mu''$. We are neglecting any series resistance in this line. Then the impedance is

$$Z_1 = \sqrt{\frac{j\omega L\mu^*}{j\omega C\kappa^* + G}} = Z_0 \sqrt{\frac{\mu^*}{\kappa^* \epsilon_0}} \quad (2)$$

and the propagation constant is

$$\gamma = \sqrt{j\omega L\mu^*(j\omega C\kappa^* + G)} = \gamma_0 \sqrt{\mu^* \kappa^* \epsilon_0} \quad (3)$$

with

$$Z_0 = \sqrt{\frac{L}{C}}, \quad \frac{G}{C} = 4\pi\sigma; \quad \gamma_0 = j\omega\sqrt{LC} = \frac{j\omega}{c}$$

and

$$\kappa^*_{\epsilon_0} = \kappa^* - j\frac{G}{\omega C} = \kappa^* - j\frac{4\pi\sigma}{\omega} \quad (4)$$

We are using the cgs system and are, therefore, including the factor 4π in the conductivity term.

The reflection coefficient from the sample, expressed as a scattering coefficient S , is then

$$S_{11} = \frac{[1 - \exp(-2\gamma l)]\rho}{1 - \rho^2 \exp(-2\gamma l)} \quad (5)$$

and the change in the transmission coefficient due to the sample, referenced to the output port of the sample, is given by

$$[S_{21} - \exp(-\gamma_0 l)] = \frac{[\exp(-\gamma l) - 1][1 + \rho^2 \exp(-\gamma l)]}{1 - \rho^2 \exp(-2\gamma l)} + [1 - \exp(-\gamma_0 l)] \quad (6)$$

Expanding the exponential term into a Taylor series and using only the linear term gives the reflection coefficient

$$S_{11} = 2\gamma l \frac{\rho}{1 - \rho^2} = \frac{\gamma_0 l}{2} \left(\mu^* - \kappa^* - \frac{4\pi\sigma}{j\omega} \right) \quad (7)$$

and the difference in the transmission coefficient

$$[S_{21} - \exp(-\gamma_0 l)] = \gamma_0 l - \gamma l \frac{1 + \rho^2}{1 - \rho^2} - \frac{\gamma_0 l}{2} \left(\mu^* + \kappa^* + \frac{4\pi\sigma}{j\omega} - 2 \right) \quad (8)$$

Equations 7 and 8 can be used for the measurement in the frequency domain.

The response to a step pulse is in the frequency domain

$$(S_{11})_{\text{step}} = \frac{S_{11}}{j\omega} = \frac{l}{2c} \left(\mu^* - \kappa^* - \frac{4\pi\sigma}{j\omega} \right) \quad (9)$$

and likewise

$$(S_{21})_{\text{step}} - \frac{\exp(-\gamma_0 l)}{j\omega} = \frac{S_{21} - \exp(-\gamma_0 l)}{j\omega} = -\frac{l}{2c} \left(\mu^* + \kappa^* + \frac{4\pi\sigma}{j\omega} - 2 \right) \quad (10)$$

It is the advantage of this approach that one obtains a linear superposition of the frequency response of permeability, permittivity, and conductivity (the latter divided by $j\omega$). This not only makes it easy to interpret the results in the frequency domain, but also allows making the transformation into the time domain separately for each term.

The Laplace transformation into the time domain then gives

$$(s_{11})_{\text{step}} = \frac{l}{2c} \left[\mathcal{L}(\mu^*) - \mathcal{L}(\kappa^*) - \mathcal{L}\left(\frac{4\pi\sigma}{j\omega}\right) \right] = \frac{l}{2c} \left[\mu(t) - \kappa(t) - 4\pi \int_0^t \sigma(t) dt \right] \quad (11)$$

and

$$(s_{21})_{\text{step}} - [S(1)]_t = -\frac{l}{2c} \left[\mu(t) - 1 + \kappa(t) - 1 + 4\pi \int_0^t \sigma(t) dt \right] \quad (12)$$

where $[S(1)]_t$ is a unit step function at the time $t = l/c$ and $\mu(t)$, $\kappa(t)$, $\sigma(t)$ are the impulse response of the permeability, permittivity, and conductivity, respec-

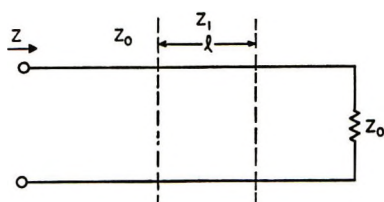


Figure 1. Coaxial line with sample and 50-ohm termination.

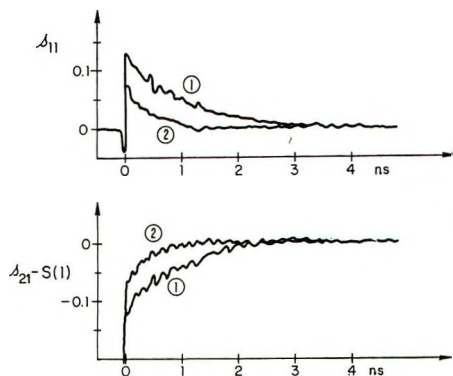


Figure 2. Reflection and transmission from a thin sample of two ferrites: (1) ferramic Q_2 , (2) ferramic Q_3 .

tively. The integral of the impulse response $\sigma(t)$ is the step response of the conductivity.

The only difference between the reflected and transmitted waves, both in the frequency and time domain, is the sign of the permeability term. This allows one to separate it from the permittivity and conductivity terms by measuring the transmission and the reflection. However, the reflection measurement will, in general, be more accurate, since the signal is directly proportional to the material constants and the sample length and can be well separated from the incident step pulse, whereas in the transmission measurement one has to take the difference between $\exp(-\gamma_0 l)$ or $S(1)$ and the relatively small value of $(S_{21})_{\text{step}}$ and $(s_{21})_{\text{step}}$, respectively.

$1/c = 3.3 \times 10^{-11} \text{ cm}^{-1} \text{ sec}$ can also be expressed as 30 ohms, since $1 \text{ ohm} = 1.1 \times 10^{-12} \text{ cm}^{-1} \text{ sec}$. This may be used for the conductivity term in eq 9-12 when expressing σ in $\text{ohms}^{-1} \text{ cm}^{-1}$.

Figures 2, 3, and 4 give some typical time responses obtained with thin-sample time domain spectroscopy for magnetic, dielectric, and conductive materials.

The results obtained in the time domain can either be transformed into the frequency domain by numerical transformation or evaluated directly. We shall explain the latter using the example of an ideal and a lossy dielectric, but will keep in mind that it is equally applicable for any dielectric or magnetic sample.

Consider a thin sample of a nonmagnetic ($\mu = 1$) Debye dielectric with no conductivity. The frequency and time response of the reflection coefficient to a step pulse is then

$$(S_{11})_{\text{step}} = \frac{l}{2c}(1 - \kappa^*) = \frac{l}{2c} \left(1 - \kappa_1 - \frac{\kappa_0 - \kappa_1}{1 + j\omega\tau} \right) \quad (13)$$

and

$$(s_{11})_{\text{step}} = \frac{l}{2c}(1 - \kappa_1)\delta(t) - \frac{l}{2c\tau}(\kappa_0 - \kappa_1)e^{-t/\tau} \quad (14)$$

Figure 5 shows the time response schematically. The area of the δ function is proportional to $(l/2c)(1 - \kappa_1)$ and the area under the curve is

$$\int_0^{\infty} s_{11}(t)dt = \frac{l}{2c}(1 - \kappa_0) \quad (15)$$

Figure 6 shows the close match between theoretical and experimental values obtained from a number of dielectrics. The low value of s_{11} for water may be due to incomplete filling of the sample cell because of the strongly hydrophobic Teflon beads.

The exponential part of the time response curve gives the relaxation time, which can be obtained simply from the slope of the $\log s_{11}$ vs. time plot. For nonideal dielectrics one obtains κ_1 and κ_0 as described above; however, the $\log s_{11}$ vs. time plot will deviate from a straight line, depending on the relaxation properties of the dielectric.

The finite response of the measuring system degrades

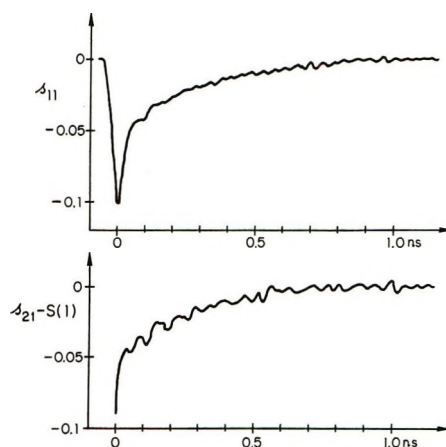


Figure 3. Reflection and transmission from a thin sample of dielectric; glycerine, 25° .

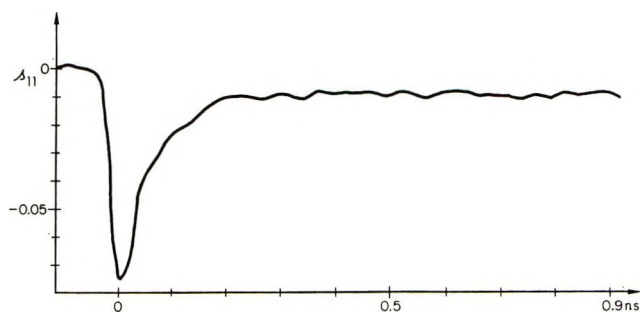


Figure 4. Reflection from a thin sample of a dielectric with conductivity; methanol, saturated with potassium chloride, 25° .

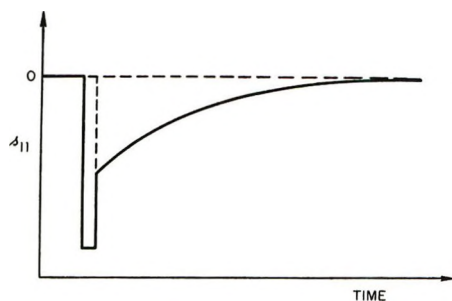


Figure 5. Schematic time response of the reflection from a thin sample of a dielectric.

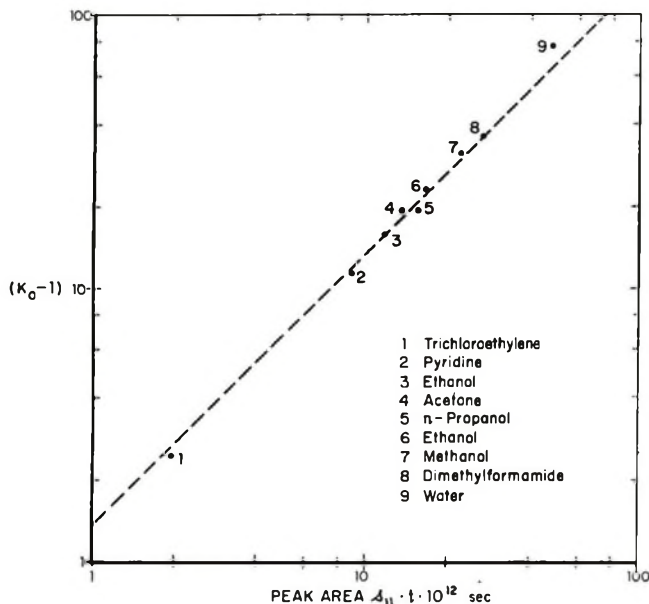


Figure 6. Experimental (points) and theoretical (dashed line) values of the static relative permittivity obtained with the thin-sample reflection method.

the δ function in eq 14 to a peak of finite width whose area is proportional to $(l/2c)(1 - \kappa_1)$.

Electrical conductivity, present in the sample, is added to the frequency or time dependence of the reflection coefficient. If the conductivity is independent of frequency, it will produce an offset of the base line of

$$(S_{11})_{\text{cond}} = 2\pi\sigma l/c = 188.5\sigma l \quad (16)$$

with σ expressed in ohms⁻¹ centimeter⁻¹.

Finally, we have to specify the error introduced by using only the first term of the Taylor expansion of eq 5 and 6. We will solve the problem for the frequency domain first.

Figure 7 shows a computer plot of the exact value of S_{11} or $[S_{21} - \exp(-\gamma_0 l)]$ vs. κ or μ for different values of $\gamma_0 l$, according to eq 5 and 6. The dashed lines give the approximate values, derived from eq 7 or 8. The difference between eq 5 and 6 (reflection and transmission, respectively) contains only the third and higher order terms of the Taylor expansion and is about 10^{-6} for the range of values plotted.

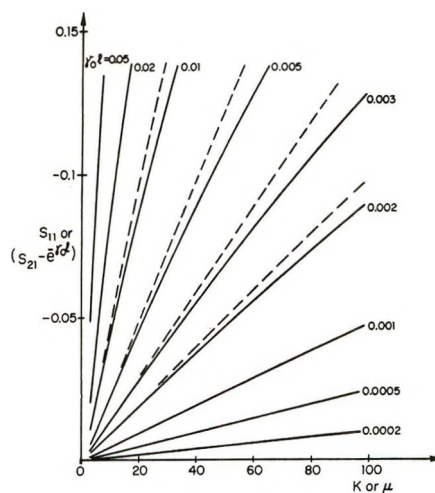


Figure 7. Reflection and transmission signal from a thin sample vs. relative permeability or permittivity for different values of $\gamma_0 l$.

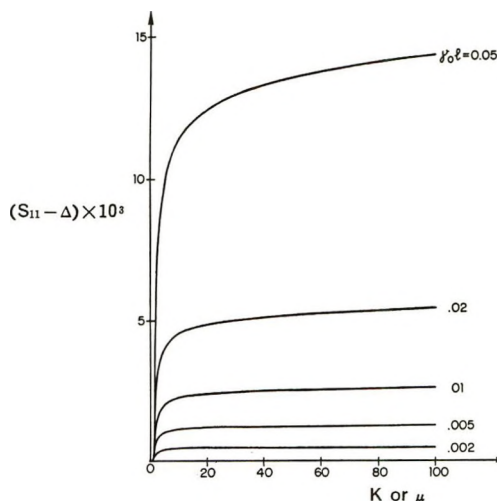


Figure 8. Error, $S_{11} - \Delta$, made using the signal amplitude, S_{11} , to correct for the thin-sample approximation in the frequency domain.

For a given value of S_{11} , the relative difference Δ of κ , derived from the exact and the approximate equations, $\Delta = (\kappa - \kappa_{\text{approx}})/\kappa$, is very closely equal to the value of S_{11} . The difference $S_{11} - \Delta$ vs. κ is plotted in Figure 8. For small values of $\gamma_0 l$ and for $\kappa \gg 1$, this difference approaches $\gamma_0 l/4$. It is therefore quite convenient to use this relation between Δ and S_{11} not only to estimate the error made in using the thin-sample approximation but also to correct for it, which in turn permits one to employ relatively thick samples, producing sufficiently strong signals for exact measurements in the frequency domain.

It is difficult to transform these relations into the time domain. Therefore, we will derive eq 11 (without conductivity term) in the time domain to obtain Δ .

Consider again a section of a transmission line of the length l , filled with a material with the permeability μ

and the permittivity κ inserted into a line of the impedance Z_0 and terminated with the same impedance. We further stipulate that μ and κ do not vary during the time interval t_r , considered in the following. Then the reflection coefficient for the first reflection will be

$$\rho = \frac{\sqrt{\mu/\kappa} - 1}{\sqrt{\mu/\kappa} + 1} \quad (17)$$

The return time within the sample is

$$t_0 = \frac{2l\sqrt{\mu\kappa}}{c} \quad (18)$$

Consecutive multiple reflections can easily be analyzed⁶ and are shown in Figure 9. They produce a reflected signal which is shown schematically in Figure 10.

The step height, referenced to V_0 , is

$$R_n = \rho + \sum_2^n \rho_i = \rho^{2n-1} \quad (19)$$

and the area of step 1 to n is

$$A_n = t_0 \sum_1^n R_i = t_0 \rho \frac{\rho^{2n} - 1}{\rho^2 - 1} \quad (20)$$

Consequently, the total area is given by

$$A_\infty = t_0 \sum_1^\infty R_i = t_0 \frac{\rho}{1 - \rho^2} \quad (21)$$

Using eq 17 and 18 gives

$$A_\infty = \frac{l}{2c}(\mu - \kappa) \quad (22)$$

which is the same as eq 11 without a conductivity term.

We now specify a time interval $t_r = nt_0$, which is defined either by the rise time of the measuring system or by the condition that μ or κ do not vary during this time. We will make an error $\Delta = (A_\infty - A_n)/A_\infty$ of the measurement of μ or κ which is

$$\Delta = \rho^{2n} \quad (23)$$

or

$$\Delta = \left(\frac{|\sqrt{\mu/\kappa} - 1|}{\sqrt{\mu/\kappa} + 1} \right)^{t_r c / l \sqrt{\mu\kappa}} \quad (24)$$

This function is shown in Figure 11. For $t_r = 33$ psec, a typical rise time of a sampling oscilloscope system, $t_r c$ is 1 cm and eq 24 can be approximated by

$$l = 0.5(\kappa - 1) \text{ for } \Delta = 2\% \quad (25)$$

$$l = 0.67(\kappa - 1) \text{ for } \Delta = 5\%$$

for $\mu = 1$. This can be used to conservatively estimate the maximum permissible sample length.

The error Δ affects also the shape of the measured response curve. Let us approximate the time response by a step function, similar to Figure 10, however now with a step time $t_r = nt_0$ as used in eq 24. Then,

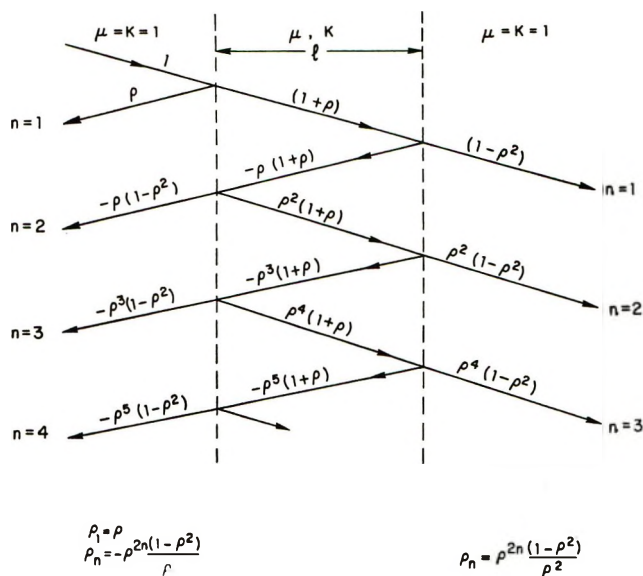


Figure 9. Multiple reflections from a transmission line with the impedance Z_1 and length l .

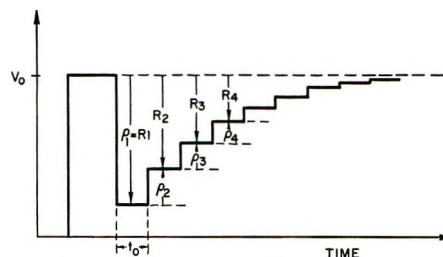


Figure 10. Schematic time response of a section of transmission with impedance Z_1 and length l .

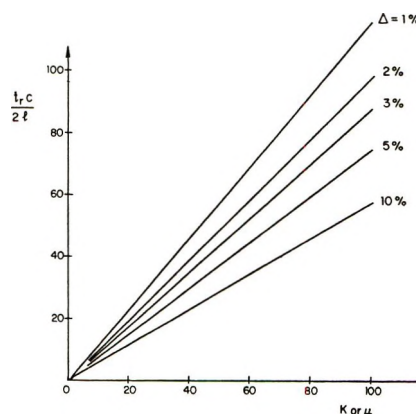


Figure 11. $t_r c / 2l$ vs. relative permeability or permittivity for different values of the relative measurement error $\Delta = \Delta\kappa/\kappa$ in the time domain.

each step with a theoretical step height $f(t/\tau)$ will have an actual value

$$f_1(t/\tau_1) = (1 - \Delta)f(t/\tau) + \Delta f((t - t_r)/\tau) \quad (26)$$

where τ_1 is a relaxation time derived from the experimental curve and τ is the true relaxation time.

(6) B. M. Oliver, *Hewlett-Packard J.*, 15 (6) (1964).

The second term in eq 26 comes from the contribution of the preceding time element and can be approximated with

$$\Delta f((t - t_r)/\tau) = - \frac{\Delta t_r}{\tau} \frac{d(f(t/\tau))}{d(t/\tau)} + \Delta f(t/\tau) \quad (27)$$

Since $\Delta t_r/\tau \ll 1$ we can set

$$\frac{\Delta t_r}{\tau} \frac{d(f(t/\tau))}{d(t/\tau)} \approx \frac{\Delta t_r}{\tau_1} \frac{d(f_1(t/\tau_1))}{d(t/\tau_1)} \quad (28)$$

and obtain

$$f(t/\tau) = f_1(t/\tau_1) + \frac{\Delta t_r}{\tau_1} \frac{d(f_1(t/\tau_1))}{d(t/\tau_1)} \quad (29)$$

On the right-hand side of eq (29) are experimental values only which permit calculation of the true time function $f(t/\tau)$ for each point in time.

Sample Cells

The required sample thickness is typically 0.1–1 mm. With solid samples it is often easy to machine, punch, or press a disk of appropriate dimensions. Investigations on thin films can be made by punching a number of disks and pressing them together until the desired thickness is obtained. These samples are then inserted into a 10-cm precision coaxial air line, similar to the one in Figure 9 of ref 2.

Two cells for liquid samples are shown in Figure 12. Both use Teflon beads which make a tight seal between inner and outer conductor, enclosing a sample cell between them. In the cell of Figure 12 (top), the inner conductor has a slightly smaller diameter at the position of the beads to maintain a 50-ohm impedance. The spacer at the center has the nominal diameter of the inner conductor and defines the cell thickness very accurately. Thus, there is no reflection due to the empty cell. The cell of Figure 12 (bottom) has a straight center conductor and two Teflon beads, made such that they have a tight press fit at the inner conductor and a slip fit at the outer conductor. The beads are pressed onto the inner conductor with a removable spacer between them. There is a well defined gap between the beads after the spacer has been removed. Since there is a small impedance mismatch due to the beads, the empty cell will produce a reflection which has to be subtracted from the measured value.

The cells are inserted into the outer conductor until the cell gap is just flush with the end face of the outer conductor. Holding the assembly vertically and applying the sample with a syringe to this end face produces a meniscus around the Teflon bead and fills the cell completely. The cell is then pushed further into the outer conductor until the second bead just disappears. The sample is now sealed between the beads, excess liquid is being wiped off, the cell is

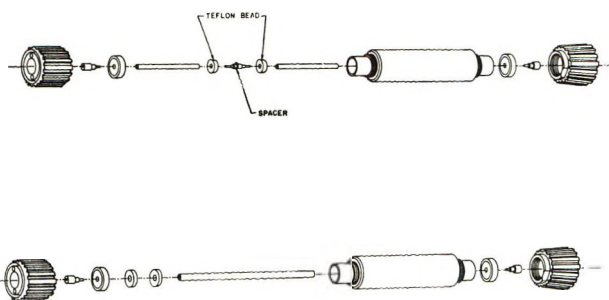


Figure 12. (Top) Thin-sample cell matched to 50 ohms impedance. (Bottom) Thin-sample cell with small impedance mismatch.

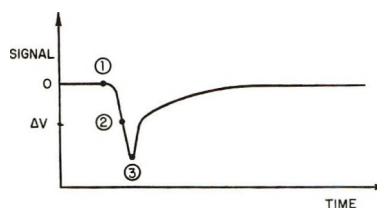


Figure 13. Three-point scanning method of Nicholson.

pushed into the final position within the outer conductor, and the connectors are fastened.

For the cell shown at the top of Figure 12, one can expect a small discontinuity capacitance due to the change in diameter of the center conductor. It depends on the dielectric constant of the material at the step and would, therefore, introduce a measurement error. However, we have not yet been able to detect any difference in results obtained with the two sample cells.

Data Acquisition and Results

Computerized data acquisition and data handling are not only convenient but also considerably improve the measurement accuracy. This improvement can be achieved by multiple scanning, which reduces baseline drift and enhances the signal-to-noise ratio, and by referencing to a time marker which suppresses time jitter and drift. Suggett⁴ and Nicolson and Ross⁵ have shown that a drift of only 1 psec in the time response of the system may cause significant measurement errors above 1 GHz after transformation into the frequency domain. It is advisable to use the three-point scanning method of Nicholson,⁷ shown in Figure 13, whereby each computer-controlled scan starts at a point (1) prior to the onset of the initial pulse and thus establishes the base line. This can be done for reflected or transmitted pulses with the single-reflection or thin-sample method. The computer then seeks a second point on the leading edge of the initial pulse at a given signal value ΔV . This point (2), being on a steep slope, defines the time reference

(7) A. M. Nicolson, *WESCON Tech. Pap.*, 13, 4, 22 (1969).

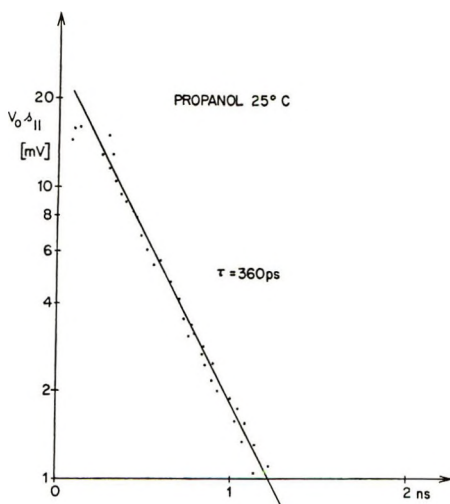


Figure 14. $\log(V_0 s_{11})$ vs. time plot for propanol at 25°.

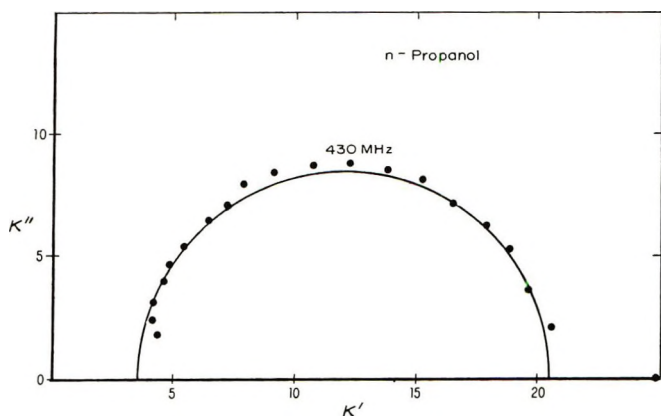


Figure 15. Cole-Cole plot of propanol at 25°.

accurately. The data-collecting scan then starts at any given point (3), which is referenced to (2) in time and to (1) in amplitude. The time and base-line reference can be carried out prior to each scan or for each measurement point.

To determine the high-frequency permittivity or permeability in the time domain, one obtains quite consistent results by measuring only the first half of the area up to the maximum peak height and multiplying by two, since the second half will often be distorted due to relaxation effects. It should be noted, however, that the measurement of the high-frequency permittivity or permeability is limited by the rise time of the measuring system. Therefore, substances with a short relaxation time will not yield the true high-frequency value but an intermediate one.

On the other hand, dedicated minicomputers or time share systems make the transformation between time and frequency domain very simple and fast. At the same time, one obtains the deconvolution of the time response with the input waveform which results in a significant improvement of the measurement accuracy at high frequencies.

Figure 14 shows the $\log(V_0 s_{11})$ vs. time plot for propanol, which has been obtained with the aid of a minicomputer by multiple scanning and subtraction of unwanted reflections, using an empty measuring cell as a reference. The relaxation time of 360 psec agrees well with literature values. Transformation into the frequency domain and deconvolution with the input waveform gives a Cole-Cole plot of Figure 15. Such results can be obtained within a few minutes.

Conclusions

The thin-sample method provides great flexibility and ease of interpretation for the measurement of dielectric and magnetic materials. The sample preparation is very simple and the sample volume small. The measurement range seems to be limited only for very high values of permeability, permittivity, or conductivity, where the required maximum sample thickness becomes too small. For low values of these parameters, one can get a sufficiently strong signal by enlarging the sample.

With the thin-sample time domain spectroscopy one obtains immediate information about the material parameters. The frequency range is limited only by the rise time of the oscilloscope-pulse generator system and duration of the applied step pulse. Combining the tdr system with a computer improves the accuracy of this method considerably, makes data acquisition and data handling very convenient, and enables transformation of the results into the frequency domain. The linear superposition of the material parameters facilitates the transformation.

On the other hand, one can make measurements in the frequency domain as well, using a vector impedance meter or a network analyzer, if information is only required at certain frequencies or if one wants to attain maximum accuracy and sensitivity. The fact that the error introduced by the thin-sample approximation in the frequency domain is closely proportional to the signal S_{11} makes it simple to correct for it.

Acknowledgment. The author wishes to thank E. F. Barnett, L. Cutler, and R. Lacey of Hewlett-Packard Laboratories and K. Giese of the University of Göttingen for valuable discussions.

Calculation of the Interaction Energy of One Molecule with Its Whole Surrounding. I. Method and Application to Pure Nonpolar Compounds

by Marie-José Huron*

Institut Français du Pétrole, 92-Rueil-Malmaison, France

and Pierre Claverie

*Laboratoire de Chimie Quantique, Institut de Biologie Physico-Chimique, 75-Paris (5e), France
(Received January 14, 1972)*

Publication costs borne completely by The Journal of Physical Chemistry

A method of calculation of the dispersion and repulsion energies of a central molecule with its whole surrounding is proposed. The total energy is calculated as a sum of interaction potentials of atomic pairs with a correction of nonadditivity on the dispersion energy. The total energy is expressed as a function of energy integrals and "calibration constants" K_{ij} . The energy integrals are calculated numerically outside a volume Ω that takes into account the form of the central molecule, as it is deduced from the van der Waals volume so as to reproduce the molecular volume. The constants K_{ij} are defined as the ratio between energy calculated by discrete summation and energy calculated by integration for the simple case of packing of spheres of radius R_j around a sphere of radius R_i . The method is applied to pure substances (hydrocarbons), and the calculated energies are compared with the vaporization energies. The agreement is very satisfactory.

I. Introduction

The aim we pursue is to calculate interaction energies of molecules and to connect these calculated energies to the thermodynamic properties. Previously, we have used a wholly discrete model;¹ this one required long computation times since it was necessary to calculate several spatial configurations of the solvent molecules around the central molecule to obtain a partial statistical average. To obtain a more efficient method, we have tried a new model with integrations on the outside of the volume of the central molecule. In the continuum models used so far,^{2,3a} the central molecule is taken to be a sphere, and the outside solvent is a medium possessing volume characteristics (polarizability by unit of volume) which correspond to macroscopic experimental data. The agreement with the experiment essentially depends on the chosen values for the radius of the sphere. As we shall see, the effect of this choice is to take into consideration the nonuniform distribution of the attractive centers of the solvent immediately near the solute. We deviate from these models essentially by the two following points. (1) To take into account the form of the molecule, we do not replace it by a sphere, but by a volume which is deduced from the van der Waals volume so as to reproduce the molecular volume. (2) In our model, the energy integrals are calibrated with regard to completely discrete models that are simple (packing of spheres of radius R_j around a central sphere of radius R_i). Therefore, it is a kind of interpolation between these discrete models rather than a calculation using macroscopic constants uniformly distributed in the volume attri-

buted to the solvent. It may be mentioned that Kihara and Jhon^{3b} have studied the solubility of gases in liquids using a convex core model which also represents the real shape of the solute molecule in a more realistic way than the previous spherical approximations.

The present model calculates dispersion energies and repulsion energies; consequently, it is convenient for nonpolar molecules in the cases where the electrostatic and induction energies are negligible. Later, we plan to extend the present model to polar molecules by using the dielectric constant of the solvent. The model is applied here to the calculation of the energies between identical molecules (pure substances), and calculated energies are compared with vaporization energies.

II. Description of the Used Model

We consider a central molecule (solute molecule) surrounded by solvent molecules; we want to calculate the interaction energy of the solute molecule with its entire surrounding assumed infinite in volume.

To calculate the energy, it is necessary to choose a potential law and to make a hypothesis on the distribution of solvent molecules around the solute molecule. The solute molecule and the solvent molecules are characterized by their geometry, the nature of their atoms, and by their molar volume.

(1) M. J. Huron and P. Claverie, *Chem. Phys. Lett.*, **9**, 194 (1971).

(2) (a) B. Linder, *J. Chem. Phys.*, **33**, 666 (1960); (b) *ibid.*, **35**, 371 (1961).

(3) (a) N. G. Bakhshiev, O. P. Girin, and I. V. Piterskaya, *Opt. Spectrosc.*, **24**, 483 (1968); (b) T. Kihara and M. S. Jhon, *Chem. Phys. Lett.*, **7**, 559 (1970).

The solute-solvent interaction energy is calculated as a sum of interaction potentials of pairs of atoms;⁴ this is true for the dispersion energy calculated with the second order of perturbation. We also take into consideration (see section II4) the nonadditive contributions which appear at the third order of perturbation.⁵⁻⁸

We use a potential function of the type of that used by Kitaygorodski⁹ for the dispersion energy and the repulsion energy. The sum of bond energies⁴ is not impossible but sets difficult problems which are not yet solved.

1. *Expression of the Dispersion and Repulsion Energies.* For nonpolar molecules, we can neglect electrostatic and induction energies, and the interaction energy between the atom i belonging to the solute molecule and the atom j belonging to the solvent molecule has the expression⁴

$$e_{ij} = e_{ij}^d + e_{ij}^r = -C_1(4R_i R_j)^3 / r_{ij}^6 + C_2 \exp[-\alpha r_{ij} / (4R_i R_j)^{0.5}] \quad (1)$$

R_i and R_j are, respectively, the van der Waals radii of atoms i and j ; r_{ij} is the distance between atoms i and j .

We call effective volume V^{eff} of the solvent (or of the solute) the molar volume of the solvent (or of the solute) divided by the Avogadro number.

A solvent molecule contains n_j atoms of type j ; the volume dv of the solvent contains dv/V^{eff} molecules of solvent and $n_j dv/V^{\text{eff}}$ atoms of type j to which is associated the energy

$$K_{ij}^d e_{ij}^d \frac{dv}{V^{\text{eff}}} n_j + K_{ij}^r e_{ij}^r \frac{dv}{V^{\text{eff}}} n_j$$

The interaction energy of the atom i of the solute with all the atoms of type j of the solvent is written

$$E_{ij} = \iiint_{\Omega_e} (K_{ij}^d e_{ij}^d + K_{ij}^r e_{ij}^r) n_j \frac{dv}{V^{\text{eff}}} \quad (2)$$

The integration volume Ω_e , which is the outside volume of the volume Ω of the solute molecule, will be specified in section II2; the "calibration constants" K_{ij} will be defined in section II3.

The interaction energy of the atom i of the solute with all the solvent is

$$E_{i_s} = \sum_j E_{ij} \quad (3)$$

A summation on all the atoms i of the solute gives us the total interaction energy of the solute with the solvent

$$E = \sum_i E_{i_s} = E_d + E_r$$

$$E = \sum_i \sum_j \frac{n_j}{V_{\text{solvent}}^{\text{eff}}} \left\{ -C_1 (4R_i R_j)^3 K_{ij}^d \iiint_{\Omega_e} \frac{dv}{r^6} + C_2 K_{ij}^r \iiint_{\Omega_e} \exp[-\alpha r / (4R_i R_j)^{0.5}] dv \right\} \quad (4)$$

In formula 4, the summation on i is a summation on all the atoms i of the solute, but the summation on j is a summation on all the distinct species of atoms of the solvent; for instance, if the solute is the methane CH_4 , and the solvent the nitrobenzene $\text{C}_6\text{H}_5\text{NO}_2$, i will vary from 1 to 5, j from 1 to 4, and the values of n_j will be 6, 5, 1, 2.

Finally, to calculate E , we have to calculate for each atom i of the solute the integrals $\iiint_{\Omega_e} dv/r^6$ and $\iiint_{\Omega_e} \exp(-\alpha r) dv$, to determine calibration constants K_{ij} , and to choose the constants of the pair potential of formula 1.

2. *Calculation of the Integrals.* It is important to notice that the integrals to calculate depend on the solute and on the species of the atoms of the solvent. For a given molar volume of the solute, we can calculate them, once for all, for every species of atoms; then it will be possible to calculate the energy for any solvent by combining these integrals according to formula 4.

a. *Transformation of Volume Integrals into Surface Integrals.* Given the necessity to calculate numerically the integrals $\iiint_{\Omega_e} F(r) dv$, it is convenient to transform them into surface integrals. We explain in Appendix A how we can do this by proper use of Ostrogradski's formula (eq 5-10). The volume integral is transformed into a surface integral by the relation

$$\iiint_{\Omega_e} F(r) dv = \iint_{\Sigma} \left[\frac{1}{r^2} \int_{\infty}^r x^2 F(x) dx \right] \vec{u} \cdot \vec{n}_e(\Omega_e) d\sigma \quad (11)$$

Σ designates the boundary of the integration volume Ω_e . $\vec{n}_e(\Omega_e)$ is the unit vector normal to Σ , directed toward the outside of Ω_e , that is, toward the inside of Ω . We have the relation $\vec{n}_e(\Omega_e) = -\vec{n}_e(\Omega)$. r is the distance from the atom i for which the integral is calculated to the current point. \vec{u} is the unit vector \vec{r}/r .

We obtain, respectively, for the dispersion integral and for the repulsion integral

$$\iiint_{\Omega_e} dv/r^6 = \iint_{\Sigma} \frac{\vec{r} \cdot \vec{n}_e(\Omega)}{3r^6} d\sigma \quad (12)$$

(4) M. J. Huron and P. Claverie, *Chem. Phys. Lett.*, **4**, 429 (1969); *ibid.*, **11**, 152 (1971).

(5) B. M. Axilrod, *J. Chem. Phys.*, **19**, 719, 724 (1951).

(6) T. Kihara, *Advan. Chem. Phys.*, **1**, 267 (1958).

(7) N. R. Kestner and O. Sinanogulu, *J. Chem. Phys.*, **38**, 1730 (1963).

(8) H. Margenau and N. R. Kestner, "Theory of Intermolecular Forces," Pergamon Press, Elmsford, N. Y., 1969, Chapter 5.

(9) A. I. Kitaygorodski, *Tetrahedron*, **14**, 230 (1961); *Proc. Acad. Sci. USSR, Phys. Chem. Sect.*, **137**, 231 (1961).

$$\iiint_{\Omega_e} e^{-ar} dv = \iint_{\Sigma} e^{-ar} \left[\frac{1}{ar} + \frac{2}{(ar)^2} + \frac{2}{(ar)^3} \right] \vec{r} \cdot \vec{n}_e(\Omega) d\sigma \quad (13)$$

We put $a = \alpha/(4R_i R_j)^{0.5}$.

We can also use Ostrogradski's formula to calculate the volume Ω of the solute (see Appendix A, eq 14-16)

$$\Omega = \iiint_{\Omega} dv = \iint_{\Sigma} \frac{1}{3} \vec{r} \cdot \vec{n}_e(\Omega) d\sigma \quad (17)$$

b. *Choice of the Integration Surface.* The integration surface Σ is selected in such a way as to take into account the form of the solute molecule.

The volume Ω of the solute is deduced from the van der Waals volume of the solute in the following way. Each van der Waals radius R_i of the atom i of the solute molecule is multiplied by the same factor λ_c that is such as the volume obtained by juxtaposition of spheres of radius $\lambda_c R_i$ and center i (i labels the atoms of the solute) is equal to the effective volume of the solute. A factor λ_s is defined in the same way for the solvent. The volume $\Omega = V_{\text{solute}}^{\text{eff}}$ of the solute is not homothetic of the van der Waals volume of the solute, since interatomic distances remain unvarying. When the temperature T varies, the effective volume varies, and λ_c varies. This leads to a variation of the energy E with the temperature, since molecules are at different distances according to the value of T . The variation of $V_{\text{solute}}^{\text{eff}}$ with T represents this effect of variation of E with T .

Our factor λ fulfills the same purpose as the "additional thickness b " introduced by Kihara and Jhon,^{3b} namely to get for the solute molecule a convenient "effective size" (taking into account the thermal expansion). More precisely, the additional radius $b/2$ relative to the solute molecule corresponds to our radius increase $R_i(\lambda - 1)$.

The integration surface Σ is obtained by the juxtaposition of parts of surface of spheres ($i, \lambda_c R_i$), the calculation of λ_c is made with the Raphson-Newton iteration formula, the starting value being $\lambda_0 = (V^{\text{eff}}/V_{\text{van der Waals}})^{1/3}$.

The calculation of the area of the constitutive parts of Σ , the boundary of the volume $\Omega = V_{\text{solute}}^{\text{eff}}$ can be made by numerical integration. The van der Waals volume and the effective volume $V^{\text{eff}} = \Omega = f(\lambda_c)$ are calculated with formula 17.

c. *Numerical Calculations of the Integrals.* The integrals to calculate have the form $\iint_{\Sigma} g(r) d\sigma$ where $g(r)$ is one of the integrands that appear in the right side of eq 12, 13, and 17.

We call S_i^e the part of the sphere ($i, \lambda_c R_i$) that belongs to Σ , the rest of the sphere being inside other

spheres. The integrals can be written as integrals on the whole sphere S_i by introducing the characteristic function $Y_{S_i^e}$ of S_i^e ; that is, the function defined by $Y_{S_i^e}(r) = 1$ if the point r belongs to S_i^e , $Y_{S_i^e}(r) = 0$ if the point r does not belong to S_i^e .

We then have

$$\iint_{S_i^e} g(r) d\sigma = \iint_{S_i} Y_{S_i^e}(r) g(r) d\sigma \quad (18)$$

After the introduction of polar angles θ and φ and of the variable $u = -\cos \theta$ and noting r_i the radius of the sphere S_i , we obtain

$$\iint_{S_i^e} g(r) d\sigma = \iint_{S_i} Y_{S_i^e}(r(\theta, \varphi)) g(r(\theta, \varphi)) r_i^2 \sin \theta d\theta d\varphi = r_i^2 \int_{-1}^{+1} du \int_0^{2\pi} Y_{S_i^e}(r(u, \varphi)) g(r(u, \varphi)) d\varphi \quad (19)$$

Equation 19 is calculated numerically by using a grid of points $[r_k (k = 1, \dots, \nu)]$ uniformly distributed on the sphere S_i ; the integral 19 is then estimated by the sum

$$\frac{1}{\nu} \sum_{k=1}^{\nu} Y_{S_i^e}(r_k) g(r_k) \quad (20)$$

We have tried two types of grids: grids obtained as the product of two uniform grids for the variables θ and φ and grids obtained by the Korobov's method¹⁰ (see Appendix B). The comparison of the results has shown that Korobov's grids give, for a same number of points of integration, a higher accuracy that is more stable when the number of points increases; finally we used the Korobov's grid with 610 points on each sphere S_i . For the molecules CO and CH₄, we have calculated the van der Waals area and volume exactly, and with the Korobov's grid we have obtained an accuracy of 1/1000.

3. *Calculation of "Calibration Constants" K_{ij}^d and K_{ij}^r .* It is necessary to introduce the calibration constants K_{ij} to get, by the integration method, results that are as close as possible to those given by a discrete sum over molecules packed around the solute molecule.

Consider the case of a pure liquid made of spherical atoms of radius a and calculate directly (without introduction of K_{ij}^d) the integral of dispersion

$$\iiint_{\Omega} \frac{1}{r^6} \frac{dv}{V^{\text{eff}}} = \frac{1}{V^{\text{eff}}} \int_R^{\infty} 4\pi r^2 \frac{dr}{r^6} = \frac{\sqrt{2}}{d_0^3} \left(\frac{4\pi}{3R^3} \right) \quad (21)$$

We can compare this result with the discrete sum which is known in this case¹¹

(10) N. M. Korobov, "Teoretiko-tchislovie metodi v priblizhenom analize" "Number-theoretical methods in applied analysis," Gosudarstvennoe Izdatel'stvo, Fiziko-Matematicheskoy Literatury, Moscow, 1963 (in Russian), Chapter III; (a) section 10, pp 146-148; (b) section 11, p 162.

(11) J. O. Hirschfelder, C. F. Curtiss, and R. B. Bird, "Molecular Theory of Gases and Liquids," Wiley, New York, N. Y., 1964, p 1040.

$$\sum_{i=1}^{\infty} n_i/r_i^6 = 14.454/d_0^6$$

In formula 21 we have put, instead of V^{eff} , its value as a function of the distance to the nearest neighbors $d_0 = 2a$, and of the packing coefficient $1/\sqrt{2}$.¹²

If in (21) we choose $R = a = d_0/2$ and $R = d_0$, we, respectively, obtain $47.39/d_0^6$ and $5.92/d_0^6$. None of these two values of R gives satisfying results; this can be assigned to the fact that the integral assumes an absolutely uniform distribution of the centers outside the solute, while the discrete sum corresponds to a distribution function that is not at all uniform. We know that in the liquid the distribution of the molecules is not uniform at short distance; now it is the distribution immediately near the central molecule which is important.

The calibration constant K_{ij} can be defined as the ratio between the energy calculated by discrete summation and the energy calculated by integration. This constant is analogous to the "factor f " introduced by Kihara and Jhon^{3b} in their formula $\Delta_2 = fn \int_{\sigma_{AB}}^{\infty} U_{AB}(\rho) \langle S_{A+\rho+B} \rangle_{\text{av}} d\rho$ for the interaction between the solute molecule and the solvent. If A and B are taken to be spheres of equal radius $a = d_0/2$, $\langle S_{A+\rho+B} \rangle_{\text{av}}$ becomes $4\pi\rho^2$, and with $U_{AB}(\rho) = 1/\rho^6$ and n (the number density of the solvent) $= 1/V^{\text{eff}}$, $n \int_{\sigma_{AB}}^{\infty} U_{AB}(\rho) \langle S_{A+\rho+B} \rangle_{\text{av}} d\rho$ reduces to our eq 21. Then our K_{ij} exactly corresponds to f . However, it must be emphasized that Kihara and Jhon use a single f , independent from the solute, for the whole solute-solvent potential (including both the dispersion and repulsion term), while we introduce specific K_{ij}^{d} and K_{ij}^{r} for the dispersion and repulsion term, and this for each kind of atoms pair (i, j) (and since the K_{ij}^{d} and K_{ij}^{r} turn out to be different, they cannot be easily reduced to a single factor independent from the solute).

Moreover, we define a method of calculation for the K_{ij}^{d} and K_{ij}^{r} depending only on the atom species i and j , while the f factor^{3b} must be apparently empirically determined for every solvent.

The constants K_{ij} are directly calculable in the simplest case of packing of spheres.

The main hypothesis that allows us to treat any molecule consists in assuming that the constants K_{ij} which correspond to the packings of spheres can be used to calibrate in the general case; in a way, we take into consideration the distribution of the atoms of the solvent around the solute, avoiding the explicit construction of a distribution function, for each type of pairs of atoms and for each solute. For a pair (i, j) of atoms, we obtain the equations defining K_{ij} by equaling calculated energy by integration, and calculated energy by discrete summation

$$K_{ij}^{\text{d}} C_1 (R_{ij}^{\text{d}})^6 \frac{1}{V_j^{\text{eff}}} \iiint_{\Omega} \frac{dv}{r^6} = C_1 (R_{ij}^{\text{d}})^6 \sum_{l=1}^{\infty} n_l / r_l^6 \quad (22)$$

$$K_{ij}^{\text{r}} C_2 \frac{1}{V_j^{\text{eff}}} \iiint_{\Omega} \exp(-a_{ij}r) dv = C_2 \sum_{l=1}^{\infty} n_l \exp(-a_{ij}r_l) \quad (23)$$

$$a_{ij} = \alpha / (4R_i R_j)^{0.5} \text{ and } (R_{ij}^{\text{d}})^2 = 4R_i R_j$$

n_l is the number of atoms of type j situated at the distance r_l of the central atom i .

When the solute is an atom i , the volume Ω is a sphere of radius $\lambda_c R_i$; when the solvent is made of identical atoms j , the effective volume V_j^{eff} of the solvent is a sphere of radius $\lambda_s R_j$. After integration and substitution of V_j^{eff} , the constants K_{ij} take the form

$$K_{ij}^{\text{d}} = (\lambda_c \lambda_s)^3 (R_i R_j)^3 \sum_{l=1}^{\infty} n_l / r_l^6 \quad (24)$$

$$K_{ij}^{\text{r}} = \frac{1}{3} (a_{ij} \lambda_s R_j)^3 \times \frac{e^{a_{ij} \lambda_c R_i}}{(a_{ij} \lambda_c R_i)^2 + 2a_{ij} \lambda_c R_i + 2} \sum_{l=1}^{\infty} n_l \exp(-a_{ij} r_l) \quad (25)$$

λ_c and λ_s have the definition given in section II2b.

To calculate the summations of formulas 24 and 25, it is necessary to build a packing of spheres of radius $\beta \lambda_s R_j$ around the central sphere of radius $\beta \lambda_c R_i$. The origin of β is the following: the sphere of radius $\lambda_c R_i$ is only used for the integration; to build the packing of spheres, we have to define packing radii R_i^{p} and R_j^{p} for the types i and j . We fix them by requiring that the packings of the spheres j alone (or i) correctly reproduce molecular volumes V^{eff} , which, respectively, are $(4\pi/3) (\lambda_s R_j)^3$ and $(4\pi/3) (\lambda_c R_i)^3$; for a packing of identical spheres, the distance d_0 between nearest neighbors is connected to the effective volume by the relation¹²

$$V^{\text{eff}} = \frac{1}{\sqrt{2}} d_0^3$$

We then obtain the packing radius R^{p}

$$R_j^{\text{p}} = \frac{d_0}{2} = \frac{1}{2} \left[V_j^{\text{eff}} \sqrt{2} \right]^{1/3} = \frac{1}{2} \left[\frac{4\pi}{3} (\lambda_s R_j)^3 \sqrt{2} \right]^{1/3} = \left(\frac{\pi}{3\sqrt{2}} \right)^{1/3} \lambda_s R_j \quad (26)$$

We note

$$\beta = \left(\frac{\pi}{3\sqrt{2}} \right)^{1/3} = 0.905 \quad (27)$$

The packing radius $\beta \lambda_s R_j$ is lower than the radius $\lambda_s R_j$ of the effective sphere. When $\lambda_c = \lambda_s = \lambda$ (it is the case for pure liquid), we can simplify the expression of K_{ij}^{d} in an important way. Indeed, instead of building a packing of spheres of radius $\beta \lambda R_j$, around a sphere of radius $\beta \lambda R_i$, we can construct a packing of

(12) E. A. Moelwyn-Hughes, "Physical Chemistry," Pergamon Press, Elmsford, N. Y., 1961, Chapter 13, p 551.

spheres of radius R_j around a sphere of radius R_i ; we pass from this packing to the first one by a similarity of ratio $\beta\lambda$; then, in the two packings, values of n_l are the same, and we have $r_l = \beta\lambda r_l^\circ$ where r_l° is the same as r_l for the packing of spheres (R_l); values of n_l and r_l° are determined once for all, independently of the value of λ that varies with T as the effective volume. K_{ij}^d takes the form

$$K_{ij}^d = \lambda^6 (R_i R_j)^3 \sum_{l=1}^{\infty} n_l / (\beta\lambda r_l^\circ)^6 = \frac{9}{32\pi^2} \sum_{l=1}^{\infty} n_l (R_{ij}^\circ / r_l^\circ)^6 \quad (28)$$

where $R_{ij}^\circ = (4R_i R_j)^{0.5}$.

The ratios $(R_{ij}^\circ / r_l^\circ)$ only depend on the ratio of the radii R_i / R_j .

In the same way, K_{ij}^r takes the form

$$K_{ij}^r = \frac{1}{3} (a_{ij} \lambda R_j)^3 \frac{\exp(a_{ij} \lambda R_i)}{(a_{ij} \lambda R_i)^2 + 2a_{ij} \lambda R_i + 2} \times \sum_{l=1}^{\infty} n_l [\exp(-a_{ij} r_l^\circ)]^{\beta\lambda} \quad (29)$$

Contrary to K_{ij}^d , K_{ij}^r depends on λ , but the values of the n_l and the most important exponentials can be calculated once for all. This way is practicable since the series quickly converges because of the rapid diminution of the exponentials; it is sufficient to take a small number of spheres (R_j) to obtain the value of the series.

We have written a program that allows us to generate a packing of spheres around any sphere and to obtain the values of the n_l and r_l° of eq 24, 25, 28, and 29. For the dispersion, we must go far enough to evaluate the series correctly; in practice, we have used between 90 and 150 spheres according to the cases, and we have replaced the missing part by an integral. We give in Table I the values of $\sum_{l=1}^{\infty} (R_{ij}^\circ / r_l^\circ)^6$. For K_{ij}^r , it is sufficient to take into account the n_1 spheres of the first shell all situated at the distance $r_1^\circ = (R_i + R_j)$ of the center i of the central atom and the n_2 nearest spheres of the following shell. The last ones are not all rigorously at the same distance from the center i , but they are at distances sufficiently near so that we can take a single mean value r_2° . We then have

$$\sum_{l=1}^{\infty} n_l [\exp(-a_{ij} r_l^\circ)]^{\beta\lambda} \simeq n_1 [\exp(-a_{ij} r_1^\circ)]^{\beta\lambda} + n_2 [\exp(-a_{ij} r_2^\circ)]^{\beta\lambda} \quad (30)$$

4. Choice of the Constants of the Potential. Kitaygorodski has calculated his energies with the function of binary interaction⁹

$$e_{ij} = 3.5 \left[- \left(\frac{r_{ij}^\circ}{r_{ij}} \right)^6 + \frac{6}{\alpha} e^\alpha \exp(-\alpha r_{ij} / r_{ij}^\circ) \right] / \left(-11.39 + \frac{6e^{\alpha/3}}{\alpha} \right) \quad (31)$$

Table I: Values of $\sum_{l=1}^{\infty} (R_{ij}^\circ / r_l^\circ)^6$, n_1 , n_2 , r_1° / R_{ij}° , and r_2° / R_{ij}°

R_i (central atom), Å	R_j , Å	$\sum_{l=1}^{\infty} (R_{ij}^\circ / r_l^\circ)^6$	n_1	r_1° / R_{ij}°	n_2	r_2° / R_{ij}°
1.20	1.20	14.454	12	1.000	4	1.453
1.20	1.70	6.971	6	1.015	3	1.301
1.20	1.77	6.643	6	1.019	3	1.347
1.70	1.20	18.216	14	1.015	3	1.110
1.70	1.70	14.454	12	1.000	4	1.453
1.77	1.20	20.629	18	1.019	2	1.187
1.77	1.77	14.454	12	1.000	4	1.453

where r_{ij}° is the equilibrium distance which is deduced from the van der Waals radii by increasing those by about 12%.¹³

For a given value of r_{ij}° , it is sufficient to fix α to determine e_{ij} . Kitaygorodski chose $\alpha = 13$ and obtained for the calculation of the sublimation energy of the crystal of methane too large a value:¹⁴ 3.57 kcal/mol, while the experimental value for the absolute zero is about 2.508¹⁵ or 2.74 kcal/mol.¹⁴

Such an overvaluation of about 15% cannot be only explained by the nonadditivity of pair interaction energies, which would reduce the dispersion energy of about 7%.⁷ To draw nearer to the experimental results, we have modified the value of α . We have calculated the energy of the CH₄ crystal with the formula given in ref 16 for the means r^{-6} and $e^{-\alpha r}$, using $\alpha = 13.80$, $r_{CC}^\circ = 3.80$ Å, $r_{HH}^\circ = 2.68$ Å, and $r_{CH}^\circ = 3.19$ Å. For a distance between carbon atoms of 4.16 Å,¹⁵ we have obtained a total dispersion energy of -3.96 kcal/mol, and a total repulsion energy of +1.18 kcal/mol; after a reduction of 7% on the dispersion energy (see later the nonadditivity effect) this gives a total energy of -2.66 kcal/mol. The same calculation for a distance of 4.11 Å¹⁶ gives a total energy of -2.69 kcal/mol (E_d after reduction = -4.19 kcal/mol; $E_r = +1.50$ kcal/mol). The value $\alpha = 13.80$ seems to us satisfactory; formula 31 becomes

$$e_{ij} = -0.1098 \left(\frac{r_{ij}^\circ}{r_{ij}} \right)^6 + 47,000 \exp(-13.80 r_{ij} / r_{ij}^\circ) \quad (32)$$

To go from (32) to (1) that contains van der Waals radii, we have to multiply the dispersion coefficient by $(r_{CC}^\circ / 2R_C)^6$ and the coefficient α by $(2R_C / r_{CC}^\circ)$.⁴ To evaluate these ratios, we have used $r_{CC}^\circ = 3.80$ Å,^{9,14}

(13) N. A. Ahmed, A. I. Kitaygorodski, and K. V. Mirskaya, *Acta Crystallogr., Sect. B*, **27**, 867 (1971).

(14) A. I. Kitaygorodski and K. V. Mirskaya, *Sov. Phys. Crystallogr.*, **9**, 137 (1964).

(15) E. A. Mason and W. E. Rice, *J. Chem. Phys.*, **22**, 843 (1954).

(16) A. I. Kitaygorodski and K. V. Mirskaya, *Sov. Phys. Crystallogr.*, **6**, 408 (1962).

Table II: Values of Calculated and Experimental Energies^a

Compound	<i>T</i> , °K	Molar volume, cm ³	λ	$E_d/2$	$E_r/2$	$E_{\text{calcd}} = E/2$	$E_{\text{exp}} = - \Delta E_{\text{v}}^{\text{exp}} $	$\Delta H_{\text{v}}^{\text{exp}}$	$E_{\text{calcd}}/E_{\text{exp}}$
Methane	111.66	37.8	1.397	-2.111	0.199	-1.91	-1.73	1.955	1.10
Ethane	184.52	54.7	1.382	-3.721	0.379	-3.34	-3.15	3.517	1.06
Propane	231.08	75.9	1.424	-4.361	0.318	-4.04	-4.03	4.487	1.00
	298.15	89.48	1.533	-2.955	0.094	-2.86	-2.95	3.542	0.97
Isobutane	261.42	97.7	1.456	-4.843	0.542	-4.57	-4.57	5.090	1.00
	298.15	105.48	1.513	-3.982	0.144	-3.84	-3.98	4.570	0.96
<i>n</i> -Butane	272.65	96.6	1.442	-5.159	0.323	-4.83	-4.81	5.352	1.00
	298.15	101.43	1.474	-4.625	0.228	-4.40	-4.44	5.035	0.99
Neopentane	282.65	119.68	1.492	-5.023	0.207	-4.82	-4.85	5.438	0.99
	298.15	123.31	1.511	-4.724	0.168	-4.56	-4.61	5.205	0.99
Isopentane	298.15	117.38	1.471	-5.542	0.271	-5.27	-5.34	5.937	0.99
	301.00	117.96	1.477	-5.451	0.255	-5.20	-5.30	5.901	0.98
<i>n</i> -Pentane	298.15	116.10	1.455	-6.006	0.339	-5.67	-5.72	6.316	0.99
	309.22	118.38	1.467	-5.730	0.294	-5.44	-5.55	6.160	0.98
<i>n</i> -Hexane	298.15	131.6	1.434	-7.508	0.490	-7.02	-6.95	7.541	1.01
	341.49	140.9	1.489	-6.213	0.268	-5.94	-6.21	6.896	0.96
Cyclohexane	298.15	108.74	1.388	-8.181	0.738	-7.44	-7.30	7.896	1.02
	353.87	116.99	1.447	-6.690	0.389	-6.30	-6.46	7.16	0.97
<i>n</i> -Decane	298.15	195.90	1.409	-13.075	1.012	-12.06	-11.68	12.277	1.03
	447.27	235.82	1.555	-7.912	0.200	-7.71	-8.50	9.388	0.91
<i>n</i> -Hexadecane	298.15	294.08	1.385	-22.116	2.032	-20.08	-18.79	19.38	1.06
	559.94	396.15	1.652	-9.334	0.107	-9.23	-11.10	12.24	0.83
<i>n</i> -Eicosane	298.15	359.83	1.376	-28.187	2.761	-25.42	-23.5	24.1	1.08
	617.0	513.9	1.704	-9.921	0.074	-9.85	-12.5	13.74	0.79
Benzene	298.15	89.40	1.332	-8.111	1.365	-6.75	-7.50	8.090	0.91
	353.25	96.04	1.376	-6.799	0.823	-5.97	-6.65	7.352	0.90

^a In kcal/mol.

and $R_C = 1.70 \text{ \AA}$ which is the van der Waals radius for saturated carbons given in ref 17. We then obtain

$$e_{ij} = -0.214(4R_i R_j)^3 / r_{ij}^6 + 47,000 \exp[-12.35r_{ij}/(4R_i R_j)^{0.5}] \quad (33)$$

It is this pair potential that we have used for the applications reported in section III, taking the van der Waals radii proposed by Bondi¹⁷ (except for R_H in aromatic molecules, see section III): $R_C = 1.70 \text{ \AA}$ for saturated carbons; $R_C = 1.77 \text{ \AA}$ for aromatic carbons, $R_H = 1.20 \text{ \AA}$ in all the cases. The potential e_{ij} of formula 33 is a true pair potential and not an effective pair potential. To take into consideration the non-additivity of the dispersion energies, we have done a correction of 7% on the total dispersion energy calculated with the hypothesis of additivity of binary interactions. A perturbation treatment to the third order would introduce forces between triplets; these forces have been evaluated to be 2–9% of the cohesive energy for crystals of rare gases⁵ and 2–11% for organic molecules.^{7,8} For the interaction between two molecules of CH_4 the reduction is 21%,⁷ but for the total energy of a crystal or a liquid, the reduction of the sum of the dispersion energies is one-third of the previous

percentage (ref 7, part F and G, ref 8, p 164), that is 7%. We have assumed that the reduction of the total dispersion energy was 7% for all hydrocarbons.

III. Applications and Discussion

The previously described model has been used for the study of pure substances. The chosen compounds are saturated hydrocarbons, these ones having negligible electrostatic energies because of the small charges carried by their atoms. The calculated energy of the central molecule with all its surrounding can be compared with twice the vaporization energy. We discuss in Appendix C the nature of the calculated energy. Table II contains the values of the calculated energies at the boiling point and at 25°, and the values of the experimental vaporization enthalpies (ref 18 and 19, p

(17) A. Bondi, "Physical Properties of Molecular Crystals, Liquids and Glasses," Wiley, New York, N. Y., 1968; A. Bondi, *J. Phys. Chem.*, **68**, 441 (1964).

(18) API, 44 Tables, "Selected Values of Properties of Hydrocarbons and Related Compounds," American Petroleum Institute Research Project No. 44, Thermodynamics Research Center, Texas A&M University.

(19) J. H. Hildebrand, J. M. Prausnitz, and R. L. Scott, "Regular and Related Solutions—The Solubility of Gases, Liquids and Solids," Van Nostrand-Reinhold, Princeton, N. J., 1970.

217). Experimental vaporization energies are deduced from vaporization enthalpies by the relation¹⁹

$$|\Delta E_v^{\text{exp}}| = |\Delta H_v^{\text{exp}}| - RT \quad (34)$$

R is the constant of perfect gases and T the absolute temperature.

RT stands for $\Delta(PV) = P\Delta V = P(V_{\text{gas}} - V_{\text{liq}})$. This replacement is valid if $V_{\text{liq}} \ll V_{\text{gas}}$ (therefore T must be sufficiently far apart from the critical temperature) and if $PV_{\text{gas}} \simeq RT$ (the vapor must be as near as possible to a perfect gas, the vapor pressure must be low). The last column of Table II shows that the obtained results are satisfactory, the agreement is very good in most cases.

We find a tendency to underestimate the energy at high temperature. Since the energy that we actually calculate can be considered as the energy of a mean configuration rather than the exact mean energy over all the configurations according to the real motion of the molecules, it is quite possible that the difference between these two energies increases with the temperature. We have tried our model on the molecule of benzene too, taking $R_C = 1.77 \text{ \AA}$, and $R_H = 1.20 \text{ \AA}$ instead of 1.00 \AA given in ref 17. We explain here the reasons of this choice. For the benzene molecule, Bondi's radii take into account the whole interaction energy implicitly, that is, the electrostatic energy as well (the benzene has a zero dipole moment, but a nonzero quadrupole moment,^{20,21} which may give a nonnegligible electrostatic energy in contrast with the case of CH_4). The electrostatic energy is repulsive for two stacked benzene molecules and gives an increased equilibrium distance which may be reproduced by attributing an increased radius to the C atoms. On the contrary the electrostatic energy is attractive when the planes of the benzene are perpendicular and gives a decreased equilibrium distance which may be reproduced by attributing a sufficiently decreased radius to the H atoms. As we need values of radii suited to the calculation of dispersion and repulsion energies, there is no reason to take Bondi's radii directly for benzene. Now, from a theoretical point of view, if we want to put London's formula under the form $(4R_i R_j)^3 / r_{ij}^6$, the radius R_i should be approximately proportional to $\alpha \sqrt{I}$ (α is the polarizability, I is the mean excitation energy); as α decreases more than I decreases when going from an aliphatic carbon to an aromatic carbon,²² it appears convenient to increase the van der Waals radius of an aromatic carbon. On the contrary, no such modifications appear for the H atoms. We have therefore used different van der Waals radii for a saturated carbon and an aromatic carbon, but the same van der Waals radius for the hydrogen of saturated and aromatic molecules.

For benzene, the calculated energies are underestimated more than for the saturated molecules of corresponding size. This is not surprising, since the electro-

static energy has not been calculated and would add a supplementary attractive contribution; without being as important as indicated in the ref 23, the electrostatic energy is probably nonnegligible.

IV. Conclusion

The proposed method seems more convenient than the continuum model based on the representation of the solute molecule by a single sphere, because it takes into consideration the real shape of the molecules. We obtain reasonable results for the methane CH_4 as well as for the decane $\text{C}_{10}\text{H}_{22}$; even for the hexadecane $\text{C}_{16}\text{H}_{34}$ and the eicosane $\text{C}_{20}\text{H}_{42}$, the results are good at 25° , the only defect being a too rapid decrease when T increases. Our model reproduces the qualitative variation of the energy as a function of T and also the small differences between the isomers as in the case of the three pentanes.

In comparison with our previous complete discrete model,¹ the computation times are considerably reduced. The longest part of the computation corresponds to the determination of the packings of spheres (about 2 min for each packing on a CDC 6600); but these characteristics are just dependent on the ratio of the radii and could be tabulated once for all as a function of this ratio. A further improvement would be to fit an analytical formula to represent these tabulated data and to be able to use the model for the binary mixtures. The step that takes an intermediate time (about 10 sec for CH_4 , 59 sec for C_5H_{12} , 110 sec for $\text{C}_{10}\text{H}_{22}$, 300 sec for $\text{C}_{20}\text{H}_{42}$) is the computation of the integrals 12 and 13, but these integrals can be calculated for a given solute independently of any solvent; they only depend on the temperature through the intermediate of the volume Ω and of the surface Σ . Therefore they could also be tabulated for a given molecule at a given temperature, for all the possible values of the van der Waals radii of the outside atoms.

The last step that depends both on the solute and on the solvent involves only simple combinations of the just-mentioned integrals and of the constants K_{ij}^d and K_{ij}^r ; accordingly, the necessary computation time is very short; actually, this last step is quite feasible on a desk calculator.

To use the model for the calculation of the energy of dissolution of a gas in a liquid, we shall have to calculate the cavitation energy^{1,24} and the solute-solvent interaction energies; besides the macroscopic value of the surface tension, the evaluation of this quantity at the microscopic level may be tried using the results on pure liquids.

(20) D. E. Stogryn and A. P. Stogryn, *Mol. Phys.*, **11**, 371 (1966).

(21) M. J. Mantione, *Int. J. Quantum Chem.*, **3**, 185 (1969).

(22) R. J. W. Le Fevre, *Adv. Phys. Org. Chem.*, **3**, 1 (1965).

(23) P. Sen and S. Basu, *J. Chem. Phys.*, **48**, 4075 (1968).

(24) H. H. Uhlig, *J. Phys. Chem.*, **41**, 1215 (1937).

The calculation of the energy of a solute molecule with a solvent assumes that the solution is sufficiently dilute; it is conceivable, however, to extend the model for solutions of arbitrary concentration by introducing in eq 4 a weighted summation on the two types of the molecules, the weights being the respective molar fractions.

In the case of molecules with nonnegligible atomic net charges, it becomes necessary to calculate the electrostatic and polarization interactions. This problem has been treated using macroscopic dielectric constants of the solvent in the case of spherical^{25,26a,27} or ellipsoidal^{26b-29} cavities. We intend to extend this treatment to a cavity limited by the surface Σ of the present model.

Appendix A

Transformation of a Volume Integral into a Surface Integral. We designate by Σ the boundary of the integration volume Ω , and we introduce a sphere $S(R)$ of radius R that completely contains Σ . (R will tend towards $+\infty$ after.) We use Ostrogradski's formula for the volume $\Omega e(R)$ included between Σ and $S(R)$

$$\iiint_{\Omega e(R)} \operatorname{div} \vec{W} dv = \iint_{\Sigma + S(R)} \vec{W} \cdot \vec{n}_e(\Omega e(R)) d\sigma \quad (5)$$

\vec{n}_e is the outside normal to Σ or $S(R)$, directed toward the outside of $\Omega e(R)$. So long as the integrals on $\Omega e(R)$ and $S(R)$ converge when $R \rightarrow +\infty$, (5) gives

$$\iiint_{\Omega e} \operatorname{div} \vec{W} dv = \iint_{\Sigma} \vec{W} \cdot \vec{n}_e d\sigma + \lim_{R \rightarrow \infty} \iint_{S(R)} \vec{W} \cdot \vec{n}_e d\sigma \quad (6)$$

Notice that, on $S(R)$, \vec{n}_e at a point \vec{R} is confused with the unit vector $\vec{u} = \vec{R}/R$. Knowing $F(r)$, we have to find \vec{W} such as $F(r) = \operatorname{div} \vec{W}$. Given any function $F(r)$, we shall have

$$F(r) = \operatorname{div} \vec{W} \text{ if } \vec{W} = f(r) \cdot \vec{r} \quad (7)$$

where $f(r)$ is defined by the differential equation

$$F(r) = rf'(r) + 3f(r) \quad (8)$$

This equation is solved by multiplying the two members by r^2 to obtain

$$r^2 F(r) = \frac{d}{dr} [r^3 f(r)] \quad (9)$$

$$\vec{W}(\vec{r}) = \left[\frac{1}{r^2} \int_{r_0}^r x^2 F(x) dx \right] \vec{u} = \left[\frac{1}{r^3} \int_{r_0}^r x^2 F(x) dx \right] \vec{r} \quad (10)$$

$\vec{W}(r)$ is only defined to a vector $(c/r^2)\vec{u}$. When c varies, the two surface integrals of (6) vary, as their sum stays constant. It is convenient to choose c (that is the integration limit r_0) so as to reduce to zero the second surface integral of (6) (out-going flow at the infinite).

Using (7) and (10) we easily show that

$$\lim_{R \rightarrow \infty} \iint_{S(R)} \vec{W} \cdot \vec{n}_e d\sigma = Rf(R) \iint_{S(R)} d\sigma = 4\pi \int_{r_0}^{\infty} x^2 F(x) dx$$

Then to reduce to zero this integral, we have to take $r_0 = \infty$; it is this value we use for the following, and we obtain formula 11 of the text. For the volume Ω of the solute, the integral $\iiint_{\Omega} dv$ corresponds to the particular case $F(r) = 1$.

In this case the Ostrogradski's formula is written

$$\iiint_{\Omega} \operatorname{div} \vec{W} dv = \iint_{\Sigma} \vec{W} \cdot \vec{n}_e(\Omega) d\sigma \quad (14)$$

As the origin of the coordinates is inside the volume Ω , it is necessary to be cautious in the determination of the vector \vec{W} such as $\operatorname{div} \vec{W} = F(r)$. The form of \vec{W} is that one obtained in (10) which is defined to a vector $(c/r^2)\vec{u}$; all these field vectors have the property $\operatorname{div} \vec{W} = F(r)$ for any point distinct from the origin, but only one of them can verify $\operatorname{div} \vec{W} = F(r)$ at the origin. Indeed, $\operatorname{div} (\vec{u}/r^2) = 4\pi\delta(\vec{r})$ as it results from Gauss's theorem in electrostatic ($\delta(r)$ is the Dirac function). We have to choose among the field vectors $\vec{W}(r)$ the one which does not contain terms \vec{u}/r^2 when $r \rightarrow 0$. As $\vec{W}(r) \rightarrow (\vec{u}/r^2) \int_{r_0}^0 x^2 F(x) dx$, a general way to satisfy this condition is to take $r_0 = 0$.

We then have

$$\vec{W}(r) = \left[\frac{1}{r^2} \int_0^r x^2 F(x) dx \right] \vec{u} = \left[\frac{1}{r^3} \int_0^r x^2 F(x) dx \right] \vec{r} \quad (15)$$

As $F(x)$ is finite at the origin ($F(r) = 1$), the transformation into surface integral can be applied for the calculation of the volume with

$$\vec{W}(r) = \frac{\vec{u}}{r^2} \int_0^r x^2 dx = \frac{\vec{r}}{3} \quad (16)$$

we then obtain formula 17 of the text.

Appendix B

Korobov's Grids for Numerical Integration. Quite generally, Korobov expresses the integral of a function $f(x_1 \dots x_s)$ on the unit hypercube by the formula

$$\int_0^1 \dots \int_0^1 f(x_1 \dots x_s) dx_1 \dots dx_s = \frac{1}{p} \sum_{k=1}^p f\left(\left\{\frac{a_1 k}{p}\right\}, \dots, \left\{\frac{a_s k}{p}\right\}\right) - R \quad (35)$$

where $\{z\}$ is the fractional part of z . The remainder

(25) L. Onsager, *J. Amer. Chem. Soc.*, **58**, 1486 (1936).

(26) (a) J. G. Kirkwood and F. H. Westheimer, *J. Chem. Phys.*, **6**, 506 (1938); (b) *ibid.*, **6**, 513 (1938).

(27) W. B. Bonnor, *Trans. Faraday Soc.*, **47**, 1143 (1951).

(28) A. Wada, *J. Chem. Phys.*, **22**, 198 (1954).

(29) T. L. Hill, *ibid.*, **12**, 147 (1944).

R may be made small by choosing the coefficients $a_1 \dots a_s$ in a convenient way. Korobov calls optimal coefficients such convenient coefficients $a_1 \dots a_s$, and studies in his book¹⁰ their properties and the methods to obtain such sets of optimal coefficients. The very short summary of Stroud³⁰ does not give any information concerning the special case $s = 2$, but this case is treated by Korobov^{10a} and we summarize his results here.

One builds the so-called Fibonacci's sequence ($Q_0, Q_1, \dots, Q_n, \dots$) defined by $Q_0 = 1, Q_1 = 1, \dots, Q_k = Q_{k-1} + Q_{k-2}$ for $k \geq 2$. The first numbers are therefore 1, 1, 2, 3, 5, 8, 13.

Then, if we take $p = Q_n$, the integers $a_1 = 1$ and $a_2 = Q_{n-1}$ are optimal coefficients relative to $p = Q_n$. Hence, according to eq 35, we have the approximate evaluation

$$\int_0^1 \int_0^1 f(x_1, x_2) dx_1 dx_2 \simeq \frac{1}{Q_n} \sum_{k=1}^{Q_n} f\left(\left\{\frac{k}{Q_n}\right\}, \left\{\frac{Q_{n-1}k}{Q_n}\right\}\right) \quad (36)$$

For the applications of the present paper, we used $Q_{n-1} = 377$ and $Q_n = 610$ corresponding to $n = 14$. In our problem, we actually calculate integrals over a part of the $(0,1) \times (0,1)$ set, namely the part S_i^e of the sphere S_i (see section II2c). Then we may, according to Korobov's theorem 25,^{10b} use the approximate evaluation

$$\int_V \dots \int_V f(x_1 \dots x_s) dx_1 \dots dx_s \simeq \frac{1}{p} \sum_{k=1}^p f\left(\left\{\frac{a_1 k}{p}\right\}, \dots, \left\{\frac{a_s k}{p}\right\}\right) \times Y_V\left(\left\{\frac{a_1 k}{p}\right\}, \dots, \left\{\frac{a_s k}{p}\right\}\right) \quad (37)$$

where $Y_V(x_1 \dots x_s)$ is the characteristic function of the domain V , that is $Y_V(x_1 \dots x_s) = 1$ if $(x_1 \dots x_s)$ belongs to V , and $Y_V(x_1 \dots x_s) = 0$ otherwise. To transform the integral 19 of the text, it is sufficient to make the change of variables $x = (u + 1)/2$ and $y = \varphi/2\pi$, which gives

$$\int_{-1}^{+1} du \int_0^{2\pi} G(u, \varphi) d\varphi = 4\pi \int_0^1 dy \int_0^1 G[u(x), \varphi(y)] dx \quad (38)$$

where G includes the characteristic function according to 37.

If one wants to use, instead of a Korobov's grid, the product of two uniform grids for φ and u , one must pay attention to the fact that $u = \pm 1$ defines the same point whatever is φ . It is therefore necessary to use for u a grid that does not contain these points, for instance

$$\varphi = 2l\pi/n \quad l = 1 \dots n$$

$$u = \left(-1 + \frac{1}{2m}\right) + \frac{k}{m} \quad k = 0, \dots, 2m - 1$$

Appendix C

The Calculation of the Energy E and of the Free Energy F . The exact mean energy of any assembly of molecules is

$$E = \frac{\int \dots \int U(\Omega) \exp(-U(\Omega)/kT) d\Omega}{\int \dots \int \exp(-U(\Omega)/kT) d\Omega} = \int \dots \int U(\Omega) f(\Omega) d\Omega \quad (C-1)$$

$U(\Omega)$ is the total interaction energy of the assembly of molecules; Ω stands for the set of all the coordinates of the molecules; $f(\Omega)$ is the "weight function"

$$f(\Omega) = \frac{\exp(-U(\Omega)/kT)}{\int \dots \int \exp(-U(\Omega)/kT) d\Omega} \quad (C-2)$$

If $U(\Omega) = \sum_{i,j} u(q_i, q_j)$ is a sum of pair interactions, (C-1) takes the form

$$E = \frac{N}{V} \int u(q_i, q_j) \rho^{(2)}(q_i, q_j) dq_j \quad (C-3)$$

where q_i (respectively, q_j) represents the set of three position and three angular variables necessary for specifying completely the position of molecule i (respectively, j). The integral in (C-3) does not depend on q_i but only on the relative position of j with respect to i .

The treatment used in this paper corresponds to (C-3) with $\rho^{(2)}$ replaced by an approximate distribution function $\rho_{\text{app}}^{(2)}$ implicitly defined by the procedure, and which is probably rather similar to the distribution function $\rho_{\text{HC}}^{(2)}$ corresponding to a liquid of hard-core molecules (the hard-core being a volume deduced from the van der Waals volume like the volume Ω defined for the solute molecule in our paper), since as emphasized in main text (see section II3). The fitting of the integrals to the results obtained from a packing of hard spheres may be considered a way of taking into account the departure of the distribution function from the constant value 1 (strictly uniform distribution) due to the steric hindrance in the hard-core liquid. Moreover, it has been argued (see, e.g., ref 31) that the changes of the distribution function and therefore of the entropy between the real and hard-core liquid are quite small (this may be more legitimate for nonpolar liquids than for polar ones) so that we are led to assume that $\rho_{\text{app}}^{(2)} \simeq \rho_{\text{HC}}^{(2)} \simeq \rho^{(2)}$. Therefore our calculated energy $\int u(q_i, q_j) \rho_{\text{app}}^{(2)}(q_i, q_j) dq_j$ would be a good approximation to the exact energy (C-3).

It seems convenient to discuss in detail some arguments according to which the use of a continuum model leads to the values of the Helmholtz free energy change

(30) A. H. Stroud, "Numerical Integration" in "Digital Computer User's Handbook," M. Klerer and G. A. Korn, Ed., McGraw-Hill, New York, N. Y., 1967, Chapters 2-5, pp 2-117.

(31) S. J. Yosim and B. B. Owens, *J. Chem. Phys.*, **39**, 2222 (1963).

ΔF rather than the energy change ΔE associated with the "turning-on" of the intermolecular interactions.^{2b,32}

These arguments^{33a,34b} arose in connection with the Debye-Hückel treatment of ionic solutions^{33b,34} and are theoretically perfectly correct, but they are of practical relevance only if the variation of the weight function $f(\Omega)$ (or of the distribution functions $\rho^{(n)}$ deduced from it), which accompanies the turning-on of the interactions, is taken into account (at least in an approximate way).

The argument may be summarized as follows. Let us call ξ the "switching" parameter of the interaction energy; we shall then consider the systems with the interaction energy $U(\xi, \Omega)$, and we shall assume that when ξ varies from 0 to 1

$$U(0, \Omega) = 0 \text{ and } U(1, \Omega) = U(\Omega) \quad (\text{C-4})$$

In the Debye-Hückel theory, where only electrostatic interactions between the ions i of charge e_i are considered, ξ is the so-called "charging parameter." For example, all ions have the charge ξe_i (Debye-Hückel charging process);^{34b} or a single ion i may have the charge ξe_i , all others having their total charge e_j (Güntelberg charging process.^{34b}) In this case, of course, we do not have $U(0, \Omega) = 0$ but rather $U_i(0, \Omega) = 0$ where U_i is the interaction energy of i with all the other ions. Eventually, ξ could be a set of several parameters (ξ_1, \dots, ξ_n). Now let us note $f(\xi, \Omega)$, the weight function for the system with interaction energy $U(\xi, \Omega)$

$$f(\Omega, \xi) = \frac{\exp(-U(\xi, \Omega)/kT)}{\int \dots \int \exp(-U(\xi, \Omega)/kT) d\Omega} \quad (\text{C-5})$$

We have

$$E(\xi) = \int \dots \int U(\xi, \Omega) f(\xi, \Omega) d\Omega = \langle U \rangle_\xi \quad (\text{C-6})$$

$$F(\xi) = -kT \log \int \dots \int \exp(-U(\xi, \Omega)/kT) d\Omega \quad (\text{C-7})$$

Quite generally, we note

$$\int \dots \int U(\xi, \Omega) f(\xi, \Omega) d\Omega = \langle F \rangle_\xi$$

Hence the derivation of (C-6) and (C-7) gives

$$\frac{\partial E}{\partial \xi} = \frac{\partial \langle U \rangle_\xi}{\partial \xi} = \left\langle \frac{\partial U}{\partial \xi} \right\rangle_\xi + \int \dots \int U(\xi, \Omega) \frac{\partial f}{\partial \xi}(\xi, \Omega) d\Omega \quad (\text{C-8})$$

$$\frac{\partial F}{\partial \xi} = \left\langle \frac{\partial U}{\partial \xi} \right\rangle_\xi \quad (\text{C-9})$$

Comparison of (C-8) and (C-9) shows that (C-10) will be in general different from zero

$$\frac{\partial \langle U \rangle_\xi}{\partial \xi} - \left\langle \frac{\partial U}{\partial \xi} \right\rangle_\xi = \frac{\partial E}{\partial \xi} - \frac{\partial F}{\partial \xi} = \int \dots \int U(\xi, \Omega) \frac{\partial f}{\partial \xi}(\xi, \Omega) d\Omega \quad (\text{C-10})$$

Now, the ΔE and ΔF associated with the interactions turned-on by ξ (they may be only a part of all the interactions, as in the case of the Güntelberg charging process) are

$$\Delta E = \int_0^1 \frac{\partial E}{\partial \xi} d\xi = \int_0^1 \left[\left\langle \frac{\partial U}{\partial \xi} \right\rangle_\xi + \int \dots \int U(\xi, \Omega) \frac{\partial f}{\partial \xi}(\xi, \Omega) d\Omega \right] d\xi \quad (\text{C-11})$$

$$\Delta F = \int_0^1 \frac{\partial F}{\partial \xi} d\xi = \int_0^1 \left\langle \frac{\partial U}{\partial \xi} \right\rangle_\xi d\xi \quad (\text{C-12})$$

As a general rule, the exact weight function $f(\xi, \Omega)$ will depend on ξ , therefore $\partial f / \partial \xi \neq 0$ and the turning-on of the interaction will therefore give $\Delta E \neq \Delta F$ according to (C-11) and (C-12).

It will be noticed that, when ξ is a charging parameter, $\partial U / \partial \xi$ is nothing but an electric potential (derivative of the energy with respect to the charge), and $\langle \partial U / \partial \xi \rangle_\xi$ is therefore the mean potential.

Hence, if this mean potential may be calculated in some way (as it is in Debye-Hückel theory by solving approximately the Poisson-Boltzmann equation^{33b,34a}) its integration according to (C-12) will actually give ΔF ; this will be the case when dealing with more general continuum models only if these models may be assumed to give the mean potential as a function of ξ with sufficient accuracy; more specifically, the variation of $f(\xi, \Omega)$ as a function of ξ should be a realistic one, otherwise the difference $\Delta E - \Delta F = \int \dots \int U(\xi, \Omega) f(\xi, \Omega) d\Omega$ (see (C-11) and (C-12)) will be completely meaningless.

Now, a rather drastic assumption consists in taking $f(\xi, \Omega) = g(\Omega)$ independent from ξ : for example, Linder^{32b} considers the case of uniform distribution functions $\rho^{(n)} = 1$; the model described in the present paper also corresponds to this assumption, since the distribution of the solvent atoms around the solute is determined only by steric considerations without any reference to the strength of the intermolecular potential. Under this condition, we have $\Delta E_{\text{app}} = \Delta F_{\text{app}}$, according to (C-10) (since $\partial f / \partial \xi = 0$) and

$$\begin{aligned} \Delta E_{\text{app}} &= \Delta F_{\text{app}} = \int_0^1 d\xi \left[\int \dots \int \frac{\partial U}{\partial \xi}(\xi, \Omega) g(\Omega) d\Omega \right] \\ &= \int \dots \int g(\Omega) \left[\int_0^1 \frac{\partial U}{\partial \xi}(\xi, \Omega) d\xi \right] d\Omega \\ \Delta E &= \int \dots \int g(\Omega) U(\Omega) d\Omega \end{aligned} \quad (\text{C-13})$$

(32) B. Linder, *Advan. Chem. Phys.*, **12**, 225 (1967); (a) p 232; (b) pp 261-264.

(33) R. H. Fowler, "Statistical Mechanics," Cambridge University Press, New York, N. Y., 1936; (a) section 8.8, pp 267-269; (b) section 8.81, pp 269-274; (c) section 13.6, 13.61, 13.62, 13.7, pp 541-552.

(34) H. Eyring, D. Henderson, B. J. Stover, and E. M. Eyring, "Statistical Mechanics and Dynamics," Wiley, New York, N. Y., 1964, Chapter 14, p 401; (a) section 1-4; (b) section 5.

since $\int_0^1 \frac{\partial U}{\partial \xi}(\xi, \Omega) d\xi = U(1, \Omega) - U(0, \Omega) = U(\Omega)$ according to (C-4). (C-13) has the same form as the exact one

$$\Delta E = \int \dots \int U(\Omega) f(\Omega) d\Omega \quad (\text{C-14})$$

and would be identical with it if the approximate weight function $g(\Omega)$ was equal to the exact final (*i.e.*, for $\xi = 1$) weight function. The uniform distribution would not be a very good approximation to $f(\Omega)$ for a liquid, and it is quite difficult to say whether the common value $\Delta E_{\text{app}} = \Delta F_{\text{app}}$ obtained in such way is closer to ΔE or to ΔF (exact values). But if we consider, as pointed out above, that the $g(\Omega)$ which cor-

responds implicitly to the model of the present paper is a reasonable approximation to the true $f(\Omega)$, then (C-13) and (C-14) actually imply that our calculated $\Delta E_{\text{app}} = \Delta F_{\text{app}}$ is a good approximation to ΔE rather than to ΔF .

On the contrary, in the reaction-field models studied by Linder,^{2,32} the weight function $f(\xi, \Omega)$ actually varies with ξ , since the reaction potential due to the surrounding actually varies with the strength of the interaction created by the central molecule (as it is also the case in Debye-Hückel theory): in these models, $\Delta E_{\text{app}} \simeq \Delta F_{\text{app}}$, and it is reasonable to assume that the ΔF_{app} (given by (C-12)) is an evaluation of ΔF rather than ΔE .

Some Comments on the Rice-Allnatt Transport Theory

by J. S. Ku and K. D. Luks*

Department of Chemical Engineering, University of Notre Dame, Notre Dame, Indiana 46556 (Received February 2, 1972)

Publication costs assisted by the National Science Foundation

Extensive computations are performed for the Rice-Allnatt transport theory in the liquid-state regime. Two existing versions of the theory, those of Rice-Allnatt and Wei-Davis, are compared and discussed. Variation of the intermolecular potential input to the theory *via* changing the hard-core locus of the modified Lennard-Jones 12-6 intermolecular potential is examined as a method to improve the predictive capability of the theory and is compared with previous efforts to adjust ("scale") the pair correlation function input to the theory with the same goal in mind. The success of this modification is shown not to be uniform. Based on the body of computations performed, the theory is critically analyzed, with suggestions made for future work.

I. Introduction

The Rice-Allnatt kinetic theory of transport^{1,2} has received considerable attention as a description of the transport properties of simple (nonpolar, spherical molecules) dense fluids.^{3,4} In a recent paper,⁵ we compared the Rice-Allnatt theory in the liquid regime with the simpler transport description of the Davis-Rice-Sengers⁶ (hereafter, DRS) square-well theory, and concluded: (1) the Rice-Allnatt theory qualitatively presents a sound picture of liquid-regime transport properties, although the magnitude of the transport coefficients predicted is uniformly lower than experiment; (2) a partial improvement of the Rice-Allnatt predictions can be achieved by systematically adjusting the experimental intermolecular potential parameters so that the Yvon-Born-Green pair correlation function theory locates its critical point in agreement with experiment.

The Rice-Allnatt theory was compared with the DRS square-well theory, since each theory has a different

manner in which it builds in the interactions of the attractive portion of the intermolecular potential. The square-well theory yields to the simplicity of the square-well intermolecular potential energy function in exchange for a reasonably rigorous binary collision description in the transport theory. In contrast, a more realistic intermolecular potential function such as the modified Lennard-Jones 12-6 potential in turn demands a many-body transport description. The Rice-Allnatt theory casts that description as a Brown-

(1) S. A. Rice and A. R. Allnatt, *J. Chem. Phys.*, **34**, 2144 (1961).

(2) A. R. Allnatt and S. A. Rice, *ibid.*, **34**, 2156 (1961).

(3) S. A. Rice and P. Gray, "The Statistical Mechanics of Simple Liquids," Interscience, New York, N. Y., 1965.

(4) S. A. Rice, J. P. Born, and H. T. Davis in "Simple Dense Fluids," H. L. Frisch and Z. W. Salsburg, Ed., Academic Press, New York, N. Y., 1968.

(5) I. B. Schrodt, J. S. Ku, and K. D. Luks, *Phys. Chem. Liquids*, **2**, 147 (1971).

(6) H. T. Davis, S. A. Rice, and J. V. Sengers, *J. Chem. Phys.*, **35**, 2210 (1961).

ian motion transport problem, *i.e.*, makes its approximation in the kinetic equation rather than in the intermolecular potential functional form.

This paper will analyze two existing versions of the Rice-Allnatt theory as well as investigate various methods by which the quantitativity of the predicted transport properties might be improved. Additional justification for this study is the relative nonexistence of an extensive numerical study of the Rice-Allnatt theory itself. It is hoped that these results and comments will serve as a guide to usage of the Rice-Allnatt theory as well as stimulate some thought with respect to its transport description and improvement of that description through alteration of the transport theory itself and/or its data input.

II. Comparison of Versions

The transport coefficients for the Rice-Allnatt theory can be written as follows.

Shear viscosity

$$\eta = \eta_K + \eta_V \quad (1)$$

$$\eta_K = \eta^* \left\{ \frac{1 + \frac{8}{5} yg^{(2)}(D)}{\frac{\zeta_H}{\zeta^*} + \frac{5}{3} \left(\frac{\zeta_s}{\zeta^*} \right)} \right\} \quad (2)$$

$$\eta_V = \eta^* \left\{ 4yg^{(2)}(D) \left[\frac{2}{5} \left(\frac{\eta_K}{\eta^*} \right) D^2 + \frac{192}{25\pi} y - \frac{576}{25\pi} \left(\frac{\bar{\zeta}}{\zeta^*} \right) y^2 D^2 \Psi^{(2)}(D) \right] + \frac{9216}{25\pi} \left(\frac{\bar{\zeta}}{\zeta^*} \right) \Theta y^3 I_\eta \right\} \quad (3)$$

Thermal conductivity

$$\lambda = \lambda_K + \lambda_V \quad (4)$$

$$\lambda_K = \lambda^* \left\{ \frac{1 + \frac{12}{5} yg^{(2)}(D)}{\frac{\zeta_H}{\zeta^*} + \frac{15}{4} \left(\frac{\zeta_s}{\zeta^*} \right)} \right\} \quad (5)$$

$$\lambda_V = \lambda^* \left\{ [4yg^{(2)}(D)] \left[\frac{3}{5} \left(\frac{\lambda_K}{\lambda^*} \right) D^2 + \left(\frac{128}{25\pi} \right) y \right] - \frac{256}{25} \left(\frac{\zeta^*}{\bar{\zeta}} \right) \Theta y I_\lambda \right\} \quad (6)$$

where

$$I_\eta = \int_D^\infty x^3 u'(x) \Psi^{(2)}(x) g^{(2)}(x) dx \quad (7)$$

$$I_\lambda = \int_D^\infty x^2 g^{(2)}(x) \left\{ u(x) - \frac{x}{3} u'(x) - \frac{x}{3} [u(x) - xu'(x)] \frac{\partial}{\partial x} \right\} \frac{\partial}{\partial \Theta} [\ln g^{(2)}(x)] dx \quad (8)$$

$$\Theta = \epsilon/kT \quad (9)$$

$$y = \pi n^*/6 = \pi n \sigma^3/6 \quad (10)$$

$$\eta^* = \frac{5}{16\sigma^2} \left(\frac{mkT}{\pi} \right)^{1/2} \quad (11)$$

$$\lambda^* = \frac{75}{64\sigma^2} \left(\frac{k^3 T}{\pi m} \right)^{1/2} \quad (12)$$

$$\zeta^* = \frac{8}{3} mn\sigma^2 \left(\frac{m}{\pi kT} \right)^{1/2} \quad (13)$$

$$u(x) = \infty \text{ for } x \leq D \\ = 4(x^{-12} - x^{-6}) \text{ for } x > D \quad (14)$$

$$u'(x) = \frac{d}{dx} u(x) \quad (15)$$

where x = the reduced intermolecular distance of separation ($=r/\sigma$), n = the number density ($=N/V$), σ = the characteristic length parameter of the Lennard-Jones 12-6 intermolecular potential, ϵ = the characteristic energy parameter of the Lennard-Jones 12-6 intermolecular potential, m = the mass of a molecule, k = the Boltzmann constant, T = the absolute temperature, and D = the reduced hard-sphere diameter in the modified Lennard-Jones potential. The subscripts K and V refer to kinetic and potential contribution to the transport properties. $\Psi^{(2)}(x)$ is the function describing the distortion part of the pair correlation function caused by the shear part of the velocity gradient, and is determined from the equation

$$\frac{\partial}{\partial x} \left[x^2 g^{(2)}(x) \frac{\partial \Psi^{(2)}(x)}{\partial x} \right] - 6g^{(2)}(x) \Psi^{(2)}(x) - x^3 \frac{\partial g^{(2)}(x)}{\partial x} = 0 \quad (16)$$

$$\Psi^{(2)}(x) = 0, x \rightarrow \infty \quad (17)$$

$$\frac{\partial \Psi^{(2)}(x)}{\partial x} = 0, x \rightarrow D_+ \quad (18)$$

The parameter D has been traditionally unity, *i.e.*, the hard-sphere cutoff has been located where $u(x) = 0$ or $x = 1$. ζ_s is the soft friction constant as calculated by the linear trajectory approximation.^{7,8} $\zeta_H = \zeta^* g^{(2)}(D)$ is the hard friction constant. $\bar{\zeta}$ is the friction factor which differs in interpretation between the two existing theoretical versions of Rice-Allnatt and Wei-Davis.^{9,10} For the Rice-Allnatt version

$$\bar{\zeta} = \zeta_s \quad (19)$$

and for the Wei-Davis version

$$\bar{\zeta} = \zeta_s + \zeta_H \quad (20)$$

(7) E. Helfand, *Phys. Fluids*, **4**, 681 (1961).

(8) J. A. Palyvos and H. T. Davis, *J. Phys. Chem.*, **71**, 439 (1967).

(9) C. C. Wei and H. T. Davis, *J. Chem. Phys.*, **45**, 2533 (1966).

(10) C. C. Wei and H. T. Davis, *ibid.*, **46**, 3456 (1967).

It has been previously pointed out¹⁰ that the effect of the Wei-Davis modification of the Rice-Allnatt formulas has been to increase the shear viscosity predictions and, in turn, decrease the thermal conductivity predictions. This is true in the state regime characteristic of typical simple liquids ($T < T_{\text{critical}}$) and can readily be seen to be caused by the roles of $\bar{\zeta}$ in the potential contributions to the transport properties. Since Rice-Allnatt (hereafter, RA) version predictions were uniformly small to begin with when compared with experiment, the Wei-Davis version (hereafter, WD) merely trades off somewhat better shear viscosity predictions (still too small) for somewhat worse thermal conductivity predictions. This conclusion can be obtained from the tables to follow and is fully documented elsewhere.¹¹

There are two other facets of this version comparison that are interesting. First of all, while the RA version yields the traditional Enskog hard-sphere transport equations¹² in the limit of $\Theta \rightarrow 0$, the WD version does not. An additional term appears in the shear viscosity

$$\eta_{WD}(\Theta = 0) = \eta_{\text{Enskog}} -$$

$$\eta^* \left\{ \frac{2304}{25\pi} \left(\frac{\zeta_H}{\zeta^*} \right) y^3 D^2 g^{(2)}(D) \Psi^{(2)}(D) \right\} \quad (21)$$

which accounts for the distortion of the pair correlation function caused by the shear part of the velocity gradient, *i.e.*, a contribution due to nonequilibrium considerations with respect to the pair correlation function. Although this difference is not overly significant at liquid temperatures ($\Theta > 0.8$), at low values of θ , the predictions of shear viscosity differ substantially in dense fluids; see Table I.

Table I: A Comparison of Rice-Allnatt Reduced Shear Viscosity and Thermal Conductivity for the Two Versions of the Rice-Allnatt Theory (RA and WD)^a

θ	η/η^*		λ/λ^*	
	RA	WD	RA	WD
0	5.184	1.989	5.731	5.731
0.2	3.878	2.274	8.578	4.493
0.4	3.025	2.392	6.834	3.910
0.6	2.560	2.494	5.609	3.581
0.8	2.409	2.653	4.700	3.325
1.0	2.502	2.897	3.998	3.079
1.2	2.784	3.256	3.438	2.830

^a For the modified Lennard-Jones 12-6 intermolecular potential with $D = 1$, as a function of Θ at $n^* = 0.6743$.

On the other hand, the presence of ζ_H in $\bar{\zeta}$ in λ_V causes thermal conductivity in the WD version to ascend uniformly to a hard-sphere value as Θ approaches 0, while for the RA version λ/λ^* ascends to a maximum due to the diminishing size of $\bar{\zeta} = \zeta_s$ in λ_V ; see Table I.

It was previously pointed out⁵ that the Rice-Allnatt theory predicted an inversion in shear viscosity such as is witnessed in experiment. At a certain temperature in the dense fluid regime $(\partial\eta/\partial T)_{n^*} = 0$. Below this temperature, shear viscosity increases with decreasing temperature, while above this inversion temperature shear viscosity increases with increasing temperature. Such a phenomenon is not found for the thermal conductivity of simple fluids. In the liquid regime, there should be an inversion temperature at each density for, say, argon near the saturated liquid state. Table II shows this inversion to be the case at all densities examined for the RA version, but the WD version does not show an inversion at high liquid densities. It is interesting to note that experimentally for liquid argon inversion occurs in the vicinity of 120-125°K near saturation.^{13,14} It is not clear from experimental data¹³ that the inversion in η will exist at the high-density $n^* = 0.818$, since shear viscosity data for argon are presently nonexistent at the high pressures needed to obtain $n^* = 0.818$ at, say, $T \sim 120^\circ\text{K}$.

Table II: The Predicted Temperature of Shear Viscosity Inversion for Liquid Argon^a as a Function of Reduced Density n^* for the Two Versions of the Rice-Allnatt Theory

n^*	$T, ^\circ\text{K}$	
	RA	WD
0.442	(103) ^b	(107) ^b
0.674	118	128
0.818	145	none

^a $\sigma = 3.405 \times 10^{-8}$ cm, $\epsilon = 1.653 \times 10^{-14}$ erg. ^b The parentheses infer that this state point lies within the two-phase region and is thus metastable or unstable. The inclusion of these points in this table is for mathematical rather than physical reasons.

III. The Effect of Varying the Hard-Core Locus in the Modified Lennard-Jones Potential on the Rice-Allnatt Transport Theory

The Rice-Allnatt theory can be derived independently of the precise functional form of the intermolecular potential. The use of the Lennard-Jones 12-6 potential (with hard sphere at $D = 1$) was chosen in previous work for two reasons: (1) it is a popular, realistic representation of the interaction between two nonpolar spheres, and (2) pair correlation function data for input into the theory had been generated earlier by Kirkwood, *et al.*, for this intermolecular

(11) J. S. Ku, Ph.D. Thesis, University of Notre Dame, Jan 1972.

(12) S. Chapman and T. G. Cowling, "The Mathematical Theory of Non-Uniform Gases," Cambridge University Press, New York, N. Y., 1961.

(13) A. deBock, W. Grevendonk, and W. Herreman, *Physica*, **37**, 227 (1967).

(14) D. E. Diller, H. J. M. Hanley, and H. M. Roder, *Cryogenics*, **286** (1970).

potential. Thus, the freedom exists to vary the basic input (the intermolecular potential) to the theory (either version), but with the obvious restrictions that pair correlation function data reasonably consistent with that potential will have to be generated and the transport functions ζ_s and $\Psi^{(2)}(x)$ recomputed accordingly. The Yvon-Born-Green integral equation (hereafter, YBG) with superposition approximation qualitatively has been shown to depict a liquid regime.^{5,15,16} Kirkwood, *et al.*,¹⁷ solved the YBG equation with the aid of a θ expansion where $\theta = \epsilon/kT$, and these are the data which have been used to compute transport properties in this paper so far.

As pointed out in our previous paper, the two-phase gas-liquid envelope for the modified Lennard-Jones 12-6 potential encompasses that of, say, liquid argon with the use of traditionally accepted potential parameters ($\sigma = 3.405 \times 10^{-8}$ cm and $\epsilon = 1.653 \times 10^{-14}$ erg). Consequently, the correlation functions of Kirkwood, *et al.*,¹⁷ that one would use at experimental saturated liquid state points would usually predict such nonphysical results as negative pressures from the virial statistical-mechanical equation of state. It was precisely because of this disturbing feature of YBG input in property prediction that scaling procedures were introduced.^{3,5} These parametrizations of pair correlation function input have uniformly improved transport property predictions, if not making them altogether satisfactory in a quantitative sense. Recent work has shown that the YBG equation behaves similarly with respect to theoretical and experimental coexistence loci for the square-well potential.¹⁶

Our interest in this section is to investigate the more fundamental modification of the input—that of the intermolecular potential forms. We feel, first of all, that the shape of the attractive portion of the potential function is not foremost in significance. The Rice-Allnatt theoretical results can be split into “core” parts depending on the contact value of the pair correlation function $g^{(2)}(x = 1)$ and into “soft” integral contributions depending on $g^{(2)}(x)$ for $x > 1$; see eq 7 and 8. These contributions basically correspond to those arising from hard and soft (Brownian) collisions, respectively. The relative size of hard and soft contribution is thus strongly dependent on the value of $g^{(2)}(x = 1)$, the pair correlation function at the core. This number is not very different from unity for the modified Lennard-Jones 12-6 potential and is substantially less than that of a hard-sphere potential because the Lennard-Jones well causes a “clustering” of nearest neighbors at $x \approx 1.12$, manifesting itself in a peak on $g^{(2)}(x)$ at that x value, decreasing the value of $g^{(2)}(x)$ at $x = 1$.

The Rice-Allnatt formulas listed in eq 1-18 are generalized with the aid of a third potential parameter D , the reduced hard-sphere diameter. Traditionally, and up to this point in this paper, the value of D has

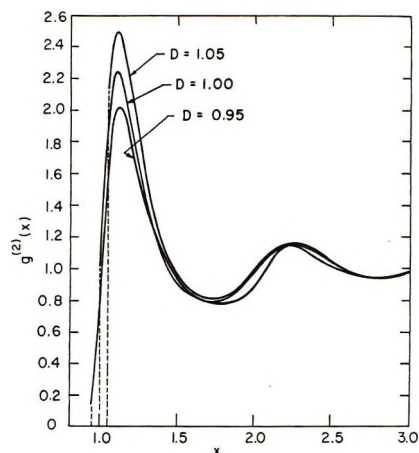


Figure 1. A comparison of pair correlation functions $g^{(2)}(x)$ varying the hard-core locus of the modified Lennard-Jones 12-6 intermolecular potential at $\theta = 0.9$ and $\eta^* = 0.6743$.

been set equal to 1, the point where a pure Lennard-Jones 12-6 potential (without hard core) would cross the zero-energy line. We wish to examine what effect variation of the hard core locus D has on Rice-Allnatt computations.

In generating the new pair correlation function for $D = 0.95$ and $D = 1.05$, the size of the core can be preserved by reducing the value of σ for $D = 1.05$ and increasing it for $D = 0.95$. In this way, as ϵ approaches 0, all three functions will become identical in an absolute as well as a reduced sense. The appropriate value of ϵ to use for each new function would have to be determined by some method such as matching second virial coefficient theory with experiment. Ku has shown¹¹ that to match reduced pressures at $n^* = 0.6743$, θ ($D = 0.95$) $<$ θ ($D = 1.0$) $<$ θ ($D = 1.05$) must always be satisfied. Qualitatively speaking, the behavior of the pressure along the isochore is very similar for all three values of D , and is certainly not as sensitive to changes in D as are the reduced transport coefficients.

Figure 1 shows pair correlation functions¹¹ at $\theta = 0.9$ and $n^* = 0.6743$ for $D = 0.95, 1.00,$ and 1.05 , which were generated from the YBG theory with θ expansion according to Kirkwood, *et al.*⁵ It should be noted that $g^{(2)}(D)$ is about 2.2 for $D = 1.05$ and only 0.1 for $D = 0.95$. In essence, by moving the hard core to $D = 0.95$ (to a position of much higher repulsive forces), the Rice-Allnatt computations are predominantly influenced by the Brownian motion contributions. On the other hand, hard collisions make a sizable contribution when $D = 1.05$, since the local molecular density is greater within the potential well. The effects of these alterations on the two versions for shear viscosity and thermal conductivity are

(15) D. A. Young and S. A. Rice, *J. Chem. Phys.*, **47**, 4228 (1967).

(16) I. B. Schrodtt and K. D. Luks, submitted for publication.

(17) J. G. Kirkwood, V. A. Lewinson, and B. J. Alder, *J. Chem. Phys.*, **19**, 139 (1951).

shown in Tables III and IV, respectively. Shear viscosity increases with increasing D for a given θ at $n^* = 0.6743$, while thermal conductivity decreases, but to a lesser degree. If one has to choose between D values, 1.05 would be preferable, although variation of the hard-core locus does not seem to be a satisfactory method of improving the usage of the theory.

Table III: A Comparison of Rice-Allnatt Reduced Shear Viscosity η/η^* for the Two Versions of the Rice-Allnatt Theory (RA and WD) for the Modified Lennard-Jones 12-6 Intermolecular Potential^a

θ	$D = 0.95$		$D = 1.05$	
	RA	WD	RA	WD
0	4.978	3.129	5.441	0.051
0.2	3.289	3.014	4.270	0.355
0.4	2.176	2.315	3.561	0.928
0.6	1.680	1.848	3.245	1.722
0.8	1.583	1.695	3.276	2.710
1.0	1.621	1.681	3.624	3.880
1.2	1.605	1.632	4.267	5.226

^a With $D = 0.95$ and $D = 1.05$ as a function of θ at $n^* = 0.6743$.

Table IV: A Comparison of Rice-Allnatt Reduced Thermal Conductivity λ/λ^* for the Two Versions of the Rice-Allnatt Theory (RA and WD) for the Modified Lennard-Jones 12-6 Intermolecular Potential^a

θ	$D = 0.95$		$D = 1.05$	
	RA	WD	RA	WD
0	5.557	5.557	5.960	5.960
0.2	29.30	7.754	5.134	4.550
0.4	18.28	9.521	4.321	3.816
0.6	12.08	9.102	3.794	3.356
0.8	8.314	7.394	3.412	3.032
1.0	5.887	5.608	3.115	2.785
1.2	4.229	4.144	2.872	2.586

^a With $D = 0.95$ and $D = 1.05$ as a function of θ at $n^* = 0.6743$.

Perhaps this trade off of success in transport computations with variation of D is not surprising from an intuitive viewpoint. First of all, by moving the hard-core locus to $D = 0.95$, one is forcing the Brownian motion mechanism to handle interactions of a highly repulsive nature in the region $0.95 < x < 1.00$. These interactions are unlikely candidates for a Brownian motion description. It follows that changing D to 1.05 moves the hard-core collision to a region of the potential energy function which is not strongly repulsive and therefore overestimates the hard-core contributions. For these reasons and because the overall qualitative features of the transport coefficients seem to be better represented for the choice $D = 1$, it is our opinion that

this value is the best choice in using the truncated Lennard-Jones potential in the Rice-Allnatt theory.

IV. Remarks

Based on the extensive computations of the Rice-Allnatt theory, its versions, and related studies of scaling and hard core locus variation, one can conclude that the Rice-Allnatt theory does present a qualitatively realistic picture of simple liquid transport properties. Injecting a greater predictive capability into the theory still remains to be achieved, if at all possible. At present, the most promising improvement arises from scaling parametrization of $g^{(2)}(x)$.^{3,5} This result could suggest that better correlation function theory could improve property predictions.

Our opinion is that the weaknesses of the Rice-Allnatt theory do not lie in the concept of categorizing collisions as hard core plus Brownian in nature, or in the customary use of the modified Lennard-Jones 12-6 potential function with $D = 1$. We feel that, in the derivation and solution of the kinetic equations, many approximations have been made, one or more of which could contribute to its failings. The derivation and solution should be subjected to reexamination, in particular the theories for the distortion function $\Psi^{(2)}(x)$ which are presently contributing to the differences in the shear viscosity between versions. The distortion function which contributes to bulk viscosity has been found to be in poor shape, as well.^{3,16} The difficulties encountered here discouraged us from including bulk viscosity in our comments.

Davis¹⁸ and Misguish and Nicolis¹⁹ have recently reexamined the derivation of the Rice-Allnatt theory and have eliminated a number of approximations of the original version. These results have not yet been tested extensively with computations.

Liquid-state pair distribution function theory is still an active area of research, and future improvements here should provide an interesting test of the transport theory in either its present state or in an improved form.

The authors hope that the computations included here, and the much more extensive computations performed by one of us (JSK) elsewhere¹¹ will serve as an intuitive aid to future transport theory developments.

Acknowledgment. The authors are grateful to the National Science Foundation for support of this work through NSF Grant No. GK-14212. Further gratitude is extended to Professor John J. Kozak of the Department of Chemistry, University of Notre Dame, and Professor H. Ted Davis of the Department of Chemical Engineering, University of Minnesota, for helpful discussions.

(18) H. T. Davis, Proceedings of the IUPAP Conference on Statistical Mechanics, Chicago, Ill., April 1971.

(19) J. Misguish and G. Nicolis in ref 18.

Scaled Particle Theory for Nonelectrolyte Solutions of Dilute Solid Solutes

by Abhijit Purkayastha and John Walkley*

Department of Chemistry, Simon Fraser University, Burnaby 2, British Columbia, Canada (Received October 4, 1971)

Publication costs assisted by the Department of Chemistry, Simon Fraser University

The entropy of solution of a solid solute dissolved in a nonpolar solvent is examined in terms of a modified Yosim cycle. It is seen to give good agreement with experiment even for those systems wherein the solute-solvent molar volume ratio is large.

The scaled particle theory, developed by Reiss, *et al.*,¹ as a statistical mechanical theory for fluids, has been used by several workers to predict the thermodynamic properties of dissolved gases.^{2,3} Common to most theories attempting to predict these properties is the assumption that the dissolution process consists of two stages: (i) the creation of a cavity in the solvent to accommodate the solute molecule and (ii) the introduction of the solute molecule into the cavity. For the solubility properties of a solid solute the two-step "hole making-hole filling" process is not suitable. One of the more interesting thermodynamic properties of such systems is the entropy of solution or, in usual notation, the $(s_2 - s_2^g)$ term.⁴ One route to the prediction of this property using scaled particle theory lies in the following imaginary six-step process similar to one discussed by Yosim.⁵

Step I. The pure solid solute at the experimental temperature is converted to a hypothetical supercooled liquid at that temperature. Scaled particle theory is not applicable to the solid phase nor does it correctly describe the melting process of solids.⁶ The entropy change for step I must therefore be obtained from experimental heat capacity data

$$\Delta s_2^I = n_2(\Delta s_{298}^f) = n_2(\Delta s_{mpt}^f - \Delta C_p^s - P \ln T_{mpt}/298)$$

(the usual notation is used throughout).

Step II. The liquid solvent and the liquid solute are separately "discharged" at constant volume to hard-sphere fluids.

$$\Delta s^{II} = -(n_1 \Delta s_{\text{charge}(1)}^{II} + n_2 \Delta s_{\text{charge}(2)}^{II})$$

Step III. The hard-sphere fluids are vaporized at constant temperature to a hard-sphere gas. Yosim⁶ obtained from scaled particle theory the entropy of vaporization of a hard-sphere fluid as

$$\Delta s_{(i)}^{\text{vap}} = n_i R \ln \left[\frac{V^g}{(V^p - ca_i^3)} + \frac{3cRn_i a_i^3 (2V^p - ca_i^3)}{2(V^p - ca_i^3)} \right]$$

Here V^p is the molar volume of the liquid, $c = \pi N_0/6$, where N_0 is Avogadro's number, a_i is the hard-sphere

diameter of the substance in the gas phase, and V^g is the molar volume of the substance in the gas phase, assumed to obey ideal gas laws.

Step IV. The ideal hard-sphere gases produced in step III are mixed at constant pressure. If we assume ideal mixing, then

$$\Delta s^{IV} = -n_1 R \ln x_1 - n_2 R \ln x_2$$

where x_1 and x_2 are the mole fraction compositions of solvent and solute.

Step V. The hard-sphere gas mixture is compressed to the volume of the solution, V_s^p . Using the Lebowitz^{1b} equation of state for a mixture of hard spheres the entropy change associated with this step can be written

$$\Delta s^V = -R(n_1 + n_2) \times \left\{ \ln \frac{V_{s,298}^g}{[V_{s,298}^p - c(n_1 a_1^3 + n_2 a_2^3)]} - 1/2c^2 \{ 3x_1^3 a_1^6 + x_1^2 x_2 (6a_1^5 a_2 - 3a_1^4 a_2^2 + 6a_1^3 a_2^3 + x_1 x_2^2 (6a_1^3 a_2^3 - 3a_1^2 a_2^4 + 6a_1 a_2^5) + 3x_2^3 a_2^6) - 6cV_s^p [x_1^2 a_1^3 + x_1 x_2 (a_1 a_2^2 + a_1^2 a_2) + x_2^2 a_2^3] [V_{s,298}^p - c(x_1 a_1^3 + x_2 a_2^3)] \}^{-2} \right\}$$

Step VI. The compressed mixture of hard spheres is now "recharged," the resulting solution being equivalent to the solvent saturated with the solute at the temperature and pressure of the experiment.

$$\Delta s^{VI} = (n_1 + n_2) \Delta s_{\text{charge}(1,2)}^{VI}$$

We define an excess entropy term

$$\Delta s^E = \Delta s^M - \sum_{i=1,2} n_i R \ln x_i$$

where Δs^M is the total entropy of mixing. Collecting

(1) (a) H. Reiss, H. L. Frisch, and J. L. Lebowitz, *J. Chem. Phys.*, **31**, 369 (1959); (b) J. L. Lebowitz, *Phys. Rev. A*, **133**, 895 (1964).

(2) R. Pierotti, *J. Phys. Chem.*, **67**, 1840 (1963).

(3) E. Wilhelm and R. Battino, *J. Chem. Thermodyn.*, **3**, 379 (1971).

(4) J. H. Hildebrand and R. L. Scott, "Solubility of Nonelectrolytes," Dover Publications, New York, N. Y., 1964.

(5) S. J. Yosim, *J. Chem. Phys.*, **43**, 286 (1965).

(6) S. J. Yosim and B. B. Owens, *ibid.*, **39**, 2222 (1963).

all entropy changes in steps I through VI and making the assumption that $x_2 \rightarrow 0$ (*i.e.*, very dilute solution) and the consequent assumption that for such dilute solutions the sum of the entropy changes associated with the "charging" and "discharging" steps may be ignored,² then we can formulate the excess entropy term. Making the substitution $V_s^p = n_1 \bar{V}_1 + n_2 \bar{V}_2$, we can then write the partial molal entropy of solution for component 2 of the mixture (the dilute solute) as

$$\begin{aligned} \Delta \bar{s}_2^E = & \Delta \bar{s}^I - R \ln (V_2^p - ca_2^3) + \\ & 3cRa_2^3(2V_{(2)}^p - ca_2^3)/(V_2^p - ca_2^3)^2 + \\ & 1/2R\{3(ca_1^3)^2 - 6ca_1^3V_{1^p}\}/(V_1^p - ca_1^3)^2 + \\ & R(\bar{V}_2 - ca_1^3)/[x_1\bar{V}_1 + x_2\bar{V}_2 - c(x_1a_1^3 + \\ & x_2a_2^3)] + R \ln [(x_1\bar{V}_1 + x_2\bar{V}_2) - c(x_1a_1^3 + x_2a_2^3)] \end{aligned}$$

The above equation gives the excess entropy of component 2 at constant pressure and may be compared to the experimental term

$$\Delta \bar{s}_2^E(\text{exptl}) = R(\partial \ln x_2 / \partial \ln T) - R \ln x_2$$

(for these very dilute solutions, since $R(\partial \ln a_2 / \partial \ln x_2) \simeq 1$). In Table I we compare experimental excess entropy of mixing data for iodine and for stannic iodide in a range of solvents with those values calculated from the expression derived above.^{7,8} The agreement is seen to be very good.

Table I: Excess Partial Molal Entropy of Solution

System	$\Delta \bar{s}_2^E(\text{calcd.})$ cal deg ⁻¹ mol ⁻¹	$\Delta \bar{s}_2^E(\text{exptl.})$ cal deg ⁻¹ mol ⁻¹
I ₂ -CCl ₄	4.34	5.04 ^a
I ₂ -c-C ₆ H ₁₂	4.50	4.42 ^a
I ₂ -CCl ₂ FCClF ₂	5.79	5.24 ^a
I ₂ -i-C ₃ H ₁₈	4.71	4.86 ^a
SnI ₄ -CCl ₄	1.35	1.67 ^b
SnI ₄ -CCl ₂ FCClF ₂	2.42	3.05 ^b

^a See ref 7. ^b See ref 8.

Systems which show a considerable disparity in solute-solvent molar volumes are of great interest. Even regular solution theory must concede that there is an entropy term for such systems for which only approximate theoretical expressions have been derived.⁴ For a solute such as tetraphenyltin(IV) the excess entropy of mixing is large; see Table II.^{9,10} Unfortunately, for this solute we cannot evaluate the entropy

term associated with the first of the proposed steps, $\Delta \bar{s}_2^I$. This term should be of constant value irrespective of the solvent, and in Table II we give values for this term obtained by subtracting the sum of the entropy terms $\Delta \bar{s}_2^{III} + \Delta \bar{s}_2^{IV} + \Delta \bar{s}_2^V$ from the experimental excess entropy of solution. It is seen that a reasonable constancy is found for the $\Delta \bar{s}_2^I$ term for the three solvents for which experimental data exist. Similar agreement is observed for the perfluoro compound, Sn(C₆F₅)₄, for which the solute-solvent volume disparity is as large as 5:1.

Table II: Comparison of $\Delta \bar{s}_2^I$ Values

System	$s_{298}^f(\text{calcd.})$ cal deg ⁻¹ mol ⁻¹	$S_2(\text{exptl.})$ cal deg ⁻¹ mol ⁻¹	$-R \ln x_2(\text{exptl})$
Sn(C ₆ H ₅) ₄ -c-C ₆ H ₁₂	9.8	32.87 ^a	16.79 ^a
Sn(C ₆ H ₅) ₄ -CCl ₄	7.8	27.36 ^a	13.56 ^a
Sn(C ₆ H ₅) ₄ -CCl ₂ FCClF ₂	8.2	33.27 ^a	19.14 ^a
Sn(C ₆ H ₅) ₄ -CCl ₄	7.0	28.38 ^b	10.66 ^b
Sn(C ₆ H ₅) ₄ -c-C ₆ H ₁₂	7.2	33.41 ^b	15.51 ^b
Sn(C ₆ H ₅) ₄ -toluene	9.0	30.22 ^b	10.62 ^b

^a See ref 9. ^b See ref 10.

If step I is removed, the process can obviously be adapted to the calculation of the $(\bar{s}_2 - \bar{s}_2^E)$ term for gases dissolved in nonpolar solvents. Battino³ has recently extended the Pierotti² theory to the calculation of $(\bar{s}_1 - s_2^E)$. Use of our proposed process for SF₆ gas gives values of -11.6 (c-C₆H₁₂ solvent) and -11.32 (C₆H₆ solvent), which compare well to the values obtained by Battino of -11.5 and -11.0; experimental values are -15.90 and -14.5 eu, respectively. Values obtained from the two theories agree, the result being independent of the supposed process of solution.

It would seem that as construed above scaled particle theory can be used to calculate the entropy of solution of dilute nonelectrolyte systems and that solute-solvent size disparity does not throw any particular strain upon the use of the theory.

(7) J. H. Hildebrand and R. L. Scott, "Regular Solutions," Prentice-Hall, Englewood Cliffs, N. J., 1962.

(8) E. B. Smith and J. Walkley, *Trans. Faraday Soc.*, **56**, 1276 (1960).

(9) M. Vitoria and J. Walkley, *ibid.*, **65**, 57, 62 (1969).

(10) A. Purkayastha, Ph.D. Thesis, Simon Fraser University, Burnaby 2, British Columbia, Canada, 1971.

Ionic Solvation Numbers from Compressibilities and Ionic Vibration

Potentials Measurements

by J. O'M. Bockris and P. P. S. Saluja*¹

Electrochemistry Laboratory, Department of Chemistry, University of Pennsylvania, Philadelphia, Pennsylvania 19104 (Received April 15, 1971)

Publication costs borne completely by The Journal of Physical Chemistry

The general aim of the present work is to extend and deepen the model of the solvent sheath near ions in aqueous solutions. The experimental measurements reported are those of the compressibility of the solution. A modification of the method earlier developed in this laboratory was used to give sound velocity at frequency of 5 MHz to an accuracy of ± 0.4 m sec⁻¹. The velocity measurements are converted into values of the compressibility, β , by the use of a well-known equation. Such measurements are then converted by the equation of Passynski into solvation numbers. It is desired to obtain individual solvation numbers. Ionic vibration potentials due to Madan and to Zana and Yeager were utilized. These give the *difference* of the masses of the ions of a salt, together with the water molecules which move with the ions when they receive an ultrasonic pulse. The individual solvation numbers were found to be Li⁺ = 4.0, Na⁺ = 4.5, K⁺ = 3.5, Rb⁺ = 3.0, Cs⁺ = 2.5; Ba²⁺ = 11.0, Ca²⁺ = 9.0, Sr²⁺ = 9.0, Mg²⁺ = 10.0; La³⁺ = 15.0, Ce³⁺ = 18.0; Th⁴⁺ = 22.0; F⁻ = 4.0, Cl⁻ = 2.0, Br⁻ = 1.8, and I⁻ = 1.5. A theoretical discussion of the meaning of the compressibility and ionic vibration potential measurements is given. It is stressed that the discussion is made on the basis of a definition of solvation number (SN). It will be noted that this solvation number definition is *time dependent*. Correspondingly, a relationship between the reorientation time of the solvent and the time during which the ion waits in its movement in solution is shown and supports the definition given. An argument is given which suggests that the compressibility and the ionic vibration potential measurements measure the same quantity.

I. Introduction

Interest in alternatives to spectroscopic methods for investigating the environment around aqueous ions increases, because hitherto the results of spectroscopic examinations have been open to great uncertainties.² Hinton and Amis^{2b} point out that nmr measurements of solvation numbers depend on whether the proton relaxation time or the proton chemical shift is used to determine the number. Depending on which approach is used, *e.g.*, for Li⁺, the results are 1 and 4, respectively; for Cs⁺, 15 and 1, respectively; and for F⁻, 9.9 and 1.6, respectively.

Three available models for the environment near the ion may be distinguished. In the classical model of Bernal and Fowler³ (*cf.* Eley and Evans⁴), an assignment of four coordinating water molecules was made, and calculations of the heat and entropy of hydration were made upon this basis. Frank and Wen⁵ introduced a "two layer model" for the solvated ion, the first layer consisting of "immobilized" water molecules, and the second layer a "structure-broken" region. A third model was expressed by Bockris and Reddy,⁶ (*cf.* Bockris,⁷ Samoilov,⁸ Conway, *et al.*,⁹ and Conway¹⁰). In it two kinds of water are in the first layer around the ion (and a structure-broken region, about a monolayer thick, is included). The coordination number is the total number of water molecules which are in contact with the ion. Another number exists—the

number of water molecules which remain associated with the ion during its movement through the solution. This is the solvation (or hydration) number. Usually, the solvation number (SN) will be less than the coordination number (CN). Solvated waters are part of the coordination sheath. With very small ions, the SN and the CN tend to be the same. With very large ions, the SN tends to be zero.

One aspect of the development of a model of the region near an ion lies in the distinction between the

(1) Correspondence should be addressed to Department of Chemistry, Cornell University, Ithaca, N. Y. 14850.

(2) (a) J. E. Desnoyers and C. Jolicoeur, "Modern Aspects of Electrochemistry," Vol. V, B. E. Conway and J. O'M. Bockris, Ed., Plenum Press, New York, N. Y., 1969, Chapter 1; (b) J. F. Hinton and E. S. Amis, *Chem. Rev.*, **67**, 367 (1967).

(3) J. D. Bernal and R. H. Fowler, *J. Chem. Phys.*, **1**, 515 (1933).

(4) D. D. Eley and M. G. Evans, *Trans. Faraday Soc.*, **34**, 1093 (1938).

(5) H. S. Frank and W. Y. Wen, *Discuss. Faraday Soc.*, No. **24**, 133 (1957).

(6) J. O'M. Bockris and A. K. N. Reddy, "Modern Electrochemistry," Vol. I, Plenum Press, New York, N. Y., 1970.

(7) J. O'M. Bockris, *Quart. Rev. Chem. Soc.*, **3**, 173 (1949).

(8) O. Ya. Samoilov, "Structure of Electrolyte Solutions and Hydration of Ions," Engl. Transl., Consultants Bureau, Inc., New York, N. Y., 1965; *Discuss. Faraday Soc.*, No. **24**, 141 (1957).

(9) B. E. Conway, R. E. Verrall, and J. E. Desnoyers, *Z. Phys. Chem. (Leipzig)*, **230**, 157 (1965).

(10) B. E. Conway, "Physical Chemistry, an Advanced Treatise," Vol. IXA, "Electrochemistry," H. Eyring, Ed., Academic Press, New York, N. Y., 1970.

solvation and the coordination number. Many authors have regarded such a distinction between the SN and the CN as nebulous. Its significance depends on a sufficiently precise definition. The coordination number may be operationally defined from X-ray measurements.^{2a,11} The solvation number may be further defined as the number of water molecules near an ion which have lost their own degrees of translational freedom. The definition of a solvation water will be brought out more clearly.

The so-called "primary" solvation water is pictured in the model as that water which has had *sufficient time* to orient out of the water structure and be attached to the ion at the maximum of interaction of ion and water, when the ion is momentarily stationary in its diffusional motion. The attachment of one such water molecule to an ion results in a change in the potential energy of about 20 kcal. With "nonsolvated water molecules which are also coordinating the ion," the model is that they have not had sufficient time to orient themselves around from the water into a position next to the ion so that the interaction is enough for them to behave as entities which have become identical with the ion. They are, therefore, left behind when the ion moves and do not count as part of the solvation sheath, *i.e.*, part of primary solvation number.

Most of the methods described in early literature as determining a "solvation number" (usually poorly defined) can be rejected because they do not give common values. If one accepts the above definition, then the following methods are claimed⁷ to determine *this* number: compressibility;¹² dielectric constant;¹³ entropy;¹⁴ partial molar volume;^{9,15} and Stokes volume.¹⁶ Each of these methods has its own limitations in interpretation; in particular, the use of Stokes' law with a factor of 6 is not justified for small particles.

One difficulty possessed by these methods (except the rejected Stokes method) is that they give the sum of the solvation numbers of the ions present and some assumption (*e.g.*, $n_{s,I^-} = 0$) has to be made concerning the evaluation of individual numbers.

There are two aims of the present work: (1) to determine the solvation number (as defined above) for a variety of ions by a combination of compressibility measurements, which can be shown (see section III1) to give the sum of the solvation numbers for the ions of a salt, and to determine the ionic vibration potentials,^{17,18} which can be shown to give the difference of such numbers (see section III2); (2) to utilize such information, together with calculations of hydration heats and entropies of hydration,¹⁹ in terms of various models, to increase knowledge of the model.

The present work reports the compressibility studies. The measurements of Zana and Yeager¹⁸ and of Madan, *et al.*,²⁰ on ionic vibration potentials have been combined with results of compressibility measurements to carry out the above indicated determinations.

II. Experimental Section

1. *Methods Available.* The determination of the sum of the solvation numbers of ions in solution may be carried out by the method originated by Passynski.¹²

The experimental determinations are the compressibilities of the solution and the solvent. Ultrasonic velocity determinations may be used for the compressibility, β , evaluations from

$$\beta = \frac{1}{u^2 \rho} \quad (1)$$

where u is the velocity of ultrasonic wave in the medium and ρ is the density of the medium.

Two main methods are available for the determination of the velocity of sound in aqueous solutions. The first is due to Carstensen²¹ and in this method a phase comparison approach is used, *i.e.*, the phase difference of the ultrasound in solution and solvent is related to the difference in the velocities of sound in these two media. Two compartments, one containing the solvent and other containing the solution, are separated by an impermeable membrane. The transducers, one in each compartment, are maintained at a constant separation. They are moved to sense nodes. Improvements to Carstensen's method have been published by Conway and Laliberte.²² A new method known as a "sing-around" technique²³ has also been published recently.

In the method due to Richards, Brauner, and Bockris (RBB),²⁴ the velocity of sound is determined in the solution, and this is compared with the well-known velocity of sound in water. One transducer is moved with respect to the other, and nodes formed by the sound passing from one to the other are compared with those due to an external oscillator to give Lissajous figures on a CRO, which indicate the distance apart of the transducers at the nodal points.

(11) R. M. Lawrence and R. F. Kruh, *J. Chem. Phys.*, **47**, 4758 (1967).

(12) A. Passynski, *Acta Physicochim.*, **8**, 385 (1938).

(13) J. B. Hasted, D. M. Ritson, and C. H. Collie, *J. Chem. Phys.*, **16**, 1 (1948); A. H. Haggis, J. B. Hasted, and T. J. Buchanan, *ibid.*, **20**, 1452 (1952).

(14) H. Ulich, *Z. Elektrochem.*, **36**, 497 (1930); *Z. Phys. Chem. (Leipzig)*, **168**, 141 (1934).

(15) E. Darmois, *J. Phys. Radium*, **2**, 2 (1941).

(16) H. Ulich, *Trans. Faraday Soc.*, **23**, 388 (1927).

(17) P. Debye, *J. Chem. Phys.*, **1**, 13 (1933).

(18) R. Zana and E. Yeager, *J. Phys. Chem.*, **71**, 521 (1967).

(19) J. O'M. Bockris and P. P. S. Saluja, *J. Phys. Chem.*, in press.

(20) G. L. Madan, P. P. S. Saluja, and J. O'M. Bockris, to be published.

(21) E. W. Carstensen, *J. Acoust. Soc. Amer.*, **26**, 858 (1954).

(22) B. E. Conway and L. H. Laliberte, *J. Phys. Chem.*, **74**, 7116 (1970); B. E. Conway and R. E. Verrall, *ibid.*, **70**, 3961 (1966).

(23) R. Garnsey, R. Boe, R. Mahoney, and T. A. Litovitz, *J. Chem. Phys.*, **50**, 5222 (1969).

(24) N. E. Richards, F. J. Brauner, and J. O'M. Bockris, *Brit. J. Appl. Phys.*, **6**, 387 (1955).

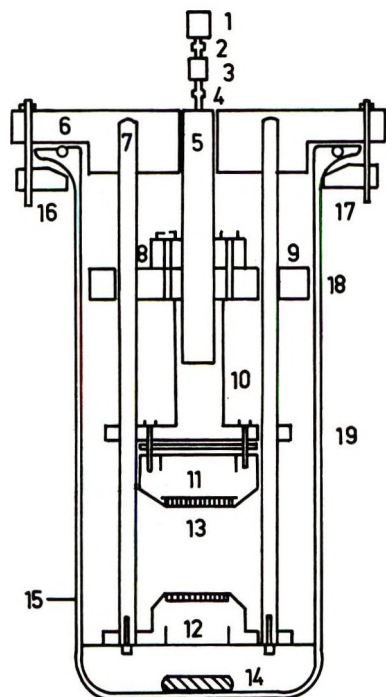


Figure 1. Acoustic interferometer: 1, stepping motor; 2, bellows coupling; 3, speed reducer (10:1); 4, universal joint; 5, micrometer screw; 6, brass head-plate; 7, stainless steel guide rods; 8, split-nut; 9, Teflon bushings; 10, stainless steel hollow cylinder; 11, receiver transducer housing; 12, source transducer housing; 13, ceramic disk transducers; 14, Teflon-coated bar magnet; 15, glass cell; 16, threaded shafts; 17, lower brass plate; 18, mounting plate for split-nut; 19, base plate for source transducer.

Both methods are of comparable value for the present situation. Minor disadvantages of the method due to Carstensen²¹ are associated with the large size of the equipment necessary, evaporation from the solution, and possible mixing due to permeability of the membranes.

2. Method Used. The apparatus is shown in Figure 1. Further details may be obtained from RBB²⁴ and from Saluja.^{25a} The present arrangement differs from that of RBB²⁴ in that the method used for determination of the position of the moving transducer was not measured with a cathetometer (RBB²⁴), but the distance moved by the transducer was measured by the use of a stepping motor.

The stepping motor moves the receiver transducer housing by rotating a nontranslating screw through the nut in the housing for a precise fraction of a turn (1/200th in the present work) for each pulse fed to it. Thus, for a screw of 20 threads per centimeter, the minimum movement which can be detected will be $1/200 \times 1/20 = 2.5 \times 10^{-4}$ cm. This accuracy is improved by utilizing a 10:1 speed reducer to 2.5×10^{-5} cm. Thus, the associated electronics in this method consist of two main parts: (a) a phase detector circuit to measure the phase changes, and (b) a design to operate the stepping motor and to count the

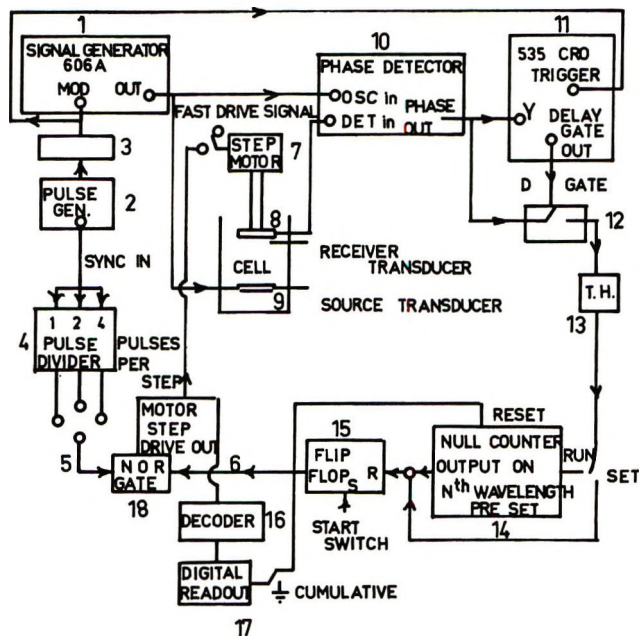


Figure 2. Block diagram of complete apparatus: 1, signal generator; 2, pulse generator; 3, amplifier; 4, pulse divider; 5, pulse output from pulse generator; 6, output from flip-flop; 7, stepping motor; 8, receiver transducer; 9, source transducer; 10, phase detector; 11, CRO; 12, D gate; 13, track-hold; 14, null counter; 15, flip-flop; 16, decoder; 17, digital read out; 18, NOR gate.

number of steps covered by it for a preset number of wavelengths.

3. Electronics. The block diagram of the associated electronics is shown in Figure 2. The pulses obtained from the pulse generator (2) (Tektronics, 161 and 162) after amplification (3) are fed to trigger an oscilloscope (11) (Tektronics 535), and another pulse output is used to modulate 5-MHz frequency signal output from the signal generator (1) (Hewlett-Packard 606A). The modulated 5-MHz output from the signal generator (1) is fed to the source transducer (9) and the signal picked up by the receiver transducer (8) is fed to the "detector-in" terminal and the second output from the signal generator to the "oscillator-in" terminal of the phase detector (10) (Figure 2). The phase detector (10) provides output pulses with amplitude proportional to the phase difference between the "oscillator-in" and the "detector-in" signals. This output is observed on the Y axis of the oscilloscope screen (Tektronics 535).

A sampled portion of the phase detector output signal is fed through a "track-hold" circuit (13) to a "null detector" (14). The sampling is done to avoid parts of the phase detector output signal, the amplitude of which is varying because of reflections. The "track-hold" circuit (13) holds the phase output voltage until

(25) (a) P. P. S. Saluja, Ph.D. Thesis, University of Pennsylvania (1971); Microfilm Order No. 71-26,080; (b) for further details about the operation of stepping motor and phase detector circuitry, see Saluja.^{25a}

another phase change occurs. When the reference signal and the received signal are completely out of phase, the null counter has no signal input and, therefore, it resets the "flip-flop" (15) which turns off the "NOR gate" (18). This turns off the motor step drive output stopping the motor (7) at the present wavelength. In all positions of the phase changes, except null, the motor step drive output is on. The null counter (14) has a provision of counting 1, 2, 4, 10, 20, and 40 wavelengths.

4. *Procedure.* The salts (obtained from J. T. Baker and Co., K & K Laboratories, Aero Chemical Corp., Lapine Scientific Co.) were dissolved in conductivity water, Hygroscopic salts were weighed in an argon drybox. About 500 ml of test solution was taken in a glass cell (15) which was inserted in the hold in the plywood lid on the thermostat. The bath temperature was controlled to within ± 0.005 to $\pm 0.01^\circ$. The acoustic interferometer was placed in the glass cell (15) with an O-ring placed on its top for tight fit. A 2-3-hr period was allowed for the attainment of thermal equilibrium. All the electronic components were then connected by shielded cables (RG-223/u). A sharp minimum is observed on the oscilloscope screen when the acoustic signal and the direct reference signal are completely out of phase. The wavelength is then determined by moving the receiver transducer by a screw driven by the stepping motor for a fixed number (in the present work 40) of minima and stopping it automatically. The number of pulses fed to the stepping motor were counted by means of a decoder (16) and digital read out (17) (see Figure 2).

After each run, the interferometer and the glass cell were removed from the bath, thoroughly washed and rinsed with both distilled water and conductivity water, dried, and made ready for the next determination. Throughout the experiments, the frequency, ν , of ultrasonic waves was determined by means of a highly accurate frequency counter (Hewlett-Packard, 524D). Thus, the ultrasonic velocity was calculated from the expression

$$\text{velocity} = (\text{number of steps per wavelength}) \times (\text{distance for each step}) \times \nu \quad (2)$$

Typical values of the number of steps per wavelength for 5-MHz ultrasonic waves ranged from 1000 to 1300.

III. Results

1. *Primary Results.* (a) The compressibilities of electrolyte solutions as a function of concentration, calculated from eq 1, are shown in Table I.

(b) Assuming the validity of Passynski's equation,¹² the total solvation number, n_{sum} , calculated from

$$n_{\text{sum}} = \frac{n_1}{n_2} \left(1 - \frac{\beta_{\text{soln}}}{\beta_{\text{solV}}} \frac{V}{n_1 \bar{V}_1^\circ} \right) \quad (3)$$

Table I: Adiabatic Compressibility and Total Solvation Number of Electrolytes as a Function of Concentration at 25°

c , mol/l.	Adiabatic compressibility $\times 10^6$, bar ⁻¹	Total solvation number of salt	c , mol/l.	Adiabatic compressibility $\times 10^6$, bar ⁻¹	Total solvation number of salt
NaF			BaBr ₂		
1.0	38.72	7.5 \pm 0.0	3.29	20.39	7.5 \pm 0.0
0.5	41.57	7.9 \pm 0.0	1.21	33.60	10.7 \pm 0.0
0.1	44.04	8.5 \pm 0.3	0.50	39.59	12.4 \pm 0.0
0.05	44.35	9.1 \pm 0.1	0.14	43.09	14.6 \pm 0.2
			0.05	44.1	15.2 \pm 0.5
NaCl			BaI ₂		
5.1	26.75	3.9 \pm 0.0	2.50	26.00	9.1 \pm 0.0
2.0	36.64	4.7 \pm 0.0	0.50	39.86	11.7 \pm 0.0
1.0	40.04	5.7 \pm 0.0	0.25	41.99	13.2 \pm 0.1
0.1	44.20	6.5 \pm 0.3	0.05	44.05	15.4 \pm 0.4
0.05	44.45	6.9 \pm 0.5	0.025	44.40	16.2 \pm 1.0
NaBr			MgCl ₂		
5.2	26.93	3.7 \pm 0.0	4.22	21.61	6.1 \pm 0.0
2.0	35.99	5.1 \pm 0.0	2.11	29.74	8.4 \pm 0.0
1.1	39.75	5.7 \pm 0.0	1.05	35.94	10.1 \pm 0.0
0.1	44.23	6.1 \pm 0.3	0.09	43.88	12.3 \pm 0.3
0.05	44.47	6.3 \pm 0.5	0.05	44.21	12.8 \pm 0.6
NaI			CaCl ₂		
5.0	28.78	3.2 \pm 0.0	4.05	22.90	5.9 \pm 0.0
2.1	36.83	4.4 \pm 0.0	2.02	30.94	8.0 \pm 0.0
1.0	40.84	4.6 \pm 0.0	1.00	36.91	9.4 \pm 0.0
0.1	44.28	5.5 \pm 0.3	0.10	43.82	11.1 \pm 0.3
0.05	44.48	6.1 \pm 0.5	0.05	44.22	12.1 \pm 0.5
LiCl			SrCl ₂		
5.0	29.93	3.3 \pm 0.0	3.11	27.38	6.2 \pm 0.0
2.0	37.15	4.5 \pm 0.0	1.50	33.91	8.5 \pm 0.0
1.0	40.60	4.9 \pm 0.0	0.80	38.42	9.5 \pm 0.0
0.1	44.30	5.3 \pm 0.3	0.10	44.04	8.8 \pm 0.3
0.05	44.49	6.0 \pm 0.4	0.03	44.45	13.2 \pm 0.8
KCl			LaCl ₃		
4.0	29.88	4.0 \pm 0.0	1.68	28.11	11.6 \pm 0.0
1.0	39.84	5.7 \pm 0.0	0.34	40.51	15.4 \pm 0.0
0.17	43.90	6.2 \pm 0.1	0.03	44.23	18.3 \pm 0.7
0.05	44.46	6.6 \pm 0.5	0.02	44.47	18.9 \pm 1.4
RbCl			CeCl ₃		
3.5	31.84	4.0 \pm 0.0	1.68	29.74	9.7 \pm 0.0
1.7	38.13	4.9 \pm 0.0	0.34	40.73	14.6 \pm 0.0
0.9	41.17	4.9 \pm 0.0	0.03	44.14	21.5 \pm 0.7
0.1	44.30	5.0 \pm 0.2	0.02	44.42	22.4 \pm 1.3
0.05	44.50	5.5 \pm 0.5			
CsCl			ThCl ₄		
5.0	28.15	3.2 \pm 0.0	1.25	29.39	14.5 \pm 0.0
1.0	42.03	3.2 \pm 0.0	0.25	40.90	18.8 \pm 0.0
0.1	44.43	3.6 \pm 0.3	0.11	42.84	21.0 \pm 0.3
0.05	44.52	5.1 \pm 0.5	0.05	43.72	22.9 \pm 0.5
			0.03	44.19	26.6 \pm 1.1
BaCl ₂					
1.65	30.90	9.9 \pm 0.0			
0.74	37.65	11.6 \pm 0.0			
0.50	39.44	12.8 \pm 0.0			
0.1	43.65	13.5 \pm 0.0			
0.05	44.14	14.6 \pm 0.5			

(where β_{soln} and β_{solv} are the compressibilities of solution and solvent, respectively, and n_1 and n_2 are, respectively, the number of moles of solvent and solute in solution; V and \bar{V}_1° are the volume of solution and partial molar volume of pure solvent) are shown in the last column of Table I. A correction of these results to allow for residual compressibility in the coordination shell is discussed in section IV1.

(c) Accuracy analysis:^{25a} the error caused by the temperature fluctuations of $\pm 0.005^\circ$ is equal to ± 0.01 m sec⁻¹ (2 m sec⁻¹ deg⁻¹ = temperature coefficient of sound velocity).

The error caused by the nonuniformity of the pitch for different portions of the screw was minimized by carrying out measurements in water and ionic solutions for certain reproducible regions of the screw. It was estimated that the accuracy of the measurements over the reproducible region was no better than 0.3 steps (7.5×10^{-6} cm) per wavelength. This corresponds to ± 0.4 m sec⁻¹ in velocity.

The error in the velocity due to changes in concentration caused by evaporation is negligible.^{25a}

The velocity was found to be independent of the mode of supply of power (continuous or discontinuous). The velocity was independent of stirring.

The estimated error in frequency, ± 4 cps, corresponds to an error in velocity of ± 0.001 m sec⁻¹.

The total error in velocity is hence ± 0.4 m sec⁻¹. The standard deviation in the velocity for ten measurements in conductivity water was ± 0.076 m sec⁻¹. Thus, velocity measurements were *ca.* 30 times more precise than those of RBB.²⁴

The corresponding error in compressibility is ± 0.02 bar⁻¹ or 0.4%.

The effects of the degree of hydrolysis and the degree of ion association (*i.e.*, ion-pair and triple ion formation) were examined. In any case, such effects were not found to be significant. Correspondingly, the probability of ion-pair and triple ion formation, in the case of divalent and trivalent ions, is significant only for ligands such as sulfate, picrate, iodate, and such polyatomic species. Except Pb²⁺, Zn²⁺, the chloride ion complexes with metal ions used in this work (*e.g.*, Mg²⁺, Ba²⁺, Sr²⁺, etc.) are not indicated. Moreover, the concentration of ion pairs and triple ions is significant only in solvents with low dielectric constant (<15). Thus, the effect has been assumed negligible in our cases.

The accuracy of the solvation number (assuming the validity of the Passynski equation¹²) is listed in Table I.

2. *Derived Results.* To separate the total SN obtained from the compressibility measurements into individual SN's, a parallel method yielding differences in cationic and anionic SN's must be used. The difference SN can be obtained by measurements of ionic vibration potential.^{17,18} This potential difference

is related to the apparent molar masses of the solvated cation, W_+ , and solvated anion, W_- , as

$$\psi_0 = 1.55 \times 10^{-7} a_0 \left[\frac{t_+}{z_+} W_+ - \frac{t_-}{z_-} W_- \right] \quad (4)$$

where a_0 is the velocity amplitude of the ultrasonic wave [the velocity amplitude (in centimeters per second) is defined as the ratio of the pressure of the ultrasonic waves to the characteristic acoustic impedance of the medium], t_+ and t_- are transference numbers, and z_+ and z_- are the charges of the cations and anions. The apparent molar mass, W_i , of the moving ion is given by the mass of the solvated ion, $(M_i)_s$, diminished by the mass of the free solvent displaced, $(V_s)_i \rho_0$, where $(V_s)_i$ is the volume of the moving ion and ρ_0 is the density of the solvent. The mass of the solvated ion, $(M_i)_s$, can be expressed as the sum of the masses of the bare ion, M_i , and that of the solvation water, $n_i M_0$, where n_i is the SN of the *i*th ion and M_0 is the molar weight of the solvent. Thus

$$W_i = M_i + n_i M_0 - (V_s)_i \rho_0 \quad (5)$$

By substituting W_i from eq 5 into eq 4, the following expression is obtained for the difference in the SN of cation and anion

$$\left(\frac{t_+}{z_+} \right) n_+ - \left(\frac{t_-}{z_-} \right) n_- = \frac{(\psi_0/a_0)}{M_0 \times 1.55 \times 10^{-7}} - \frac{1}{M_0} \left(\frac{t_+}{z_+} M_+ - \frac{t_-}{z_-} M_- \right) + \frac{\rho_0}{M_0} \left[\frac{t_+}{z_+} (V_s)_+ - \frac{t_-}{z_-} (V_s)_- \right] \quad (6)$$

For water

$$\left(\frac{t_+}{z_+} \right) n_+ - \left(\frac{t_-}{z_-} \right) n_- = \frac{\psi_0/a_0}{2.79} + A \quad (7)$$

where ψ_0/a_0 is expressed in microvolts cm⁻¹ sec and A is a constant for a given electrolyte. The evaluation of A requires t_+ , t_- , M_+ , M_- , $(V_s)_+$, and $(V_s)_-$. M_+ and M_- are the atomic weights of the ions, t_+ and t_- are taken from a compilation due to Conway,²⁶ and from Zana and Yeager.¹⁸ The parameters $(V_s)_+$ and $(V_s)_-$ can be obtained from a calibration curve due to Nightingale²⁷ for the Stokes' radii and solvated radii for small ions. The relevant parameters are listed in Table II. In using eq 7, the concentration dependence of transference numbers were examined. The effect was found to be negligible, in cases where $t_+ \simeq t_-$, the transference number is little dependent on concentration (*e.g.*, for KCl).

(26) B. E. Conway, "Electrochemical Data," Elsevier, Amsterdam, 1952.

(27) E. R. Nightingale, Jr., *J. Phys. Chem.*, **63**, 1381 (1959).

Table II: Relevant Parameters to Obtain Individual Solvation Number

Electrolyte	t_+ (infinite dilution)	t_- (infinite dilution)	$(V_s)_+$ $\text{cm}^3 \text{mol}^{-1}$	$(V_s)_-$ $\text{cm}^3 \text{mol}^{-1}$	A	$\psi_0/a_0, \mu\text{V cm}^{-1} \text{sec}$			
						0.05 N	0.1 N	1.0 N	5.0 N
NaF	0.076	0.524	115.8	110.1	-0.20	1.0 ^a	1.0	0.9	Insol
NaCl	0.396	0.604	115.8	92.4	0.14	1.1 ^a	1.0	0.7	(0.7) ^c
NaBr	0.392	0.608	115.8	90.7	1.66	-2.8 ^a	-2.8	-2.6	(-2.6)
NaI	0.395	0.605	115.8	91.5	3.23	-6.4	-6.4	-5.7	(-5.7)
LiCl	0.336	0.664	140.7	92.4	0.40	0.1 ^b	0.1	0.05	(0.0)
KCl	0.490	0.510	91.5	92.4	-0.20	1.7 ^b	1.7	1.7	(1.7)
RbCl	0.511	0.489	89.9	92.4	-1.42	5.2 ^b	5.2	(5.2)	(5.2)
CsCl	0.500	0.500	89.9	92.4	-2.78	8.1 ^b	8.1	(8.1)	(8.1)
BaCl ₂	0.454	0.546	166.4	92.4	-1.35	4.2 ^a	4.2	3.6	(3.6)
BaBr ₂	0.448	0.552	166.4	90.7	-0.03	1.8 ^a	1.6	0.8	(0.8)
BaI ₂	0.452	0.548	166.4	91.5	1.45	-1.7 ^a	-1.8	-2.0	(2.03)
MgCl ₂	0.410	0.590	197.9	92.4	0.12	1.1 ^a	1.0	1.0	(1.0)
CaCl ₂	0.438	0.562	176.5	92.4	-0.12	1.1 ^a	1.1	1.0	0.8
SrCl ₂	0.438	0.562	176.5	92.4	-0.70	2.6 ^a	2.5	2.1	1.8
LaCl ₃	0.476	0.524	233.1	92.4	-0.82	3.9 ^a	3.7	3.2	(3.2)
CeCl ₃	0.460	0.540	233.1	92.4	-0.91	3.8 ^a	3.8	3.0	2.5
ThCl ₄	0.485	0.515	330.9	92.4	-0.95	3.4 ^a	3.2	2.9	(2.9)

^a G. L. Madan, P. P. S. Saluja, and J. O'M. Bockris, to be published. ^b R. Zana and E. Yeager, *J. Phys. Chem.*, **71**, 521 (1967).

^c Values in parentheses are extrapolated values.

However, in a calculation for NaCl with t_+ (and t_-) dependent on concentration the solvation number for Na^+ changed by less than 0.2. Thus, the effect is negligible.

The individual solvation numbers are obtained from eq 7 and the sum of the solvation number of the electrolyte from the compressibility method (see Table III). The solvation numbers obtained by the present method are also compared with the values obtained from other methods (see Table IV).

An alternative method of calculating solvation number from density and ionic vibration potential measurements was considered. The calculations indicated values which are typically two units higher (see Table V).

However, it was deemed a less appropriate method with which to proceed. The reason is that partial molar volume values which are utilized in the method are separated out from the thermodynamically valuable total partial molar volumes of the entire electrolyte, and they do not give rise to values which are therefore thermodynamically meaningful. Were we to utilize this method, we would get into controversial questions, such as: Does the density measurement concern the same packing and therefore the same local density as that which occurs during ionic vibration potential measurements? How is the partial molar volume of the electrolyte broken up?

Thus, the present method is a clear, independent, and entirely a new method for the attack upon the problem of the environment around the ion. It is distinct from older methods.

3. Phenomenology of Individual Solvation Number.

(a) Solvation Number as a Function of Concentration.

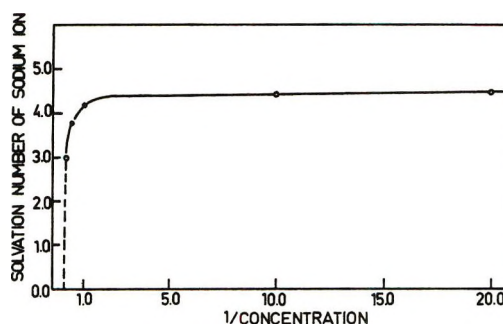


Figure 3. SN of sodium ion against reciprocal of concentration of alkali halide solution.

The solvation number (SN) decreases with increase in concentration. A typical plot of SN against $1/\text{concentration}$ (c) is shown in Figure 3. It is seen from Figure 3 that SN approaches zero at high concentration ($>5.0 M$) and is independent of concentration up to concentration of about $1.5 N$ for monovalent ions. A point of inflection is obtained on the $\text{SN}-1/c$ plot. The concentrations for the inflection point for different ions are listed in Table VI.

(b) *The SN as a Function of Charge/Size Ratio of the Cations.* The SN of alkali metal cations decreases with increasing size. An extrapolation of the plot of SN against $1/(\text{ionic radius}, r_1)$ indicates that singly charged cations and anions with ionic radii greater than $ca. 2.7 \text{ \AA}$ remain unsolvated (see Figures 4 and 5).

The SN of divalent ions (except for Mg^{2+}) varies in a trend opposite to that of the monovalent ions, *e.g.*, the SN of Ba^{2+} (11) is larger than that of Ca^{2+} (9.0) (see Figure 6).

(c) *SN of Cl^- as a Function of Cations.* A plot of SN of Cl^- against charge/radius (z/r) or cation in-

Table III: Absolute Values of Ionic Solvation Number vs. Concentration at 25°

Electrolyte	Concn	SN of cation	SN of anion	Electrolyte	Concn	SN of cation	SN of anion
NaF	1.0	4.0	3.5	BaBr ₂	3.29	5.7	0.9
	0.5	4.3	3.6		1.21	7.9	1.4
	0.1	4.6	3.9		0.50	9.2	1.6
NaCl	5.1	2.8	1.1	BaI ₂	0.14	11.1	1.8
	2.0	3.2	1.5		0.05	11.6	1.8
	1.0	3.8	1.9		2.50	7.4	0.9
	0.1	4.4	2.1		0.50	9.2	1.3
	0.05	4.7	2.2		0.25	10.3	1.5
NaBr	5.2	3.0	0.7	MgCl ₂	0.05	11.9	1.8
	2.0	3.8	1.3		0.025	12.6	1.8
	1.1	4.2	1.5		6.22	5.1	0.5
	0.1	4.4	1.7		2.11	6.8	0.8
NaI	0.05	4.5	1.8	CaCl ₂	1.05	8.1	1.0
	5.0	3.1	0.1		0.09	9.7	1.3
	2.1	3.8	0.6		0.05	10.1	1.4
	1.0	4.0	0.6		4.05	4.5	0.7
	0.1	4.3	1.2		2.02	5.0	1.0
LiCl	0.05	4.6	1.5	SrCl ₂	1.00	7.1	1.2
	5.0	2.6	0.7		0.10	8.3	1.4
	2.0	3.4	1.1		0.05	9.1	1.5
	1.0	3.7	1.2		3.11	4.4	0.9
	0.1	3.9	1.4		1.50	6.0	1.3
KCl	0.05	4.4	1.6	LaCl ₃	0.80	6.9	1.3
	4.0	2.4	1.6		0.10	6.6	1.1
	1.0	3.3	2.4		0.03	9.8	1.7
	0.17	3.6	2.6		1.68	9.4	0.7
RbCl	0.05	3.8	2.8	CeCl ₃	0.34	12.3	1.0
	3.5	2.4	1.6		0.03	14.8	1.2
	1.7	2.8	2.1		0.02	15.3	1.2
	0.9	2.8	2.1		1.68	7.5	0.7
	0.1	2.9	2.1		0.34	11.6	1.0
CsCl	0.05	3.1	2.4	ThCl ₄	0.03	17.4	1.4
	5.0	1.7	1.5		0.02	18.1	1.4
	1.0	1.7	1.5		1.25	11.9	0.6
	0.1	1.9	1.7		9.25	15.4	0.8
BaCl ₂	0.05	2.7	2.4		0.11	17.4	0.9
	1.65	6.9	1.5		0.05	18.4	1.1
	0.74	8.2	1.7		0.03	22.0	1.1
	0.50	9.0	1.9				
	0.10	9.7	1.9				
	0.05	10.5	2.0				

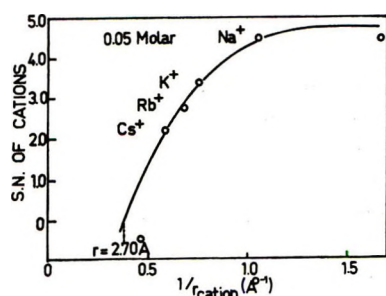


Figure 4. SN plotted as a reciprocal of cationic radius.

indicates that the solvation number is diminished in the presence of multiply charged cations (see Figure 7). The SN of a chloride ion, at a given concentration, has values of 2.4 ± 0.2 and 1.2 ± 0.1 in the presence of Cs^+ and La^{3+} , respectively.

IV. Discussion

1. *Validity of Method.* (a) *Compressibility Method.* The fundamental assumption of the method of Pasyński¹² is that the solvated water molecules have zero compressibility. For liquid water, the total compressibility consists of two parts,^{28,29} about 64% configurational and 36% vibrational. [In consideration of compressibility for water near ions, one considers the total internal pressure created by those ions on the water. Therefore, one must make a plot of the compressibility^{30,31} against total pressure (equal to the sum

(28) W. M. Slie, A. R. Donfor, and T. A. Litovitz, *J. Chem. Phys.*, **44**, 3712 (1966); C. M. Davis, Jr., and T. A. Litovitz, *ibid.*, **42**, 2563 (1965).

(29) D. Eisenberg and W. Kauzman, "The Structure and Properties of Water," Oxford University Press, Oxford, 1969.

Table IV: Ionic Solvation Numbers Obtained by the Present Method Compared with Literature Data

Ion	Present method	Passynski ^a compressibility	Ulich ^b entropy	Ulich ^c mobility	Average ^d of 3 methods	Darmois ^e density	Compressibility		Azam ^h theor.	Broersma ⁱ nmr	Hindman ^j nmr	Fabricand ^k nmr	Creekmore, et al. ^l nmr
							Allam ^f	Stuehr ^g and Yeager					
Li ⁺	4.5	5-6	5	3.5	5 ± 1	2.5	2.7	5-6	6	4	1 ± 1	3.4	
Na ⁺	4.5	6-7	4	2.0	5 ± 1	4.8	3.9	7.0	5	3.1	3.6 ± 1	4.6	
K ⁺	3.8	6-7	3		4 ± 2	1.0	(3.2)	6.0	3	2.1	(6)	4.6	
Rb ⁺	3.0	...	3		3 ± 1	2	1.6	9.9 ± 2	4.0	
Cs ⁺	2.5	1.0	14.6 ± 2	3.9	
F ⁻	4.0	2.0	5		4 ± 1	4.3	(3.2)	2.0	5	1.6	9.9 ± 2	...	
Cl ⁻	2.2	0-1	3		1 ± 1	1	3	0	13.2 ± 2	...	
Br ⁻	1.8	0	2		1 ± 1	...	2.6	0-1	2	0	16.2 ± 2	...	
I ⁻	1.5	0	1		1 ± 1	...	2.1	0	0	0	21.8 ± 2	...	
Ba ²⁺	11.0	16	8	5.0	9	13.0	
Mg ²⁺	10.0	16	13	10.5	14	...	7.0	15.0	
Ca ²⁺	9.0	...	10	7.5	12	

^a A. Passynski, *Acta Physicochim.*, **8**, 385 (1938). ^b H. Ulich, *Z. Elektrochem.*, **36**, 497 (1930). ^c H. Ulich, *Trans. Faraday Soc.*, **23**, 388 (1927). ^d B. E. Conway and J. O'M. Bockris, "Modern Aspects of Electrochemistry," Vol. 1, Butterworths, London, 1954. ^e E. Darmois, *J. Phys. Radium*, **8**, 117 (1942); footnote d. ^f D. S. Allam and W. H. Lee, *J. Chem. Soc. A*, 426 (1966). ^g J. Stuehr and E. Yeager, "Physical Acoustics," Vol. II, part A, W. P. Mason, Ed., Academic Press, New York, N. Y., 1965, Chapter 6. ^h A. M. Azzam, *Can. J. Chem.*, **38**, 993 (1960). ⁱ S. Broersma, *J. Chem. Phys.*, **27**, 481 (1957). ^j J. C. Hindman, *ibid.*, **36**, 1000 (1962). ^k B. P. Fabricand, S. S. Goldberg, R. Leifer, and S. G. Ungar, *Mol. Phys.*, **7**, 425 (1964). ^l R. W. Creekmore and C. N. Reilly, *J. Phys. Chem.*, **73**, 1563 (1969).

Table V: Comparison of Absolute Values of Ionic Solvation Numbers Obtained by Present Method and Those from the Data on Partial Molal Volume and Stokes' Law Radii

Ion	Values of ionic solvation number from present method	Values of ionic solvation numbers from partial molal volume and Stokes' law radii data
Li ⁺	4.0	8.4
Na ⁺	4.5	6.8
K ⁺	3.5	5.5
Rb ⁺	3.0	4.5
Cs ⁺	2.5	4.1
F ⁻	4.0	6.0
Cl ⁻	2.0	3.8
Br ⁻	1.8	3.4
I ⁻	1.5	2.8
Mg ²⁺	10.0	13.0
Ca ²⁺	9.0	11.2
Sr ²⁺	9.0	11.0
Ba ²⁺	11.0	10.1

Table VI: Concentration at Which SN Shows a Rapid Fall

Ion	Electrolyte used	Concentration, mol l. ⁻¹ at inflection point on SN-1/c graph
Na ⁺	NaCl	1.67
Na ⁺	NaBr	1.67
Na ⁺	NaI	1.54
Li ⁺	LiCl	1.82
K ⁺	KCl	1.68
Ba ²⁺	BaCl ₂	1.15
Ba ²⁺	BaBr ₂	1.10
Mg ²⁺	MgCl ₂	0.80
Ca ²⁺	CaCl ₂	0.95
La ³⁺	LaCl ₃	0.67
Ce ³⁺	CeCl ₃	0.36

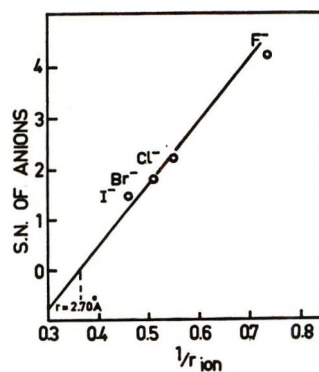
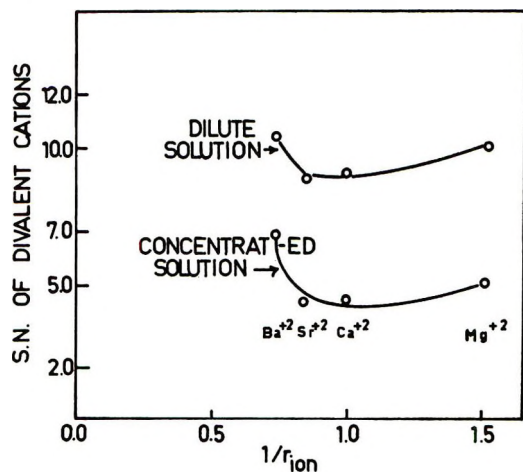
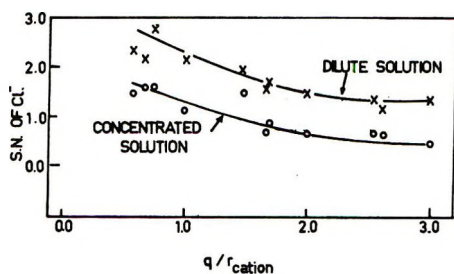


Figure 5. SN of anions against reciprocal of radius.

(30) P. G. Tait, "Physics and Chemistry of the Voyage of H.M.S. Challenger," Vol. II, part IV, 1888.
 (31) J. E. Desnoyers, R. E. Verrall, and B. E. Conway, *J. Chem. Phys.*, **43**, 243 (1965).

Figure 6. SN vs. $1/r_{ion}$ for divalent ions in chloride solutions.Figure 7. SN of Cl^- plotted against charge/size ratio of cations.

of an internal pressure already existing in liquid water and that of the external pressure). Thus, the so-called "zero pressure" compressibility for water, namely, $45 \times 10^{-6} \text{ bar}^{-1}$, corresponds to the internal pressure of water, namely, $1.6 \times 10^3 \text{ bars}$.] Considering solvated water molecules, *i.e.*, those in contact with, and oriented towards the ion, they are out of the solvent structure and, therefore, automatically lose their 64% of the structural or configurational compressibility. The remaining compressibility of solvation water can be obtained from a graph^{30,31} of β against pressure (see Figure 8), provided effective pressure on the solvated water can be calculated.

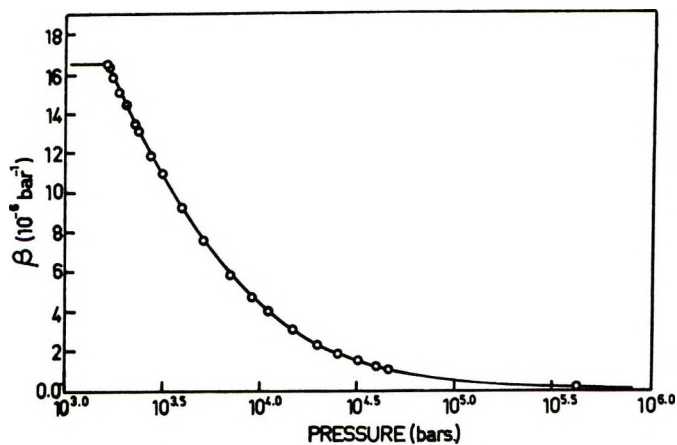
The effective pressure, P_{eff} , on the solvated water molecule arises from the ion-dipole forces and is given by

$$P_{eff} = -\left(\frac{\partial U_r}{\partial r}\right) / A_{dip} \quad (8)$$

or

$$P_{eff} = \frac{2ze\mu \cos \theta}{\epsilon r^3 A_{dip}} \quad (9)$$

where e is the electronic charge, μ is the dipole moment of the water molecule, r is the ion-water distance, dielectric constant, ϵ , equal to unity in the first layer, and $\cos \theta = 1$ by the definition of solvation water. The area of dipole, A_{dip} , can be taken as equal to

Figure 8. Compressibility, β , of water as a function of pressure.

$(v_w)^{2/3}$, where $v_w = (V_w/N)$; V_w is the molar volume of the solvent and N is Avogadro's number. Equation 9, expressed numerically, is

$$P_{eff} = \frac{183.05 \times 10^4}{(r_i + r_w)^3} \text{ (bars)} \quad (10)$$

where r_i and r_w are radii of the ion and water molecule expressed in angstroms (see Table VII).

Table VII: Calculated Values of Effective Pressure, P , and Local Vibrational Compressibility of Water in Primary Hydration Sheath of Ions

Ions	Pressure P , bars	Compressibility $10^{-12}, (\text{dyn cm}^{-2})^{-1}$
Li ⁺	22.88×10^4	0.21
Na ⁺	14.10×10^4	0.34
K ⁺	9.00×10^4	0.53
Rb ⁺	7.66×10^4	0.64
Cs ⁺	6.20×10^4	0.76
F ⁻	8.71×10^4	0.55
Cl ⁻	5.53×10^4	0.85
Br ⁻	4.87×10^4	0.95
I ⁻	4.06×10^4	1.13
Ba ²⁺	17.60×10^4	0.27
Sr ²⁺	21.32×10^4	0.23
Ca ²⁺	26.82×10^4	0.18
Mg ²⁺	41.88×10^4	0.12
Al ³⁺	80.06×10^4	0.06
La ³⁺	33.12×10^4	0.15
Ce ³⁺	31.98×10^4	0.15
Th ⁴⁺	56.42×10^4	0.09

The remaining (*i.e.*, after loss of the configurational) compressibility, corresponding to effective pressure on the solvated water molecule is obtained from β - p plot^{30,31} (see Figure 8 and Table VII). It is seen that the remaining compressibility of solvated water molecules in the vicinity of the ion is effectively zero, in agreement with Passynski's assumption. The local compressibility of solvent water in regions near the ion can also be determined from a theory of electro-

striction worked out by Desnoyers, Verrall, and Conway.³¹

The interpretation of the anomalous changes in the compressibility-radius relation which occur when the radius of the ion is $>3.7 \text{ \AA}$ (*i.e.*, tetraalkylammonium ions), led Conway and Verrall³² to conclude that changes in the compressibility are not only due to electrostricted water but that these large ions cause structure promotion. This structured water around large ions has a lower compressibility than does the bulk water. These large ions have also been described as undergoing hydrophobic hydration, whereas our conclusions apply only to ions of fairly low radius. Such ions are, therefore, said to undergo hydrophilic hydration.^{2a}

What is the compressibility, β_{NSCW} , of nonsolvational coordinated water molecules? By definition, if a coordinated water molecule is not a solvated water, it is not oriented towards the ion. The vibrational compressibility of NSCW molecules will hence correspond to the force arising from the induced dipole and quadrupole interactions with the ion.

The ion-quadrupole interaction energy for the NSCW is not directly calculable without assumptions. Thus, the sign of the quadrupole moment which has been accepted for the calculation of the interaction of ion with water molecules when the waters are oriented as with SCW, is taken from experiment.³³ The value of p_w and the sign of the quadrupole interaction, for the NSCW, must be argued. Thus, in Figure 9a, there is clearly more repulsion than in 9b. The sign will therefore be such that the interaction energy due to the quadrupole interaction is positive for the cation and negative for the anion. Such energies have to be, therefore, appropriately added to the induced dipole interaction energy.

As to the value of p_w , we have *arbitrarily* accepted values due to Buckingham.³³

In analogy with eq 9, the effective pressure of a cation on a molecule will then be

$$P_{\text{eff}}(\text{NSCW}) = \frac{2\alpha_w(z e_0)^2}{\epsilon r^5 A_{\text{dip}}} - \frac{3ze_0 p_w}{3r^4 A_{\text{dip}}} \quad (11)$$

where p_w is the quadrupole moment of a water molecule.

In a typical case for example, that of sodium, the pressure on a solvated coordination water is 1.4×10^5 bars. The corresponding pressure due to the sodium ion on a nonsolvated coordination water molecule is 7×10^3 bars. Reference to the graph of β against pressure^{30,31} shows $\beta_{\text{vib,NSCW}}$ is $7 \times 10^{-6} \text{ bar}^{-1}$, namely 80% of the total compressibility. For NSCW near anions, the two forces, ion-induced dipole and non-quadrupole, are additive as discussed above. For Cl^- , the compressibility of NSCW molecule is obtained to be about $30 \times 10^{-6} \text{ bar}^{-1}$. A correction must be made for this in Passynski equation¹² (*cf.* the cationic case noted above).

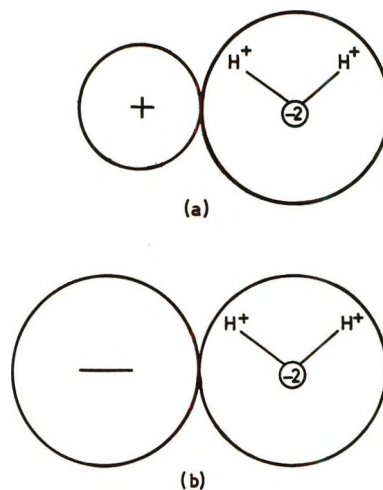


Figure 9. Orientation of a NSCW molecule near to an ion.

The present approach to the determination of "solvation number" implies that the water molecules referred to as solvated are incompressible and the other members of the coordination waters are compressible. This is only 80% true (for Na^+) as the present approach shows. Thus, a correction should be made to the calculation of solvation numbers corresponding to the fact that NSCW molecule is 20 to 30% compressed. It can be shown that this correction amounts to a value not more than 0.5 in the SN of individual ions in any case.

The correction in the case of NaCl at 1.0 *M* solution is found to be only 0.15. We have, therefore, not amended any results for this factor.

(b) *Ionic Vibration Potential Method.* The vibration potentials^{17,18} arise from the different inertial characteristics of the ions. When a sonic pulse strikes the ions, they both move in the same direction but the ion which has a lesser mass moves further, and, for example, if it is an anion, there is an anion lead over the cations. Thus, there is a separation of the two ions and a potential difference, which can be measured by placing electrodes at a distance apart of about half the wavelength of the sonic pulse, arises.

The question is, to what mass does the reaction refer. Here we come to the definition of the primary solvation number^{6,7} which is used in the model. Thus, the latter is the number of the solvent molecules which move with the ion under its motion. The identity of the numbers obtained from this method and those from compressibility measurements is explained below.

The vibration potential values are, by definition, connected to the masses of the ions *which move*. Thus, the mass difference measured by the ionic vibration potential will tend to be that of the ions together with

(32) B. E. Conway and R. E. Verrall, *J. Phys. Chem.*, **70**, 3961 (1966).

(33) A. D. Buckingham, *Discuss. Faraday Soc.*, **24**, 151 (1957); *Quart. Rev. Chem. Soc.*, **13**, 183 (1959).

their primary hydration sheath. This is clearly seen with cations. Thus, here, a typical interaction energy is that of Na^+ with SCW of *ca.* 20 kcal mol⁻¹, whereas that of the same ion with a NSCW is *ca.* 1 kcal mol⁻¹. On the other hand, each NSCW is bound to the solvent structure with three H bonds so that its binding energy is *ca.* $3/4 \times 10 = 7.5$ kcal mol⁻¹. However, with anions the situation is less clear. Thus, a typical interaction energy with SCW is *ca.* 18 kcal mol⁻¹, whereas for the interaction with NSCW (where the quadrupole energy adds to the induced dipole) the interaction energy is *ca.* 7 kcal mol⁻¹, whereas that of the NSCW with the solvent is only slightly greater.

2. *Interpretation of Phenomenology.* (a) *Dependence of Solvation Number on Concentration for Ions.* The diminution of the SN with increasing concentration (Figure 3) can be rationalized in terms of the overlapping of the solvation shells of neighboring ions. If this model is correct, then the average separation, l_{obsd} , of the ions at concentration corresponding to the inflection point on the SN-1/c plot should be linearly related to the size of the solvated ions.

Now the average separation of ions in a solution is given by^{6,34}

$$l \text{ (in } \text{\AA}) = Ac^{-1/3} \quad (12)$$

where A has values of 9.40, 8.21, 7.46, and 6.93 for 1:1, 2:1, 3:1, and 4:1 electrolytes, respectively, and c is the concentration in moles per liter. The calculated average separation from the size of the solvated ions of an electrolyte will be equal to $(r_+ + 2r_w)$ and $(r_- + 2r_w)$.

A plot of l_{calcd} against l_{obsd} from eq 8 corresponding to inflection point concentration on SN-1/c plot gives a straight line (see Figure 10 and Table VIII). If the model is correct, the slope should be 45°. The observed slope is 33-35°.

(b) *Dependence of Solvation Number on Radius for Divalent Ions.* In respect to the phenomenology of the SN for divalent ions (Figure 6), two factors must be

Table VIII: Average Separation of Ions at Point Inflection in and That Calculated with the Size of the Ion

System	l_{calcd} (with size of solvated ion)	l_{obsd}
NaCl	8.36	7.93
NaBr	8.50	7.93
NaI	8.70	8.14
LiCl	8.00	7.70
KCl	8.70	7.90
BaCl ₂	8.76	7.84
BaBr ₂	8.90	7.95
MgCl ₂	8.07	8.84
CaCl ₂	8.40	8.35
LaCl ₃	8.56	8.54
CeCl ₃	8.50	10.50

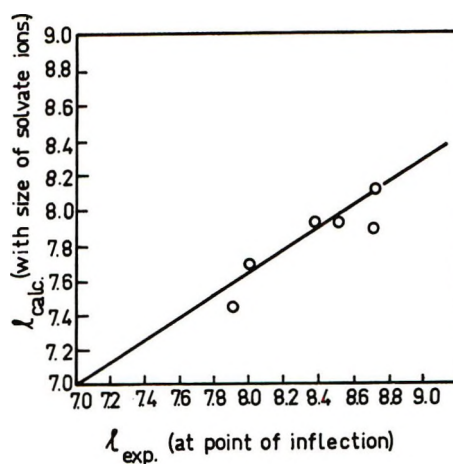


Figure 10. The size of the solvated ions as a function of average solvation at inflection point on SN-1/concentration plot.

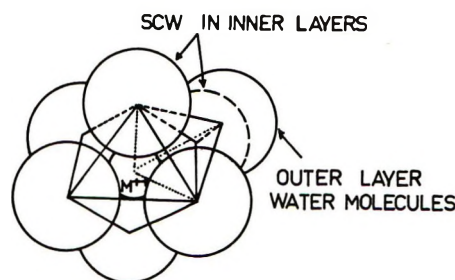


Figure 11. Solvation waters around a small divalent ion.

considered: (a) the volume available for packing solvation waters in the first shell; (b) the ionic field at the center of a water dipole. Both factors are size dependent. For a small divalent ion, (Mg^{2+}) (with an SN of ~ 10), the available volume in the first shell is small; *i.e.*, the excess solvation waters, given by the difference between the SN and the inner shell CN, may still be oriented (and not in direct contact) towards the ion but at a distance intermediate to that between the first layer and second layer³⁵ as shown in Figure 11. For a larger size divalent ion (say Ba^{2+}), with an SN of 12, all the solvation waters can be oriented in the first shell because the space as well as orienting ionic field is sufficient in the first shell compared to the field to orient a dipole in the intermediate layer around a small ion (Mg^{2+}) (see Figure 11). The trend of the SN-1/ r_{ion} plot is thus qualitatively in agreement with the model discussed.

(c) *SN of Cl^- as a Function of Cations.* The differences of the solvation number of the chloride ion in the presence of different cations is puzzling. Such results are not due to difficulties in experimental results. Indeed, a similar effect of alkali metal cations on the

(34) R. A. Robinson and R. H. Stokes, "Electrolyte Solutions," Academic Press, New York, N. Y., 1955.

(35) B. E. Conway and J. O'M. Bockris, *Electrochim. Acta*, **3**, 340 (1961).

partial molar volume of Cl^- (\bar{V}_{Cl^-}) has been obtained by Zana and Yeager.¹⁹ \bar{V}_{Cl^-} varies from 26.5 to 23.5 $\text{cm}^3 \text{mol}^{-1}$ in going from Li^+ to Cs^+ . The effect of divalent cations is also evidenced by an average value of 20 $\text{cm}^3 \text{mol}^{-1}$ for \bar{V}_{Cl^-} .

We suggest, but only qualitatively, that the effect may arise from the fact that the mobility of Cs^+ and Cl^- are about equal (76) but less than that of Li^+ (39). Thus, Li^+ seems to wait longer at a given site compared to that of Cs^+ . So, the probability of knocking off water from the solvent ion shell of Cl^- during its diffusional movement is higher in the ionic atmosphere of Li^+ compared to that of Cs^+ .

3. *SN in Terms of Motion near an Ion.* The model⁶ suggests that the solvation number depends on the time $\tau_{\text{ion, wait}}$ during which an ion remains at a site during its diffusion in the solution compared with $\tau_{\text{water, orient}}$ for a solvent dipole, after arrival next to it of an ion in the water structure. Hence, SN/CN is a function of ratio of ion-wait and water-orientation times. Thus, if $\tau_{\text{water, orient}}/\tau_{\text{ion, wait}} \rightarrow \infty$, $\text{SN}/\text{CN} \rightarrow 0$; if $\tau_{\text{ion, wait}}/\tau_{\text{water, orient}} \rightarrow \infty$, $\text{SN}/\text{CN} \rightarrow 1$.

It is possible to calculate $\tau_{\text{water, orient}}$ from an equation due to Conway, Bockris, and Linton³⁶ for the field induced changes in the rotational frequencies of water after the arrival in their vicinity of ions. These workers showed that the new frequency was given by

$$w_{\text{field due to ion}} = w_0 \text{ field } (f/P) \quad (13)$$

where $w_{\text{field due to ion}}$ and $w_0 \text{ field}$ are the field-induced and zero-field rotational frequencies of water, *i.e.*, frequency of water near to an ion and very far from the ion. f is the ionic field acting on the ion. Hence

$$\tau_{\text{water, orient field}}^0 = \tau_{\text{water, orient}}^0 \left(\frac{P}{f} \right) \quad (14)$$

Using eq 13 and 14 and a value³⁶ of $P = 3.5 \times 10^{-4}$ dyn molecule⁻¹, where P is the average force in pure water independent of angle of rotation, an average

Table IX: Solvation Number in Terms of Motion Near an Ion

Ions	SN/CN	$\tau_{\text{ion, wait}}^a$ $\times 10^{-11}$	$\tau_{\text{water, orient}}$ $\times 10^{-11}$ sec	$\tau_{\text{ion, wait}}/\tau_{\text{water, orient}}$
Li^+	0.67	4.38	1.485	2.94
Na^+	0.67	3.37	2.40	1.40
K^+	0.57	2.87	3.78	0.76
Rb^+	0.47	2.70	4.43	0.61
Cs^+	0.30	2.70	5.48	0.50

^a From the Einstein-Schmolowski relation, with average jump distance of 3.0 Å.

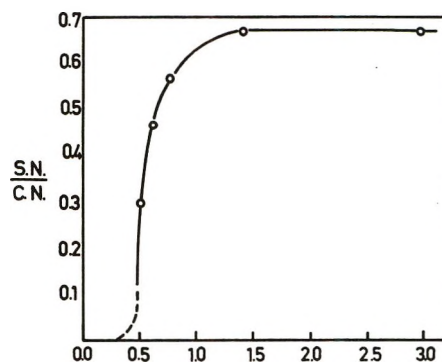


Figure 12. SN/CN plotted against ratio of ion-wait and water-orientation times for monovalent ions.

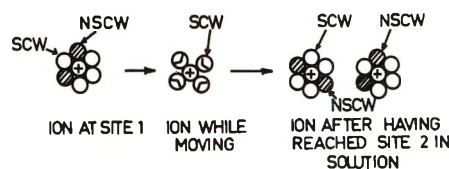


Figure 13. SN in terms of motion near an ion.

value of $\tau_{\text{water, orient}}^0$ given by Hertz, *et al.*,³⁷ of 0.6×10^{-11} sec, the CN from Lawrence^{1,11,38} and the SN from Table II, the results are in Figure 12 and Table IX and are consistent with the model. An attempt to represent this is shown in Figure 13.

4. *Indication of the Model for the Region near an Ion from Model Calculations of Thermal Quantities.* As has been shown elsewhere,¹⁹ numerical calculations of the heat and entropy of the solvation of ions can be made more consistent with the experimental values if the model used involves "oriented solvational" and "nonsolvational" coordination waters.^{39,40}

Acknowledgments. The authors wish to acknowledge with gratitude the financial support given by the Office of Saline Water. One of us, J. O'M. Bockris, wishes to acknowledge discussions with Dr. W. McCoy of that office and with Professor B. E. Conway, University of Ottawa.

(36) B. E. Conway, J. O'M. Bockris, and H. Linton, *J. Chem. Phys.* **24**, 834 (1956).

(37) H. G. Hertz, *Angew. Chem., Int. Ed. Engl.*, **9**, 124 (1970).

(38) R. M. Lawrence, Ph.D. Thesis, University of Arkansas (1965).

(39) NOTE ADDED IN PROOF. Since the submission of this article, Hinton and Amis⁴⁰ have published an extensive review on solvation number of ions calling the attention particularly to the need of the determination of individual solvation number of the ion for the understanding of the structure of solvation shells. In fact, this is the main aim of the work we have reported in the present article and elsewhere.¹⁹

(40) J. F. Hinton and E. S. Amis, *Chem. Rev.*, **71**, 627 (1971).

Ion-Pair Aggregation in Solutions of Complexes of Carbanion

Salts and Macrocyclic Polyethers

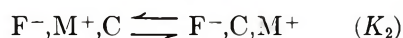
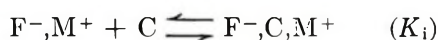
by U. Takaki, T. E. Hogen Esch, and J. Smid*¹

Chemistry Department, College of Environmental Science and Forestry, State University of New York, Syracuse, New York 13210 (Received February 7, 1972)

Publication costs assisted by the Petroleum Research Fund and National Science Foundation

Interaction of macrocyclic polyethers or crown ethers (C) and tight ion pairs of fluorenyl salts (F^-,M^+) in ethereal solvents leads to the formation of two isomeric ion pair complexes, *viz.*, crown-complexed contact ion pairs (F^-,M^+,C) and crown-separated ion pairs (F^-,C,M^+). The ratio of the concentrations of the two species was found to depend on the carbanion salt concentration, and evidence is presented that aggregation of the crown-separated ion pairs is the principal cause of this phenomenon. Values for the aggregation constant of the equilibrium $2F^-,C,M^+ \rightleftharpoons (F^-,C,M^+)_2$ were obtained in tetrahydrofuran, 2-methyltetrahydrofuran, and tetrahydropyran, with M^+ being sodium or potassium.

Macrocyclic polyethers or crown ethers, a class of powerful cation binding compounds,² form stable 1:1 and, sometimes, 2:1 complexes with carbanion salts such as the alkali and alkaline earth salts of fluorenyl.^{3,4} In low-polarity media the salt-crown complexes are ion pairs, and they can exist in two isomeric forms.⁴ The crown ether (denoted by C), when added to a solution of tight fluorenyl ion pairs, can coordinate externally to the ion pair (F^-,M^+,C), but its interaction with the cation may also induce ion-pair separation (F^-,C,M^+)



In the case of fluorenyl salts, the two isomeric ion pairs, which have also been observed in the presence of other cation-complexing agents such as poly(glycol dimethyl ethers),⁵ are easily distinguishable by their different optical absorption maxima.

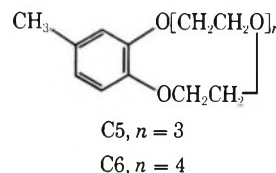
While the ratio $K_2 = F^-,C,M^+/F^-,M^+,C$ varies considerably with temperature and solvent polarity,⁴ the preceding scheme describing the complex formation predicts that K_2 should be independent of the concentrations of crown ether and carbanion salt. This was indeed found for most of the investigated fluorenyl-crown systems as long as the carbanion concentration did not exceed a few times $10^{-3} M$.⁴ Above this concentration, a pronounced shift in favor of the crown-separated ion pairs was detected.

The cause of this phenomenon is the subject of the present investigation. The systems fluorenylsodium-4'-methylbenzo-15-crown-5 and fluorenylpotassium-4'-methylbenzo-18-crown-6 in tetrahydrofuran (THF), 2-methyltetrahydrofuran (MTHF), and tetrahydropyran (THP) as solvents were selected, since the constants K_2

fall within a range of values that is convenient from an experimental point of view. The results suggest that aggregation of crown-separated ion pairs, F^-,C,M^+ , constitutes the most probable cause for the increase in the fraction of separated-ion-pair complexes at high carbanion concentrations.

Experimental Section

The two crown compounds, 4'-methylbenzo-15-crown-5 and 4'-methylbenzo-18-crown-6 (depicted below and denoted by C5 and C6, respectively) were



synthesized by utilizing the general procedures for preparation of the crown ethers as outlined by Pedersen,² with 4-methylcatechol (Aldrich) as the starting material. The final products, recrystallized from petroleum ether (30–60°), were obtained in 57% (C5) and 52% (C6) yield, the respective melting points being 51.2–52° and 54–55°.

(1) To whom correspondence should be addressed.

(2) C. J. Pedersen, *J. Amer. Chem. Soc.*, **89**, 2495, 7017 (1967); **92**, 386 (1970); H. K. Frensdorff, *ibid.*, **93**, 600, 4648 (1971); R. M. Izatt, D. P. Nelson, J. H. Rytting, B. L. Haymore, and J. J. Christensen, *ibid.*, **93**, 1619 (1971); E. M. Arnett and T. C. Moriarity, *ibid.*, **93**, 4908 (1971); G. Eisenman, S. M. Ciani, and G. Szabo, *J. Membrane Biol.*, **1**, 294 (1969); D. Bright and M. R. Truter, *J. Chem. Soc. B*, 1545 (1970).

(3) T. E. Hogen Esch and J. Smid, *J. Amer. Chem. Soc.*, **91**, 4580 (1969); K. H. Wong, G. Konizer, and J. Smid, *ibid.*, **92**, 666 (1970).

(4) U. Takaki, T. E. Hogen Esch, and J. Smid, *ibid.*, **93**, 6760 (1971).

(5) R. V. Slaters and M. Szwarc, *ibid.*, **89**, 6043 (1967); L. L. Chan, K. H. Wong, and J. Smid, *ibid.*, **92**, 1955 (1970).

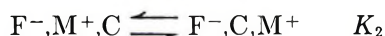
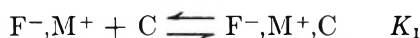
Fluorenylsodium and -potassium were prepared in tetrahydrofuran under high vacuum by mixing the dianion of 1,1,4,4-tetraphenylbutane with a slight excess of fluorene.⁶ For experiments carried out in other media, the THF was removed under vacuum and replaced by the required solvent, which was distilled from a carbanion solution to assure its purity. The purification of THF, MTHF, and THP has been described elsewhere.⁷

The crown ether-fluorenyl salt mixtures were prepared in an all-glass enclosed and evacuated apparatus by adding a slight excess (about 5–10%) of the solid crown compound *via* a break-seal to a carbanion solution of approximately 10^{-3} M. The solution could be concentrated stepwise to a maximum of about 2×10^{-2} M by evaporating the solvent into an adjacent compartment. Above this carbanion concentration the crown-salt complexes start to precipitate. Dilution down to about 10^{-4} M was accomplished by transferring part of the solution to the side compartment and distilling the solvent back by cooling. Optical cells of different path lengths were attached to the apparatus to record the absorption spectrum by means of a Cary 14 spectrophotometer after each concentration change.

The fractions of the tight and loose ion-pair complexes, F^-,M^+,C and F^-,C,M^+ , were calculated from the known molar absorptivities, ϵ_m , at the respective absorption maxima. The following ϵ_m values were used:⁴ 14,000 for $F^-,C5,Na^+$ (λ_m 373 nm) and $F^-,C6,-K^+$ (λ_m 373 nm); 12,000 for $F^-,Na^+,C5$ (λ_m 359 nm) and $F^-,K^+,C6$ (λ_m 364 nm). Details describing the determination of these molar absorptivities and the calculation of the ion pair fractions can be found elsewhere.^{4,8}

Results and Discussion

The binding of crown ethers to fluorenyl contact ion pairs in ethereal solvents was found to proceed in the following manner⁴



Experimentally one measures the ratio, R , of the concentration of all separated ion pairs to that of all contact ion pairs

$$R = \frac{[F^-,C,M^+] + [F^-,C,M^+,C]}{[F^-,M^+] + [F^-,M^+,C]}$$

and it can be shown⁴ that

$$R = \frac{K_2 + K_3[C]}{1 + 1/K_1[C]}$$

To simplify the investigation, systems were chosen

for which $K_1[C] \gg 1$ and $K_3[C] \ll K_2$. This means that all contact ion pairs are of the type F^-,M^+,C , and the fraction of separated 2:1 ion-pair complexes is negligibly small. These conditions are met for the systems $C5-F^-,Na^+$ and $C6-F^-,K^+$ in the concentration range of our measurements.⁴ To further assure the absence of 2:1 complexes, the ratio of crown ether to F^-,M^+ was kept between 1.0 and 1.1 (a slight excess is needed to avoid the presence of noncomplexed F^-,M^+ ion pairs). In essence, therefore, one measures the concentration dependence of the ratio $R = K_2 = [F^-,C,M^+]/[F^-,M^+,C]$. This ratio, according to the preceding complexation scheme, should be independent of carbanion or crown ether concentration.

The first set of data in Table I refers to the system $F^-,Na^+-C5-THP$, with C5 in considerable excess over F^-,Na^+ . (Even under these conditions there is no evidence for 2:1 complexes of C5 with F^-,Na^+ .) The ratio R appears to be constant as long as the total carbanion concentration is less than about 2×10^{-3} M. However, above this concentration R considerably increases, not only in THP, but also in THF and MTHF, as shown by the remaining set of experiments listed in Table I. The same behavior is observed with the F^-,K^+-C6 mixture in both THF and THP.

Table I: Dependence of the Ratio, R , of Crown-Separated to Crown-Complexed Contact Ion Pairs on the Total Concentration of Fluorenyl Ion Pairs at 25°

Solvent THP			Solvent THF ^a		
$[F^-,Na^+]_0^b$ $\times 10^3$ M	$[C5]^b \times$ 10^2 M	R	$[F^-,Na^+]_0^b$ $\times 10^3$ M	$[F^-,Na^+,C5]$ $\times 10^3$ M	R
0.233	3.60	0.595	2.07	0.696	1.79
1.27	3.58	0.588	2.87	0.911	1.94
4.01	3.56	0.579	4.67	1.40	2.12
5.61	3.54	0.573	5.29	1.54	2.22
13.5	3.45	0.599	8.83	2.39	2.45
75.0	2.85	0.769	16.0	3.80	2.94

Solvent THP			Solvent MTHF		
$[F^-,Na^+]_0^b$ $\times 10^3$ M	$[F^-,Na^+,C5]$ $\times 10^3$ M	R	$[F^-,Na^+]_0^b$ $\times 10^3$ M	$[F^-,Na^+,C5]$ $\times 10^3$ M	R
3.24	2.07	0.565	0.900	0.601	0.495
5.00	3.13	0.593	1.45	0.968	0.503
7.76	4.55	0.705	2.82	1.80	0.569
10.2	5.82	0.750	4.41	2.82	0.567
11.4	6.31	0.818	7.50	4.58	0.639
15.3	7.95	0.929	11.6	6.76	0.719
17.9	8.96	1.00	13.9	7.68	0.809
22.1	10.5	1.09	21.0	11.0	0.905

^a In this series of experiments the ratio $[C5]_0/[F^-,Na^+]_0 = 0.93$, and corrections were made for the presence of a small amount of uncomplexed F^-,Na^+ ion pairs. ^b $[F^-,Na^+]_0$ denotes the total concentration of fluorenyl salt; $[C5]$ refers to the C5 not bound to F^-,Na^+ .

(6) T. Ellingsen and J. Smid, *J. Phys. Chem.*, **73**, 2712 (1969).

(7) T. E. Hogen Esch and J. Smid, *J. Amer. Chem. Soc.*, **88**, 307 (1966).

(8) L. Ambroz, K. H. Wong, and J. Smid, *Anal. Chem.*, **44**, 872 (1972).

The increase in the fraction of crown-separated ion pairs is most probably caused by ion-pair aggregation. Aggregation of carbanion salts is very common in hydrocarbon media,⁹ but in ethereal solvents only lithium salts such as alkyllithium, vinylithium, and allyllithium are more or less extensively aggregated.¹⁰ In THF, benzylolithium¹⁰ and polystyryllithium^{9,11} are believed to be monomeric. However, the fluorenyl salts appear to be an exception, probably because of their planar structure. Kinetic and thermodynamic evidence suggests that fluorenyllithium is associated in THF and other ethereal solvents,¹² and recent colligative property measurements on 9-(2-hexyl)fluorenyllithium in THF show a finite equilibrium to exist between monomeric and dimeric ion pairs of this salt over a 0.002–0.04 M concentration range.¹³

In our system one may anticipate three kinds of dimeric ion pair aggregates, *viz.*, $(F^-, M^+, C)_2$, $(F^-, C-M^+)(F^-, M^+, C)$, and $(F^-, C, M^+)_2$, assuming that experimental conditions are such that only F^-, C, M^+ and F^-, M^+, C ion pairs are present. Instead of $R = K_2$, one now obtains the following expressions

for $(F^-, M^+, C)_2$

$$R = \frac{K_2}{1 + 2K_a[F^-, M^+, C]} \quad (1)$$

for $(F^-, M^+, C)(F^-, C, M^+)$

$$R = \frac{K_2 + K_a K_2 [F^-, M^+, C]}{1 + K_a K_2 [F^-, M^+, C]} \quad (2)$$

and for $(F^-, C, M^+)_2$

$$R = K_2 + 2K_2^2 K_a [F^-, M^+, C] \quad (3)$$

Aggregation of crown-complexed contact ion pairs (case 1) would lead to a decrease in the value of R at higher F^-, M^+, C concentrations, contrary to our experimental findings. Cross-association of the two kinds of ion pair (case 2) would result in a higher R value at higher carbanion concentration in solvents where $K_2 < 1$, but R would decrease for systems with $K_2 > 1$. In both cases the R value should approach unity at a very high F^-, M^+, C concentration. However, Table I shows that while in THP and MTHF the R value of the system $C5-F^-, Na^+$ ($K_2 < 1$) does increase with $[F^-, M^+, C]$, it also increases in THF, where $K_2 > 1$. Therefore, only the assumption that crown-separated ion pairs will form dimeric aggregates (case 3) appears to be consistent with our experimental observations, since in that case the ratio R increases at higher carbanion concentration irrespective of the value of K_2 . If this is indeed correct, then a plot of R vs. $[F^-, M^+, C]$ should yield a straight line. Such plots are depicted in Figures 1 and 2, and the predicted linearity appears to exist for all the investigated systems (assuming aggregates higher than dimers will result in equations that yield curved plots).

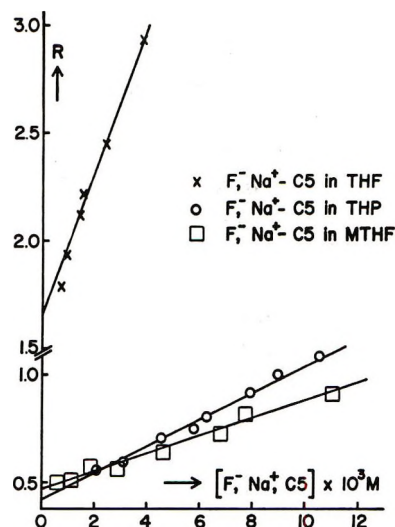


Figure 1. Plot of R (ratio of all separated to all contact ion pairs) vs. $[F^-, Na^+, C]$ in THF (\times), MTHF (\square), and THP (\circ) at 25°.

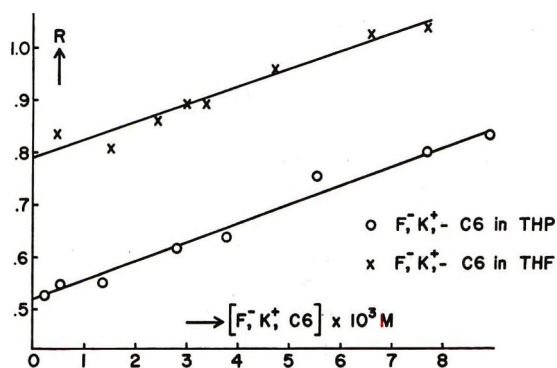


Figure 2. Plot of R vs. $[F^-, K^+, C]$ in THF (\times) and THP (\circ) at 25°.

Values for the constants K_2 and K_a , obtained from the slopes and intercepts of the respective lines, are collected in Table II. Generally, the data show the expected qualitative dependence on the dielectric constant D , the association being more prevalent in media of lower D . Undoubtedly, the detailed structure of the solvent molecules is also important, as the complexed ion pairs may still carry a few solvent molecules, especially the crown-separated ion pairs where the alkali ion is more exposed to the solvent.⁴ This in turn affects the aggregation and may explain the behavior in the THF-dioxane mixture, which resembles that of pure THF.

(9) S. Bywater and D. J. Worsfold, *Can. J. Chem.*, **40**, 1564 (1962); J. E. Roovers and S. Bywater, *Trans. Faraday Soc.*, **62**, 701 (1966); M. Morton and L. J. Fetters, *J. Polym. Sci., Part A*, **2**, 3311 (1964).

(10) P. West and R. Waack, *J. Amer. Chem. Soc.*, **89**, 4395 (1967); R. Waack and M. A. Doran, *ibid.*, **91**, 2456 (1969); P. West, R. Waack, and J. I. Purmort, *ibid.*, **92**, 840 (1970).

(11) D. N. Bhattacharyya, C. L. Lee, J. Smid, and M. Szwarc, *J. Phys. Chem.*, **69**, 612 (1965).

(12) T. E. Hogen Esch and J. Smid, *J. Amer. Chem. Soc.*, **89**, 2764 (1967); L. L. Chan and J. Smid, *ibid.*, **90**, 4654 (1968).

(13) M. M. Exner, R. Waack, and E. C. Steiner, Abstracts, 161st National Meeting of the American Chemical Society, Los Angeles, Calif., 1971, No. ORGN 184.

Table II: Aggregation Constants of Crown-Separated Fluorenyl Ion Pairs in Ethereal Solvents at 25°

Ion pair	Crown	Solvent	D^a	K_a, M^{-1}	K_2
F^-, Na^+	C5	THF	7.40	62.0	1.65
		MTHF	6.24	87.0	0.43
		THP	5.61	168	0.48
		THF-dioxane (1:1)	4.75	86	
F^-, K^+	C6	THF		26.6	0.79
		THP		66.0	0.52

^a The values for the dielectric constants were taken from the following references: D. Nicholls, C. Sutphen, and M. Szwarc, *J. Phys. Chem.*, **72**, 1021 (1968) (THP and MTHF); T. E. Hogen Esch and J. Smid, *J. Amer. Chem. Soc.*, **88**, 318 (1966) (THF); M. van Beylen, D. N. Bhattacharyya, J. Smid, and M. Szwarc, *J. Phys. Chem.*, **70**, 157 (1966) (THF-dioxane).

The conclusion that aggregation apparently occurs preferentially between the crown-separated ion pairs is not unexpected, as the enlarged ion-pair dipoles will more strongly interact with one another. Of equal importance is the distance of approach between the two ion pairs of the aggregate. In this respect, the crown-complexed contact ion pair seems to have a less favorable structure. The alkali ion is believed to be located above the plane of the fluorenyl ring,¹⁴ and the aggregates of the two isomeric ion pairs can probably best be represented by sandwich-type structures² such as those depicted schematically in Figure 3 (other structures are also conceivable). The alkali ion in the separated ion pair occupies the center of the nearly planar polyether ring, and a second fluorenyl carbanion can approach the cation rather easily, at the possible cost of removing a few solvent molecules still attached to the alkali ion. On the other hand, a close association between a fluorenyl anion and a crown-complexed contact ion pair is hindered as the alkali ion is sandwiched in between the crown ether and the carbanion with which it is associated.

The stronger interaction that apparently exists between crown-separated ion pairs appears to be reflected

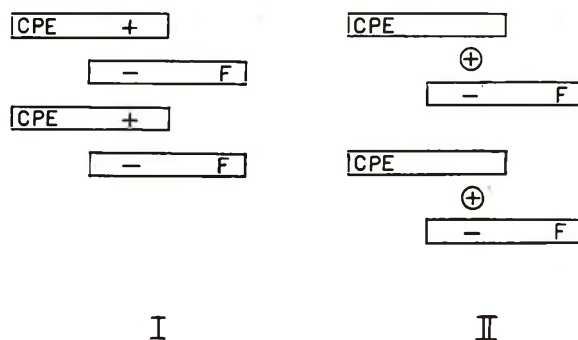


Figure 3. Possible structures of the ion-pair aggregates (F^-, C, M^+)₂ (I) and (F^-, M^+, C)₂ (II).

in the solubility behavior of the crown complexes. On several occasions we observed that addition of crown ethers to fluorenyl salts in ethereal solvents lowers the solubility of the salt when a crown-separated ion pair is formed. This is particularly striking for the complex of fluorenyllithium with dibenzo-14-crown-4, which is a separated ion pair in THF and THP with a solubility of less than $10^{-4} M$. On the other hand, the solubility of many salts in hydrocarbon solvents is known to increase on addition of crown ethers.² The decrease of K_2 (see Table II) with decreasing solvent polarity indicates that crown-complexed contact ion pairs are favored in less polar solvents.⁴ For example, the K_2 for the system C5- F^-, Na^+ in diethyl ether was found to be very small, with no evidence of the existence of separated ion pairs, all the crown ether being bound in the form of F^-, M^+, C species. While a lower dielectric constant generally favors aggregation, the formation of crown-complexed contact ion pairs hinders the ion-pair aggregation and promotes the solubility of the salt.

Acknowledgment. The support of this research by the National Science Foundation (GP 26350) and by the Petroleum Research Fund, administered by the American Chemical Society, is gratefully acknowledged.

(14) J. A. Dixon, P. A. Gwinner, and D. C. Lini, *J. Amer. Chem. Soc.*, **87**, 1379 (1965).

Initial Reaction of Nitrogen with Zirconium at 1440°

by R. A. Sallach

*Physical and Mechanical Metallurgy, Division 5531, Sandia Laboratories, Albuquerque, New Mexico 87115
(Received June 17, 1971)*

Publication costs assisted by the U. S. Atomic Energy Commission

The reaction of nitrogen with zirconium at 1440° and pressures between 2 and 10 mTorr was followed using a microbalance and a radiant-heat furnace. At constant pressure there is an initial linear reaction whose duration is inversely proportional to the square of the pressure and which is followed by a transition to a parabolic regime. The linear portion corresponds to the reaction of nitrogen with a β -Zr surface and continues while the α -Zr phase is formed, ending when the α -Zr surface saturates and a thin ZrN layer forms. In the linear regime the sticking coefficient is independent of gas pressure and has the same value for both the β -Zr and α -Zr surfaces—between 0.05 and 0.08.

Introduction

In many high-temperature reactions between metals and gases, a coherent product film forms on the surface of the metal and further reaction is limited by some diffusion process occurring through the product film. For later times, the reaction is well described by the so-called parabolic rate law; that is, the reaction proceeds at a rate inversely proportional to the square root of time. However, this law is physically impossible at $t = 0$, since there the rate becomes infinite. Also, in the derivation of the parabolic law, the assumption is made that all interfacial concentrations are constant and at their "equilibrium" values. This assumption cannot be justified at very early times. Clearly then, such reactions must have an initial regime (although its duration may be very short for the usual reaction conditions) where the reaction is governed by other processes.

There was interest in determining the characteristics of this initial regime and in observing the transition to the parabolic rate law. Because this regime is expected to last only until a critical, probably very thin product film had formed, experiments seemingly would have to be carried out at very low pressures using very sensitive techniques, hence precluding direct gravimetric measurements. These criteria may be relaxed when the metal has a large capacity for dissolving the gas interstitially and in addition the interstitial atom has a diffusion coefficient large enough that most of the incident gas passes into the interior and the surface concentration changes relatively slowly.

The nitridation of zirconium was considered to be a suitable reaction for study in that there is a large solubility of nitrogen in zirconium metal.¹ The reaction has the additional advantage that only one nitride phase is produced. Previous investigations²⁻⁴ have shown that the nitridation reaction follows parabolic kinetics at temperatures below 1000°, *i.e.*, a low diffusion coefficient for N in Zr. The reaction has also

been studied at higher temperatures^{5,6} but only at 1 atm pressure. In this work the pressure was reduced to the 10^{-3} – 10^{-2} Torr range and exploratory experiments were carried out at progressively higher temperatures until convenient experimental conditions were obtained at 1440°.

Experimental Section

The experimental apparatus pairs a Research Inc. dual-elliptical radiant-heat furnace with a Cahn Electrobalance. With this combination, samples up to a gram in mass can be brought to 1000 to 1600° in about 40 sec, while mass changes of 10 μ g can be detected. Other components include a capacitance manometer, used for pressure measurement, and an automatic pressure controller. Regulation of gas pressure was $\pm 10^{-4}$ Torr or $\pm 3\%$, whichever is greater. Temperatures were measured with a Pt–Pt–10% Rh thermocouple mounted immediately below the Zr sample. The thermocouple was placed in an alumina holder whose diameter was comparable to the sample and whose exterior was fitted with a thin Pt sheath in order to better match the emissivity of the sample. The thermocouple voltage was measured with a digital voltmeter; temperature could be maintained constant to $\pm 2^\circ$, but overall accuracy is probably no better than $\pm 25^\circ$ when sample shape and emissivity are considered. A continuous record of the balance signal was obtained with a strip-chart recorder.

In a typical experiment, the apparatus was evacuated to $\leq 5 \times 10^{-5}$ Torr and then back-filled to the

(1) M. Hansen, "Constitution of Binary Alloys," 2nd ed, McGraw-Hill, New York, N. Y., 1958, p 995.

(2) E. A. Gilbransen and K. F. Andrew, *J. Metals*, **185**, 515 (1949).

(3) A. Dravnieks, *J. Amer. Chem. Soc.*, **72**, 862 (1950).

(4) C. J. Rosa and W. W. Smeltzer, *Electrochem. Technol.*, **4** (3-4), 149 (1966).

(5) M. W. Mallett, E. M. Baroody, H. R. Belson, and C. A. Papp, *J. Electrochem. Soc.*, **100**, 103 (1953).

(6) M. W. Mallett, J. Belle, and B. B. Oeland, *ibid.*, **101**, 1 (1954).

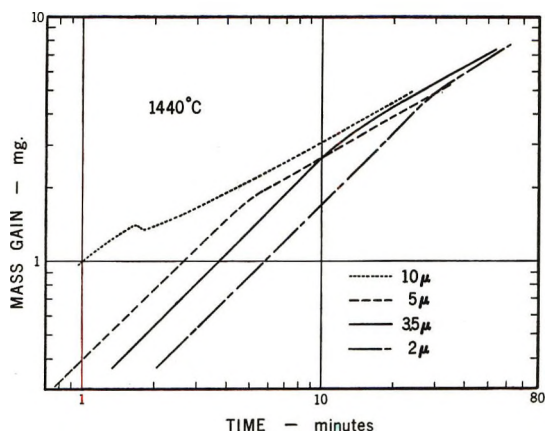


Figure 1. Experimental curves for the reaction of N_2 with Zr. Pressure is expressed in microns (μ) or milli Torr.

desired pressure before turning on the furnace. About 40 sec elapsed before the temperature stabilized at 1440° and the pressure fluctuations disappeared. Valid recorder traces were obtained after this time.

Samples were cut from reactor grade (Reactive Metals, Inc., Niles, Ohio) zirconium sheets and milled into rectangular parallelepipeds with dimensions $0.060 \times 0.130 \times 1.125$ in. A small hole was drilled at one end through which a small section of alumina tube was inserted to prevent contact of the zirconium with the platinum suspension wire. The nitrogen gas was of high purity; >99.99% is claimed by the supplier (Cryogenic Rare Gas Laboratories, Inc., Newark, N. J.).

Results and Discussion

The data from four experiments at 1440° are shown in Figure 1. The pressures (2, 3.5, 5, and 10 μ) are those for a location about 22 cm above the samples. The effective pressures at the metal surface are presumed to be close to these values, but this is difficult to verify as large temperature gradients in the gas do exist near the sample surface (the temperature of the surrounding quartz tube, 1 cm away, is only $\sim 600^\circ$), and the mean-free path of the gas is of the same magnitude as the dimensions of the samples.

All experiments showed similar qualitative features; that is, there was an initial constant rate regime followed at some later time by a transition to parabolic kinetics. Pertinent features are listed in Table I. The constancy of the quantities $P\tau^{1/2}$ and F/P shows, respectively, that the duration of the initial regime is inversely proportional to the square of the pressure and that the rate of reaction is directly proportional to pressure.

These relationships are consistent with the view that the initial regime corresponds to reaction of gas with an unsaturated metal surface and that the transition to parabolic kinetics occurs when the surface becomes saturated with respect to that gas.

Table I: Characteristics of the Linear N_2 -Zr Reaction

Run No.	1	2	3	4
Gas pressure, P , μ	2	3.5	5	10
Rate of weight gain in linear portion, F , $\mu\text{g}/(\text{cm}^2 \text{ sec})$	1.20	1.84	2.57	a
Duration of linear portion, τ , min	24	10	3.5	$\sim 1^a$
$P\tau^{1/2}$	10	11	9	$\sim 10^a$
F/P	0.6	0.5	0.5	a

^a Linear portion too short to obtain quantitative data.

The Zr-N phase diagram¹ indicates that at later times three phases should be present: (1) an interior β -phase solid solution overlaid with (2) an α -phase solid solution and (3) a surface film of ZrN. It is proposed that these phases form sequentially as the reaction proceeds. Since a previous study of zirconium nitridation by Mallet, *et al.*,⁵ had indicated that the thickness of the outer layers (ZrN + α -Zr) was small compared to the diffusive penetration of nitrogen into the β -phase alloy, the transition to parabolic kinetics was first interpreted to occur when the β -phase surface was saturated with nitrogen. On this physical basis, a one-dimensional expression for the consumption of gas by a single-phase metal as a function of time was derived.⁷ Thus

$$M(t) = Ft, t \leq \tau \quad (1A)$$

$$M(t) = F\tau + 4F\sqrt{\tau(t-\tau)} \left[\frac{1}{\pi} - \phi(r) \right], t \geq \tau \quad (1B)$$

where F is the linear reaction rate, τ is the time at which the surface saturates with gas and the transition to parabolic kinetics begins, and

$$\phi(r) = \int_0^\infty \text{ierfc}(ry) \text{erfc}(y) dy$$

$$r = \sqrt{\frac{t-\tau}{\tau}}$$

(During review Prager⁸ noted that the problem treated here also arose in chronopotentiometry. From that literature an expression for the surface flux at $t > \tau$ was abstracted⁹ and was integrated to yield the alternative equations

$$M(t) = Ft, t \leq \tau$$

$$M(t) = F \left\{ t \left(\frac{1}{2} + \frac{1}{\pi} \arcsin \left(\frac{2\tau - t}{t} \right) \right) + \frac{2}{\pi} \sqrt{(t-\tau)} \right\}, t > \tau$$

(7) R. A. Sallach, SC-DR-71093, Sandia Corp., Albuquerque, N. M.

(8) S. Prager, private communication.

(9) T. Berzins and P. Delahay, *J. Amer. Chem. Soc.*, **75**, 4205 (1953).

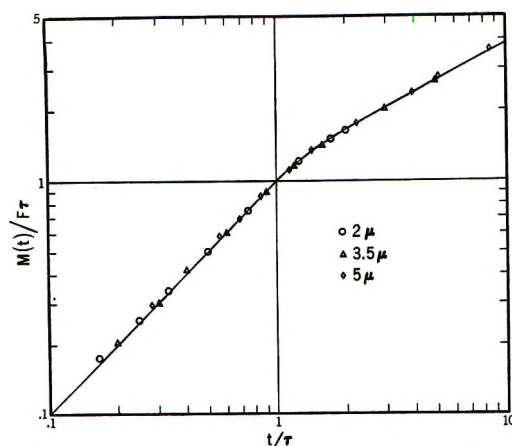


Figure 2. Representative points from the experimental curves are plotted for comparison with the theoretical curve (solid line) using normalized coordinates.

which are numerically equivalent to eq 1A and 1B.)

The experimental data can be fit to these expressions remarkably well, as shown in Figure 2, where representative points are plotted. However, later metallographic examination of the specimens showed that while the ZrN layer indeed is thin ($\sim 1\text{--}2\ \mu$), the thickness of the α -phase solid solution is appreciable, up to 15% of sample thickness. This confirms the findings of Salibekov, *et al.*,¹⁰ whose report was discovered after these experiments were completed.

Several additional specimens were then nitrided at $2\text{-}\mu$ gas pressure for various times, from which it was determined that saturation of the β -phase surface (appearance of α -phase) occurs at about $0.5\ \tau$ and that the transition to parabolic kinetics really starts when the α -phase surface saturates (first appearance of ZrN).

A reexamination of the data shows *no* inflection in rate when the β phase saturates. This result is unexpected and implies that either the surface structures of the α and β phases do not differ significantly or the adsorption of gas at the metal surface depends only weakly on surface structure. The former seems more plausible.

The fine fit of the data to an expression derived on the basis of an erroneous physical picture was perplexing until it was realized that the controlling features are the conditions at the metal-gas interface. That is, it really does not matter what occurs in the interior so long as the boundary conditions at the interface are met. Any reaction which has a constant flux at the surface for $t < \tau$ and constant surface concentration afterward will follow the derived curve. However, any calculations based on τ and F must of course be consistent with the true situation.

One can obtain estimates of the diffusion coefficient of nitrogen in the β phase from these experimental data. During the linear reaction regime the concentration of nitrogen in the β phase will be¹¹

$$C^\beta(x, t) = 2F\sqrt{\frac{t}{D_\beta}} \operatorname{ierfc}\left(\frac{x}{2\sqrt{D_\beta t}}\right)$$

Evaluating this expression at $x = 0$, $t = \tau_\beta$ gives

$$D_\beta = \frac{\tau_\beta (2F)^2}{\pi (C_s^\beta)^2} \quad (2)$$

where C_s^β is the saturation solubility of N in the β phase at 1440° and τ_β is the time at which the β -phase surface saturates. Precise values for τ_β are not known, but it is about $0.5\ \tau$, as stated earlier. Mallett, *et al.*,⁵ have reported on the solubility limits for the β phase, from which one calculates $C_s^\beta = 0.028\ \text{g of N/cm}^3$ at 1440° . In combination with the present data for F and τ_β , values for D_β between 1 and $2 \times 10^{-6}\ \text{cm}^2/\text{sec}$ are calculated. This compares favorably with the value 1.5×10^{-6} reported by Mallett, *et al.*,⁵ based on hardness measurements.

The proportionality between the measured gas pressure and the measured rate of weight gain in the initial regime implies that a constant fraction of the gas incident on the "clean" metal surface enters into reaction. This fraction or sticking coefficient, α , is calculated with

$$\alpha = F / [(5.833 \times 10^{-2}) P (MT^{-1})^{1/2}] \quad (3)$$

where F is the measured rate ($\text{g}/(\text{cm}^2\ \text{sec})$), P is the pressure (Torr), M is the molecular weight of the gas, and T is the absolute temperature ($^\circ\text{K}$). The value for α will depend, of course, on one's choice for the effective temperature and pressure of the gas near the metal surface. If one assumes that the measured pressures are representative and the gas temperature is that of the metal surface, then $\alpha \sim 0.07\text{--}0.08$, whereas if the gas temperature is that of the surrounding quartz wall, then $\alpha \sim 0.05\text{--}0.06$. In either case only a relatively small amount of incident gas reacts.

Summary

The initial stages of the nitridation of zirconium at 1440° have been studied. There is first a linear reaction which corresponds to the reaction of the gas with a bare metal surface. This linear reaction continues through the saturation of the β -phase surface and the nucleation of the α phase, ceasing when the α -phase surface saturates and the formation of ZrN begins. At this time the reaction kinetics begin a transition to the typical parabolic kinetics observed by other investigators at lower temperatures.

The linear rate of reaction is proportional to the gas pressure, while the duration of the linear regime is inversely proportional to the square of pressure.

The sticking coefficient lies between 0.05 and 0.08, and it apparently is independent of surface structure of the metal.

(10) S. Ye. Salibekov, Yu V. Levinskiy, V. C. Khvostikov, and M. Kh. Levinskaya, *Fiz. Metal. Metalloved.*, **18**, 858 (1964).

(11) H. Carslaw and J. Jaeger, "Conduction of Heat in Solids," Oxford University Press, London, 1947.

A Gas Chromatographic Reactor Study of the Kinetics of Dicyclopentadiene Dissociation¹

by Stanley H. Langer* and James E. Patton

Department of Chemical Engineering, University of Wisconsin, Madison, Wisconsin 53706 (Received November 11, 1971)

Publication costs assisted by the Petroleum Research Fund

The application of the gas chromatographic column as a chemical reactor and source of kinetic data was studied using the unimolecular dissociation of dicyclopentadiene as a model reaction. Rate constants and kinetic parameters were measured in a number of solvents (stationary phases) in the range of 180–200°. Solvents included hexatriacontane, a silicone, poly(phenyl ether), a polyester, and trixylyl phosphate. Solvent effects were not great and kinetic data from the gas chromatographic reactor (gcr) were consistent with earlier studies in the gas and liquid phase. Differences could be interpreted. Mobile or gas-phase rate constants could be determined with somewhat less accuracy than liquid-phase rate constants. The gcr must be used with care but is shown to have the advantage of permitting detection of impurities and side reactions as well as being operable and giving satisfactory results in their presence. Precautions and conditions for operating the gcr effectively are indicated. The gcr is shown to be well suited for the study of reactions involving volatile products and reactants. Concurrent determination of their activity coefficients and excess thermodynamic functions for mixing in the solvent is also possible. The gcr, therefore, should be especially valuable for aiding in the conciliation of kinetic and thermodynamic factors.

Full recognition of the value of the gas chromatographic column as a chemical reactor for the study of homogeneous reactions has not been accorded to date. In preceding publications,^{2–4} several earlier important applications to pseudo-first-order reactions were reviewed. The use of the chromatographic reactor to study a first-order reaction involving a volatile product as well as volatile reactant has also been demonstrated.^{3a} Such reactions often are difficult to study with conventional batch-type reactors. Herein, we report the results of a more extensive investigation of the dicyclopentadiene dissociation reaction in several potentially useful high-temperature solvents (stationary phases) in order to illustrate features and advantages as well as conditions for favorable operation of the gas chromatographic reactor. Simultaneously derived solution thermodynamic data for reactants and products calculated from chromatographic characteristics are also presented. A series of earlier investigations of the dicyclopentadiene dissociation as well as related literature data on physical properties make possible a number of useful thermodynamic observations^{5,6} for comparison with kinetic data for different solvents.

The reactor is the chromatographic column itself. Reactant introduced as a pulse is continuously converted to product, sometimes by reaction in both gas and liquid phases, as it travels through the column. Separation of product is initiated immediately and continues during the entire passage of reactant through the column. Product dilution and concerted reaction and separation processes minimize reverse reaction as well as side reactions and autocatalysis.

The gas chromatographic reactor (gcr) benefits from other features inherent in chromatography—small sample size, minimal heat effects, and simple control of operating variables. Separation from any potential inhibiting or complicating impurity also takes place. Unfortunately, the need for careful temperature control makes most standard commercial gas chromatographic equipment unsuitable for kinetic studies.

We chose the dicyclopentadiene dissociation reaction for study in the gas chromatographic reactor because of its first-order homogeneous nature and the relative simplicity of the reaction, as well as the availability of earlier investigations of the reaction for comparison.

Theory

The most convenient approach to the gas chromatographic reactor utilizes a continuous model of a homogeneous column.^{2,7,8} From a material balance on a

(1) (a) Presented in part at 158th National Meeting of the American Chemical Society, New York, N. Y., Sept 1969; (b) taken in part from the Ph.D. Thesis of J. E. P., Department of Chemical Engineering, University of Wisconsin, 1970.

(2) S. H. Langer, J. E. Patton, and J. Y. Yurchak, *Ind. Eng. Chem.*, **61** (4), 10 (1969).

(3) (a) G. L. Pratt and S. H. Langer, *J. Phys. Chem.*, **73**, 2095 (1969); (b) see also E. Gil-Av and Y. Herzberg-Minzly, *J. Chromatogr.*, **13**, 1 (1964).

(4) J. Y. Yurchak, M.S. Thesis, Chemical Engineering Department, University of Wisconsin, Madison, Wis., 1966.

(5) S. H. Langer and J. H. Purnell, *J. Phys. Chem.*, **67**, 263 (1963).

(6) S. H. Langer, B. M. Johnson, and J. R. Conder, *ibid.*, **72**, 4020 (1968).

(7) (a) E. Glueckauf, *Trans. Faraday Soc.*, **51**, 34 (1955); (b) L. Lapidus and N. Amundson, *J. Phys. Chem.*, **56**, 984 (1952).

(8) J. H. Purnell, "Gas Chromatography," Wiley, New York, N. Y., 1962, pp 94–99.

reactant pulse in a gas chromatographic column, a differential equation is obtained, the solution to which relates reactant concentration to position in column, x , and time, t . Relationships may then be derived which will allow the determination of first-order rate constants.

Components of a mixture injected into the column are transported by the usually inert carrier gas. Each species is partitioned between the mobile gas phase and the liquid phase (which may be coated on a porous solid support). If mass transfer is relatively rapid and the distribution isotherms are linear, the concentrations of each reactant, C , in the gas and liquid phases are related by the partition coefficient K , a function of temperature only^{2,5} here.

$$K = C_l/C_g \quad (1)$$

Heats of solution and reaction are negligible because of the small sample size, so that the column temperature and partition coefficients are constant. If the column is operated under conditions such that diffusion is not a major factor^{9,10} (the residence time distribution is small), a material balance on the reactant in a differential section of the chromatographic reactor undergoing a first-order or pseudo-first-order reaction in both phases yields

$$f_l \left(\frac{\partial C_l}{\partial t} \right) + f_g \left(\frac{\partial C_g}{\partial t} \right) = -f_g \left(\frac{\partial [u(x)C_g]}{\partial x} \right) - f_g k_g C_g - f_l k_l C_l \quad (2)$$

where f_l and f_g are the volume fractions of liquid and gas phase, respectively, per unit volume of column, $u(x)$ is the linear velocity of gas in the column at distance x from the end of the column, and k_l and k_g are first-order rate constants in the indicated phases.

Boundary and initial conditions are

$$C_g(0, t) = \phi(t); \quad C_g(x, 0) = 0 \quad (3)$$

$C_g(x, t)$ is the concentration of reactant in the carrier gas (mobile phase) at distance x and time t in the column, $C_l(x, t)$ is the concentration of reactant in the stationary phase, and $\phi(t)$ is an arbitrary input function. Gas-phase velocity is dependent upon position because the finite pressure drop across the column causes the compressible gas to travel faster as it progresses through the column.¹¹

Combining eq 1 and 2

$$(1 + f_l K/f_g) \frac{\partial C_g}{\partial t} + \frac{\partial [u(x)C_g]}{\partial x} + \left(k_g + \frac{k_l f_l K}{f_g} \right) C_g = 0 \quad (4)$$

This partial differential equation can be solved^{12,13} with the aid of Laplace transforms for $u(x)C_g(x, t)$ with the given boundary and initial conditions.

$$u(x)C_g(x, t) = u(0)\phi[t - (1 + f_l K/f_g)\tau(x)] \times \exp[-(k_g + k_l f_l K/f_g)\tau(x)] \quad (5)$$

where

$$\tau(x) = \int_0^x \frac{dx'}{u(x')}$$

Physically $f_l K/f_g$ is equivalent to the ratio of liquid-phase to gas-phase residence time or k' , the solute mass distribution coefficient.¹⁴ $\tau(x)$ is the time required for the gas to travel from the column inlet to a point x . For a column of length L , $\tau(L)$ is the residence time in the gas phase, t_g , and $(1 + f_l K/f_g)\tau(L)$ is $t_g + t_l$, the total time in gas plus liquid phases.

The total reactant entering a column of cross section A is

$$W_{in} = \int_0^\infty AMf_g u(0)\phi(t)dt = AMf_g u(0) \int_0^\infty \phi(t)dt \quad (6)$$

where M is the molecular weight of the reactant.

The amount leaving the column is

$$W_{out} = \int_0^\infty AMf_g u(L)C_g(L, t)dt = AMf_g u(0) \exp(-k_g t_g - k_l t_l) \int_0^\infty \phi(t - t_g - t_l)dt \quad (7)$$

If $\phi(t)$ is bounded and equal to 0 for $t < 0$ (no reactant is present in the column before injection), then $\int_0^\infty \phi(t)dt$ must equal $\int_0^\infty \phi(t - t_l - t_g)dt$ and eq 6 and 7 can be combined to eliminate the integral.

$$W_{out}/W_{in} = \exp(-k_g t_g - k_l t_l) \quad (8)$$

Equation 8 generally does not depend upon the shape of the input function ($\phi(t)$). Furthermore, $\tau(x)$ need be evaluated only at the outlet of the column, where it is simply t_g .

The recorded response of a detector at the outlet of a column in which material reacts as it passes through the column is called a reactor chromatogram. Since the

(9) This is a reasonable proposition. For discussion, see W. A. Blanton, C. H. Byers, and R. P. Merrill, *Ind. Eng. Chem., Fundam.*, **7**, 611 (1968); see also M. Suzuki and J. M. Smith, *Chem. Eng. Sci.*, **26**, 221 (1971).

(10) Axial dispersion in gas-phase tubular reactors is discussed in (a) H. Kwart, S. F. Sarnier, and J. H. Olson, *J. Phys. Chem.*, **73**, 4056 (1969); (b) D. G. Retzlaff, B. M. Coul, and J. Coul, *ibid.*, **74**, 2455 (1970).

(11) A. T. James and A. J. P. Martin, *Biochem. J.*, **50**, 679 (1952).

(12) F. B. Hildebrand, "Advanced Calculus for Applications," Prentice-Hall, Englewood Cliffs, N. J., 1962, pp 55-60.

(13) G. A. Gaziev, V. Yu Filinovskii, and M. I. Yanovskii, *Kinet. Katal.*, **4**, 688 (1963).

(14) (a) A. Goldup, G. R. Luckhurst, and W. T. Swanton, *Nature (London)*, **193**, 333 (1962); (b) D. H. Desty, A. Goldup, G. R. Luckhurst, and W. T. Swanton, "Gas Chromatography, 1962," M. Van Swaay, Ed., Butterworths, London, 1962, p 67.

area under a peak is proportional to the total weight of the corresponding compound which passes the detector, eq 8 can be rewritten

$$\ln (S_R^0/S_R) = k_1 t_1 + k_g t_g \quad (9)$$

where S_R is the reactant peak area from a reactor chromatogram and S_R^0 would be the reactant area from a hypothetical detector located at the inlet. Inclusion of an inert compound with the reactant produces a constant peak of area S_I . Adding $\ln (S_I)$ to both sides of eq 9 and rearranging

$$\ln (S_I/S_R) = k_{app} t_1 + \ln (S_I/S_R^0) \quad (10)$$

where the apparent rate constant, k_{app} , would be

$$k_{app} = k_1 + (t_g/t_1)k_g \quad (11)$$

The initial area ratio S_I/S_R^0 is the same if all samples are taken from the same reaction mixture. S_R , S_I , and t_1 are measured readily. For reactions which take place only in the liquid phase, $k_g t_g$ may be eliminated. In a packed column where t_g is very small relative to t_1 , the effect of the gas rate constant could be ignored. As we will show, a reasonable estimate of k_g is accessible from a gas chromatographic study when the extent of gas-phase reaction is significant. Fortunately, the reaction under consideration has recently been carefully investigated in the gas phase by two different groups^{10a,15} so that we have available unusually accurate data. Most of our work is based on the value of $k_g = 10^{13.01} \exp(-33,970/RT) \text{ sec}^{-1}$ by Herndon, *et al.*,¹⁵ which was initially accessible to us.

Experimental Section

Our apparatus, based on an earlier model,^{5,8} was designed to give constant temperature control over a wide range of operating conditions. The 9×36 -in. cylindrical air bath was located inside a $14 \times 14 \times 36$ -in. aluminum box containing vermiculite-insulated walls. A 7-in. diameter copper cylinder inside the oven carried 12 33-in. Marinite strips on which nichrome heating wire was noninductively wound. A 6.7-in. centrifugal Torrington fan powered by a $1/3$ -horsepower, 3450-rpm motor pulled air down the inner cylinder and pushed it up the annular section between the inner cylinder and the oven wall. The temperature was controlled by means of an external resistor switched in and out of the nichrome heating wire circuit which operated at constant voltage. A nickel resistance thermometer sensed the oven temperature for the controller so that the temperature was controlled to $\pm 0.01^\circ$ during the course of an experiment. The oven temperature, measured with a precision deep-immersion thermometer calibrated against an NBS thermometer, was corrected for the small ($<0.1^\circ$) spatial temperature variation along the column.

A Brooks 8943 ELF precision needle valve maintained the helium carrier gas flow within $\pm 0.5\%$. The

detector was a Gow Mac Model 460 thermal conductivity cell. Carrier gas passed into the oven and through the reference side of the cell before passing through the Carle 3510 on-column injector. This eliminated the need for a second (reference) column and preheated the carrier gas.

Columns. The columns were made with well-cleaned 304 stainless-steel tubing of 0.194-in. internal diameter. Column length varied from 6 to 12 ft depending upon the retention of reactant in the liquid phase and percentage liquid on the support. The packing material consisted of 15–25% liquid phase uniformly coated on 60–80 mesh Gas Chrom Q (Applied Science Labs), chosen for its inert properties. Approximately 2.5 g of packing per column foot was used.

Sample Injection. Samples (0.4 μl) taken from a 2:3 dicyclopentadiene (3a,4,7,7a-tetrahydro-4,7-methanoindene, Matheson Coleman and Bell) and *m*-bromochlorobenzene (Eastman Chemicals) mixture were injected with a 10- μl syringe. Since the reaction is endothermic by 17 kcal¹⁶ and the heat of vaporization is approximately 10 kcal,¹⁶ complete conversion to product would require only 0.02 cal and reactant vaporization only 0.01 cal. Air taken into the syringe before the injection sample served as a marker for gas phase residence time.

Procedure. Eight to twelve runs were made in the determination of each rate constant. For the most part, runs were made in duplicate at regularly spaced reactant residence times. The longest residence time corresponded to 30–70% conversion.

Columns were generally operated at a flow rate in the general region of maximum efficiency so that the earlier approximation of negligible diffusional spreading is truly applicable.

Analysis. Typical reactor chromatograms from this work are shown in Figure 1. Reactant residence time in the liquid phase, t_1 , is measured from the air peak, A, to the maximum in R. The gas-phase residence time for all components, t_g , is measured from the time of injection to A, the retention time of air. The inert peak area is S_I . Reactant peak area, S_R , must be corrected for product interference in the eluted peak, approximated as area under the dotted line in Figure 1 or between AB' and the base line in Figure 2. Figure 2 depicts a typical eluted reacting peak. A reasonable estimate of the reactant area in the product peak is found by taking the area between AF and the base line in Figure 2. AF bisects the angle between the extrapolation of the product curve (AE) and a horizontal line to the point where the extrapolation leaves the

(15) W. C. Herndon, C. R. Grayson, and J. M. Manion, *J. Org. Chem.*, **32**, 526 (1967); this study also contains a good literature review on the dicyclopentadiene decomposition.

(16) (a) H. S. Hull, A. F. Reid, and A. G. Turnbull, *Aust. J. Chem.*, **18**, 249 (1965); (b) A. G. Turnbull and H. S. Hull, *ibid.*, **21**, 1789 (1968).

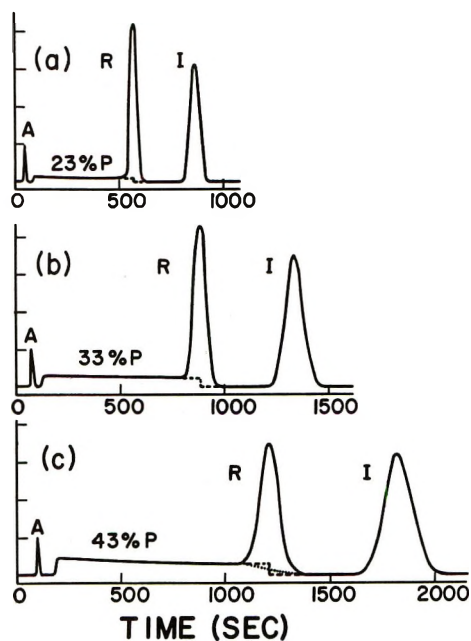


Figure 1. Typical reactor chromatograms for dicyclopentadiene dissociation in a 8.5-ft, 0.25-in. column containing hexatriacontane (20%) on Gas Chrom Q, 60–80 mesh; A is air peak, P is product, R is reactant, I is inert reference: (a) $F = 48.1 \text{ cm}^3/\text{min}$, (b) $F = 30.8 \text{ cm}^3/\text{min}$, and (c) $F = 22.1 \text{ cm}^3/\text{min}$ at column temperature of 180.1° . (Area under dashed line in (c) approximates area under dotted line, the true interference.)

product curve (parallel to the base line). That is $AFD \approx DCB'$. The uncertainty of the reactant area in the product peak is represented by the shaded line ADB' . A rather complete argument for this approximation has been presented elsewhere.⁴ From a simplified point of view, when one-fourth of the reactant peak is eluted, the product will be appearing at the column outlet at a rate about the same or slightly less than three-fourths of the production rate observed at A, and when one-half of the peak is eluted this rate is the same or slightly less than one-half the rate at A. The dashed lines of Figure 1 in the reactor chromatograms and the chromatogram base line enclose the estimated areas of product peak in the reactant peak. With more specific detectors, of course, this might be determined exactly.

Reactant areas were found either with a planimeter measurement on recorder traces or from a recorder equipped with a Disc Integrator, appropriate corrections being made as discussed above.

Results

Plots of \ln (inert area/reactant area) against dicyclopentadiene residence time in the liquid phase are shown in Figure 3 for reaction in 20% hexatriacontane liquid on Gas Chrom Q (60–80 mesh). These curves were arbitrarily adjusted to pass through the origin using eq 10. The data give linear first-order plots for the three temperatures shown, substantiating the fact

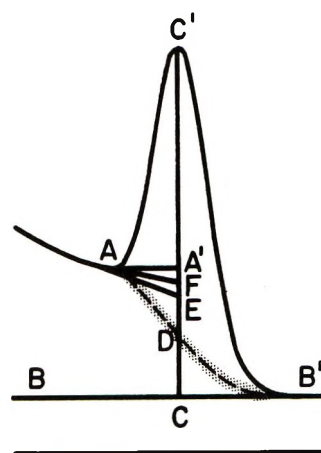


Figure 2. Illustration of correction of reactant peak for product interference. Area under ADB' approximated as area between AF and base line (see text). With 81% conversion here, correction is greater than under normal conditions.

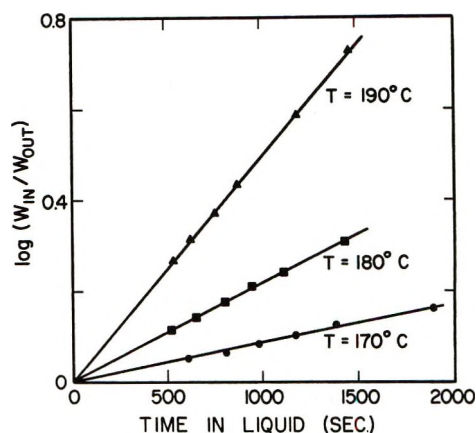


Figure 3. First-order rate plots of \ln (inert area/reactant area) at various temperatures (see eq 10) for dicyclopentadiene dissociation in hexatriacontane. Indicated points are averages of duplicate runs. Plots have been arbitrarily adjusted to pass through origin.

that the first-order reaction is essentially irreversible at our conditions up to conversions of 70%. Similar plots were obtained for the same liquid phase at 15 and 25% liquid column loading. The apparent rate constants obtained from eq 10 were then converted to liquid-phase rate constants using eq 11 and the k_g expression of Herndon, *et al.*¹⁵ Rate constant values are tabulated in Table I. The t_g values were obtained from the residence time of air peaks after injection. Increasing the liquid phase from 15 to 25% by weight of total column packing was equivalent to decreasing the ratio of surface area of solid support to weight of liquid phase from 5.7 to 3.0 m^2/g of liquid phase.¹⁷ The rate constants are independent of surface area in this range, which would be evidence against any surface-

(17) D. M. Ottenstein, *J. Gas Chromatogr.*, **1**, 11 (1963).

Table I: Liquid-Phase Rate Constants for Dicyclopentadiene Dissociation in *n*-Hexatriacontane on Gas Chrom Q

% C ₂₆ H ₅₄ (in packing)	$k_1 \times 10^4, \text{sec}^{-1}$			
	170.0°	180.1°	185.2°	189.8°
15		4.59 ± 0.12	6.99 ± 0.10	10.66 ± 0.21
20	1.87 ± 0.08	4.64 ± 0.07	7.10 ± 0.06	10.40 ± 0.09
25	1.98 ± 0.07	4.61 ± 0.06	7.22 ± 0.14	10.51 ± 0.08
Av	1.92	4.61	7.10	10.52

$$k_{\text{hexatriacontane}} = 10^{13.51 \pm 0.16} e^{-(34950 \pm 340/RT)} \text{sec}^{-1}$$

$$k_{\text{paraffin}}^a = 10^{13.0 \pm 0.2} e^{-(34200 \pm 400/RT)} \text{sec}^{-1}$$

^a Reported in ref 15.

catalyzed reaction in these instances. We found this not to be true in our earlier work with the surface-catalyzed decomposition of trioxane,^{2,18} where the rate constant decreased with increasing liquid-phase loading. The data of Table I show no particular trend and indicate a reproducibility of 1–2% generally except at 170° when conversion tended to be low. Least-squares analysis of these data give rate constants somewhat higher (see Table I) than those of Khambata and Wasserman,¹⁹ who studied the same reaction in British Pharmacopeia paraffin, a mixture of hydrocarbons having a lower molecular weight but similar solvent properties to hexatriacontane. They used a static technique which involved colorimetrically analyzing a cyclopentadiene derivative after vaporization from the reaction mixture. Favorable data comparison certainly validates the gas chromatographic reactor as a source of homogeneous, first-order reaction rate constants. It must be remembered that cyclopentadiene tends to react with dicyclopentadiene^{1b,20} in the reaction mixture to form higher molecular weight products which would not be detected in some earlier work.¹⁹ Reverse reaction (association) under the macroscopic conditions employed might also have caused a slight diminution of apparent rate constant.

The gcr technique need not be limited to the study of reactions which have previously been studied in the gas phase. Equation 11 permits an estimate of the gas-phase rate constant, since increasing the percentage of liquid phase decreases the ratio of time spent in the gas to the liquid phase. For a particular column, the ratio t_g/t_l is a constant not dependent on flow rate in the useful range. However, it can be varied by changing the percentage of liquid phase relative to solid support. With eq 11 and a plot of k_{app} vs. t_g/t_l , a reasonable determination can be made of k_g . Such plots are shown for hexatriacontane in Figure 4. The gas-phase rate constants determined from the slope of these plots are 3.89 ± 0.62 and $10.92 \pm 1.82 \times 10^{-4} \text{sec}^{-1}$, respectively, which are in satisfactory agreement with the values calculated from Herndon's equation:¹⁵ 4.18 and $9.41 \times 10^{-4} \text{sec}^{-1}$. The relatively large standard deviations in the gas-phase constant calculated from eq 11 arise from the fact that the t_g/t_l ratios are small

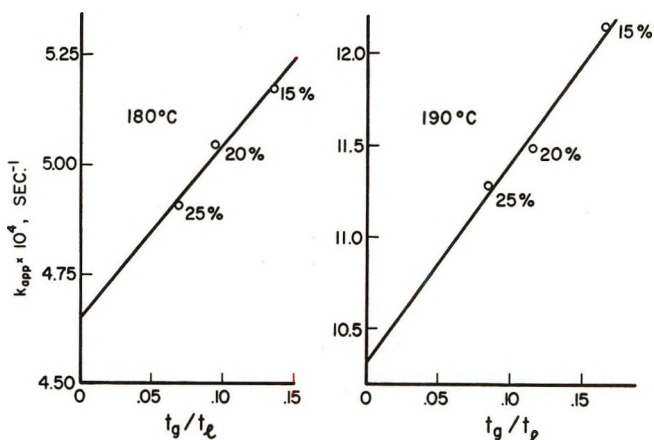


Figure 4. Plots of t_g/t_l vs. apparent rate constant to determine gas-phase rate constant from the slope and liquid-phase rate constant from the intercept (see eq 11). t_g/t_l varied by changing percentage of hexatriacontane liquid phase in the column.

(0.15) and the differences in these ratios are also small and somewhat imprecise. The liquid-phase rate constants, obtained from the intercepts, are more precise: 4.65 ± 0.06 and $10.31 \pm 0.21 \times 10^{-4} \text{sec}^{-1}$ at 180 and 190°, respectively. More accurate determination of the liquid-phase constants is really a consequence of a broader generalization. If the reactant is fairly soluble in the liquid phase ($K > 20$), the ratio t_g/t_l is small so that the liquid-phase rate constant is not very sensitive to changes in k_g .

Customarily chromatographic injector ports are operated at a higher temperature than the column²¹ to ensure rapid vaporization and introduction of sample. This may be a poor procedure for systems involving potential gas-phase reactions. Figure 5 illustrates the effect of this practice for a reaction taking place in a 25% hexatriacontane column at about 180°. Addi-

(18) S. H. Langer, J. Y. Yarchak, and C. M. Shaughnessy, *Anal. Chem.*, **40**, 1749 (1969).

(19) B. S. Khambata and A. Wasserman, *J. Chem. Soc.*, 375 (1939).

(20) B. Raistrick, R. H. Shapiro, and D. M. Newitt, *ibid.*, 1761 (1939); see also P. J. Wilson and J. H. Wells, *Chem. Rev.*, **34**, 1 (1944).

(21) F. H. Pollard and C. J. Hardy, *Chem. Ind. (London)*, 1145 (1955).

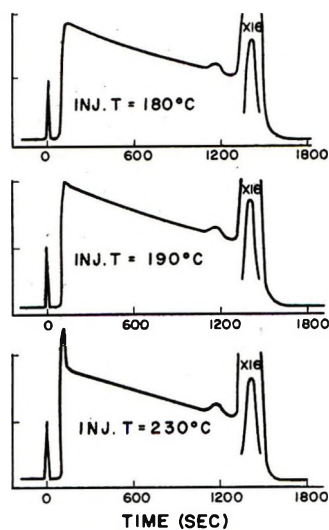


Figure 5. Effect of injector temperature on "preconversion" of dicyclopentadiene in the injector. Product spike from "preconversion" is eliminated when injector is operated at column temperature of 180°. $F = 50.2 \text{ cm}^3/\text{min}$ and $P_1/P_0 = 1.68$ for 12-ft, 25% *n*-hexatriacontane column.

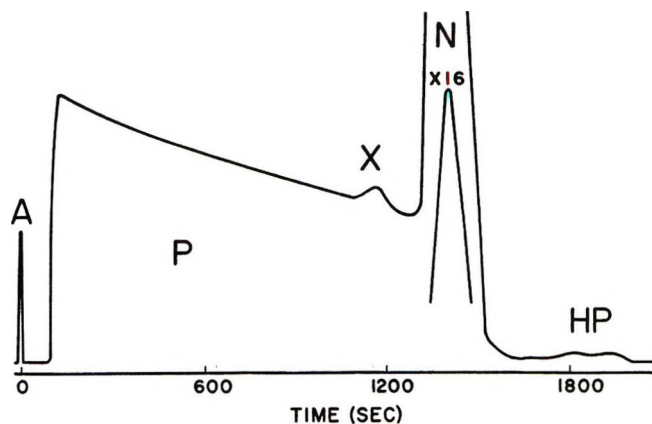
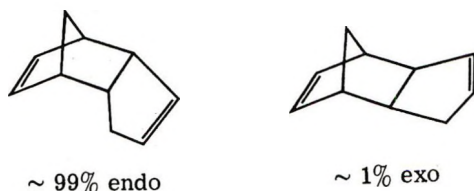


Figure 6. Enlarged reactor chromatogram illustrating detection of exo isomer impurity (X) and higher polymer by-product (HP). Column temperature = 180.6°, flow = 50.2 cm^3/min at column temperature. Conversion 53% on 12-ft, 1/4-in. column containing hexatriacontane (25%) on Gas Chrom Q.

tional product formed by the faster reaction in the injection port 50° above column temperature is obvious from the spike appearing in the reactor chromatogram; some distortion of the chromatogram is even apparent for a temperature of 190°, only 10° above the reactor temperature. Consequently, care must be taken in adjusting injector temperature to minimize the effect of reaction in the port.

Some further advantages of the chromatographic kinetic technique are apparent from the reactor chromatogram of Figure 6. Commercial dicyclopentadiene is a mixture of two geometric isomers.



The exo form is considerably less reactive than the endo isomer ($k_{\text{exo}}/k_{\text{endo}} < 0.04$ in the gas phase at 200°¹⁵). With many kinetic techniques, the reactant would first have to be recrystallized to remove the exo impurity which might interfere with subsequent analysis. Since the gr separates the two isomers in the column while reaction is proceeding, no prior purification is necessary and neither the exo form nor cyclopentadiene derived from it interferes with the kinetic analysis. The exo isomer appears as a small peak, X, on the product curve, where it does not complicate the measurement of the endo reactant area. At 180° the separation factor is 1.21 in hexatriacontane columns.

The continuous separation of the product cyclopentadiene in the gr is a further advantage here. As

earlier indicated, potential reaction of the product monomer with unreacted dimer by a Diels-Alder mechanism to give a higher molecular weight product^{1b,20} is a possibility. This higher molecular weight material is indicated as HP in the chromatogram of Figure 6. Of course, the continuous separation and removal of product, as contrasted with the situation in batch reactors, tend to minimize contact of cyclopentadiene with its dimer and formation of any high molecular weight products.

Rate constants obtained using the gas chromatographic reactor with the techniques described here for a variety of stationary phases or solvents are shown in Table II. Despite the classical nature of this reaction there has been a paucity of kinetic data for different types of solvents.^{19,22,23} However, as recognized earlier and confirmed here, solvent effects are relatively small; increases of the order of only 50% in rate are observed for decomposition in a variety of solvents. Furthermore, there apparently is little correlation with solvent power, represented in Table II by K , the partition coefficient, or V_g^T , the retention volume per gram of liquid phase. Solvents containing highly polar groups or solvating groups enhance rate to the greatest extent as compared to the more hydrocarbonlike solvents such as the phenylmethyl Silicone DC 550 and hexatriacontane.

An Arrhenius plot for comparison of our data with other gas and hydrocarbon solvent data is shown in Figure 7. It is apparent that the rate constants in solvents are slightly greater than those in the gas phase, unlike the comparison based on earlier data.^{3a} The

(22) J. B. Harkness, G. B. Kistiakowsky, and W. H. Mears, *J. Chem. Phys.*, **5**, 682 (1937).

(23) K. Laidler, "Chemical Kinetics," 2nd ed, McGraw-Hill, New York, N. Y., 1965, p 200.

Table II: Solvent Effects in Dicyclopentadiene Dissociation

Solvent	First-order rate constants, $k \times 10^4 \text{ sec}^{-1}$			log A , sec^{-1}	E_A , kcal/mol
	180.1°	189.8°	199.8°		
1. Versamid 900	5.08 ± 0.19	11.7 ± 0.3	28.6 ± 0.5	14.7 ± 0.3	37.3 ± 0.6
2. Silicone DC 550	4.65 ± 0.15	10.9 ± 0.2	26.0 ± 0.6	14.6 ± 0.1	37.2 ± 0.2
3. PDEAS ^a	5.73 ± 0.12	13.7 ± 0.3	30.5 ± 0.4	14.2 ± 0.4	36.1 ± 0.9
4. Apiezon L	4.72 ± 0.04	10.8 ± 0.1	24.9 ± 0.3	14.0 ± 0.1	36.0 ± 0.3
5. Igepal CO-880 ^b	5.75 ± 0.22	12.8 ± 0.1	29.6 ± 0.4	13.8 ± 0.2	35.4 ± 0.5
6. Hexatriacontane	4.61 ± 0.03	10.6 ± 0.1	28.8 ± 0.2	13.5 ± 0.2	35.0 ± 0.3
7. Poly(phenyl ether) (six ring)	5.73 ± 0.10	12.6 ± 0.1	28.8 ± 0.2	13.3 ± 0.3	34.3 ± 0.7
8. Gas ^c	4.28	9.41	20.6	13.0 ± 0.3	34.0 ± 0.6
9. Trixylyl phosphate	5.91 ± 0.07	12.3 ± 0.3	27.4 ± 0.6	12.7 ± 0.5	33.0 ± 1.0

^a Phenyl-diethanolamine succinate. ^b Nonylphenoxypolyoxyethylene ethanol. ^c Reference 15.

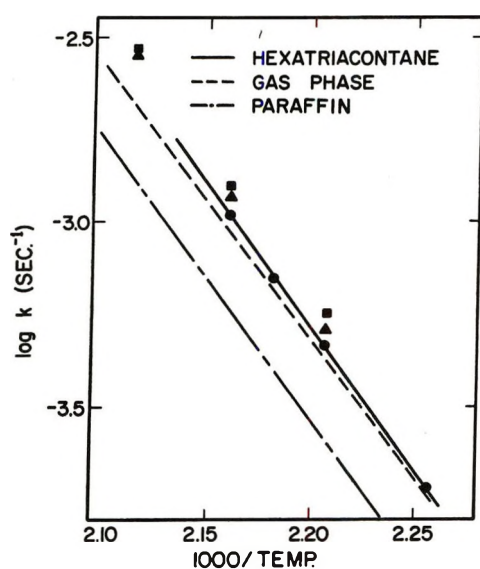


Figure 7. Arrhenius plots for dicyclopentadiene decomposition: (●) gas chromatographic reactor data; compared with earlier results of Herndon, *et al.*,¹⁵ and Khambata and Wasserman¹⁹ in paraffin solvent. Data for Versamid 900 (▲) and poly(phenyl ether) (■) are also shown.

more recent results would be expected to be more accurate generally. The early procedures for measuring gas phase rate constants,²² involving pressure changes, probably gave slightly erroneous results because of the formation of by-product higher molecular weight materials, as discussed already. The difficulty in eliminating by-product formation completely even with chromatographic separation is illustrated by the results of Figure 6.

Traditionally, workers in kinetics tend to look to frequency factors or energies of activation for explanations of change in rate. Often, a "compensation effect" is operative, in which rates surprisingly are little changed with solvent because of the interaction of orientation and energetic factors. We have discussed this compensation effect earlier,⁵ as have others, in connection with thermodynamic investigations. Energies of activation,

E_A , and frequency factors, A , are listed in Table II in order of decreasing E_A and A values. These data immediately suggest the existence of a "compensation effect."²⁴ Consistent then is the fact that a favorable preexponential factor (reflecting orientation or solvation?) is accompanied by a higher activation energy (tending to be unfavorable). One can advance an argument in terms of the possibility that a solvated or otherwise favorably stabilized activated intermediate state might require a higher activation energy for formation of product.

The relationship between E_A and A is more evident if transformed to ΔH^\ddagger and ΔS^\ddagger , respectively, the enthalpy and energy of activation, since

$$\Delta H^\ddagger = E_A - RT \quad (12)$$

and

$$\Delta S^\ddagger = -R \ln \frac{kT_e}{hA} \quad (13)$$

The strong linear nature of the relationship is apparent from Figure 8, in which there is a plot of ΔH^\ddagger vs. ΔS^\ddagger . Such isokinetic relationships are common in chemical kinetics²⁵ when the reaction proceeds through the same mechanisms in all solvents. At the *isokinetic temperature*, given by the slope of the ΔH^\ddagger vs. ΔS^\ddagger plot, variations in the rate constant from the dominant reactant-solvent interaction are at a minimum. The isokinetic temperature here is 453°K, 180°C. This happens to be the lower temperature of the present investigation, and it might be argued that the observed relationship is a consequence of an error in E_A together with the highly correlated nature of E_A and A . However, this seems unlikely, since the range of activation energies is 4.3 kcal/mol, seven times the average standard deviation.

In previous work,^{5,6} we used corrected retention volumes per gram at column temperature to calculate

(24) See ref 23 or other kinetic texts.

(25) J. E. Leffler and E. Grunwald, "Rates and Equilibria of Organic Reactions," Wiley, New York, N. Y., 1963.

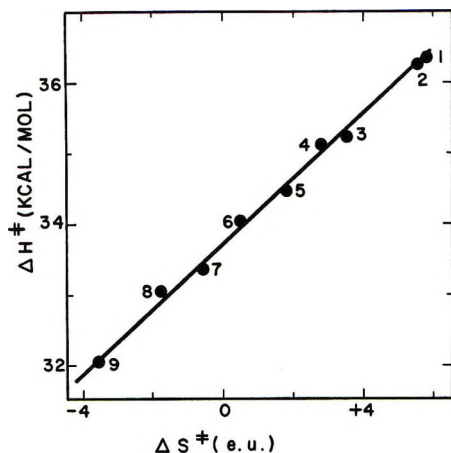


Figure 8. Linear relationship between enthalpy and entropy of activation for dicyclopentadiene dissociation. Solvent key in Table II.

activity coefficients of eluted solutes in stationary liquid phases with a relatively simple equation. Related thermodynamic quantities for solution were then calculated from activity coefficient-temperature data. However, at high solute vapor pressure, a more complex expression is needed to calculate and extract the true activity coefficient of the solute at infinite dilution in the stationary phase.²⁶⁻²⁸ Unfortunately, the second virial coefficient of pure solute vapor as well as the second virial coefficient of solute in carrier gas and other data are needed.

A simplified expression for the estimation of true activity coefficients for this investigation is developed in the Appendix, where estimates and values of critical parameters are also given. Since the term involving solute-carrier gas interaction is a net small correction, the final expression used here for γ_f^∞ , the corrected solute activity coefficient at infinite dilution, is

$$\ln \frac{\gamma_f^\infty}{\gamma_p^\infty} = -\frac{p_2^0}{RT}(B_{22} - v_2^0) \quad (14)$$

where B_{22} is the second virial coefficient of pure solute, v_2^0 is the molar volume of pure solute, p_2^0 is the vapor pressure of solute, and γ_p^∞ is calculated from^{6,14}

$$V_g^T = \frac{RT}{M_s \gamma_p^\infty p_2^0} \quad (15)$$

where M_s is the molecular weight of the stationary phase. Parameters necessary for using eq 14 are given in Table VI. In this instance, fortunately, the vapor pressure data of Turnbull, Hull and Reid¹⁶ are available for both product and reactant.

Some activity coefficient data for reactant and product are presented in Table III for stationary phases for which adequate data are available (molecular weight of Versamid unknown). Activity coefficients of product relative to reactant, with the exception of poly(phenyl ether), decrease in the solvents with higher rate con-

stants for dicyclopentadiene dissociation. Generally faster rates correlate with high reactant activity coefficients and with solvents containing relatively polar groups.

While retention values for cyclopentadiene in Table III were measured from the retention time of pure cyclopentadiene, we have found on comparing with reactor chromatograms that the cyclopentadiene retention volume corresponds to the time at which cyclopentadiene has reached 0.5-0.6 of its maximum value. This might be anticipated by analogy with frontal analysis.²⁹ We are investigating this further and hope to report shortly.

The measured activity coefficient for a solution of small molecules in solvent of much higher molecular weight can be considered from the Flory-Huggins treatment to be the product of thermal, γ_t^∞ , and athermal activity coefficients, γ_a^∞ . The calculated athermal activity coefficient is an attempt to take into account the effect due to differences in molecular size.^{5,6,30} This approach gives at infinite dilution

$$\gamma_a^\infty = \frac{1}{m} e^{[1-(1/m)]} \quad (15a)$$

where m is the size ratio of the solution molecules, approximated as the molar volume ratio of solvent to that of solute. The athermal activity coefficient has a maximum value of unity at $m = 1$. With the measured activity coefficient and the calculated value of γ_a^∞ , values of γ_t^∞ can then be calculated.

The calculated values for γ_a^∞ in the systems studied here are included in Table III. Comparison with values of γ_f^∞ of Table III shows that these are approximately the same size, with the athermal activity coefficient somewhat smaller. This would suggest that size effects represent a significant contribution to the low values of the activity coefficient in our systems. Almost all of the γ_t^∞ values would fall in the range of 1.2-2.5, indicating some positive deviation from Raoult's law for product and reactant.

According to transition state theory for a unimolecular reaction³¹

$$k_1 = k_0 \frac{\gamma_R}{\gamma_\ddagger} \quad (15b)$$

where γ_R and γ_\ddagger are activity coefficients for reactant and activated complex and k_0 is the rate constant in an

(26) D. H. Everett, *Trans. Faraday Soc.*, **61**, 1637 (1965).

(27) J. R. Conder and J. H. Purnell, *ibid.*, **64**, 1505 (1968).

(28) D. E. Martire and L. Z. Pollara in "Advances in Chromatography," Vol. 1, J. C. Giddings and R. A. Keller, Ed., Marcel Dekker, New York, N. Y., 1966, pp 335-362.

(29) (a) J. H. Purnell, "Gas Chromatography," Wiley, New York, N. Y., 1962, pp 95-102; (b) E. Gluekauf, *Trans. Faraday Soc.*, **51**, 34 (1955).

(30) J. Ashworth and D. H. Everett, *ibid.*, **56**, 1609 (1960).

(31) A. A. Frost and R. G. Pearson, "Kinetics and Mechanism," Wiley, New York, N. Y., 1961, pp 127-130.

Table III: Properties in Indicated Stationary Phases

Solvent	Mol wt	K^{180}	V_g^{180} , cm ³ /g	V_g^{200} , cm ³ /gm	γ_f^∞ (180°)	γ_f^∞ (200°)	γ_a^∞
A. Dicyclopentadiene							
1. Versamid 900	...	55.6	64.0	44.2			
2. Silicone DC 550	1722	60.6	67.0	45.5	0.283	0.278	0.20
3. PDEAS	3422	32.9	30.3	25.2	0.314	0.298	0.13
4. Apiezon L	1230	76.2	97.1	66.0	0.335	0.331	0.24
5. Igepal CO-880	880	55.8	57.1	39.0	0.651	0.632	0.40
6. Hexatriacontane	507	82.6	121.4		0.532		0.46
7. Poly(phenyl ether) (six ring)	538.6	83.9	80.4	55.4	0.757	0.729	0.61
9. Trixylyl phosphate	410.5	83.1	81.5	50.4	0.978	1.050	0.72
B. Cyclopentadiene							
1. Versamid 900		4.9	5.6	4.4			
2. Silicone DC 550		5.2	5.7	4.5	0.26	0.26	0.16
3. PDEAS		3.7	3.4	3.2	0.22	0.28	0.10
4. Apiezon L		5.4	6.9	5.6	0.37	0.39	0.19
5. Igepal CO-880		5.6	5.7	4.6	0.51	0.54	0.32
6. Hexatriacontane		5.9	8.7		0.58		0.37
7. Poly(phenyl ether) (six ring)		6.1	5.8	4.8	0.82	0.85	0.51
9. Trixylyl phosphate		5.9	6.5	4.7	0.92	1.18	0.60

ideal medium. If the gas phase is assumed ideal, then the gas-phase rate constant is k_0 and the activity coefficient of the activated complex at infinite dilution can be calculated from

$$\gamma_{\pm}^\infty = \gamma_R^\infty \frac{k_g}{k_1} \quad (16)$$

Admittedly, the gas phase may not be ideal and the assumption $k_0 = k_g$ may lead to some error. However, all values of γ_{\pm}^∞ so calculated would be in error by the same factor. Relative values of γ_{\pm}^∞ using the data of Tables II and III are given in Table IV.

Table IV: Relative Activity Coefficient (Gas = 1.00) of Activated Complex

	180°	200°
Gas	1.000	1.000
Silicone DC 550	0.257	0.22
PDEAS	0.237	0.20
Apiezon L	0.276	0.27
Igepal CO-880	0.485	0.44
Hexatriacontane	0.492	0.45
Poly(phenyl ether)	0.566	
Trixylyl phosphate	0.705	0.79

The nature of eq 16 is to combine kinetic results with thermodynamic observations (activity coefficients) to give the activity coefficients of Table IV. Assuming, for argument, the validity of using the gas-phase rate constant as ideal, the data of Table IV permit comparison of the activity coefficients of the activated com-

plex with those of reactants and products presented in Table III. For most of the systems reported here, the activity coefficient of the activated complex lies below that of either product or reactant, an unexpected result.

A plot of $\ln \gamma_{\pm}^\infty$ against both $\ln \gamma_R^\infty$ and $\ln \gamma_P^\infty$ (R = reactant, P = product) is approximately linear. If now it is assumed that the excess partial molar free energy of mixing at infinite dilution, $\Delta \bar{G}_{e,i}^\infty$, of the transition state actually lies between that of product and reactant, then

$$\ln \gamma_{\pm}^\infty = \chi \ln \gamma_P^\infty + (1 - \chi) \ln \gamma_R^\infty + \text{constant} \quad (17)$$

where

$$\Delta \bar{G}_{e,i}^\infty = RT \ln \gamma_i^\infty \quad (18)$$

and χ is determined by similarity of the activated complex to reactant ($\chi = 0$) or to product ($\chi = 1$).³² The constant arises from the possibility that γ_{\pm}^∞ may be in error by a constant factor, k_0/k_g . Similarly, γ_P^∞ and γ_R^∞ may be in error in all solvents by constant factors because of some vapor pressure or fugacity error at each temperature. In using logarithms and the form of eq 17, these factors are combined in the constant. Least-squares analysis of activity coefficient data at 200° gives $\chi = 0.40 \pm 0.17$. A plot of $\ln \gamma_{\pm}^\infty$ vs. $0.6 \ln \gamma_R^\infty + 0.4 \ln \gamma_P^\infty$ is linear with a slope of unity and an intercept of -0.29 . This relationship may be expressed as

$$\gamma_{\pm}^\infty = e^{-0.29} (\gamma_R^\infty)^{0.6} (\gamma_P^\infty)^{0.4} \quad (19)$$

(32) See ref 25, pp 157-170.

Table V: Excess Partial Thermodynamic Quantities

Solvent	Dicyclopentadiene				Cyclopentadiene			
	$\Delta\bar{G}_e^\infty$, cal/mol	$\Delta\bar{H}_e^\infty$, kcal/mol	$\Delta\bar{S}_e^\infty$, eu	$\Delta\bar{S}_a^\infty$, eu	$\Delta\bar{G}_e^\infty$, cal/mol	$\Delta\bar{H}_e^\infty$, kcal/mol	$\Delta\bar{S}_e^\infty$, eu	$\Delta\bar{S}_a^\infty$, eu
2. Silicone DC 550	-1169	0.54	3.70	3.66	-1214	-1.73	-1.10	3.64
3. PDEAS	-1082	0.91	4.30	4.73	-1361	-0.94	0.93	4.66
4. Apiezon L	-1009	0.52	3.30	3.25	-886	-1.06	-0.36	3.33
5. Igepal CO-880	-400	0.75	2.50	2.12	-612	-1.24	-1.36	2.27
6. Hexatriacontane	-597	0.59	2.69	1.79	-484	-0.52	-0.08	1.98
7. Poly(phenyl ether) (six ring)	-270	0.75	2.20	1.15	-158	-0.71	-1.18	1.36
9. Trixylyl phosphate	12	-1.36	-2.99	0.77	60	-5.34	-11.84	1.01

Equation 19 can be substituted into eq 15b to give a rate-correlating equation dependent on activity coefficients of products and reactants in the specified solvent. Considering the intricacies and lore of the long-standing discussion concerning the precise mechanism of the reverse Diels–Alder reaction,³³ it does not seem feasible to interpret this result further here. However, the potential of the gas chromatographic reactor for obtaining concurrent kinetic and activity coefficient data for future kinetic study is apparent.

In addition to the excess partial molar free energy (eq 18), other excess partial molar quantities can be obtained from standard expressions.^{5,6}

$$R \frac{\partial \ln \gamma^\infty}{\partial(1/T)} = \Delta\bar{H}_e^\infty \quad (20)$$

and

$$\Delta\bar{G}_e^\infty = \Delta\bar{H}_e^\infty - T\Delta\bar{S}_e^\infty \quad (21)$$

where $\Delta\bar{G}_e^\infty$ is the excess partial molar free energy of mixing, $\Delta\bar{H}_e^\infty$ is the (excess) partial molar enthalpy of mixing, and $\Delta\bar{S}_e^\infty$ is the excess partial molar entropy of mixing. These are tabulated in Table V for both dicyclopentadiene reactant and cyclopentadiene product. The data for the latter are considerably less accurate because of the relatively small retention volume of cyclopentadiene. Some recognition must also be made of the limited accuracy of the correction procedures to activity coefficients, despite the fact that these seem to be the best possible at the present time. Since these corrections are applied for all solvents, the thermodynamic quantities stand in the same relative order despite any errors.

For comparison, the entropy of mixing due to size difference between solutes and solvents, calculated from the Flory–Huggins expression for athermal contribution to the activity coefficient *vide supra*, are included in Table V. The activity coefficient is considered to be the product of independent thermal contributions, γ_t^∞ , and athermal contributions, γ_a^∞ , so that^{5,6,30}

$$\ln \gamma_t^\infty = \frac{\Delta\bar{H}_e^\infty}{RT}; \quad \ln \gamma_a^\infty = \frac{-\Delta\bar{S}_a^\infty}{R} \quad (22)$$

Since γ_a^∞ has a maximum value of unity at $m = 1$, $\Delta\bar{S}_e^\infty$ is positive for other values of m if only molecular size differences contribute to the athermal activity coefficient.

In Table V, the calculated entropy contribution due to size difference for dicyclopentadiene in a number of solvents is close to the observed partial molar entropy of solution to give unusually good agreement.^{5,6,30} The approximate rigid ellipsoid shape of the dicyclopentadiene molecule which limits molecular interactions and entanglements with the linear or helical solvent molecules may account for this. Perhaps there is special general validity of the Flory–Huggins treatment for similar systems involving polycycloalkanes such as adamantane or polycycloalkenes and linear polymerlike molecules such as higher alkanes or silicones.

In trixylyl phosphate there is a strong discrepancy between calculated and observed entropies for dicyclopentadiene, indicating a molecular solvation orientation requirement accompanying solvation similar to systems that we have described elsewhere.^{5,6} In most of our systems, it is apparent from the excess enthalpy values that it is essentially a size effect that gives a negative deviation from Raoult's law for the dicyclopentadiene solute. Excess thermodynamic quantities for cyclopentadiene are less accurate because of small retention volumes and the generally lower accuracy of activity coefficients at higher corresponding temperatures. Nevertheless, it is apparent that with systems of the type that are studied here, not only are activity coefficient or excess free energy data available, but it is also possible to break these down further to contributing factors, *i.e.*, excess enthalpies and entropies. Trixylyl phosphate is an exceptional solvent among those of Table V because there appears to be strong solvation of reactant and product with an unfavorable entropy requirement. The result is one of the higher dissociation rates with a low activation energy moderated by a partially compensating low frequency factor.

(33) H. Kwart and K. King, *Chem. Rev.*, **68**, 415 (1968) (ref 1b and others are quoted here); recent discussion in R. A. Grieger and C. A. Eckert, *J. Amer. Chem. Soc.*, **92**, 7149 (1970).

Table VI: Thermodynamic Properties from Various Correlations

Quantity	Dicyclopentadiene			Cyclopentadiene		
	180.1°	189.8°	199.8°	180.1°	189.8°	199.8°
Critical temperature, °K ^a		660°			504°	
Critical pressure, atm ^a		30.4			51	
Critical volume, cm ³ /mol ^a		446			225	
Vapor pressure, atm ^{b,c}	1.204	1.524	1.921	18.42	20.66	23.09
Molar volume, cm ³ /mol	155	156	157	116 ^d	121 ^d	126 ^d
B_{22} , cm ³ /mol ^{e,f}	-1491	-1416	-1340	-364	-346	-320
B_{22} , cm ³ /mol ^f	68			42		
$\exp[-p_2^0(B_{22} - v_2^0)/RT]$	1.055	1.065	1.077	1.267	1.288	1.304
$\exp[\bar{p}(B_{22} - v_2^0)/RT]$	1.000			0.999		
$\gamma_i^\infty/\gamma_p^\infty$	1.055	1.065	1.077	1.267	1.288	1.304

^a R. C. Reid and T. K. Sherwood, "The Properties of Gases and Liquids," 2nd ed, McGraw-Hill, New York, N. Y., 1966. Lyderson's methods in Chapter 2. ^b Reference 16b. ^c Reference 16a. ^d Reference 20. ^e E. A. Guggenheim and C. J. Wormald, *J. Chem. Phys.*, **42**, 3775 (1965). ^f K. S. Pitzer and R. F. Curl, *J. Amer. Chem. Soc.*, **79**, 2369 (1957).

In PDEAS there is apparently a relatively favorable frequency factor accompanying a slightly high activation energy giving one of the higher rate constants. This apparently is reflected in an abnormally low entropy requirement for interacting product cyclopentadiene, the structure of which contributes to the transition state. These examples are meant to be illustrative only. It is apparent though that these and similar data which are accessible through the gas chromatographic reactor should assist significantly in interpretation of factors influencing reaction rates, especially after an adequate body of data is accumulated.

Some caution is required in any explanation and correlation of solvent effects with large solvent molecules of the type encountered here, since the critical solvent action assisting reaction may take place in a limited domain of the solvent structure. Net solution interactions observed through thermodynamic measurements may be the result of many varied solution interactions, some acting counter to each other.³⁴ Nevertheless, with systematic changes in solvent structure, identification of important solution and kinetic factors will be possible.

The gas chromatographic reactor is limited in application to kinetic studies^{1b,2-4} of selected systems. Homogeneous first-order reactions or pseudo-first-order reactions are most suited to the chromatographic approach. However, where applicable, the gcr can be used to obtain kinetic data accurately and effectively over a wide temperature range and with a variety of solvents. Furthermore, this reactor gives access to an unprecedented amount of solution thermodynamic data to assist in the correlation and interpretation of kinetic phenomena.

Acknowledgment. We are grateful to the American Oil Company and the Petroleum Research Fund, administered by the American Chemical Society, for support of this work.

Appendix

The expression for the activity coefficient of a solute at infinite dilution and zero total pressure, γ_i^∞ , may be shown to be, for a very small amount of injected solute^{26-28,35}

$$\ln(\gamma_i^\infty/\gamma_p^\infty) = \frac{P_0 j_3^4}{RT} [2B_{23} - \bar{v}_2^\infty] - \frac{p_2^0}{RT} [B_{22} - v_2^0] \quad (1A)$$

where eq 15 is applied to calculate γ_p^∞ in hydrogen, helium, or nitrogen. Here, \bar{v}_2^∞ is the partial molar volume of solute at infinite dilution, v_2^0 is the molar volume of pure solute, B_{22} is the second virial coefficient of the pure vapor, B_{23} is the cross virial coefficient for solute vapor with carrier gas, and

$$j_3^4 = \frac{3(P_i/P_0)^4 - 1}{4(P_i/P_0)^3 - 1} \quad (2A)$$

The B_{33} term has been eliminated since the carrier gas is helium and close to ideal.

Data used in the calculation of γ_i^∞ are given in Table VI. Since with helium ($2B_{23} - \bar{v}_2^\infty$) is almost always smaller than 75 cm³/mol,²⁷ the error in discarding the first correction on the right-hand side of eq 1A is less than $\pm 0.3\%$ for $\gamma_i^\infty/\gamma_p^\infty$. The lack of experimental B_{23} data supports this approach. Since B_{22} is negative it is augmented by v_2^0 so that eq 1A reduces to

$$\ln(\gamma_i^\infty/\gamma_p^\infty) = -\frac{p_2^0}{RT}(B_{22} - v_2^0) \quad (3A)$$

when helium is used as carrier gas.

(34) S. H. Langer, *Anal. Chem.*, **39**, 524 (1967); S. H. Langer and R. J. Sheehan in "Progress in Gas Chromatography," J. H. Purnell, Ed., Interscience, New York, N. Y., 1968, pp 289-323.

(35) A. J. B. Cruickshank, B. W. Gainey, and C. L. Young, *Trans. Faraday Soc.*, **64**, 337 (1968).

This correction is usually significant when the vapor pressure is greater than 0.5 atm, and it becomes increasingly important at higher temperatures. The major difficulty in applying eq 3A is the scarceness of experimentally determined virial coefficients. There are several correlations for B_{22} based on the theory of corresponding states, but here one often encounters

the absence of critical data needed to use them. Group contribution methods are available to estimate the necessary critical constants. Constants, some calculated data, and pertinent references for calculation and estimation are given in Table VI. The data of Table VI support the simplification of eq 1A to 3A and also include constants for use of eq 3A.

Solubility of Methanol in Compressed Nitrogen, Argon, Methane, Ethylene, Ethane, Carbon Dioxide, and Nitrous Oxide. Evidence for Association of Carbon Dioxide with Methanol in the Gas Phase¹

by B. Hemmaplardh and A. D. King, Jr.*

Department of Chemistry, University of Georgia, Athens, Georgia 30601 (Received February 7, 1972)

Publication costs assisted by The National Science Foundation

The solubility of methanol in compressed N_2 , Ar, CH_4 , C_2H_4 , C_2H_6 , CO_2 , and N_2O has been measured over the pressure range of 10–60 atm at temperatures spanning 15–60°. Second cross virial coefficients representing deviations from ideality caused by methanol–gas interactions have been evaluated from these data. The cross virial coefficients involving methanol vapor with carbon dioxide are found to be more negative than expected if physical forces alone were operative. This anomaly is interpreted as indicating the existence of chemical association between methanol and CO_2 in the gas phase. Values of $K_{a,q}$ and standard enthalpies and entropies of association are estimated.

Introduction

Previous measurements of the solubility of water in various compressed gases indicated that water is considerably more soluble in dense CO_2 and N_2O than in ethane, even though all three gases have similar physical properties.² The enhanced solubility of water in these two gases was considered as resulting from the chemical association of water vapor with CO_2 and N_2O . Alcohols are similar chemically to water in that they not only have the capacity of forming hydrogen bonds but they also undergo addition reactions with acid anhydrides. Thus simple alcohols might be expected to exhibit enhanced solubilities in compressed CO_2 and N_2O as was found in the case of water.

This paper reports measurements of the solubility of methanol in a series of compressed gases including carbon dioxide and nitrous oxide. Methanol was chosen for this study for two reasons: (a) it is the simplest member of the alcohol family and (b) there is already direct evidence that it forms a 1:1 adduct with condensed CO_2 at low temperatures.³ Metal salts of

this adduct, commonly called methyl carbonates, are well known and commercially important compounds.

Experimental Section

The experimental technique used here to determine vapor concentrations of methanol in the various compressed gases is a modification of the method used by Prausnitz and Benson⁴ and is described in detail in ref 5. The method entails saturating the gas to be studied with methanol vapor under pressure in a series of saturation cells and subsequently expanding this gas–vapor mixture into a low-pressure system where the methanol vapor is removed from the gas stream by a series of cold traps maintained at -80° to -70° depending on the gas studied. In these experiments, the

(1) This work was supported by the National Science Foundation.

(2) C. R. Coan and A. D. King, *J. Amer. Chem. Soc.*, **93**, 1857 (1971).

(3) W. Hempel and J. Seidel, *Ber.*, **31**, 3000 (1898).

(4) J. M. Prausnitz and P. R. Benson, *AIChE J.*, **5**, 161 (1959).

(5) C. R. Coan and A. D. King, Jr., *J. Chromatogr.*, **44**, 429 (1969).

amounts of methanol collected were relatively large, ranging from 0.8 to 1.5 g depending upon the temperature and duration of each run. With methanol, the trapping efficiency of the individual cold traps was very high (ca. 90%) so that only three cold traps were necessary to attain maximum removal of methanol vapor from the gas stream. Before calculating mole fractions, each value of the total weight recorded was corrected for losses of methanol vapor under the assumption that the gas exiting the last trap was in equilibrium with liquid methanol at the temperature of the cold bath.

Initial data taken at each temperature were examined for variations of vapor concentration with flow rate and number of saturation cells, indicating incomplete saturation. With flow rates of less than 0.5 l./min, it was found that three saturation cells were necessary to ensure saturation up to 37°, while two cells were sufficient for higher temperatures. By the same token, all second cross virial coefficients calculated from the mole fraction data were examined for directional trends with pressure indicating experimental errors or mean field effects at the higher densities. No such trends were observed.

The hydrocarbon gases and nitrous oxide used in these experiments (CP grade) were obtained from Matheson Co., Inc., while argon, nitrogen, and carbon dioxide were purchased from Selox Corp., having quoted purities of 99.995, 99.9, and 99.5%, respectively. Reagent grade absolute methanol was used in all experiments.

Results and Discussion

The experimentally determined vapor concentrations of methanol in the various gases will not be tabulated here for the sake of brevity.⁶ These mole fractions are related to the total pressure of the system, P , by⁴

$$y_2 = \frac{(1 - x_1)P_2^0 \left(\frac{\phi_2^0}{\phi_2}\right)}{P} \exp\left[\frac{V_2^{0(L)}(P - P_2^0)}{RT}\right] \quad (1)$$

where P_2^0 and $V_2^{0(L)}$ represent saturated vapor pressure and molar volume of pure methanol (component 2) at temperature T . Here x_1 is the mole fraction of dissolved gas (component 1) at P and T , while ϕ_2^0 and ϕ_2 designate fugacity coefficients of pure methanol and methanol vapor in the dense gas medium, respectively. A fugacity coefficient is a function of density and temperature. For densities sufficiently low that contributions from third and higher order virial coefficients can be neglected, the fugacity coefficient, ϕ_2 , can be expressed in terms of the virial equation of state as

$$\ln \phi_2 = (2/V)[y_2 B_{22}(T) + y_1 B_{12}(T)] = \ln Z \quad (2)$$

Here V and Z denote the molar volume and compressibility factor of the gaseous mixture having a composition specified by the mole fractions y_1 and y_2 . The symbols $B(T)$ designate second virial coefficients repre-

sented deviations from ideality caused by pair interactions indicated by the subscripts. Equations 1 and 2 can be combined and solved iteratively using any of the experimentally determined y_2 and the appropriate virial expansions for the molar volume V and compressibility factor Z to yield a value for $B_{12}(T)$ for that particular methanol-gas system.²

Average values of second cross virial coefficients calculated in this manner from the experimental mole fraction data are listed in Table I. Values for molar volume and vapor pressure of methanol listed in ref 7 and 8 were used in these calculations. For gases other than N_2 and CO_2 , for which experimental data exist over wide pressure ranges,⁹ gas solubilities in the liquid phase were estimated as a function of pressure through Henry's law expressed in terms of fugacity. Values for the Henry's law constants were calculated from solubility data found in ref 10-12 and are listed in Table II. In these calculations it was assumed that the entropy of solution of these gases in methanol at 1 atm was sufficiently independent of temperature that accurate estimates of Henry's law constants at 15, 50, and 60° could be obtained through linear extrapolations of log concentration vs. log T . Fugacity coefficients were derived from the PVT data in ref 13-18. The pure-component second virial coefficients occurring in the expansions for ϕ_2 , V , and Z in eq 1 and 2 were obtained from ref 13, 15, and 19-24.

(6) Listings of the experimentally determined vapor mole fraction data will appear following these pages in the microfilm edition of this volume of the journal. Single copies may be obtained from the Business Operations Office, Books and Journals Division, American Chemical Society, 1155 Sixteenth St., N.W., Washington, D. C. 20036, by referring to code number JPC-76-2170. Remit check or money order for \$3.00 for photocopy or \$2.00 for microfiche.

(7) J. Timmermans, "Physico-Chemical Constants of Pure Organic Compounds," Vol. 1, Elsevier, New York, N. Y., 1950.

(8) T. E. Jordan, "Vapor Pressures of Organic Compounds," Interscience, New York, N. Y., 1954.

(9) I. P. Krichevskii and E. S. Lebedeva, *Zh. Fiz. Khim.*, **21**, 715 (1947).

(10) A. Lannung, *J. Amer. Chem. Soc.*, **52**, 68 (1930).

(11) F. L. Boyer and L. J. Bircher, *J. Phys. Chem.*, **64**, 1330 (1960).

(12) W. Kunerth, *Phys. Rev., Ser. 2*, **19**, 512 (1922).

(13) A. Michels, Hub. Wijker, and Hk. Wijker, *Physica*, **15**, 627 (1949).

(14) A. Michels and G. W. Nederbragt, *ibid.*, **3**, 569 (1936).

(15) A. Michels and M. Geldermans, *ibid.*, **9**, 967 (1942).

(16) A. Michels, S. R. DeGroot, and M. Geldermans, *Appl. Sci. Res. A*, **1**, 55 (1947).

(17) J. A. Beattie, C. Hadlock, and N. Poffenberger, *J. Chem. Phys.*, **3**, 93 (1935).

(18) L. J. Hirth and K. A. Kobe, *J. Chem. Eng. Data*, **6**, 233 (1961).

(19) A. P. Kudchadker and P. T. Eubank, *ibid.*, **15**, 7 (1970).

(20) A. Michels, H. Wouters, and J. DeBoer, *Physica*, **1**, 587 (1934).

(21) D. R. Douslin, R. H. Harrison, R. T. Moore, and J. P. McCullough, *J. Chem. Eng. Data*, **9**, 358 (1964).

(22) A. Michels, W. van Staaten, and J. Dawson, *Physica*, **20**, 17 (1954).

(23) A. Michels and C. Michels, *Proc. Roy. Soc., Ser. A*, **153**, 201 (1935).

(24) H. W. Schamp, E. A. Mason, and K. Su, *Phys. Fluids*, **5**, 769 (1962).

Table I: Second Class Virial Coefficients for Methanol with Various Gases

Gas	Temp, °C	$B_{12}(T),^a$ cm ³ /mol
N ₂	15.0	-91 ± 3
	25.0	-81 ± 4
	37.0	-72 ± 2
	50.0	-67 ± 3
	60.0	-64 ± 2
Ar	15.0	-102 ± 2
	25.0	-87 ± 4
	37.0	-77 ± 3
	50.0	-72 ± 2
	60.0	-71 ± 4
CH ₄	15.0	-130 ± 6
	25.0	-114 ± 7
	37.0	-103 ± 4
	50.0	-97 ± 4
	60.0	-95 ± 2
C ₂ H ₄	15.0	-279 ± 6
	25.0	-247 ± 6
	37.0	-213 ± 7
	50.0	-192 ± 6
	60.0	-179 ± 4
C ₂ H ₆	15.0	-306 ± 5
	25.0	-276 ± 8
	37.0	-234 ± 4
	50.0	-220 ± 7
	60.0	-203 ± 7
CO ₂	15.0	-352 ± 7
	25.0	-308 ± 5
	37.0	-265 ± 8
	50.0	-237 ± 3
	60.0	-217 ± 7
N ₂ O	15.0	-253 ± 5
	25.0	-231 ± 8
	37.0	-194 ± 7
	50.0	-176 ± 7
	60.0	-161 ± 5

^a Error expressed as average deviation from mean.

These methanol-gas cross virial coefficients are shown graphically in Figure 1. A comparison with critical constants listed in Table III shows that, with the exceptions of CO₂ and N₂O, these cross virial coefficients exhibit the usual pattern of increasing in magnitude as the critical temperature of the gas increases. With regard to CO₂ and N₂O, it has been pointed out previously^{25,26} that these two gases differ from the others in Table III in that their molecules possess large quadrupole moments while having relatively low polarizabilities, with the result that quadrupolar interactions play a significant role in determining the critical properties of these gases. As a result, the experimental critical constants for these two gases are not an appropriate index for comparing intermolecular interactions in mixed systems where dispersion forces are expected to be the dominant mode of interaction. It is possible, however, to make accurate estimates of the critical properties that these two gases would exhibit in the ab-

Table II: Henry's Law Constants for Methanol-Gas Systems

System	Temp, °C	$k_H,$ atm	Ref
CH ₃ OH-Ar	15	2765	10
	25	2838	10
	37	2922	10
	50	3012	10
	60	3079	10
CH ₃ OH-CH ₄	15	990.1	11
	25	1153	11
	37	1375	11
	50	1656	11
	60	1892	11
CH ₃ OH-C ₂ H ₄	15	141.7	11
	25	227.8	11
	37	392.9	11
	50	702.1	11
	60	1059	11
CH ₃ OH-C ₂ H ₆	15	163.1	11
	25	246.9	11
	37	397.5	11
	50	660.2	11
	60	944.9	11
CH ₃ OH-N ₂ O	15	200.6	12
	25	222.1	12
	37	248.6	12
	50	278.9	12
	60	333.2	12

sence of quadrupolar interactions,²⁷ and these hypothetical parameters have been used to correlate cross virial coefficients data for a number of mixed systems.^{28,29} The values appropriate to these two gases are listed in parentheses in Table III. It is seen that the modified critical temperature for N₂O falls in the same order relative to the other gases as do the cross virial coefficients of Figure 1, while a discrepancy remains in the case of CO₂.

Guggenheim and McGlashan³¹ have shown that second cross virial coefficients data for gaseous mixtures consisting of small molecules conform to the principle of corresponding states when reduced using the following rules to generate pseudocritical constants appropriate to each mixture

$$T_{12}^c = (T_1^c T_2^c)^{1/2} \quad (3)$$

$$V_{12}^c = (1/6[(V_1^c)^{1/3} + (V_2^c)^{1/3}]^3) \quad (4)$$

This is illustrated in Figure 2 for various binary mixtures containing ethane. It is seen that, within experi-

(25) D. Cook and J. S. Rowlinson, *Proc. Roy. Soc., Ser. A*, **219**, 405 (1953).

(26) J. S. Rowlinson, *Trans. Faraday Soc.*, **50**, 647 (1954).

(27) A. D. King, Jr., *J. Chem. Phys.*, **49**, 4083 (1968).

(28) H. Bradley, Jr., and A. D. King, Jr., *ibid.*, **52**, 2851 (1970).

(29) G. C. Najour and A. D. King, Jr., *ibid.*, **52**, 5206 (1970).

(30) S. Gupta and A. D. King, Jr., *Can. J. Chem.*, **50**, 660 (1972).

(31) E. A. Guggenheim and M. L. McGlashan, *Proc. Roy. Soc., Ser. A*, **206**, 448 (1951).

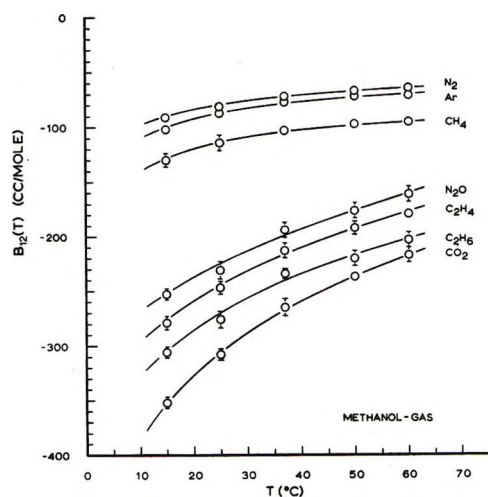


Figure 1. Second cross virial coefficients of methanol with N_2 , Ar, CH_4 , N_2O , C_2H_4 , C_2H_6 , and CO_2 .

Table III: Critical Constants and Molecular Parameters

Substance	$T^c, ^\circ K^a$	$V^c, cm^3/mol$	$\alpha \times 10^{28}, cm^3 b$	Av polarizability, $\alpha \times 10^{28}, cm^3 b$	Quadrupole moment, $\theta \times 10^{26}, esu cm^2 c$
N_2	126.15	90.1	17.6		-1.52
Ar	151.15	75.3	16.3		
CH_4	190.55	99	26.0		
C_2H_4	282.36	129	42.6		+1.5
C_2H_6	305.43	148	44.7		-0.65
CO_2	304.19 (241)	94.0 (108)	26.5		-4.3
N_2O	310 (277)	97.9 (104)	30.0		-3.0
CH_3OH	512.58	118	32.2		

^a Critical constant data taken from A. P. Kudchadker, *et al.*, *Chem. Rev.*, **68**, 659 (1968), and from K. A. Kobe and R. E. Lynn, *ibid.*, **52**, 117 (1953). ^b Data taken from H. A. Landolt and R. Börnstein, "Zahlenwerte und Funktionen," Vol. 1, 6th ed, Springer, Berlin, 1951; Part 1, p 401; Part 2, p 509. ^c Recommended values from D. E. Stogryn and A. P. Stogryn, *Mol. Phys.*, **24**, 1002 (1956). Ethylene is assumed to be axially symmetric.

mental error, second cross virial coefficients reduced using eq 3 and 4 describe the same curve as the reduced coefficients of the pure component gases. More importantly, the cross virial coefficients involving CO_2 conform well with the principle of corresponding states when the modified critical constants in Table III are used in conjunction with eq 3 and 4. Since molecules of ethane are isoelectronic and structurally similar to those of methanol, the excellent correlation found in Figure 2 not only gives one confidence that the modified critical constants of Table III are appropriate reducing parameters for mixed systems involving the quadrupolar gases with methanol but also suggests that the second cross virial coefficients of methanol with CO_2 are in fact anomalously large in comparison with magnitudes expected if physical forces alone were operative. The large difference between cross virial coefficients of

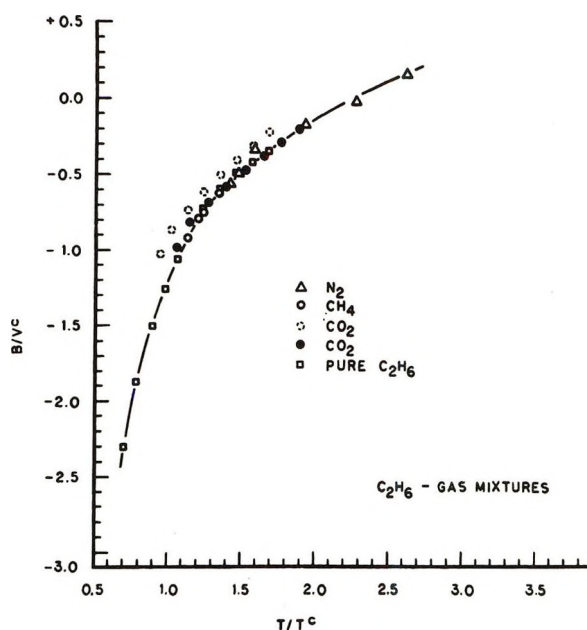


Figure 2. Reduced second cross virial coefficients of ethane with various gases shown as a function of reduced temperature. Ethane- CO_2 data reduced using experimental critical constants are indicated by broken circles. Solid circles denote the same data reduced using critical constants for CO_2 which have been modified to exclude effects of quadrupolar interactions.

methanol with N_2O and those with CO_2 precludes one from attributing any such anomaly to dipole-quadrupole forces since molecules of N_2O and CO_2 have quite similar quadrupole moments as well as polarizabilities.

The difference in behavior of methanol vapor with CO_2 is illustrated dramatically in Figure 3, where the cross virial coefficients involving methanol are shown after having been reduced with critical constants derived from eq 3 and 4 using the modified critical constants for CO_2 and N_2O . It is seen that, with the exception of CO_2 , the reduced methanol-gas virial coefficients correlate well in describing a single function of reduced temperature. While the increased scatter of this data as compared to that of Figure 2 is undoubtedly a reflection of the larger errors associated with the cross virial coefficients measured for the methanol-gas systems, some of this scatter may be caused by dipole-induced dipole, quadrupole-induced dipole, and dipole-quadrupole forces, whose magnitudes would be expected to vary one system to the next. However, it is well established experimentally³² that for mixed systems such contributions are generally quite small in comparison with dispersion force contributions over the temperature ranges encountered here. Estimates using equations³³ based on earlier derivations by Pople³⁴ predict that such interactions should contribute between -8 and -14 cm^3/mol to the total value of the in-

(32) D. H. Knoebel and W. C. Edmister, *J. Chem. Eng. Data*, **13**, 312 (1968).

(33) S. Kielich, *Acta Phys. Pol.*, **20**, 433 (1961).

(34) J. A. Pople, *Proc. Roy. Soc., Ser. A*, **221**, 508 (1954).

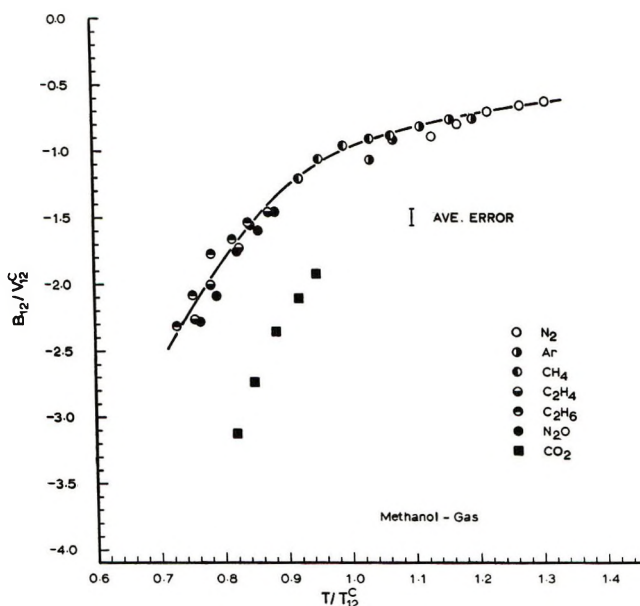


Figure 3. Reduced second cross virial coefficients for methanol-gas systems shown as a function of reduced temperature. Critical constants modified to exclude quadrupolar effects are used for N_2O and CO_2 .

dividual cross virial coefficients. On a reduced basis, this amounts to about 0.1 unit, which is of the order of average experimental error among the data in Figure 3. Thus it can be reasonably assumed that the upper curve of Figure 3 accurately describes the reduced behavior of second cross virial coefficients of methanol-gas mixtures which interact by virtue of physical forces. It follows, therefore, that the discrepancy of the CO_2 must be explained on the basis of chemical interactions.

There are three possible modes of chemical association that can be invoked to explain these data. The first involves hydrogen bonding, with methanol being the proton donor and the carbonyl oxygens of CO_2 acting as acceptor sites. There are several lines of evidence that argue against this explanation, however, the two strongest being (a) that low-temperature infrared spectra of carbon dioxide films containing water do not reveal any structure that cannot be assigned to vibrations of crystalline CO_2 or water present in monomeric and dimeric forms³⁵ and (b) that chloroform, a relatively good proton donor with carbonyl group acceptors,³⁶ does not exhibit enhanced solubility in compressed CO_2 .³⁷

An alternative explanation is that a reversible esterification reaction is taking place in the gas phase, producing the monomethyl ester of carbonic acid. Uncatalyzed reactions between simple alcohols and acid anhydrides in the condensed phase are quite general.³⁸ This particular reaction has been investigated in detail by Faurholt,³⁹ who not only pointed out that reactions between CO_2 and water-free methanol are analogous to those of CO_2 and water-forming carbonic acid, but also estimated the equilibrium ratio of the methyl ester to

CO_2 to be $a_{CH_3OCOOH}/a_{CO_2} = 10^{-2}$ at 18° . This is only slightly larger than that for carbonic acid, $a_{H_2CO_3}/a_{CO_2} = 1-3 \times 10^{-3}$.⁴⁰ Furthermore, reactions closely resembling those above, between alcohols and formaldehyde to form hemiacetals, are known to occur in the vapor phase.⁴¹

Finally, the possibility exists that methanol and CO_2 combine to form simple donor-acceptor complexes in the gas phase, with methanol being the electron donor and CO_2 the Lewis acid acceptor. Many reactions of this type involving alcohols can be cited; for example, the well-known complexes of alcohols with iodine.⁴² Similarly, the unusually large solubility of solid CO_2 in unsaturated hydrocarbons has been explained in terms of complexation involving π donation by unsaturated compounds towards CO_2 .⁴³

Lambert, Rowlinson, and coworkers⁴⁴⁻⁴⁶ have shown that for gaseous systems in which weak chemical bonding is present in addition to the usual physical interactions, the resulting association can be treated from a mass action standpoint, allowing the second virial coefficient for such a system to be expressed as a sum of two terms, describing the physical and chemical contributions to nonideality separately. For weakly associated binary systems, the expression for the second cross virial coefficient becomes

$$B_{12}(T) = B_{12}(T)_{phys} - RT/2K_P \quad (5)$$

where $B_{12}(T)_{phys}$ represents deviations from ideality caused by physical forces and K_P is the equilibrium constant describing, in this case, the dissociation of the methanol- CO_2 adduct into its two components, CO_2 and methanol

$$K_P = P_{CH_3OH}P_{CO_2}/P_{CH_3OCOOH}$$

When eq 5 is written in reduced form, it becomes

$$B_{12}(T)/V_{12}^c = B_{12}(T)_{phys}/V_{12}^c - (RT_{12}^c/2V_{12}^c)(T/T_{12}^c)(1/K_P)$$

Thus it is seen that values of K_P are readily evaluated

(35) M. E. Jacox and D. E. Milligan, *Spectrochim. Acta*, **17**, 1196 (1961).

(36) G. C. Pimentel and A. L. McClellan, "The Hydrogen Bond," W. H. Freeman, San Francisco, Calif., 1960, p 197.

(37) Unpublished data from this laboratory.

(38) E. E. Royals, "Advanced Organic Chemistry," Prentice-Hall, Englewood Cliffs, N. J., 1954, p 605.

(39) C. Faurholt, *Z. Phys. Chem.*, **126**, 227 (1927).

(40) D. M. Kern, *J. Chem. Educ.*, **37**, 14 (1960).

(41) M. W. Hall and E. L. Piret, *Ind. Eng. Chem.*, **41**, 1277 (1949).

(42) G. Briegleb, "Elektronen-Donator-Acceptor-Komplexe," Springer-Verlag, Berlin, 1961.

(43) J. H. Hildebrand, J. M. Prausnitz, and R. L. Scott, "Regular and Related Solutions," Van Nostrand-Reinhold, Princeton, N. J., 1970, p 163.

(44) E. A. Alexander and J. D. Lambert, *Trans. Faraday Soc.*, **37**, 421 (1941).

(45) J. D. Lambert, G. A. H. Roberts, J. S. Rowlinson, and V. J. Rowlinson, *Proc. Roy. Soc., Ser. A*, **196**, 113 (1949).

(46) J. S. Rowlinson, *Trans. Faraday Soc.*, **45**, 974 (1949).

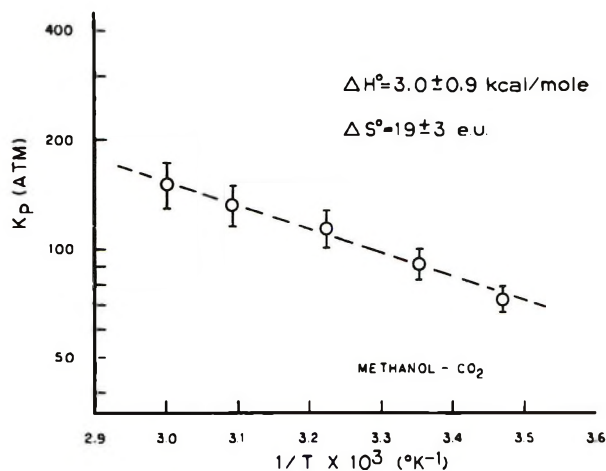


Figure 4. Equilibrium constants for dissociation of the methanol-CO₂ adduct plotted logarithmically as a function of reciprocal temperature.

from the data of Figure 3 by identifying $B_{12}(T)_{\text{phys}}/V_{12}$ with reduced cross coefficients corresponding to physical interactions (upper curve) and $B_{12}(T)/V_{12}^{\circ}$ with the lower curve for CO₂ with methanol. Using $V_{12}^{\circ} = 113/\text{mol}$ and $T_{12}^{\circ} = 351^{\circ}\text{K}$, one obtains values for K_p of 73 ± 6 , 91 ± 9 , 114 ± 14 , 132 ± 18 , and 151 ± 23 atm at 15, 25, 37, 50, and 60° , respectively. These equilibrium constants are shown plotted logarithmically as a function of reciprocal temperature in Figure 4. The standard enthalpy and entropy of dissociation (standard state of 1 atm, 298°K) corresponding to the K_p are

$$\Delta H^{\circ} = 3.0 \pm 0.9 \text{ kcal mol}^{-1}$$

$$\Delta S^{\circ} = 19 \pm 3 \text{ eu}$$

These data, when combined with tabulated heats of formation and entropies of the reactants,⁴⁷ yield the following values for the standard heat of formation and third-law entropy of the adduct at 298°K

$$\Delta H_f^{\circ} = -145.1 \pm 0.9 \text{ kcal mol}^{-1}$$

$$S^{\circ} = 89 \pm 3 \text{ eu}$$

A comparison of the experimental heat of formation with estimates based on the assumption of group additivity⁴⁸ lends support to assigning this adduct as being the monomethyl ester of carbonic acid, since the standard heat of formation estimated in this manner, $\Delta H_f^{\circ} = -145.1 \text{ kcal mol}^{-1}$, agrees exactly with that found experimentally. On the other hand, the third-law entropy estimated under the same assumption, $S^{\circ} = 76 \text{ eu}$, is considerably smaller than the value derived from the experimental data. However, this latter discrepancy of 13 eu may represent an error inherent in the group approximation for entropies of these compounds. For example, S° estimated for the closely related compound, methyl formate, is smaller than the experimental value by 12 eu.⁴⁸

Finally, in comparing these results with those obtained earlier for various gas-water systems,² one finds that the equilibrium constants for the vapor-phase methanol-CO₂ adducts are substantially the same as those for the water vapor-CO₂ system, just as was found for the corresponding quantities in the liquid phase. Nitrous oxide, on the other hand, differs markedly in its chemical reactivity toward methanol and water. The results here indicate that N₂O is totally unreactive toward methanol in the gas phase, while the extent of reaction of N₂O with water vapor was significant. At present we can venture no explanation for this difference in the vapor-phase behavior of CO₂ and N₂O.

(47) "Selected Values of Thermodynamic Properties," National Bureau of Standards Circular 500, U. S. Government Printing Office, Washington, D. C., 1952.

(48) S. W. Benson, *et al.*, *Chem. Rev.*, **69**, 279 (1969). In these calculations it is assumed that the contribution of the carbonyl group bound to two oxygen atoms is the same as that in esters of carboxylic acids.

Thermodynamic Parameters for the Cyclooctatetraene Anion Radical

Disproportionation as a Function of Ion Pairing in Hexamethylphosphoramide

by Gerald R. Stevenson* and Jesus Gilberto Concepción

University of Puerto Rico, Rio Piedras, Puerto Rico 00981 (Received February 4, 1972)

Publication costs assisted by the University of Puerto Rico

The thermodynamic parameters controlling the cyclooctatetraene anion radical, dianion, neutral molecule disproportionation equilibrium constant have been studied in hexamethylphosphoramide. It has been observed that K_{eq} varies with the counterion, and this has been attributed to the entropy and not the enthalpy term. The thermodynamic parameters show that the potassium cation is not solvated as well as the sodium cation by hexamethylphosphoramide. This is the first report of ion pairing for hydrocarbon anion radicals in hexamethylphosphoramide.

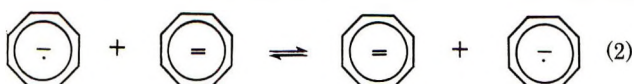
Electron spin resonance (esr) spectral parameters for organic anion radical solutions are strongly influenced by ion pairing.¹ Conductivity measurements carried out on these solutions also are often indicative of ion pairing.² However, when the esr spectral parameters (coupling constants and line widths) are independent of gegenion and there is no evidence for ion pairing in conductivity measurements, the ions involved are considered to be free ions or fully dissociated ions. Hydrocarbon anion radicals are considered to be fully dissociated in hexamethylphosphoramide (HMPA),³ since HMPA has been recognized to be the most powerful solvating agent for alkali metal ions.^{3,4}

Thermodynamic parameters controlling reaction equilibria and activation parameters controlling reaction kinetics might be more sensitive functions of ion pairing than esr parameters or conductivities. The equilibrium constant for the cyclooctatetraene (COT) anion radical disproportionation reaction (eq 1) has been quan-



titatively observed in tetrahydrofuran⁵ and liquid ammonia.⁶ In the latter solvent the equilibrium constant was found to vary by a factor of a million with the alkali metal. Here we report the equilibrium constants and the thermodynamic parameters controlling the disproportionation equilibrium (eq 1) as a function of counterion in HMPA to determine if hydrocarbon anion radicals in HMPA are really free ions or if esr parameters are simply too insensitive to detect weakly associated ions.

The energies of activation and the rate constants for the electron transfer reaction between the dianion and anion radical (eq 2) have also been investigated for



several COT-HMPA-metal systems.

Experimental Section

X-Band esr spectra were recorded using a Varian E-3 esr spectrometer. The temperature was controlled using a Varian V-4557 variable temperature controller. Nmr spectra were recorded at room temperature using a Varian T-60 spectrometer. Line widths of the nmr line at half-height due to electron transfer were determined from the measured line width minus the line width of the dianion in the absence of anion radical.

The HMPA was dried with potassium metal in bulb b (Figure 1) and was distilled into bulb a which contained a known amount of alkali metal. This distillation was carried out at 10^{-4} mm of Hg, and bulb a was kept in a Dry Ice-acetone bath (-78°). A weighed portion of degassed COT was then distilled into bulb a from the vacuum line. With both stopcocks closed the mixture in bulb a was allowed to warm to room temperature, and the alkali metal dissolved to form the COT dianion and anion radical. Nmr and esr samples of this solution were made by taking an aliquot of the solution into the side arm (c). The anion radical concentration was determined using the system COT-THF-Li as a spin concentration standard as previously described.⁶

Results

Solutions of COT in HMPA will dissolve small amounts of alkali metals to form the COT dianion and

(1) (a) N. Hirota, *J. Phys. Chem.*, **71**, 127 (1967); (b) M. C. R. Symons, *ibid.*, **71**, 172 (1967); (c) N. Hirota, *J. Amer. Chem. Soc.*, **89**, 32 (1967).

(2) (a) E. Grunwald, *Anal. Chem.*, **26**, 1696 (1954); (b) S. Winstein, E. Clippinger, A. H. Fainberg, and G. C. Robinson, *J. Amer. Chem. Soc.*, **76**, 2597 (1954).

(3) G. Levin, J. Jagur-Grodzinski, and M. Szwarc, *ibid.*, **90**, 6421 (1968).

(4) H. Normant, *Angew. Chem., Int. Ed. Engl.*, **6**, 1046 (1967).

(5) H. L. Strauss, T. J. Katz, and G. K. Fraenkel, *J. Amer. Chem. Soc.*, **85**, 2360 (1963).

(6) F. J. Smentowski and G. R. Stevenson, *J. Phys. Chem.*, **73**, 340 (1969).

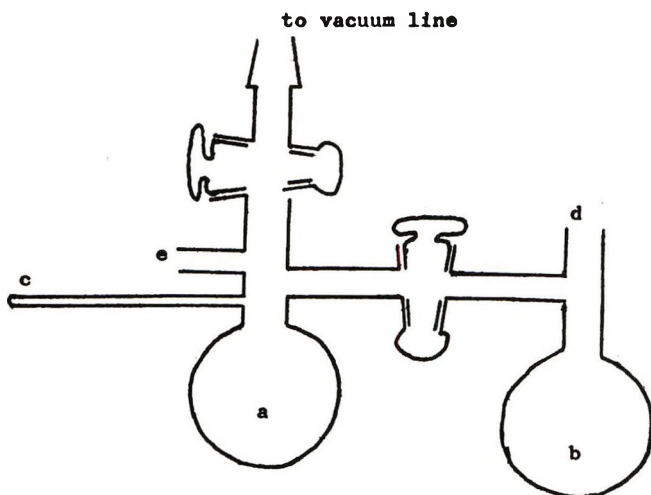


Figure 1. High-vacuum apparatus for reducing COT in HMPA. Inlets e and d allow addition of the alkali metal; they are subsequently sealed off.

anion radical. These solutions yield the expected nine-line esr pattern for the COT anion radical. The proton coupling constant of 3.18 ± 0.01 G is independent of the alkali metal used (K, Na, or Li).

The disproportionation equilibrium constant is a function of the alkali metal counterion. For the systems COT-HMPA-Li, COT-HMPA-Na, and COT-HMPA-K the equilibrium constants are 5×10^{-4} , 2×10^{-3} , and 2×10^{-5} , respectively. It is surprising that the value for sodium does not lie between those for lithium and potassium. Rieger, *et al.*,⁷ have shown that ion pairing shifts the disproportionation equilibrium to the left (eq 1). Since the value for sodium is larger than that for the other two metals, the sodium ion must be better solvated in HMPA. There is less ion pairing for the sodium reduction than for either the potassium or lithium reduction.

Assuming a Lorentzian line shape, the anion radical concentration is proportional to the esr peak height (I) times the square of the extrema to extrema line width (Δw). The equilibrium constant can then be expressed as shown in eq 3, where B is simply a proportionality

$$K = \frac{(BI\Delta w^2)^2}{\left[\text{COT}^- \right] \left[\text{COT} \right]} \quad (3)$$

constant. A simple revised van't Hoff plot of $\ln(I\Delta w^2)$ vs. $1/RT$ should yield a straight line with a slope of $-\Delta H^\circ/2$ (Figure 2). For all three systems a straight line was obtained. The corresponding thermodynamic parameters are shown in Table I.

From Table I it is clear that the variance of K_{eq} with counterion is mainly due to the entropy and not the enthalpy term. Comparing the systems COT-HMPA-K and COT-HMPA-Na, we see that the enthalpies are almost identical, but the entropies differ by 20 entropy

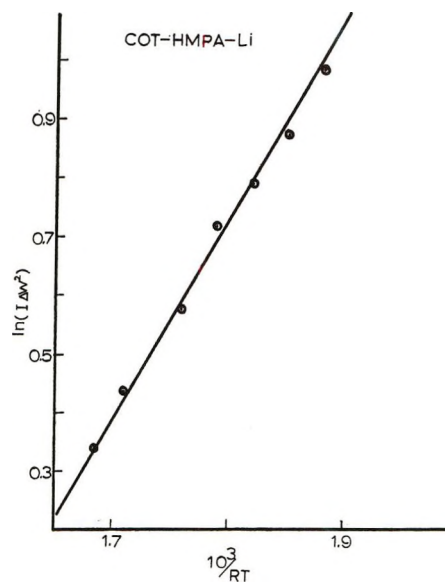


Figure 2. Plot of $\ln(I\Delta w^2)$ vs. $10^3/RT$ for the system COT-HMPA-Li.

Table I: Thermodynamic Parameters for the COT Disproportionation Equilibrium in HMPA at 25°

Metal	ΔG° , kcal/mol	ΔH° , kcal/mol	ΔS° , cal/deg mol	K_{eq}
Li	4.5 ± 0.3^a	-7.8 ± 1	-29 ± 2	$(5.0 \pm 2) \times 10^{-4}$
Na	3.6 ± 0.3	-4.2 ± 0.3	-26 ± 1	$(2.3 \pm 1) \times 10^{-3}$
K	6.3 ± 0.2	-4.6 ± 0.7	-46 ± 1	$(2.3 \pm 1) \times 10^{-5}$

^a All errors are standard deviations.

units. The entropy term for the sodium reduction is larger than for either of the other two systems. This indicates that the sodium ion does not associate with the dianion and anion radical as strongly as does the potassium ion. The equilibrium constants indicate that ion pairing follows the order: K > Li > Na.

When two moles of potassium react with one mole of COT in HMPA, no esr signal is obtained, but this solution gives a sharp singlet upon nmr analysis at 5.9 ppm due to the dianion. Addition of small amounts of COT neutral molecule broadens the dianion line. The rate constant for the electron transfer (eq 2) can be estimated with the use of eq 4, where $\delta\omega$ is the esr

$$2\pi\Delta\nu = \frac{k\delta\omega \left[\text{COT}^- \right]}{\delta\omega^2 + k \left[\text{COT} \right]} \quad (4)$$

hyperfine splitting constant in radians per second,

(7) R. D. Allendolfer and P. H. Rieger, *J. Amer. Chem. Soc.*, **87**, 2336 (1965).

$\Delta\nu$ is the half-height line width due to electron transfer, and k is the second-order rate constant.⁸

The rate constant for the system COT-HMPA-K is about 10^4 l./mol sec. This is a very slow electron transfer relative to the values found in liquid ammonia⁹ and for the system COT-THF-K,⁵ all of which have a rate constant greater than 10^8 . The slow rate of electron transfer for the HMPA system is presumably due to the relatively high viscosity of this solvent.

The energies of activation for all three systems were obtained from a plot of $\ln(w)$ vs. $1/RT$ ¹⁰ and are 0.92 ± 0.03 , 1.2 ± 0.1 , and 1.51 ± 0.1 kcal/mol for the systems COT-HMPA-Li, COT-HMPA-Na, and COT-HMPA-K, respectively.

Conclusions

The disproportionation equilibrium constants for the COT-solvent-metal systems are a very sensitive

function of metal ion association. Ion association has been found even in HMPA where only free ions were thought to exist. No set of esr spectral parameters or conductivity measurements has been able to detect this ion association of cation and hydrocarbon anion radical in HMPA. Further, small differences in the energies of activation for the electron transfer reactions have been observed as a function of the counterion.

Acknowledgments. The authors gratefully acknowledge support of this work by Research Corporation. We wish to thank Dr. Luis Lizardi for helpful discussion.

(8) T. J. Katz and G. K. Fraenkel, *J. Amer. Chem. Soc.*, **82**, 3784, 3785 (1960).

(9) F. J. Smentowski and G. R. Stevenson, *ibid.*, **91**, 7401 (1969).

(10) F. J. Smentowski and G. R. Stevenson, *ibid.*, **89**, 5120 (1967).

The Barrier to Internal Rotation in Amides. IV. *N,N*-Dimethylamides;

Substituent and Solvent Effects

by Torbjörn Drakenberg,* Kjell-Ivar Dahlqvist, and Sture Forsén

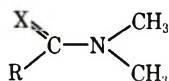
Division of Physical Chemistry, The Lund Institute of Technology, Chemical Center, P.O.B. 740, S-220 07 Lund 7, Sweden (Received November 17, 1971)

Publication costs assisted by The Lund Institute of Technology

Activation parameters for internal rotation about the N-CO bond in several *N,N*-dimethylalkylamides, in various solvents, have been determined by the pmr total line shape technique. The effect on the torsional barrier of variations in the alkyl group as well as the solvent have been found to be significant; the origin of these effects is discussed. Additionally, the results of extended Hückel theory calculations of the N-CO torsional barrier are presented.

Introduction

The hindered internal rotation of the dimethylamino group in substituted amides ($X = O$) and thioamides ($X = S$) has been shown by nuclear magnetic resonance (nmr) spectroscopy to be strongly dependent on



the nature of the substituent, R.^{1,2} Thus, the magnitude of the torsional barrier is found to be lowered when R is electron donating (for example, CH_3O- , CH_3S- , or $R-C=C-$) and raised when R is electron withdrawing (for example, $N\equiv C-$ or $EtCO-$).

For *N,N*-dimethylamides the major influence of R,

where R is an alkyl group such as CH_3- , CH_3CH_2- , $(CH_3)_2CH-$, or $(CH_3)_3C-$, on torsion about the N-C(O) bond may be assumed to arise from the following interactions: inductive, steric, and hyperconjugative. Relative to *N,N*-dimethylformamide, each of these effects is expected to lower the amide rotational barrier. Inductive and steric influences increase while hyperconjugative influences decrease, in the order: CH_3- , CH_3CH_2- , $(CH_3)_2CH-$, $(CH_3)_3C-$.

The purpose of the present work was to study quantitatively the influence of various alkyl groups, and addi-

(1) C. W. Fryer, F. Conti, and C. Franconi, *Ric. Sci., Parte 2, Sez. A*, **35**, 788 (1965).

(2) J. Sandström, *J. Phys. Chem.*, **71**, 3218 (1967).

tionally, solvents, on the activation parameters for the hindered internal rotation of the dimethylamino group. To obtain activation parameters of sufficient accuracy to draw reliable conclusions about the influence of the substituent R on the N-C(O) torsional barrier, kinetic data were evaluated from the exchange-broadened nmr signals of the dimethylamino protons of the various amides utilizing an iterative computer fitting of theoretical to experimental digitized spectra.

Experimental Section

Materials. *N,N*-Dimethylformamide (DMF) and *N,N*-dimethylacetamide (DMA) were of commercial quality (Fluka AG, Switzerland) and distilled prior to use. The *N,N*-dimethylpropionamide (DMP) and *N,N*-dimethylpivaloylamide (DMPiv) were prepared by reaction of the corresponding acid chloride with dimethylamine and purified by fractional distillation. The boiling points of these compounds were in agreement with literature values. Deuterated *N,N*-dimethylisobutyramide-*d*₁, (CH₃)₂CDCON(CH₃)₂ (DMiBu) was the generous gift of Dr. R. E. Carter of this Institute; a deuterated compound was necessary since the methine and *N*-methyl proton signals overlapped. The solvents, acetone-*d*₆, decalin, hexane, C₂Cl₄, and D₂O, were of commercial quality and used without further purification. [Since it has been observed that the torsional barrier in amides is sensitive to trace acids we have, as a control, prepared samples using freshly purified solvents (C₂Cl₄ and C₆H₁₂). The coalescence temperature was found to be unchanged.]

The sample solutions were prepared directly in 5-mm nmr tubes. The sample compositions are given in Tables I and III. A small amount of TMS was added to each sample.

Instruments. The nmr spectra were recorded on a Varian A-60A spectrometer equipped with a variable temperature probe and a V-6040 temperature controller.

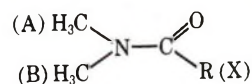
The shifts were measured by means of the side-band technique using a Hewlett-Packard audiofrequency oscillator Model 202 and a Hewlett-Packard frequency counter Model 5512. The rf field was kept sufficiently low so as to prevent saturation of the signals; sweep rates of 0.05, 0.1, and 0.2 Hz/sec were used. A scale expansion of 1 Hz/cm was used for all amides investigated except for DMPiv, for which a scale expansion of 2 Hz/cm was employed. The calibration of the scale expansion was frequently checked by the side-band technique.

Temperature Measurements. The sample temperatures for all compounds studied except DMPiv were obtained from the temperature-dependent chemical shift difference of the CH₃- and OH signals of a methanol-water mixture (molar ratio 1:2) placed in a sealed capillary centered in the sample tube.³ For DMPiv the exchange broadening of the N(CH₃)₂ signals coincided with exchange broadening of the CH₃ and OH signals of the internal methanol-water thermometer, thus preventing accurate temperature measurements near coalescence. A capillary filled with pure methanol was therefore used as the internal thermometer. Both internal thermometers were calibrated in separate experiments against a copper-constantan thermocouple as previously described.³ The temperatures thus obtained are estimated to be accurate to ±0.4°.

Evaluation of the Rate Parameters

The rate of rotation around the N-C(O) bond in the amides of this study was obtained at appropriate temperature intervals by a complete line shape analysis of the exchange-broadened dimethylamino signals, employing a computerized fitting of theoretical to experimental spectra as described in detail in an earlier paper.³ The iterative computer program used in the fitting procedure was based on Chandler's iterative subroutine, STEFIT. [This subroutine has been developed by J. P. Chandler, Physics Department, Indiana University, and is available through the Quantum Chemistry Program Exchange.]

For DMF, DMA, and DMP long-range couplings between the *N*-methyl protons and those of the substituent R were observed; the line shape equation derived from the McConnell relations was therefore modified to accommodate this coupling. The coupling constants, *J*_{AX} and *J*_{BX} (see below), were determined



by analysis of the dimethylamino signals in the slow-exchange limit (see Table I). Values of the coupling constants found at the fast exchange limit were, in all cases, the mean of the low temperature values. With

Table I: The Chemical Shift Difference between the CH₃-N Signals, Δν, and the Coupling Constants between the CH₃-N and R-Group Protons

Compound	Δν, Hz		<i>J</i> _{trans} , Hz	<i>J</i> _{cis} , Hz
	At <i>T</i> _c - 5°	At <i>T</i> _c - 50°		
Neat DMF	8.7	9.4	0.8	0.5
DMF in C ₂ Cl ₄ ^a	5.4	6.2	0.5	0.3
DMF in decalin ^a	4.3	4.9	0.5	0.3
Neat DMA	10.4	10.7	0.5	0.2
DMA in acetone ^a	10.0	10.5	0.5	0.1
DMA in water ^a	9.3	9.6	1.1	0.4
Neat DMP	8.9	9.1	0.5	0.0
DMP in acetone ^a	8.8	8.6	0.5	...
Neat DMiBu- <i>d</i> ₁	12.6	13.4
DMiBu in acetone ^a	12.2	13.0
DMPiv in acetone ^a	20.1	20.5 ^b

^a 10 mol % amide. ^b Measured at *T*_c - 20°.

(3) T. Drakenberg, K.-I. Dahlqvist, and S. Forsén, *Acta Chem. Scand.*, **24**, 694 (1970).

Table II: The Activation Parameters for the Hindered Internal Rotation in Some Amides^a

Amide	E_a , kcal/mol	ΔF^\ddagger_{298} , kcal/mol	ΔH^\ddagger , kcal/mol	ΔS^\ddagger , cal/mol K	T_c , °C
Formamide ^b	19.2 ± 0.2	17.8 ± 0.1	18.5 ± 0.1	2.7 ± 1	
Neat DMF	21.3 ± 0.1	20.9 ± 0.1	20.5 ± 0.1	-1.4 ± 1	119
Neat DMF ^c	20.5	21.0	20.2	-1.7	119
DMF in C ₂ Cl ₄	21.6 ± 0.3	20.7 ± 0.1	20.8 ± 0.3	0.4 ± 2	109
DMF in decalin	20.4 ± 0.3	20.3 ± 0.1	19.6 ± 0.3	-2.4 ± 2	100
Neat DMA	19.0 ± 0.1	18.1 ± 0.1	18.3 ± 0.1	0.7 ± 1	69
Neat DMA- <i>d</i> ₃ ^d	19.6	18.2	19.0	2.7	69
DMA in acetone	19.6 ± 0.3	18.0 ± 0.1	19.0 ± 0.3	3.1 ± 2	66
DMA in water	19.8 ± 0.1	19.3 ± 0.1	19.1 ± 0.1	-0.8 ± 1	91
Neat DMP	16.6 ± 0.1	17.2 ± 0.1	16.0 ± 0.1	-4.1 ± 1	53
DMP in acetone	16.1 ± 0.2	17.0 ± 0.1	15.4 ± 0.2	-5.3 ± 2	50
Neat DMiBu	16.4 ± 0.4	16.5 ± 0.1	15.8 ± 0.4	-2.4 ± 2	45
DMiBu in acetone	16.4 ± 0.2	16.5 ± 0.1	15.7 ± 0.2	-2.5 ± 1	43
DMPiv in acetone	11.6 ± 0.1	11.5 ± 0.1	11.2 ± 0.1	-1.0 ± 1	-50
DMPiv in methylene chloride ^e	11.5	12.2	10.9	-4.3	-40

^a The errors, as given here, represent a 90% confidence interval in the least-squares deviation calculations. ^b From T. Drakenberg and S. Forsén, *J. Phys. Chem.*, **74**, 1 (1970). ^c From ref 7, ΔF^\ddagger determined at 401 K. ^d From ref 8. ^e From ref 9.

Table III: Activation Parameters for Internal Rotation in DMA (DMA-*d*₃) in Different Solvents^a

Solvent	Amide mol %	ΔH^\ddagger	ΔS^\ddagger	ΔF^\ddagger_{298}	ΔF^\ddagger_{343}	E_a	T_c , °C
Neat	100	18.3	0.7	18.1	18.1	19.0	69
Neat ^b	100	19.0	2.7	18.2	18.1	19.6	69
Acetone- <i>d</i> ₆	10	19.0	3.2	18.0	17.9	19.6	66
DMSO- <i>d</i> ₆ ^b	9.5	20.0	4.7	18.6	18.4	20.6	73
D ₂ O ^c		20.3	2.7	...	19.3	21.0	...
D ₂ O	10	19.1	-0.8	19.31	19.36	19.8	91
Formamide ^d	9.9	20.3	~3	19.3	19.2	20.9	...
Cyclohexane ^e	10	17.1	...	47.1
Cyclohexane ^e	5	17.0	...	46.0
Cyclohexane ^e	1	16.8	...	37.7

^a Energies in kcal/mol. ^b DMA-*d*₃, ref 8. ^c DMA-*d*₃, P. A. Temussi, T. Tancredi, and F. Quadrifoglio, *J. Phys. Chem.*, **73**, 4227 (1969). ^d DMA-*d*₃, R. C. Neuman, Jr., and V. Jonas, *J. Amer. Chem. Soc.*, **90**, 1970 (1968). ^e ΔF^\ddagger evaluated only at the coalescence temperature, using τ values from the equation $\tau = \sqrt{2}/\pi \cdot \delta\nu$.

the exception of DMPiv the chemical shift difference ($\Delta\nu_{AB}$) between the *N*-methyl signals was studied from a temperature of at least 50° below the coalescence temperature (T_c) to approximately 5° below T_c . In the slow exchange region, $\Delta\nu_{AB}$ was obtained directly from the frequency separation of the pertinent signals, while in the exchange-broadened region below T_c , $\Delta\nu_{AB}$ was determined in the line shape analysis procedure. For all amides of this study the value of $\Delta\nu_{AB}$ was found to decrease slightly with increasing temperature. Since the temperature dependence of $\Delta\nu_{AB}$ was reasonably linear, $\Delta\nu_{AB}$ at T_c and higher temperatures was determined by linear extrapolation. Values of $\Delta\nu_{AB}$ at $T_c - 5^\circ$ and $T_c - 50^\circ$ are given in Table I. The effective spin-spin relaxation time, T_2^{eff} , was determined at both the slow and fast exchange limits. When differing values of T_2^{eff} were ob-

tained at these limits, values of T_2^{eff} at intermediate temperatures were determined by linear interpolation.

The experimental rate data have been used in conjunction with the Arrhenius equation in the form

$$\ln(1/\tau) = -E_a/RT + \ln A \quad (1)$$

to calculate E_a (see column 2, Table II), and the Eyring equation (assuming a transmission coefficient of unity) in the form

$$\ln(1/\tau T) = -\Delta F^\ddagger/RT + \ln(k/h) = -\Delta H^\ddagger/RT + \Delta S^\ddagger/R + \ln(k/h) \quad (2)$$

to calculate ΔF^\ddagger , ΔH^\ddagger , and ΔS^\ddagger (Tables II and III). The error limits given in these tables assume only random errors. These errors for E_a , ΔH^\ddagger , and ΔS^\ddagger are most likely too small,³ more realistic limits being ± 0.7

kcal/mol for E_a and ΔH^\ddagger and ± 3 cal/mol K for ΔS^\ddagger . The free energy of activation, however, when evaluated near coalescence, is found to be quite insensitive to systematic errors, and, as a result, the error for ΔF^\ddagger may be assumed to be determined only by statistical random errors.

Extended Hückel Calculations

The barrier to internal rotation about the N-C(O) bond in amides has been calculated using extended Hückel theory.⁴ Two sets of input parameters for the Coulomb integrals, *A* and *B*, have been used; set *A* was obtained from Herman and Manne,⁵ set *B* from Scheraga, *et al.*⁴ (see Table IV). The Slater orbital exponents were identical in both sets (Table IV). The ground state geometry was taken to be that in which the NCO fragment and all the atoms directly bound to it form a plane; the transition state has been assumed to be that one in which the -COR fragment has been twisted out of this plane by 90°, a planar geometry about nitrogen being assumed. Bond distances are given in Table V. The four bond angles around the N-C(O) bond have been varied to obtain an energy minimum for both initial and transition states (see Table VI). The calculated values for the barrier to internal rotation are reported in Table VII. Attempts to minimize the total energy by varying the C=O and N-C(O) bond lengths, however, resulted in unrealistic values, greater than 1.45 Å for the C=O bond length in the ground state and 1.52 Å for the N-C(O) bond length in the transition state.

Table IV: Extended Hückel Input Parameters

Atom	Slater orbital exponent	Coulomb integrals				1s
		Set A		Set B		
		2s	2p	2s	2p	
C	1.625	-19.20	-11.79	-21.40	-11.40	...
N	1.950	-25.72	-15.44	-26.00	-13.40	...
O	2.275	-33.86	-17.19	-32.30	-14.80	...
H	1.000	13.6

Table V: Bond Distances Used in the Extended Hückel Calculations (in Å)

Bond	Distance
C-H	1.09
N-H	1.00
N-CH ₃	1.47
N-CO	1.32
C=O	1.24
C-C	1.53

Results and Discussion

The activation parameters for formamide and several *N,N*-dimethylamides, obtained by an nmr total line

shape method are presented in Tables II and III. The agreement between our data for neat DMF and DMA, respectively, and those obtained by Rabinovitz and Pines^{6,7} and by Neuman, *et al.*,⁸ for DMF and DMA, respectively, is quite good; however, there is a small discrepancy in ΔF^\ddagger between our data for DMPiv (acetone) and that of Graham and Diel⁹ (methylene chloride). This difference may be partly explained by the fact that both values are determined at a temperature far from T_c and partly by the fact that we have taken different routes for calculation. Graham and Diel⁹ calculated ΔF^\ddagger *via* the Arrhenius equation assuming a constant E_a , while we have assumed that ΔH^\ddagger and ΔS^\ddagger are constants calculated directly from a least-squares fit of $\ln(1/\tau T)$ vs. $1/T$. If we calculate ΔF^\ddagger at T_c using the Arrhenius activation parameters, the discrepancy is less than 0.2 kcal/mol.

Solvent Effects. Reliable data for the effect of various solvents on the barrier to internal rotation in amides are scarce. Rabinovitz and Pines^{6,7} have found that at a given temperature the internal rotation rate about the N-C(O) bond in DMF increases with increasing dilution of the amide in CCl₄; they propose that this variation is the result of a change in the amide-amide association equilibrium. The fact that the barrier decreases with increasing dilution indicates that the barrier in the monomer is lower than in the dimer (oligomer). However, this is most probably not the only effect of an inert solvent on the rotational barrier. We have found that there is a significant difference between the rotational barrier of DMF in C₂Cl₄ and decalin, namely, that the DMF barrier (ΔF^\ddagger_{373}) in decalin is *ca.* 0.2 kcal/mol lower than that in C₂Cl₄. Calsolari, *et al.*,¹⁰ have studied the barrier to internal rotation in DMF and DMA in a number of solvents and found that the barrier varies with solvent; unfortunately, their values, are, in our opinion, not of sufficient accuracy for a discussion of solvent effects. They have concluded, however, that from the variation of the chemical shifts of the *N*-methyl signals with temperature, in both a neat sample and in samples dissolved in ketones or ethers, that the ketone-amide and ether-amide interaction is of the same nature as the amide-amide interaction. This seems to be borne out in the present work at least for ketones, since the rota-

(4) J. Yan, F. Momany, R. Hoffman, and H. Scheraga, *J. Phys. Chem.*, **74**, 420 (1970).

(5) Z. S. Herman and R. Manne, Preliminary Research Report No. 224, Quantum Chemistry Group for Research in Atomic, Molecular and Solid-State Theory, Uppsala University, Uppsala, Sweden.

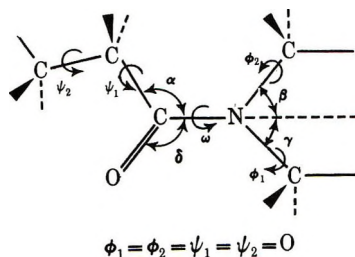
(6) M. Rabinovitz and A. Pines, *J. Chem. Soc. B*, 1110 (1968).

(7) M. Rabinovitz and A. Pines, *J. Amer. Chem. Soc.*, **91**, 1585 (1969).

(8) R. C. Neuman, Jr., W. R. Woolfenden, and V. Jonas, *J. Phys. Chem.*, **73**, 3177 (1969).

(9) L. L. Graham and R. E. Diel, *ibid.*, **73**, 2696 (1969).

(10) A. Calsolari, F. Conti, and C. Franconi, *J. Chem. Soc. B*, 55 (1970).

Table VI: Bond Angles as Obtained from Extended Hückel Calculations

	Formamide		DMF		DMA		DMP		DMiBu		DMPiv	
ω	0	90	0	90	0	90	0	90	0	90	0	90
α	124	125	124	125	128	125	126	123	126	125	126	121
β	60	60	58	60	56	60	55	60	56	60	51	60
γ	-60	-60	-58	-60	-61	-60	-60	-60	-59	-60	-63	-60
δ	-117	-117	-118	-117	-116	-117	-116	-117	-117	-117	-116	-116
ϕ_1	60	60	0	60	0	60	60	60	0	60
ϕ_2	60	60	60	60	60	60	0	60	60	60
ψ_1	0	60	0	0	60	60	0	0
ψ_2	0	0	0	0	0	0

Table VII: The Barrier to Internal Rotation in Amides as Calculated with an Extended Hückel Program^a

Parameter set	Formamide	DMF	DMA	DMP	DMiBu	DMPiv
A	15.57	21.13	14.61	14.55	13.36	6.68
B	20.66	26.45	18.93	18.63	17.94	11.92

^a Energy in kcal/mol.

tional barrier for neat DMA, DMP, and DMiBu is within 0.2 kcal/mol of the barrier for 10 mol % acetone solutions (Table II). From Table III it can be seen that the ketone–amide and the amide–amide interaction increases the barrier (ΔF^\ddagger) to internal rotation in DMA by more than 1 kcal/mol. A similar variation of the barrier with solvent has previously been observed in several α -haloacetanilides.¹¹ Siddall, *et al.*,¹² have studied the association between *N*-methyl-*N*-benzyl-*o*-chlorobenzamide and phenol in *o*-dichlorobenzene solution, and found that the rotational barrier increases with increasing phenol concentration, *ca.* 2.5 kcal/mol from a solution without phenol to one with excess of phenol. These authors¹² attempted to explain this observation with a simple model, assuming that phenol–amide association exists only in the initial state of the amide and that rotation proceeds either in the unassociated amide or with a simultaneous phenol–amide dissociation. With this model it was, however, not possible to explain the observed low entropy of activation. They therefore postulated that the phenol–amide interaction must be extended over domains larger than phenol amide pairs and that the internal rotation and rupture of one hydrogen bond will not seriously disturb the molecules in this domain.

When amides are dissolved in proton-donating solvents, a marked increase in the rotational barrier is observed (Table III) and is most likely due to hydrogen bonding to the amide oxygen. If the hydrogen bond is ruptured in the rotation about the amide bond, one should expect to find a large positive entropy of activation, which has not been obtained to date for amides, when a careful total line shape analysis has been used to determine the rate constants. To explain this nearly zero entropy of activation we have either to adopt the model proposed by Siddall, *et al.* (see above),¹² or to assume that the hydrogen bond is not broken in the internal rotation. The second model is the simpler, and we see no reason why it should be ruled out.

From the above, we conclude that the barrier to internal rotation in tertiary amides is sensitive, but not extremely so, to the solvent. Thus amide–amide associations in neat amides, as well as the amide–ketone associations in acetone solutions, increase the barrier by *ca.* 1 kcal/mol, while hydrogen bonding can increase the barrier by *ca.* 2–3 kcal/mol, compared to the barrier in a dilute solution in a nonpolar solvent. It is thus necessary to take cognizance of such effects, when comparing barrier values for different amides.

Substituent Effects. Voluminous data on the barrier to internal rotation in various amides are available; unfortunately, however, most of them are sufficiently unreliable, due to the use of approximate (single parameter) formulas for characterizing the line shapes of the exchange-broadened signals. Moreover, the use of various solvents for these studies militates against the direct comparison of barrier heights, even when the solvent is non-proton-donating.

(11) J. C. Chupp and J. F. Olin, *J. Org. Chem.*, **32**, 2297 (1967).(12) T. H. Siddall, III, E. L. Pye, and V. E. Stewart, *J. Phys. Chem.* **74**, 594 (1970).

The following discussion will therefore be based on data found for the 10 mol % solutions of DMA, DMP, DMiBu, and DMPiv in acetone-*d*₆ and for neat DMF. [When the capillary for the sample temperature measurement is inserted in the nmr tube, the acetone boils below 100°, even though the tube is sealed. It was therefore necessary to use alternate solvents for DMF.] As noted above, the barrier for the neat amide appears to be approximately equal to the barrier for the amide dissolved in acetone; it is, therefore, reasonable to use the data obtained from neat DMF in a comparison of barriers determined in acetone.

We estimate an uncertainty in $\Delta F_{298}^{\ddagger}$ of ± 0.1 and $+0.5$ kcal/mol for DMA, DMP, and DMiBu, and DMF and DMPiv, respectively. The larger uncertainty in the latter values, however, should not affect this discussion since the ΔF^{\ddagger} values for the latter are well separated from the former.

As seen from inspection of Table II, the barrier height to internal rotation in *N,N*-dimethylamides is affected by the substituent, R, decreasing in the order R = H, CH₃, CH₃CH₂, (CH₃)₂CD, and (CH₃)₃C. This trend is undoubtedly the result of a combination of steric, inductive, and hyperconjugative effects. From the present data, it is not possible to distinguish between inductive and hyperconjugative effects; however, from a comparison with the *cis*:*trans* isomer ratios for *N*-methylformamide (NMF) and *N*-methylacetamide (NMA) the steric effect for DMA can be approximated. Thus for both NMF and NMA, the *s-trans* diastereomer is seen to be the more stable by *ca.* 1.6^{13,14} and *ca.* 2.8^{14,15} kcal/mol, respectively; these ratios appear to be solvent independent.¹³⁻¹⁵ For NMF the stabilization of the *s-trans*, relative to the *s-cis* isomer may be the result of a net attractive interaction between the carbonyl oxygen and the *N*-methyl protons. *Ab initio* (LCAO-MO-SCF) calculations of the energy difference between the *s-cis* and *s-trans* conformers of methyl formate¹⁶ yield a similar result, namely that the *s-trans* conformer is *ca.* 9 kcal/mol lower in energy than the *s-cis* conformer. A component analysis indicates that this is due to a net electrostatic attraction between the carbonyl oxygen and the O-methyl protons. Additionally, it has been observed that the *s-cis* conformer of propionaldehyde is preferred by approximately 1 kcal/mol over the *s-trans* conformer.^{17,18} From these results we might therefore assume that the *s-cis*:*s-trans* ratio in NMF is primarily determined by net electrostatic attractions and that this attraction is the same for both NMF and NMA. Using this assumption it can then be concluded that, in NMA, the steric repulsion between a *cis N*-methyl and *C*-methyl is approximately 1-1.5 kcal/mol.

This values or a slightly higher value for the steric repulsion should also obtain for DMA. [DMA is more crowded about nitrogen than NMA; therefore, NMA has a greater possibility of being stabilized by small changes in the bond angles.] We believe that the *N*-methyl-*C*-methyl steric repulsion in the ground state of DMA decreases the barrier to internal rotation by *ca.* 1.5-2 kcal/mol relative to DMF, and that the inductive and/or hyperconjugative effects are responsible for the remaining *ca.* 1 kcal/mol. Preliminary data from this laboratory indicate that the free energy of activation for internal rotation in acetamide is *ca.* 1 kcal/mol lower than that for formamide.

The slight decrease in the barrier on going from DMA to DMP to DMiBu is probably the result of a combination of the above effects. From the available data, however, it is not possible to determine the individual contributions. For DMPiv, on the other hand, it is clear that the large decrease in barrier height, relative to the other amides, must be due to the steric repulsion between the *tert*-butyl and the *N*-methyl group protons.

In Table VII, the energies obtained from the extended Hückel calculations are given, from which it is apparent that parameter set *B* is in better agreement with experiment. The variation in the barrier to internal rotation caused by various substituents is, however, reflected in both these calculations. Scheraga, *et al.*,^{4,19} have carried out similar calculations using the extended Hückel (parameter set *B*) and CNDO methods; however, the angles, α , β , γ , and δ (see Table VI), were not varied. As a result they obtained no marked change in the barrier height on going from formamide to DMF, which demonstrates the necessity of minimizing the energy by varying the bond angles, to obtain the correct substituent effects; the difference between DMF and DMA was, however, approximately that found in our calculations.

Acknowledgment. We wish to thank Dr. W. Egan for helpful discussions and valuable linguistic criticism. This work was supported by a grant from the Swedish Natural Science Research Council.

(13) L. A. LaPlanche and M. T. Rogers, *J. Amer. Chem. Soc.*, **86**, 337 (1964).

(14) R. H. Baker and G. J. Boudreaux, *Spectrochim. Acta, Part A*, **23**, 727 (1967).

(15) T. Drakenberg and S. Forsén, *Chem. Commun.*, in press.

(16) H. Wennerström and S. Forsén, *J. Phys. Chem.*, in press.

(17) S. S. Butcher and E. B. Wilson, Jr., *J. Chem. Phys.*, **40**, 1671 (1964).

(18) G. J. Karabatsos and N. Hsi, *J. Amer. Chem. Soc.*, **87**, 2864 (1965).

(19) F. A. Momany, R. F. McGuire, J. F. Yan, and H. A. Scheraga, *J. Phys. Chem.*, **74**, 2424 (1970).

COMMUNICATIONS TO THE EDITOR

Identification of Reaction Intermediates by Microwave Spectroscopy. The Catalytic Reactions between Propylene and Deuterium over Zinc Oxide

Publication costs assisted by Sagami Chemical Research Center

Sir: It has been generally considered that the hydrogenation and isomerization of unsaturated hydrocarbons over various metals proceeds through the same reaction intermediate,¹ the half-hydrogenated state. The authors previously studied² the mechanism of the catalytic reaction between propylene and deuterium over ZnO and suggested that a π -allyl species was the reaction intermediate of the exchange reaction, on the basis of the deuterium distribution determined by microwave spectroscopy. The deuterium addition to propylene, on the other hand, seemed to proceed *via* interaction between the chemisorbed hydrocarbons and deuterium molecules in the ambient gas.

It is very interesting to note that the formation of a π -allyl species of zinc oxide has also been observed by Dent and Kokes³ by means of an infrared spectroscopic technique. Infrared spectroscopy is one of the most powerful techniques for studying the nature of surface species, but even if a certain chemical species is detected on the catalyst surface, it does not follow that it is necessarily a reaction intermediate. In this communication, the identification of the reaction intermediate in the propylene–deuterium exchange reaction over zinc oxide will be reported and the mechanism of the deuterium addition to propylene will also be discussed.

As described in the previous report,² the deuterium distribution of the product propylene- d_1 suggested that the reaction intermediate of the propylene–deuterium exchange reaction was a π -allyl species. In the initial stage of the exchange reaction, only propylene-3- d_1 ($H_3DC \cdot CH=CH_2$) was formed, but in the latter stages three kinds of monodeuteriopropylene, 3- d_1 , *cis*-1- d_1 , and *trans*-1- d_1 ($H_3C \cdot CH=CHD$), were formed in the approximate ratio of 3:1:1, while, propylene 2- d_1 ($H_2C \cdot CD=CH_2$) was not observed during the reaction. These results exclude the associative adsorption mechanism of propylene which would produce the half-hydrogenated state of the normal propyl or isopropyl radical, which would give propylene-2- d_1 (100%) or propylene-3- d_1 :*cis*-1- d_1 :*trans*-1- d_1 = 3:1:1, respectively. They also exclude the σ -allyl adsorption

mechanism because of the deuterium distribution of the d_1 species (and d_2 species) but the possibility of a concerted (push-pull) exchange mechanism remains.

To distinguish this mechanism from that of a π -allyl intermediate, the deuterium distribution in the propylene- d_2 was observed as shown in Figure 1. It is obvious from the figure that at the beginning of the reaction, propylene-1,3- d_2 ($H_2DC \cdot CH=CHD$) and propylene-3,3- d_2 ($HD_2C \cdot CH=CH_2$) are formed in equal amounts (50:50), which indicates that the 1 and 3 carbons of the propylene become equivalent in the reaction intermediate. These results exclude a concerted mechanism which would give only the 1,3- d_2 species of d_2 -propylene at the beginning of the reaction. These experimental results lead to the conclusion that the π -allyl species, which was detected on the catalyst surface by Dent and Kokes, is the real intermediate of the propylene–deuterium exchange reaction over ZnO.

On the other hand, in the deuteration of propylene over ZnO, propane- d_2 was predominant from the beginning of the reaction, which suggests that the π -allyl species is not the reaction intermediate in this process as discussed previously.^{2,3} To confirm this, the deuterium distribution of propane- d_2 was studied and is

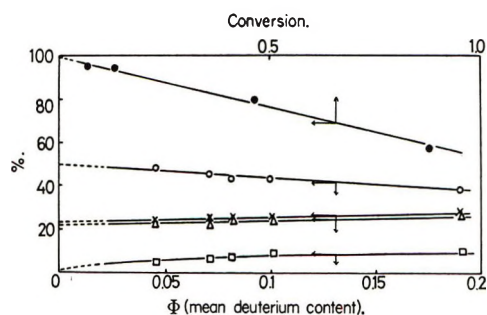


Figure 1. The deuterium distribution in propylene- d_2 and propane- d_2 molecules; $P_{C_3H_6} = P_{D_2} = 12.5$ cm, ZnO (10 g), room temp: O, $HD_2C \cdot CH=CH_2$ (3,3- d_2); Δ , $H_2DC \cdot CH=CHD$ (*cis*) (1,3- d_2); \times , $H_2DC \cdot CH=CHD$ (*trans*) (1,3- d_2); \square , $H_3C \cdot CH=CD_2$ (1,1- d_2); \bullet , $H_3C \cdot CHD \cdot CH_2D$ (1,2- d_2 -propane).

$$\Phi = \sum_{i=1}^6 id_i / 6 \sum_{i=0}^6 d_i$$

(mean deuterium content)

conversion = propane/(propylene + propane).

- (1) G. C. Bond, "Catalysis by Metals," Academic Press, London, 1962.
- (2) S. Naito, Y. Sakurai, H. Shimizu, T. Onishi, and K. Tamaru, *Trans. Faraday Soc.*, **67**, 1529 (1971).
- (3) A. L. Dent and R. J. Kokes, *J. Amer. Chem. Soc.*, **92**, 6709, 6718 (1970).

shown in Figure 1. This demonstrates that propane 1,2- d_2 ($\text{CH}_2\text{D}\cdot\text{CHD}\cdot\text{CH}_3$) is predominantly formed at the beginning of the reaction. These results indicate that propane- d_2 is formed by the simple addition of deuterium to the double bond of normal propylene or to the propyl group in the surface. Consequently, it is concluded that the hydrogenation and isomerization proceed through different reaction intermediates over zinc oxide.

Acknowledgment. The authors wish to thank Dr. Shuji Saito for his continuous help during the measurement of microwave spectra.

SAGAMI CHEMICAL RESEARCH CENTER
OHNUMA, SAGAMIHARA, KANAGAWA-KEN
JAPAN

SHUICHI NAITO*
TOSHIHIKO KONDO
MASARU ICHIKAWA

DEPARTMENT OF CHEMISTRY
THE UNIVERSITY OF TOKYO
HONGO, BUNKYO-KU, TOKYO, JAPAN

KENZI TAMARU

RECEIVED MARCH 16, 1972

Kinetic Oscillations in the Oxidation of 2,4-Pentanedione by Bromate Ion, Catalyzed by Manganese(II)

Publication costs borne completely by The Journal of Physical Chemistry

Sir: The increasing interest which is currently being shown in the oscillatory kinetics of Belousov's reaction (bromate oxidation of malonic acid)¹⁻³ prompts us to report our observations on a related system in which the organic acid is replaced by 2,4-pentanedione. Several novel features make the diketone oxidation worthy of attention, particularly since in contrast to both the malonate-bromate reaction and the well-known hydrogen peroxide-iodate reaction, no permanent gas is evolved, so that experiments can be conducted in a materially (if not thermally) "closed" situation.

Our chief findings may be most succinctly summarized as follows.

(i) In acid solution, with Mn(II) present, the bromate ion oxidation of 2,4-pentanedione proceeds in a periodic fashion. Fluctuations in the absorbance of the solution begin to build up immediately on mixing the reagents, as Figure 1 shows, with only a very brief induction period.

(ii) The reaction is affected by stirring in the sense that the oscillations damp away more rapidly if stirring is discontinued. We originally thought it possible that dissolved oxygen could be responsible for this effect in a system which was open to the atmosphere. However, a stirring effect exactly similar to that shown in Figure 1 was observed in a sealed system where the components had been rigorously degassed by standard

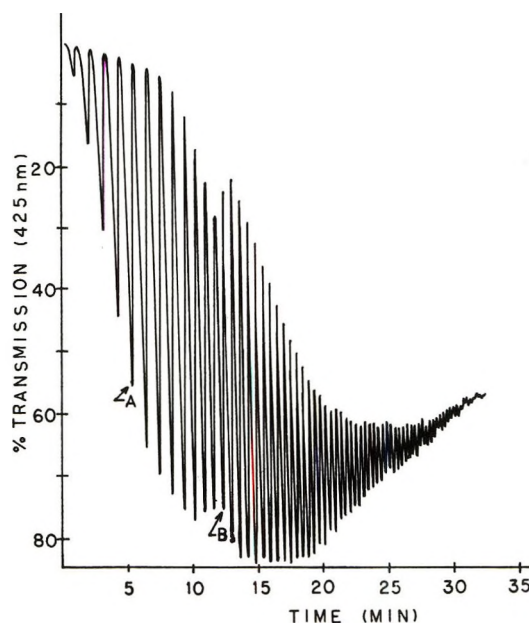


Figure 1. Transmission changes in a solution containing 2,4-pentanedione (0.05 M), MnSO_4 (0.017 M), and KBrO_3 (0.07 M) in 1 M H_2SO_4 at 25°, 8-cm light path. Magnetic stirring was stopped at A and restarted at B.

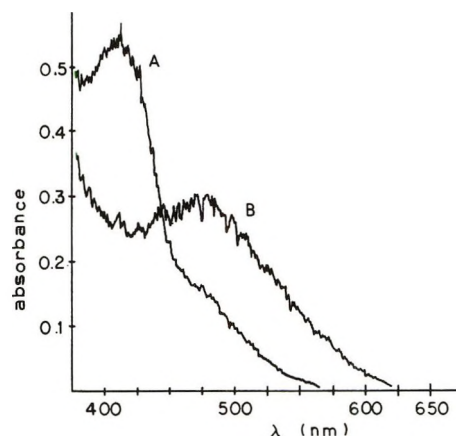


Figure 2. Spectra of the transient intermediates, obtained by the flow method. The initial concentrations after mixing for KBrO_3 , MnSO_4 , and 2,4-pentanedione were (A) 0.052, 0.037, 0.022 M and (B) 0.30, 0.42, and 0.025 M, respectively, in 1.5 M H_2SO_4 .

freeze-thaw-pump methods under high-vacuum conditions before mixing. We therefore conclude that the mechanism of this reaction includes at least one heterogeneous step which involves neither gas evolution nor the presence of atmospheric oxygen. The origin of the heterogeneity may be similar to that suggested by Kasperek and Bruice¹ for the cerium-catalyzed malonate-bromate reaction, namely transient formation

- (1) G. J. Kasperek and T. C. Bruice, *Inorg. Chem.*, **10**, 382 (1971).
- (2) A. N. Zaikin and A. M. Zhabortinski, *Nature (London)* **225**, 535 (1970).
- (3) R. M. Noyes, R. J. Field, and E. Kőrös, *J. Amer. Chem. Soc.*, **94**, 1394 (1972).

of a colloidal form of a complex of the catalyst ion. In addition, the temperature fluctuations recently found in reactions of this type⁴ raise the possibility that the systems are thermally (rather than chemically) heterogeneous.

(iii) Since there is no well-defined induction period, a simple flow method was used to obtain spectra of the colored intermediates. In these experiments, the components, after mixing, entered a flow-through cuvette in the sample compartment of a spectrophotometer. The two typical spectra shown in Figure 2 were obtained with a constant flow rate such that the reaction was monitored close to the maximum of the second or third oscillation. As Figure 2 shows, the color changes appear to be the result of two broad bands with maxima at 410 nm (yellow intermediate) and 475 nm (pink intermediate), respectively, which oscillate in phase but

with relative intensities which depend on initial concentrations of the reactants. The nature of the intermediates responsible for these spectra has not yet been established, although the position and shape of the pink band correspond closely to the spectrum of Mn(III) at the same acid concentration.

More detailed studies of this system, including characterization of the organic products, are continuing in this laboratory.

Acknowledgment. This work was supported by the Simmons College Fund for Research.

(4) U. Franck and W. Geiseler, *Naturwissenschaften*, **58**, 52 (1971).

DEPARTMENT OF CHEMISTRY
SIMMONS COLLEGE
BOSTON, MASSACHUSETTS 02115

PETER G. BOWERS*
KAREN E. CALDWELL
DEBORAH F. PRENDERGAST

RECEIVED APRIL 12, 1972

what's happening on the frontiers of chemical research?



*in short, critical articles
that cover all areas of
chemical research.*

Whether you are a practicing chemist, professor or student, you want to keep up with the latest developments. Yet few of you have the time to read thoroughly all the journals of primary publications.

ACCOUNTS fills the gap.

Written by investigators active in the fields reviewed, ACCOUNTS' concise, brief articles place recent developments in perspective—and relate them to earlier work and their probable future significance.

Once you start relying on ACCOUNTS to keep you informed, you'll wonder how you got along without its monthly arrival.

*Complete and mail back
the form below. We'll
prove how valuable this
publication can be to you.*

American Chemical Society / 1155 Sixteenth Street, N.W., Washington, D.C. 20036

Please send me ACCOUNTS OF CHEMICAL RESEARCH at the following subscription rates:

ACS members:	<input type="checkbox"/> U.S. \$ 5.00	<input type="checkbox"/> Canada, PUAS \$ 9.00	<input type="checkbox"/> Other Nations \$10.00
Nonmembers:	<input type="checkbox"/> U.S. \$15.00	<input type="checkbox"/> Canada, PUAS \$19.00	<input type="checkbox"/> Other Nations \$20.00

Name _____ Title _____

Employer _____

Address: Home Business _____

City _____ State/Country _____ Zip _____

Nature of employer's business? Manufacturing or processing Academic Government
 Other

(Please indicate)

Note: Subscriptions at ACS Member Rates are for personal use only.

I am an ACS member I am not an ACS member

Payment must be made in U.S. currency, by international money order, UNESCO coupons, U.S. bank draft; or order through your book dealer.

Here is the ideal way to obtain the most reliable reference data available today! All you need is a subscription to the new **JOURNAL OF PHYSICAL AND CHEMICAL REFERENCE DATA** published by the American Chemical Society and the American Institute of Physics for the National Bureau of Standards.

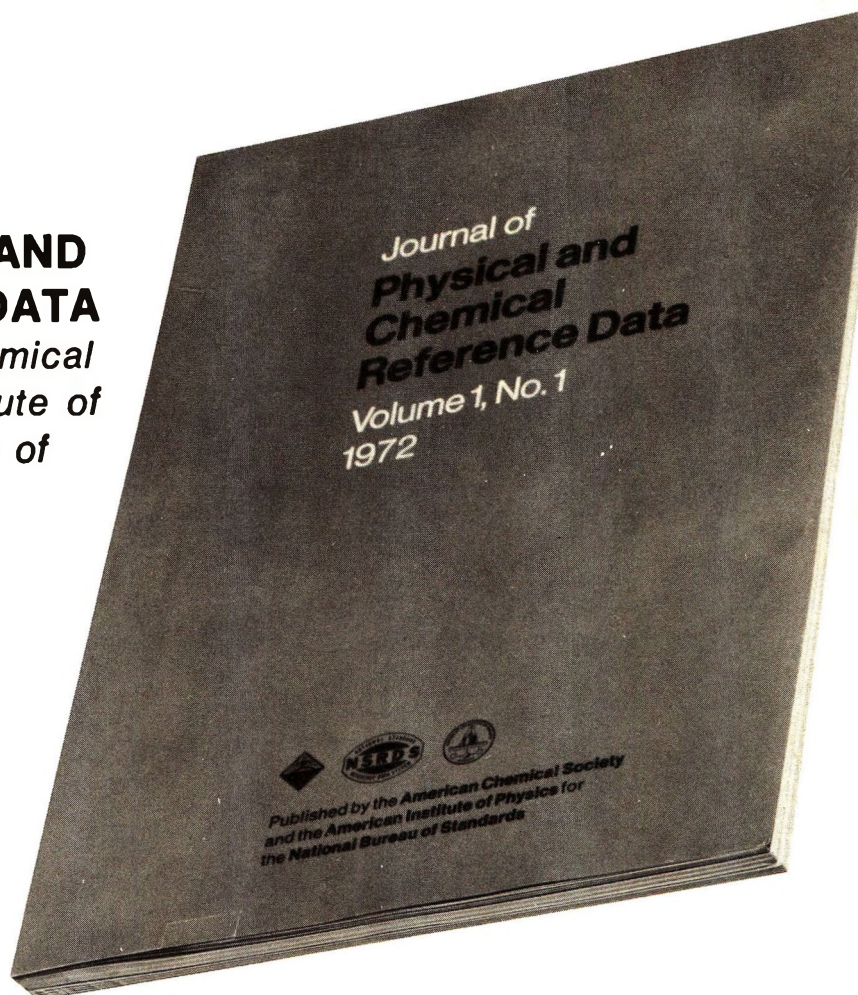
The *Journal of Physical and Chemical Reference Data* fills an important gap in the literature of the physical sciences. Its subject matter is the quantitative numerical data of physics and chemistry. As the new publication vehicle of the National Standard Reference Data System, the *Journal* will contain carefully evaluated data, with recommended values and uncertainty limits chosen by experts in each field. Critical commentary on methods of measurement and sources of error, as well as full references to the original literature, will be an integral part of each compilation.

Examples of some of the critical compilations scheduled for publication in the four issues of Volume 1 (1972) include:

- Tables of Molecular Vibrational Frequencies, Part 5, T. Shimanouchi
- Gaseous Diffusion Coefficients, by T. R. Marrero and E. A. Mason
- The Spectrum of Molecular Oxygen, by P. Krupenie
- Thermal Conductivity of the Elements, by C. Y. Ho, R. W. Powell and P. E. Liley
- Selected Values of Critical Supersaturation for Nucleation of Liquids from the Vapor, by G. M. Pound
- Gas Phase Reaction Kinetics of the Hydroxyl Radical, by W. E. Wilson, Jr.
- Selected Values of Heats of Combustion and Heats of Formation of Organic Compounds Containing the Elements CHNOPS, by E. S. Domalski
- Microwave Spectra of Molecules of Astrophysical Interest: Formaldehyde, Formamide, Thio-Formaldehyde, by D. R. Johnson, F. J. Lovas and W. H. Kirchhoff

Future compilations are expected to cover areas such as the following:

- Band gaps in semiconductors
- Nuclear moments
- Atomic energy levels and transition probabilities
- Diffusion in metals
- Electron swarm data
- Elastic constants of metals
- Surface tension of liquids
- Properties of molten salts
- Activity coefficients of electrolytes
- Equation of state of atmospheric gases
- Ionization and appearance potentials



The *Journal of Physical and Chemical Reference Data* is intended to be a definitive source of reliable data on physical and chemical properties. Just fill in the order form at the bottom of this page to receive this invaluable reference source.

JOURNAL OF PHYSICAL AND CHEMICAL REFERENCE DATA
AMERICAN CHEMICAL SOCIETY
1155 Sixteenth Street, N.W.
Washington, D.C. 20036

Yes, I would like to receive the JOURNAL OF PHYSICAL AND CHEMICAL REFERENCE DATA at the one-year rate checked below:

	U.S.	Canada	PUAS	Other Countries
AIP and ACS members	\$20.00	\$20.00	\$23.00	\$23.00
Nonmembers	\$60.00	\$60.00	\$63.00	\$63.00

Bill me Bill company Payment enclosed

Name _____

Street _____ Home
 Business

City _____ State _____ Zip _____